All of physics is either impossible or trivial.
It is impossible until you understand it, and then it becomes trivial.

– Ernest Rutherford (1871-1937)

The most incomprehensible thing about the world is that it is comprehensible.

– Albert Einstein (1879-1955)

University of Alberta

Fundamental Properties of Quantum Solid ^{4}He

by

James Christian Day

A thesis submitted to the Faculty of Graduate Studies and Research in partial fulfillment of the requirements for the degree of **Doctor of Philosophy**.

Department of Physics

Edmonton, Alberta
Spring 2008

Library and Archives Canada

Published Heritage Branch

395 Wellington Street
Ottawa ON K1A 0N4
Canada

Bibliothèque et Archives Canada

Direction du Patrimoine de l'édition

395, rue Wellington
Ottawa ON K1A 0N4
Canada

Your file Votre référence
ISBN: 978-0-494-45414-5
Our file Notre référence
ISBN: 978-0-494-45414-5

NOTICE:
The author has granted a non-exclusive license allowing Library and Archives Canada to reproduce, publish, archive, preserve, conserve, communicate to the public by telecommunication or on the Internet, loan, distribute and sell theses worldwide, for commercial or non-commercial purposes, in microform, paper, electronic and/or any other formats.

The author retains copyright ownership and moral rights in this thesis. Neither the thesis nor substantial extracts from it may be printed or otherwise reproduced without the author's permission.

AVIS:
L'auteur a accordé une licence non exclusive permettant à la Bibliothèque et Archives Canada de reproduire, publier, archiver, sauvegarder, conserver, transmettre au public par télécommunication ou par l'Internet, prêter, distribuer et vendre des thèses partout dans le monde, à des fins commerciales ou autres, sur support microforme, papier, électronique et/ou autres formats.

L'auteur conserve la propriété du droit d'auteur et des droits moraux qui protège cette thèse. Ni la thèse ni des extraits substantiels de celle-ci ne doivent être imprimés ou autrement reproduits sans son autorisation.

In compliance with the Canadian Privacy Act some supporting forms may have been removed from this thesis.

While these forms may be included in the document page count, their removal does not represent any loss of content from the thesis.

Conformément à la loi canadienne sur la protection de la vie privée, quelques formulaires secondaires ont été enlevés de cette thèse.

Bien que ces formulaires aient inclus dans la pagination, il n'y aura aucun contenu manquant.

Canada

Abstract

The recent torsional oscillator results of Kim and Chan seem to suggest a supersolid phase transition in solid ^{4}He, at 200 mK, confined in Vycor. We have used a capacitive technique to directly monitor density changes for ^{4}He confined in Vycor at low temperature and have used a piezoelectrically driven diaphragm to study the pressure-induced flow of solid ^{4}He into the Vycor pores. Our measurements showed no indication of a mass redistribution in the Vycor that could mimic supersolid decoupling and put an upper limit of about 3 nm/s on any pressure-induced supersolid flow in the pores of Vycor.

Torsional oscillator results later revealed that the effect also exists in the bulk solid, at 200 mK. We have (again) used a piezoelectrically driven diaphragm to study the flow of bulk solid ^{4}He through an array of capillaries. Our measurements showed no indication of low temperature flow, placing stringent restrictions on supersolid flow in response to a pressure difference. Any supersolid fraction present in the ^{4}He moves at a velocity less than 1.2×10^{-12} m/s, a value which is at least seven orders of magnitude smaller than the critical velocities inferred from the torsional oscillator measurements.

Contemporary experiments and theory now indicate that extended defects are somehow involved in the torsional oscillator results. Such defects should also affect the solids mechanical behaviour. Lastly, we report on a measurement of the shear modulus of solid ^{4}He at low frequencies and strains. We observe large increases below 200 mK, with the same dependence on measurement amplitude, ^{3}He impurity concentration and annealing as the decoupling seen in the torsional oscillator experiments. This unusual elastic behaviour is explained in terms of a dislocation network that is pinned by ^{3}He at the lowest temperatures but becomes mobile above about 100 mK. The frequency changes in the torsional oscillator experiments appear to be related to the motion of these dislocations, perhaps by disrupting a possible supersolid state.

I would like to dedicate this thesis to my parents, Sue and Fred, who taught me to think for myself.

Acknowledgements

The biggest thanks go to my supervisor, John Beamish, for his generous support, patience, and encouragement throughout the course of my degree. I couldn't have hoped for a better combination of mentor, colleague, and friend.

The expert technical assistance of Don Mullin, Greg Popowich, Tony Walford, Gilbert Lachat, Paul Zimmermann, and Boris Tomasevic was invaluable and greatly appreciated. I would also like to express my gratitude to Yolande Peske and Steve Rogers, for always providing me with liquid helium with a smile (even when the request was made with ridiculously short notice).

Special recognition is extended to Toby Herman and Alex Syshchenko for all of their help in and around the lab, and to my wife, Suzanne, for everything else.

Financial support for this work is gratefully acknowledged from the Natural Sciences and Engineering Research Council of Canada, as well as support from the University of Alberta.

Table of Contents

1 Introduction 1

2 Background 3
- 2.1 A brief history of helium . . . 3
- 2.2 Superfluidity in liquid ^{4}He . . . 5
- 2.3 Solid helium - some basics . . . 16
- 2.4 (Super)solid ^{4}He . . . 19
  - 2.4.1 The early years . . . 19
  - 2.4.2 The Kim and Chan renaissance . . . 23
  - 2.4.3 The later years . . . 29
- 2.5 Current state of the field . . . 42

3 Experimental Methods 44
- 3.1 Gas handling system . . . 44
- 3.2 Dilution refrigeration . . . 45
- 3.3 Pressure measurements . . . 50
- 3.4 Temperature measurements . . . 52
  - 3.4.1 Thermometry . . . 52
- 3.5 Computer control . . . 59

4 Dielectric Measurements of Helium Freezing in Vycor 60
- 4.1 Experimental design . . . 64
  - 4.1.1 Cell construction . . . 64
  - 4.1.2 Vycor sample . . . 64
- 4.2 Measurements in Vycor . . . 66
  - 4.2.1 Capacitance as a measure of density . . . 67
  - 4.2.2 Freezing and melting under confinement . . . 71
  - 4.2.3 Typical thermodynamic path . . . 75
- 4.3 Onset of freezing . . . 77
- 4.4 Hysteresis between freezing and melting . . . 80
- 4.5 At lower temperatures . . . 80
- 4.6 Conclusions . . . 87

5 Pressure Induced Flow of Solid Helium (Vycor) 89
- 5.1 Vycor experimental design . . . 89
  - 5.1.1 Cell construction . . . 90
  - 5.1.2 Piezo-mechanics . . . 90
- 5.2 Measurements in Vycor . . . 93

5.3 High temperature squeezing 94
5.3.1 Elastic response of Vycor to ΔP 95
5.3.2 Plastic response of Vycor to ΔP 97
5.4 Low temperature squeezing 101
5.5 Sensitivity to sample history 104
5.6 Conclusions 109

6 Pressure Induced Flow of Solid Helium (Bulk) 110
6.1 Bulk experimental design 110
6.1.1 Glass capillary array sample 111
6.1.2 Cell construction 113
6.2 Measurements in bulk (without GCA) 117
6.3 Measurements in bulk (with GCA) 122
6.4 High temperature squeezing 130
6.5 Low temperature squeezing 133
6.6 AC pressure induced flow 135
6.7 Conclusions 135

7 Shear Modulus Study of Solid Helium 139
7.1 Experimental design 140
7.1.1 Cell construction 140
7.1.2 PZT transducers 141
7.2 Measurements in sample 143
7.3 Shear modulus in gap 149
7.3.1 Sample 300ppb29.3 149
7.3.2 Sample 300ppb34.0 152
7.3.3 Sample 300ppb33.3 153
7.3.4 Frequency dependence 155
7.3.5 Amplitude dependence 156
7.3.6 Hysteresis 160
7.4 Acoustic resonance in cell 165
7.4.1 Acoustic resonance peak position 167
7.5 ^{3}He dependence 200
7.5.1 Acoustic resonance peak position at 1ppb ^{3}He 202
7.6 Annealing and stress effects 210
7.7 Discussion 222
7.7.1 Dislocation basics 223
7.7.2 Dislocation specifics 226
7.7.3 In summary 236

8 Summary 237
8.1 Summary of background material 237
8.2 Summary of experimental results 238
8.2.1 Dielectric measurements of helium freezing in Vycor 238
8.2.2 Pressure-induced flow of solid helium 240
8.2.3 Shear modulus study of solid helium 244

Bibliography 248

List of Tables

2.1 Basic quantum parameters for the inert gas solids 17
2.2 Estimates of the thermodynamic functions of solid ^{4}He along the melting curve 18

3.1 Fixed points of the ^{3}He melting curve 56
3.2 Fixed points of PLTS-2000 56

7.1 Simulation response of the lowest resonant mode to changes in the shear and bulk modulus 183

List of Figures

2.1 Phase diagram of ^{4}He 6
2.2 Normal and superfluid density of He II 9
2.3 Dispersion curve for liquid ^{4}He 14
2.4 Schematic of a torsional oscillator 24
2.5 Torsional oscillator with Vycor disk used by Kim and Chan 25
2.6 Torsional oscillator resonant period as a function of temperature of solid ^{4}He in Vycor glass 26
2.7 Torsional oscillator resonant periods as a function of temperature for a variety of solid helium samples 27
2.8 Newly proposed phase diagram of liquid and solid ^{4}He 28

3.1 Schematic diagram of the gas handling system 46
3.2 Phase diagram for a mixture of ^{3}He-^{4}He 47
3.3 Schematic dilution refrigerator operation 48
3.4 Vapour pressures of ^{3}He and ^{4}He 49
3.5 Schematic Straty-Adams pressure gauge 52
3.6 Germanium resistance thermometer 54
3.7 ^{3}He melting curve 55
3.8 ^{3}He melting curve thermometer 57
3.9 ^{60}Co nuclear orientation thermometer 59

4.1 Torsional oscillator measurement of H_2 in Vycor 61
4.2 Phase diagram of ^{4}He confined in Vycor 62
4.3 Molar volume change of ^{4}He confined in Vycor 63
4.4 Increased latent heat of freezing of ^{4}He confined in Vycor 63
4.5 Schematic of the freezing cell 65
4.6 Image of the freezing cell 65
4.7 TEM image of porous Vycor glass 66
4.8 Schematic of electrode deposition onto Vycor 67
4.9 Image of the Vycor capacitor 68
4.10 Schematic image of the Vycor capacitor 68
4.11 1.8 K ^{4}He adsorption isotherm in Vycor 70
4.12 Gibbs free energy of a nucleating spherical droplet 74
4.13 Phase diagram of ^{4}He confined in Vycor 74
4.14 Typical thermodynamic path 76
4.15 Density capacitance jumps 78
4.16 Solid-liquid density change associated with freezing 79
4.17 Hysteresis between melting and cooling 80

4.18 Vycor capacitance, from 4 K to 30 mK 81
4.19 Variation of the capacitance in Suprasil glass as a function of temperature 82
4.20 ^{4}He in Vycor at SVP 83
4.21 Density change of solid ^{4}He in Vycor at low T and at 36.6 bar . . . 84
4.22 Density change of solid ^{4}He in Vycor at low T and at 53.6 bar . . . 84
4.23 Low temperature stability of density at 36.6 bar 85
4.24 Low temperature stability of density at 57 bar 86

5.1 Schematic image of the Vycor squeezing cell 91
5.2 Image of the Vycor squeezing cell 91
5.3 Schematic of a piezo-electric single layer element 92
5.4 Image of the PZT stack 93
5.5 Density capacitance response of helium-filled Vycor to a rapid compression of the surrounding helium 94
5.6 Density capacitance during cooling at 36.2 bar and 54.0 bar 97
5.7 Determination of the activation energy of the quasi-particles in the pressure-induced flow of solid ^{4}He in Vycor 100
5.8 Density capacitance change for a compression at 88 mK 101
5.9 Density capacitance change for a compression at 75 mK 102
5.10 Density capacitance change for a compression at 101 mK 103
5.11 Deformation history dependence of pressure-induced flow 105
5.12 Thermal history dependence of pressure-induced flow 106
5.13 Overnight background drift 107
5.14 Squeezing during background drift at 1.9 K 108
5.15 Squeezing during background drift at 1.8 K 108
5.16 Squeezing during background drift at 1.5 K 109

6.1 SEM image of glass capillary array 111
6.2 Another SEM image of glass capillary array 112
6.3 Yet another SEM image of glass capillary array 112
6.4 Schematic for the bulk squeezing cell 114
6.5 Close-up schematic for the bulk squeezing cell 114
6.6 Image of the bulk squeezing cell 115
6.7 Block diagram for the bulk squeezing experiment 116
6.8 Schematic for the open squeezing cell 117
6.9 ^{4}He melting curve 118
6.10 Thermodynamic path for the solid ^{4}He sample in open squeezing cell 119
6.11 Pressure response to squeezes in open bulk cell containing solid ^{4}He at 1.60 K 120
6.12 Pressure response to squeezes in open bulk cell containing solid ^{4}He at 750 mK 121
6.13 Pressure response to squeezes in open bulk cell containing solid ^{4}He at 50 mK 121
6.14 Elastic deformation of solid helium in a channel 122
6.15 Pressure response to squeezes in liquid ^{4}He 125
6.16 Thermodynamic path for solid ^{4}He sample in open squeezing cell with GCA 126

6.17 Elimination of pressure gradients through annealing 126
6.18 Pressure response to squeezes in solid ^{4}He at 500 mK 128
6.19 Pressure response to squeezes in solid ^{4}He at 1.95 K 128
6.20 Linearity of the pressure response to the compressions as a function of applied voltage 129
6.21 Bulk ^{4}He: Temperature dependence of pressure response to a compression/decompression near the melting point of a 42.0 bar sample with a 0.3 ppm ^{3}He impurity concentration 131
6.22 Bulk ^{4}He: Temperature dependence of pressure response to a compression/decompression near the melting point of a 41.2 bar sample with a 0.3 ppm ^{3}He impurity concentration 132
6.23 Solid ^{4}He response at 500 mK and 35 mK 133
6.24 Solid ^{4}He response at 500 mK and 75 mK 134
6.25 Block diagram for the ac squeezing experiment 136
6.26 AC pressure response in solid ^{4}He at low temperatures 137

7.1 Schematic of the shear cell 141
7.2 Image of the shear cell 142
7.3 Block diagram for the shear experiment 144
7.4 Horizontal offset in the transducers 146
7.5 Liquid ^{4}He background signal in the shear cell 147
7.6 Raw signal of solid ^{4}He in the shear cell 148
7.7 Measurement of the shear modulus of solid ^{4}He 148
7.8 Thermodynamic path for sample 300ppb29.3 150
7.9 Shear modulus anomaly in sample 300ppb29.3 as a function of temperature, measured at 2000 Hz 151
7.10 Typical NCRI fraction (65 bar) in a torsional oscillator operating at 910 Hz 151
7.11 Thermodynamic path for sample 300ppb34.0 152
7.12 Shear modulus anomaly in sample 300ppb34.0 as a function of temperature, measured at 2000 Hz 153
7.13 Thermodynamic path for sample 300ppb33.3 154
7.14 Shear modulus anomaly in sample 300ppb33.3 as a function of temperature, measured at 2000 Hz 154
7.15 Shear modulus anomaly as a function of frequency 155
7.16 Shear modulus anomaly as a function of strain amplitude at 2000 Hz in sample 300ppb33.3 157
7.17 Shear modulus anomaly as a function of strain amplitude at 200 Hz in sample 300ppb33.3 158
7.18 Shear modulus anomaly as a function of strain amplitude at 200 Hz and 2000 Hz in sample 300ppb33.3 158
7.19 Shear modulus anomaly as a function of strain amplitude at 2000 Hz and 200 Hz in sample 300ppb33.3 at 18 mK 159
7.20 Behaviour of the shear modulus anomaly at 2000 Hz, cooled at high drive, as a function of decreasing and then increasing strain in sample 300ppm33.3 162

7.21 Behaviour of the shear modulus anomaly at 2000 Hz, cooled at low drive, as a function of increasing and then decreasing strain in sample 300ppm33.3 164
7.22 Behaviour of the shear modulus anomaly at 2000 Hz, cooled at high drive, as a function of decreasing and then increasing strain in sample 300ppm33.1 165
7.23 Behaviour of the shear modulus anomaly at 2000 Hz, cooled at low drive, as a function of increasing and then decreasing strain in sample 300ppm33.1 166
7.24 Behaviour of the resonance peak at 18 mK, as a function of drive amplitude 168
7.25 Behaviour of the resonance peak at 18 mK, at a drive amplitude of 1425.8 mV, 356.2 mV, and 34.6 mV 169
7.26 Behaviour of the resonance peak at 18 mK, at a drive amplitude of 34.6 mV, 10.9 mV, and 3.4 mV 169
7.27 Behaviour of the resonance peak at 18 mK, at a drive amplitude of 3.4 mV, 1.1 mV, and 332 μV 170
7.28 Behaviour of the resonance peak at 18 mK, at a drive amplitude of 332 μV, 102 μV, and 32 μV 170
7.29 Behaviour of the resonance peak at 18 mK, at a drive amplitude of 32 μV, 8 μV, and 2 μV 171
7.30 Hysteretic behaviour of the acoustic resonance at 126 mV drive amplitude and 50 mK, in sample 300ppb29.3 172
7.31 Hysteretic behaviour of the acoustic resonance at 760 μV drive amplitude and 50 mK, in sample 300ppb29.3 173
7.32 Non-hysteretic behaviour of the acoustic resonance at 22 μV drive amplitude and 50 mK, in sample 300ppb29.3 173
7.33 Acoustic resonance in sample 001ppb33.4 at 18 mK, scaled by its low drive amplitude 174
7.34 Acoustic resonance in sample 300ppb33.3 at 300 mK 175
7.35 Acoustic resonance in sample 300ppb33.3 at 300 mK, with an overlaid Lorentzian fit 176
7.36 Acoustic resonance in sample 300ppb33.3 at 18 mK 177
7.37 Acoustic resonance in sample 300ppb33.3 at 18 mK with a rough estimate of the true shape of the peak 178
7.38 Acoustic resonance in sample 300ppb33.3 at 18 mK, with an overlaid Lorentzian fit 179
7.39 Acoustic resonance in sample 300ppb33.3 as a function of temperature (from the "front") 180
7.40 Acoustic resonance in sample 300ppb33.3 as a function of temperature (from the "back") 181
7.41 Peak position of the acoustic resonance in sample 300ppb33.3 as a function of temperature, compared to the associated shear modulus anomaly 182
7.42 Dissipation in the acoustic resonance in sample 300ppb33.3 as a function of temperature, compared to its peak position 184
7.43 Change in dissipation of the acoustic resonance in sample 300ppb33.3 as a function of the scaled change in resonance frequency 185

7.44 Acoustic resonance in sample 300ppb34.0 at 300 mK 186
7.45 Acoustic resonance in sample 300ppb34.0 at 33 mK 187
7.46 Acoustic resonance in sample 300ppb34.0 at 18 mK, with an overlaid Lorentzian fit 188
7.47 Acoustic resonance in sample 300ppb34.0 as a function of temperature (from the "front") 189
7.48 Acoustic resonance in sample 300ppb34.0 as a function of temperature (from the "back") 190
7.49 Acoustic resonance in sample 300ppb34.0 compared to shear modulus anomaly 191
7.50 Acoustic resonance in sample 300ppb34.0 and its dissipation 191
7.51 Change in dissipation of the acoustic resonance in sample 300ppb34.0 as a function of the scaled change in resonance frequency 192
7.52 Acoustic resonance in sample 300ppb34.0 at 200 mK 193
7.53 Acoustic resonance in sample 300ppb34.0 at 33 mK 194
7.54 Acoustic resonance in sample 300ppb29.3 as a function of temperature (from the "front") 195
7.55 Acoustic resonance in sample 300ppb29.3 as a function of temperature (from the "back") 196
7.56 Acoustic resonance in sample 300ppb29.3 compared to shear modulus anomaly 197
7.57 Acoustic resonance in sample 300ppb29.3 and its dissipation 197
7.58 Change in dissipation of the acoustic resonance in sample 300ppb29.3 as a function of the scaled change in resonance frequency 198
7.59 Summary of the change in dissipation of the acoustic resonance as a function of the scaled change in resonance frequency 199
7.60 Shear modulus anomaly in solid ^{4}He at 2000 Hz, for different ^{3}He impurity concentrations 200
7.61 Shear modulus anomaly at 2000 Hz and NCRI at 1072 Hz in solid ^{4}He at 1 ppb ^{3}He impurity concentration 201
7.62 Shear modulus anomaly at 2000 Hz and NCRI at 910 Hz in solid ^{4}He at 0.3 ppm ^{3}He impurity concentration 202
7.63 Shear modulus anomaly as a function of frequency in an isotopically purified sample 203
7.64 Thermodynamic path for sample 001ppb33.4 204
7.65 Acoustic resonance in sample 001ppb33.4 at 150 mK 204
7.66 Acoustic resonance in sample 001ppb33.4 at 24 mK 205
7.67 Acoustic resonance in sample 001ppb33.4 as a function of temperature (from the "front") 206
7.68 Acoustic resonance in sample 001ppb33.4 as a function of temperature ("back") 207
7.69 Acoustic resonance in sample 001ppb33.4 compared to shear modulus anomaly 208
7.70 Acoustic resonance in sample 001ppb33.4 and its dissipation 208
7.71 Dissipation of the acoustic resonance in sample 001ppb33.4 as a function of the scaled change in resonance frequency f_r 209
7.72 Annealing time for sample 001ppb33.4 at 1.70 K 211
7.73 Effect of annealing on shear modulus anomaly in sample 001ppb33.4 211

7.74 Effect of annealing on resonant frequency in sample 001ppb33.4, at 25 mK 212
7.75 Effect of stressing on shear modulus anomaly in sample 001ppb33.4 . 213
7.76 Effect of stressing on resonant frequency in sample 001ppb33.4 . . . 214
7.77 Annealing time for sample 300ppb33.3 at 1.70 K 215
7.78 Effect of annealing on shear modulus anomaly in sample 300ppb33.3 216
7.79 Effect of annealing on resonant frequency in sample 300ppb33.3, at 18 mK 216
7.80 Effect of annealing on resonant frequency in sample 300ppb33.3, at 400 mK 217
7.81 Effect of stressing on shear modulus anomaly in sample 300ppb33.3 . 218
7.82 Effect of stressing on shear modulus anomaly in sample 300ppb33.3, with data shifted 219
7.83 Effect of annealing on shear modulus anomaly in sample 300ppb29.3 220
7.84 Effect of annealing on resonant frequency in sample 300ppb29.3, at 50 mK 221
7.85 Effect of annealing on resonant frequency in sample 300ppb29.3, at 200 mK 221
7.86 Effect of stressing on shear modulus anomaly in sample 300ppb29.3 . 222
7.87 Schematic of an edge dislocation 224
7.88 Schematic of dislocation movement 227
7.89 Schematic of a dislocation network, pinned at the intersection of dislocations 228
7.90 Schematic of a dislocation network, pinned at the intersection of dislocations and by ^{3}He impurity atoms 229
7.91 Bowed out dislocation 230
7.92 Schematic of a (cubic) dislocation network, pinned at the intersection of dislocations 234
7.93 Schematic of an "annealed" (cubic) dislocation network, pinned at the intersection of dislocations 235

Chapter 1

Introduction

For almost a century, physicists have wrestled with the baffling character of helium. Every other element embraces the solid phase at ambient pressure and the zero of temperature with the exception of helium. Below 2.17 K, ^{4}He undergoes the weirdest and most wonderful of transitions: it becomes a superfluid and flows with perfect ease. This occurs for quantum mechanical reasons as its atoms, especially compared to those of other elements, behave less like particles and more like quantum waves. At sufficiently low temperatures, many collapse into a single quantum wave in a process known as Bose-Einstein condensation; in this condition, the atoms don't simply perform as a whole, they become whole.

Since the late 1960s, theorists have speculated that something similar might happen in solid ^{4}He, made by pressurizing the low temperature liquid to twenty-five times atmospheric pressure. It was anticipated that such a transition would effectively cause the solid to possess superfluid-like properties; for that reason, the state was dubbed as 'supersolid'. Perhaps vacancies within the crystal could Bose-Einstein condense to form a free-flowing fluid of their own, which would mimic the flow of atoms through the liquid, or maybe even some of the atoms themselves undergo Bose-Einstein condensation. The counter-intuitive notion of supersolidity was breath-taking and mind-blowing. Unfortunately, no one had ever seen any hint of a flowing solid. Until recently, that is.

In 2004, results were published in support of a supersolid phase in ^{4}He. The concept of supersolidity was poised to become an empirical reality. Somehow, ^{4}He was proving to be more peculiar than we already knew it to be. The experiment which caused the stir was one in which solid ^{4}He was witnessed not to rotate as a solid body should (an effect observed and understood in the superfluid state).

Great science has since ensued, as the observation has been independently confirmed and other signatures of the remarkable behaviour have been sought. After all, extraordinary claims require extraordinary evidence.

The dilemma facing helium physicists today is multifaceted and far from cut-and-dry. While it could be argued that the key query is the nature of the supersolid mechanism, many physicists continue to reserve judgment about the supersolid interpretation until more evidence comes in. This dissertation should assist both camps, as the fundamental aim of this thesis is to provide a few more pieces of objective evidence to the puzzle.

Direction was provided through recognition of the limitations of and gaps in previous research, as well as the unresolved conflicts in the field that still require investigation. A torsional oscillator was the probe from which the supersolid interpretation sprang, based on inferential changes in density below 200 mK of the solid ^{4}He within; however, torsional oscillators are probes of both a sample's inertial and elastic properties. The ambition of our work was to rule out inertial-mimics and to directly probe the elastic properties of solid ^{4}He alone.

Thusly motivated, our experiments were intended to test the robustness of the supersolid claim and to provide scrutiny to some of the more obvious alternate explanations. With these aims, polycrystalline samples of ^{4}He were grown and studied. First, solidification under confinement was examined over a range of pressures as density changes associated with freezing and subsequent cooling in nanometer-sized pores was investigated between 30 mK and melting temperatures. Second, pressure-induced flow of solid ^{4}He was studied, both for ^{4}He confined to nanometer-sized pores and in bulk, and again at temperatures between 30 mK and melting. Finally, an investigation of the elastic properties was performed, as a direct measure of the shear modulus of bulk solid ^{4}He was made, as a function of temperature and frequency. The effects of ^{3}He isotopic impurity concentration, as well as measurement amplitude and thermodynamic history were also studied.

This dissertation is organized as follows. Chapter 2 presents background material covering a brief history of helium physics and an introduction to superfluidity and supersolidity (the motivating force behind this thesis). Chapter 3 is a description of the experimental techniques common to all experiments presented. Chapters 4, 5, 6, and 7 report and discuss our experimental results on solid ^{4}He. The essential results are summarized in Chapter 8.

Chapter 2

Background

Helium is an exceptional thing; this chapter is written to provide support for that claim and context for the research upon which this thesis is developed. We begin with a very brief history of helium physics. A whirligig tour through superfluidity is then provided, serving as a warm-up to the concepts and terminology encountered in the subsequent sections on quantum solids and supersolidity. The work presented here is discussed largely in chronological order, and touches on both theoretical and experimental studies. A comprehensive discussion is beyond the scope of this thesis, and the reviews by Meisel [1] and Prokof'ev [2] are brought to the attention of the interested reader. After having established the state of the field, the chapter concludes by introducing the questions broached by this thesis.

2.1 A brief history of helium

Helium was first created roughly 13.7 billion years ago, in the moments following the Big Bang. About 13.7 billion years later, in 1868 during a solar eclipse in India, French astronomer Pierre Jules César Janssen took careful examination of the solar chromospheric spectrum and, among many other bright lines, helium (from the Greek word "Helios", for Sun) was discovered. Over a quarter century elapsed before helium was found on Earth, in a sample of uranium ore by Sir William Ramsey, in 1895.

The story begins in earnest in the Netherlands. With the establishment of a cryogenic laboratory at the University of Leiden in the mid 1900s, Heike Kamerlingh Onnes was preparing to verify the van der Waals law of corresponding states over a large range of temperatures. His efforts to reach extremely low temperatures culminated in the liquefaction of ^{4}He in 1908. Using the Joule-Thomson effect,

Kamerlingh Onnes lowered the temperature of the ^{4}He down to 0.9 K, the coldest temperature ever achieved on earth at the time. It was on account of these low temperature studies that he was awarded the Nobel Prize in 1913 [3]. Kamerlingh Onnes pursued an extremely diverse program of investigations, including: thermodynamics; radioactivity; observations on optical, magnetic and electrical phenomena, such as the study of fluorescence and phosphorescence; the magnetic rotation of the polarization plane; absorption spectra of crystals in a magnetic field; the Hall effect; dielectric constants; and especially the resistance of metals. In 1911, following the observation of persistent electrical currents, Kamerlingh Onnes uncovered the superconducting nature of pure metals such as mercury, tin and lead at very low temperatures. Essentially all of his work gradually gained importance and international fame; pertinent to this thesis, it was breaking the 1 K barrier that allowed for the birth of helium physics.

Three decades passed before the superfluid properties of ^{4}He were concomitantly discovered in 1938 by John Allen and Don Misener [4], publishing experimental evidence that the hydrodynamics of liquid helium were not classical below 2.2 K, and by Pyotr Kapitza [5] (in the same issue of Nature) observing frictionless flow and through introduction of the term "superfluid" to qualify this anomalous behaviour. The 30 year gap between the liquefaction of ^{4}He and the discovery of superfluidity was likely due in combination to the great interest generated by superconductivity and the relatively small number of researchers actually working on low temperature studies at the time. Kapitza was awarded the Nobel Prize in Physics in 1978 for his low temperature research [3], shared with Penzias and Wilson (who won for their discovery of the cosmic microwave background radiation). Although they made essentially the same discovery as Kapitza, Allen and Misener did not receive a Nobel Prize: Kapitza is generally the one credited with the discovery of superfluidity.

As the empirical evidence supporting a superfluid state began to grow, theoretical work began in an effort to (best) explain and understand this new and highly unusual state of matter. Later in 1938, Fritz London [6] worked out the theory of an ideal Bose-Einstein gas, explaining the phenomenon of superfluidity in terms of Bose-Einstein condensation (BEC). (Almost 70 years later, the connection between superfluidity and BEC is still a matter of debate and study.) Laszlo Tisza [7] carried the argument further by suggesting a phenomenological representation of superfluidity, the "two-fluid model" for liquid ^{4}He. This particular suggestion was

also made independently and worked out in considerable detail by Lev Landau [8] three years later, in 1941. Landau was awarded the 1962 Nobel Prize for Physics for his pioneering theories for condensed matter, especially liquid helium [3]. Without a doubt, ^{4}He was weird and worth studying.

Countless experiments on ^{4}He followed over the next half century. Studies on the liquid state consistently provided results which astounded researchers with their counterintuitive character. Beyond its zero-viscosity state, other notable features include: persistent mass currents; superfluid film flow and self-emptying beakers; high thermal conductivity (tending to infinity for small heat currents); thermo-mechanical effects; second-, third- and fourth-sound; quantized vortices; and irrotational flow.

Compared to its liquid counterpart, solid ^{4}He seemed to be a relatively normal substance, although it had been shown to possess some unique characteristics and interesting features. For example, it is the only element which requires substantial pressures to solidify, even at absolute zero. Additionally, solid ^{4}He has a large molar volume and is accompanied by an exceptionally high compressibility. It wasn't until 2004 that Eun-Seong Kim and Moses Chan of Pennsylvania State University observed phenomena [9, 10] in solid ^{4}He that got scientists wondering if helium physics was on the verge of capturing yet another Nobel Prize.

2.2 Superfluidity in liquid ^{4}He

Before diving deep into the subject of superfluidity in solids, it is helpful to first wade through some of the basics of superfluidity in liquids (a somewhat less counterintuitive phenomenon). This section does just that, identifying the necessary concepts and terminology, and providing a roller-coaster introduction to superfluidity in liquid ^{4}He; those seeking for depth with breadth are directed to standard reference books [11, 12, 13].

Immediately below its boiling point, ^{4}He behaves as an ordinary liquid with a small viscosity. However, at 2.17 K it undergoes an unusual transition. This transition is signalled by a specific heat anomaly, whose characteristic shape has led to the name "λ-point" being given to the temperature (T_λ) at which it occurs. Observation of the liquid through this transition reveals a remarkable alteration in its appearance. Above T_λ, vapour bubbles form within the liquid in the customary way and the whole liquid is violently agitated (simple boiling at reduced pressures).

Once the transition point is reached, however, the liquid becomes absolutely still and no more bubbles are formed. We infer that T_λ marks the transition between two different forms of liquid, as shown in Figure 2.1, conventionally referred to as He I (the normal fluid) above T_λ and He II (the superfluid) below it. He I behaves in the normal fashion of a low-viscosity low-density liquid, but the properties of He II are strikingly different. The quantum nature of He II is unarguably bizarre and many of the phenomena it displays are aptly described as "super".

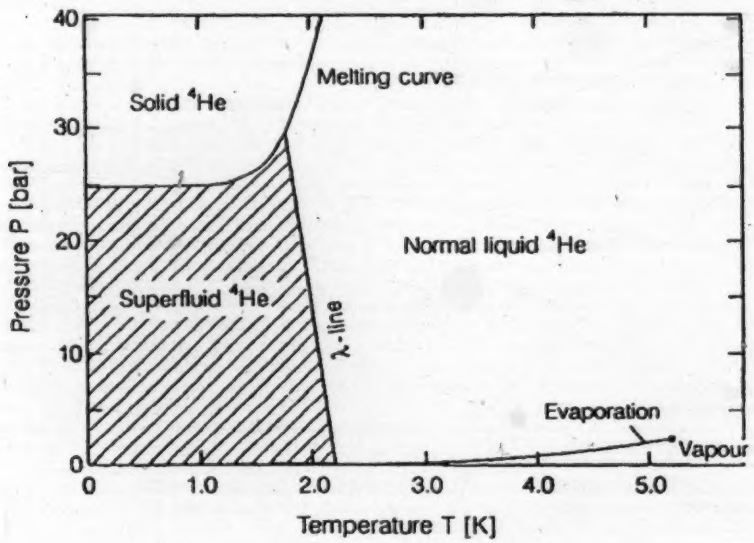

Figure 2.1: Phase diagram of ^{4}He [11].

One of its most unusual properties is revealed when its viscosity is measured. Experiments to determine the viscosity of He II can be divided into two classes: those designed to measure viscous resistance to flow, and those which detect the viscous drag on a body moving through the liquid.

Results typical of the former method come from flow viscometry experiments which measure the flow velocity of He II through narrow channels of varying widths (a flow viscometer). In experiments of this sort, the flow rate is found to be almost independent of the pressure along the channel [14]. In fact, the flow is found to be

very much larger than that expected from measurements above T_λ. And not only is it not proportional to applied pressure, but the flow becomes large at the smallest applied pressure difference and then saturates, staying effectively constant when further pressure is applied. Of course, the flow is clearly limited by other effects, which we will discuss shortly. Clearly, though, this suggests that the viscosity of He II is virtually zero. This zero-viscosity conclusion is supported by persistent current measurements [15]. In these, a liquid ^{4}He-filled torus-shaped vessel was set into rotation; when the vessel was brought to rest, the He II continued to flow, showing no reduction in angular velocity over a twelve-hour period, and indicating that He II can flow without dissipation.

Results typical of the latter method involve rotation viscometers. In these, a solid cylinder is made to rotate while submerged in a bath He II, the torque applied to the cylinder providing a measure of the viscosity of the fluid in which it is submerged. Experiments of this sort demonstrate the existence of a viscous drag [16]. Somehow, strangely, He II is capable of being both viscous and non-viscous at the same time.

This apparent contradiction is the essence of the two-fluid model [7], in terms of which many of the properties of He II can be explained. According to this model, He II behaves as if it were a mixture of two liquids: one, the normal fluid, possessing an ordinary viscosity ($\eta_n \neq 0$); the other, the superfluid, being capable of frictionless flow past obstacles and through narrow channels ($\eta_s = 0$). Each have their own effective density, such that the total density of the fluid is constant ($\rho = \rho_n + \rho_s$), and the normal fraction is the fluid component which carries entropy ($S_n \neq 0$ and $S_s = 0$). He II is also capable of two different motions at the same instant. Each have their own distinct local velocity, so that the total current density is given by the sum of the products of the density and velocity of each fraction ($\mathbf{j} = \rho_n \mathbf{v}_n + \rho_s \mathbf{v}_s$). (This approach, in which the two fluids are treated independently, is most useful when the velocities are small. At higher velocities, the superfluid flow becomes dissipative, the normal fluid exhibits turbulence, and there is the possibility of interaction between the two. When these factors are allowed for, the two-fluid equations become rather complicated. But, for small velocities, these hold.) To avoid any misunderstanding, however, it must be clearly stated that the two fluids cannot be physically separated; it is not permissible even to regard some of the atoms as belonging to the normal fluid and the remainder to the superfluid. ^{4}He atoms are bosons, and therefore are all identical.

In the light of the two-fluid model, the seemingly discrepant results from the viscosity measurements described above make sense. In any mixture of two fluids, the viscosity as measured by the flow viscometer must be dominated by the smaller of the two viscosities, since the "thinner" fluid can find its way through the narrow tube much more readily than the "thicker" one. On the other hand, the viscosity as measured by the rotation viscometer will be dominated by the larger of the two viscosities, since the large drag force exerted by the "thicker" fluid will prevail over the smaller force of the "thinner" one.

The validity of the two-fluid model is most strikingly demonstrated in the experiment devised by Andronikashvili [17], in which a pile of closely- and equally-spaced thin metal discs were suspended by a torsion fibre and made to perform oscillations in liquid helium. The period of the oscillations in such a torsional pendulum is given by $P = 2\pi(I/\kappa)^{1/2}$, where I is the moment of inertia of the system and κ is the torsion constant of the fibre. The moment of inertia has a component that comes from the pendulum itself, I_{osc}, and a component that comes from whatever helium mass is being dragged with it, I_{He} (i.e., $I = I_{osc} + I_{He}$). The two-fluid model predicts that only the normal fluid fraction can contribute to the moment of inertia of the pendulum ($I_{He} \propto \rho_n = \rho_{He} - \rho_s$). As the low temperature density of liquid helium is essentially constant, any observed change in the period of oscillations is equal to a change in the density of the normal fluid component, and therefore to the negative change in the density of the superfluid component ($\Delta P \propto -\Delta\rho_s$). The disc spacing was sufficiently small to ensure that above T_λ all the fluid between the discs was dragged with them. However, below T_λ the period of oscillation decreased sharply, indicating that not all the fluid in the spaces was being entrained by the discs. This result confirmed the prediction that the superfluid fraction would have no effect on the torsion pendulum. The experiment gives a direct method of measuring the variation of ρ_n with temperature and, by inference, ρ_s, as shown in Figure 2.2. Note that He II is almost entirely superfluid below 1 K.

Early experiments designed to measure the thermal conductivity of He II showed that it is very high, tending to infinity for small heat currents. In fact, it is not possible to establish a temperature gradient in bulk superfluid helium (a result which explains the sudden cessation of boiling as the liquid is cooled through T_λ). In an ordinary liquid (like the normal fluid phase of helium), a bubble forms when the local temperature is sufficiently greater than that at the free surface. In He II,

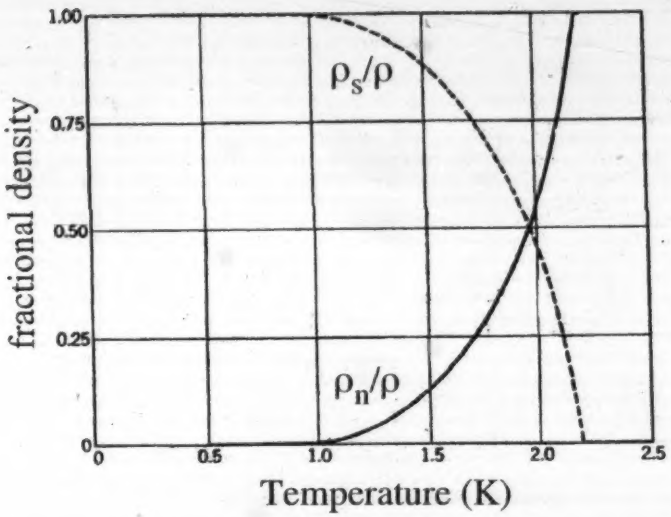

Figure 2.2: Normal and superfluid density of He II according to the two-fluid model, as inferred from period changes in a torsional oscillator experiment. Modified from [11]

supposing that a large enough temperature fluctuation were to occur, it would decay so quickly that a bubble would not appear. Therefore, evaporation of He II takes place only at the free surface.

A temperature gradient can be set up between two volumes of bulk He II provided that they are connected only by a superleak (i.e., a channel through which only the superfluid component can flow). A common form of superleak is a tube packed tightly with fine powder: the spaces between the particles form winding channels of varying width (typically about 100 nm) which allow the superfluid to pass but clamp the normal fluid in place. If heat is supplied to one side of the superleak, a pressure head is set up as well as a temperature difference. This happens because the superfluid fraction flows from the low temperature side to the high temperature side of the superleak. Since ρ_s/ρ increases with decreasing temperature, we infer that the superfluid moves to the region of higher temperature in order to reduce the temperature gradient.

Such manifestation of the thermo-mechanical effect shows clearly that heat transfer and mass transfer in He II are inseparable. The steady supply of heat to the bulk liquid, achieved, for example, by passing a direct current through a resistor, and its

removal elsewhere into a constant-temperature reservoir cause internal convection. Normal fluid flows from the source to the sink of heat, whilst superfluid flows in the opposite direction, under the constraint that the total density remains constant everywhere (i.e., counterflow of ρ_s and ρ_n). Thus heat is not transferred in He II by the ordinary process of conduction and simple convection of the whole fluid. Only the normal fluid fraction carries heat; superfluid flow by itself cannot transport heat.

When the heat supply is made to vary periodically, by passing alternating current through the resistor, the two fluids can be made to oscillate in anti-phase with one another. Once more, this has no effect on the total density ρ which remains constant throughout. The result is that the local value of ρ_s/ρ (and, consequently, the local temperature) undergoes oscillations. In this way, He II is able to propagate temperature waves, called second-sound (distinguished from first-sound, the ordinary longitudinal pressure waves involving fluctuations in the total density at constant temperature).

In addition to first- and second-sound in He II, two other unattenuated modes of wave propagation in this liquid are possible. Both are characterized by the fact that the normal component of the fluid is locked in place and only the superfluid component oscillates in the wave propagation. Third-sound occurs in the film adsorbed on a surface and is an oscillation of the thickness of the film (in which the temperature and pressure variations are small). Fourth-sound is a bulk effect and is a compressional wave of only the superfluid component in a superleak material.

More fundamental than the absence of dissipation, however, is the behavior of a superfluid under rotation. If we consider a rotating vessel, the normal fluid behaves in the expected way, undergoing solid-body rotation. The superfluid, on the other hand, experiences vortex motion: a series of vortex lines threads the fluid in the rotating vessel. Superfluid rotates around each vortex line and the angular momentum associated with each vortex is quantized.

Another rotation-related phenomena, and most apposite to this thesis, is non-classical rotational inertia (NCRI). NCRI is (essentially) the failure of a superfluid to rotate with its container. However, there is more to it than simply that. The phenomenon of NCRI is, by definition, characteristic of the equilibrium state of the system, and is quantum-mechanical in origin; it should be carefully distinguished from the apparently similar phenomenon of persistent currents, which is a metastable effect [18]. To help understand some of the subtleties involved, we consider some of

the rotational properties of a superfluid. We will begin by performing some thought experiments with a narrow annular channel; if the annulus is filled with ^{4}He, then we can observe two conceptually distinct (though related) phenomena.

The first is true NCRI (i.e., the Hess-Fairbank effect [19]) and occurs when the system appears to come out of equilibrium with its container. To better illuminate this definition, imagine taking an annulus filled with water and setting it on an old-fashioned turntable, which is then set into rotation. After some relatively short period of time, the water will come into rotation with the annulus and will thereafter rotate with it, as long as the turntable continues to rotate. When the rotation is halted, the water will also then gradually come to rest.

Imagine now that we do the same experiment with liquid ^{4}He, starting above T_λ and rotating *very* slowly. The ^{4}He behaves in exactly the same way as the water, gradually coming into rotation with its container. Now suppose that, while still rotating with this very low angular velocity, we cool the system through T_λ. At first, the liquid ^{4}He *appears* to come out of equilibrium with the container as we cross the lambda line (i.e., to cease to rotate even though the container is still rotating). In fact, as we reduce the temperature of our system to zero, the liquid ^{4}He appears to come completely to rest in the frame of reference of the laboratory. It is clear that this behaviour cannot simply reflect very long relaxation times, since it is the liquid which has come out of equilibrium from the container: the "non-rotating" state must be the true thermodynamic state. This is the exact analogue of the Meissner-Ochsenfeld effect in a superconductor [20], in which magnetic field lines are excluded from the superconductor when it is cooled to below its critical temperature. It becomes convenient to define the superfluid fraction f_s of liquid ^{4}He in terms of the experimentally observed value of the temperature dependent moment of inertia, relative to its classical value, $I(T) = I_{classical}[1 - f_s(T)]$.

The second phenomenon is the following. Again, imagine an annulus filled with liquid ^{4}He and at a temperature above T_λ. The system is once more set into rotation, but this time at a significantly greater angular velocity. As we cool through T_λ, we now see very little change: for all intents and purposes, the liquid continues to rotate with its container. The difference arises when we then stop rotating our container: the liquid ^{4}He within continues to rotate, apparently indefinitely. It can be shown that for the container stationary the rotating state cannot be the thermodynamic equilibrium one, so what we are seeing here is an example of an extremely long-lived

metastable state, sometimes referred to as metastability of superflow.

A phenomenological understanding of both the Hess-Fairbank effect and the metastability of superflow may be obtained if two separate assumption are made. First, that the atoms in a condensate can have only integral values $\ell\hbar$ of their angular momentum, corresponding in the annular geometry to an angular velocity of rotation $\ell\hbar/mR^2 = \ell\omega_c$. Second, that the passage of an atom from one value of ℓ to another is impeded by a high free-energy barrier. Then it is intuitively plausible that on cooling through T_λ with $\omega \ll \omega_c$ the condensate will prefer to come to rest. On the other hand, if the angular velocity of the container is $\gg \omega_c$, say $n\omega_c$, where n is not necessarily an integer, then on cooling through T_λ the condensate will simply "choose" the value of ℓ that most closely matches its angular velocity to the container; in particular, if the latter is $\gg \omega_c/2$, the condensate will simply choose the integer ℓ closest to n, and the difference between ℓ and n will be barely observable, so that the liquid appears to continue to rotate with the container. However, when the rotation stops the free-energy barrier prevents relaxation back down to $\ell = 0$.

Superfluidity is a quantum mechanical effect and it is clear that the pure superfluid constitutes the ground state of He II. The ^{4}He atom has a resultant spin of zero, and is therefore a boson; an assembly of ^{4}He atoms is governed by Bose-Einstein statistics. As is well-known, an ideal boson gas of particles with non-zero rest mass exhibits the phenomena of BEC. At low temperatures, the particles crowd into the same quantum state, corresponding to the lowest single-particle energy level of the system, forming a condensate. The crucial distinguishing feature of a Bose-Einstein condensate is that the many parts that make up an ordered system not only behave as a whole, they become whole; their identities merge or overlap in such a way that they lose their individuality entirely. The condensation begins at the critical temperature and is complete at absolute zero. Liquid ^{4}He behaves in the same way, in that T_λ is the temperature which marks the onset of condensation and the condensate is associated with the superfluid fraction of He II. The existence of a condensate and its correlation with the occurrence of superfluidity is something to be kept in mind. It is also worth noting that many of the effects described above are also seen in BEC of gases.

So far, however, we have really just considered the particles in the ground state of a superfluid system (i.e., the condensate) and it seems plausible that a superfluid current is to be equated with motion of the condensate. While the existence of a

condensate is a necessary condition for superfluidity to occur, it is not a sufficient condition. Whether or not superflow can happen depends additionally on the nature of the thermally excited states. The excitation spectrum of He II, commonly referred to as the Landau curve, is shown in Figure 2.3 (as obtained from neutron-scattering experiments [21], and as suggested by Landau [8]).

The excitation spectrum is sharply defined, indicating that the excitations are long-lived (however, as the temperature is increased above 1.2 K, the spectrum develops a width and becomes progressively less well-defined, a consequence of the rapid growth of the number of excitations and the frequency of collisions between them). The existence of the finite energy gap for these excitations at ~ 2 Å^{-1}, called rotons, is crucial for the occurrence of superfluidity. At temperatures well below T_λ, this excitation spectrum is sufficient to account for the thermal properties of He II. In particular, it implies that there are no other excitations in He II with a spectrum lying below the Landau curve; this specifically excludes free-particle motion. With that, it is possible to derive what is known as the Landau criterion for superfluidity and apply it the excitation spectrum of He II.

Imagine a body of large mass M moving at velocity $\mathbf{V_i}$ through a volume of He II, at a low enough temperature so that it is effectively pure superfluid. So long as $\mathbf{V_i}$ is low enough, the body will experience no drag from the superfluid. This will change only when $\mathbf{V_i}$ reaches a critical value v_{Landau} at which it is possible for an excitation to be created out of the superfluid. This will cause a loss in the kinetic energy of the body, which is dissipated in the form of thermal excitation energy, that is as heat. Thus, as soon as it reaches v_{Landau}, the body begins to suffer drag. In order to determine v_{Landau}, we need to find the minimum value of $\mathbf{V_i}$ at which an excitation can appear. Suppose that the creation of one excitation with energy $\varepsilon(\mathrm{p})$ and momentum $\mathbf{p}$ causes the body's velocity to decrease from $\mathbf{V_i}$ to $\mathbf{V_f}$. Conservation of energy and of momentum imply

$$\frac{1}{2}M\mathbf{V_i}^2 = \frac{1}{2}M\mathbf{V_f}^2 + \varepsilon(\mathrm{p}) \tag{2.1}$$

and

$$M\mathbf{V_i} = M\mathbf{V_f} + \mathbf{p}. \tag{2.2}$$

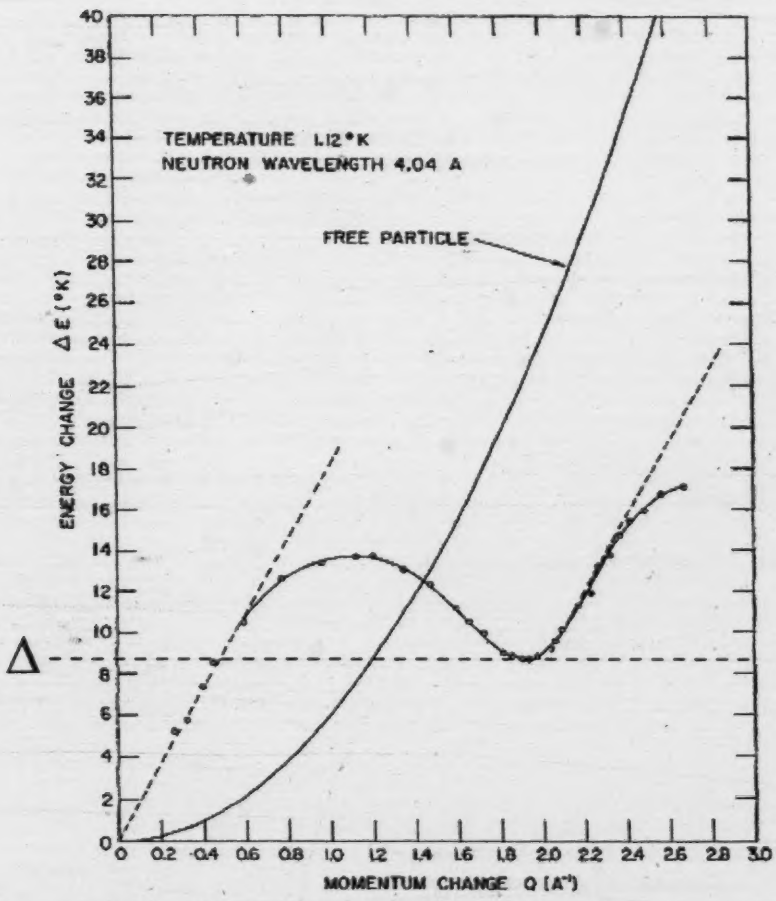

Figure 2.3: Dispersion curve for liquid ^{4}He at 1.12 K, under it normal vapour pressure [21]. The parabolic curve rising from the origin represents the theoretically calculated dispersion curve for free helium atoms at absolute zero. The open circles correspond to the energy and momentum of the measured excitations. A smooth curve has been drawn through the points as a guide to the eye. The broken curve rising linearly from the origin is the theoretical phonon branch calculated from a velocity of sound of 237 m/s. The dotted curve drawn through the point 2.27 Å^{-1} has been drawn with a slope equal to the velocity of sound.

Together, Equations 2.1 and 2.2 give

$$\varepsilon(\mathrm{p}) - \mathbf{p} \cdot \mathbf{V_i} + \mathrm{p}^2/2M = 0. \tag{2.3}$$

If we then assume that M is large enough that the last term in Equation 2.3 can be neglected, and with θ as the angle between $\mathbf{p}$ and $\mathbf{V_i}$, we then have

$$\mathrm{p}\ V_i\ cos\ \theta = \varepsilon(\mathrm{p}) \tag{2.4}$$

and since $\cos\theta \leq 1$, the condition

$$V_i \geq \frac{\varepsilon(\mathrm{p})}{\mathrm{p}} \tag{2.5}$$

must be satisfied in order for an excitation to be created. Thus, the critical velocity, $\mathrm{v}_c = \mathrm{v}_{Landau}$, is given by

$$\mathrm{v}_{Landau} = \left[\frac{\varepsilon(\mathrm{p})}{\mathrm{p}}\right]_{min}. \tag{2.6}$$

Superfluidity can therefore occur if

$$\mathrm{v}_{Landau} > 0, \tag{2.7}$$

a condition which is known as the Landau criterion for superfluidity [8]. Minimum values of $\varepsilon(\mathrm{p})/\mathrm{p}$ are found when

$$\frac{d\varepsilon(\mathrm{p})}{d\mathrm{p}} = \frac{\varepsilon(\mathrm{p})}{\mathrm{p}}. \tag{2.8}$$

There are two solutions for Equation 2.8 on the He II excitation curve. One occurs at the origin (and at all points of the linear part of the spectrum). In this region

$$\mathrm{v}_{Landau} = \frac{\varepsilon(\mathrm{p})}{\mathrm{p}} = 239 \text{ m/s (phonons)}, \tag{2.9}$$

which indicates that the critical velocity for the creation of phonons is the velocity of first sound. The second solution occurs when the straight line passing from the

origin to the curve near the roton minimum touches the excitation spectrum. From this we obtain

$$v_{Landau} \simeq \frac{\Delta}{p} = 58 \text{ m/s (rotons)}. \tag{2.10}$$

If we apply this treatment to the excitation spectrum of the free particle (a parabola), the condition of Equation 2.8 is satisfied only at the origin, giving

$$v_{Landau} = 0 \text{ m/s (free particles)}. \tag{2.11}$$

A Landau velocity of zero means that superfluidity is impossible in any system where free particle motion can take place. Thus it is the energy gap Δ, together with the lack of any other thermal excitations below the Landau curve, which ensures a finite value of v_{Landau} in He II.

2.3 Solid helium - some basics

With the necessary concepts and terminology for superfluids now in place, we will shift our focus to the solid phase.

Solid helium is also a rather unusual thing. It behaves quite differently from the heavier inert gas solids (Ne, Ar, Kr, Xe) and solid helium is a uniquely 'quantum' (as opposed to 'classical') solid. Its inimitable nature can be recognized without looking beyond the phase diagram, as presented back in Figure 2.1.

A key feature of the phase diagram is that liquid ^{4}He does not freeze when cooled under its vapour pressure (the helium isotopes are unique in this regard). In fact, solid ^{4}He is only stable under a pressure of at least 25 bar. This reluctance to solidify results from a combination of two factors: weak binding forces between helium atoms and significant non-thermal energy of helium atoms.

^{4}He atoms possess filled, spherically-symmetric electronic shells and, as a result, the van der Waals attraction between atoms is weak. Moreover, ^{4}He atoms are subject to two distinct forces in the limiting cases of large and short distance, as are all neutral atoms. At long range there exists an attractive force (the van der Waals attraction), and at short range there exists a repulsive force (the result of overlapping electron orbitals, referred to as Pauli repulsion). The Lennard-Jones potential is a

simple mathematical model that represents this behavior and effectively captures the essential features of the ^{4}He atom interaction:

$$V(r) = 4\epsilon\left[\left(\frac{\sigma}{r}\right)^{12} - \left(\frac{\sigma}{r}\right)^{6}\right] \tag{2.12}$$

where r is the interatomic separation. For accurate calculations, more realistic potentials are required. All the same, the Lennard-Jones parameters provide an easy way to characterize the strength, ϵ, and range, σ, of the interaction. Table 2.1 compares these parameters of the inert gas solids. As can readily be seen, ^{4}He occupies the shallowest of potential wells by a considerable measure.

gas	ϵ (K)	σ (nm)	m (amu)	Λ
Xe	230.4	0.392	131.30	0.064
Kr	164.0	0.362	83.80	0.103
Ar	119.8	0.340	39.944	0.186
Ne	36.7	0.279	20.183	0.577
^{4}He	10.2	0.262	4.004	2.61
^{3}He	10.2	0.262	3.017	3.01

Table 2.1: Basic quantum parameters for the inert gas solids [22].

^{4}He atoms also are light and the effect of low atomic mass is to ensure a high value of zero-point energy. A ^{4}He atom occupies a certain volume, bounded by the atoms immediately surrounding it, and on average is contained within a sphere of volume equal to the atomic volume V_a (and that sphere has radius $R \sim V_a^{1/3}$). By the Heisenberg Uncertainty Principle, a particle confined to such a cavity has an uncertainty in its momentum, $\Delta p \sim \hbar/R$. Consequently, it must possess some kinetic energy of localization (i.e., zero-point energy) $E_0 \sim (\Delta p^2)/2m_4 \sim \hbar^2/2m_4R^2$, where m_4 is the mass of a ^{4}He atom. In terms of the atomic volume, the zero-point energy may be written as $E_0 \sim \hbar^2/2m_4V_a^{2/3}$. When this effect is coupled to weak interatomic attractive forces, it becomes clear why ^{4}He refuses to solidify without the help of significant external pressures. Even once frozen, this zero-point energy leads to a greatly increased molar volume, and to unusually large displacements of the atoms in their oscillations about their equilibrium positions. In addition, the large molar volume is accompanied by an exceptionally high compressibility, so it is

possible to study the properties of a simple lattice over a great range of densities. Correspondingly, solid ^{4}He also possesses a weak shear modulus (i.e., small elastic constants) and relatively low sound speeds.

The basic character of solid ^{4}He may be revealed in the phonon (p) specific heat C_V^p (that which arises from the vibration of the atoms about their lattice points). At low temperature, the heat capacity is well-described by the Debye model

$$C_V^p = \frac{12\pi^4}{5} N_A k \left(\frac{T}{\theta_D}\right)^3, \tag{2.13}$$

where N_A is Avagadro's number, k is Boltzmann's constant, and θ_D is the Debye temperature. θ_D is obtained by fitting to the observed C_V^p and is roughly the temperature of a crystal's highest normal mode of vibration (the characteristic energy of the phonons).

As shown in Table 2.2, θ_D is significantly larger than the melting temperatures of ^{4}He (i.e., the zero-point energy is much greater than the thermal energy). For example, at absolute zero, solid ^{4}He with a molar volume of 20 cm^3 has about 225 J of zero-point energy, but the addition of less than 1 J of thermal energy is enough to cause melting. Table 2.2 also shows the ratio r/R_0, of the mean square amplitude of vibration of the atoms to the distance between nearest neighbours, again determined via the Debye model. According to the Lindemann criterion of melting, a solid melts once $r/R_0 \sim 0.15$: a clear indication that solid ^{4}He is not inherently stable.

Molar volume (cm^3)	Melting temp. T_M (K)	Debye temp. θ_D (K)	T_M/θ_D	Zero-point energy (J mol^{-1})	Thermal energy (J mol^{-1})	r/R_0
20.0	2.12	24.0	0.088	224.4	0.71	0.303
18.0	3.40	31.5	0.108	294.8	2.05	0.277
16.0	5.35	42.5	0.126	397.7	4.98	0.251
14.0	8.65	57.0	0.152	531.7	13.31	0.228

Table 2.2: Estimates of the thermodynamic functions of solid ^{4}He along the melting curve [23].

A classical treatment is clearly inadequate for helium, as quantum effects are simply too significant. The degree of 'quantumness' of a solid can be characterized

by the de Boer [24] parameter, which is essentially the ratio of zero-point energy to potential energy

$$\Lambda = \frac{h}{\sigma\sqrt{m\epsilon}}, \tag{2.14}$$

where h is Planck's constant and m is the mass of the atom in atomic mass units. A sizeable Λ, shown in Table 2.1, means that the large wave functions (WFs) of neighboring atoms in the lattice will overlap, leading to direct nuclear exchange integrals and tunnelling between sites. (In solid ^{3}He, which has a nuclear spin of $\frac{1}{2}$, this exchange can be observed through nuclear magnetic resonance experiments and in thermodynamic properties.) This can manifest itself in the non-thermal motion of defects through the crystal, such as vacancies, impurities, and even dislocations. Due to the periodic potential presented by the lattice (the Peierls potential), this tunnelling may become coherent under certain conditions and allow defects to propagate through the crystal.

Quantum effects play an important role in the fluid phase, as superfluidity exemplifies, and are likewise significant in the solid phase; consequently, it is both important and interesting to study the fundamental properties of quantum solid ^{4}He.

2.4 (Super)solid ^{4}He

Theorists have long speculated that something similar to the superfluidity that occurs in the liquid phase might also happen in the solid phase. This section reviews the theoretical and experimental work that has addressed the question of the possibility of a superfluid phase in solid ^{4}He, although a comprehensive discussion is beyond the scope of this thesis. The excellent reviews by Meisel [1] and Prokof'ev [2] are again recommended to the interested reader.

2.4.1 The early years

The first fundamental work was carried out by Penrose and Onsager [25], who generalized the mathematical description of BEC, making it applicable to a system of interacting particles. A first-principles argument was presented, indicating that superfluid ^{4}He in equilibrium shows BEC. (Conversely, they also showed why one would not expect BEC to occur in a solid.) Landau and Lifshitz [26] extended on this

effort and with a generalized mathematical description of BEC in place, theorists were free to consider the possibility of observing BEC in a solid.

As an interesting aside that receives scant attention, a second 'type' of supersolidity has been identified [27]. Using a modified procedure to derive hydrodynamics, it has been argued that a certain class of crystal will be able to sustain a persistent entropy flux rather than a persistent mass current and has a propagating mode connected to temperature fluctuations.

2.4.1.1 Theory

Some of the earliest work came from Andréev and Lifshitz [28], whose theoretical efforts led them to the conclusion that, at sufficiently low temperatures, localized defects or impurities within a crystal will transform into excitations that move freely through the lattice. Instead of the ordinary diffusion of defects, there arises a fluid flow consisting of these excitations ("defectons" and "impuritons"). At absolute zero, and in crystals with large zero-point energy (such as solid ^{4}He), zero-point defects may exist and the number of sites in an ideal crystal lattice may not coincide with the number of atoms. This is not surprising since for finite values of Λ an atom is not localized at a definite site, and therefore the requirement that the number of sites be equal to the number of atoms is not compulsory. Such a crystal would be neither a solid nor a liquid and within it two kinds of motion would be possible; one with the properties of motion in an elastic solid, the second with the properties of motion in a liquid. Most important, under certain conditions the liquid type of crystal motion would possess the property of superfluidity. In other words, they conclude that the supersolid state exists.

Chester [29] would also speculate on the topic, concluding that BEC can occur in a state which exhibits crystalline ordering, in contrast to the claims of Penrose and Onsager [25]. It is added that a quantum crystal can only have a Bose-Einstein condensate if it has a finite fraction of vacancies. However, it is stated with certainty that crystalline ordering would prevent the appearance of anything like normal superfluid properties, in contrast to the claims of Andréev and Lifshitz [28], although the point is conceded that the physical implications of the argument put fourth rely on how accurately the states used actually represent real physical systems.

Following this proposal, Leggett [30] suggested (and Saslow later concurred [31]) that NCRI very probably occurs if the solid is Bose-Einstein condensed (although

the associated superfluid fraction is shown to be very small, probably $\leq 10^{-4}$). Anomalous macroscopic effects are then predicted and direct tests are proposed. The first test advocated is to rotate the solid in the form of an annulus below its transition temperature; then the apparent moment of inertia should be slightly less than the classical value (and, more relevantly, temperature dependent). A second test would be to rotate the solid above its presumed critical angular velocity and then bring the container to rest; if it is assumed that the NCRI is associated with the metastability of flow states as in other superfluid systems, a persistent residual angular momentum should be expected.

Shortly thereafter, Guyer [32] describes the essential physical content of the previous three works and scrutinizes them in light of the large body of data on quantum crystals. Two possible mechanisms by which particles in solid ^{4}He can acquire the mobility necessary to permit the kinds of motions that would lead to BEC and superfluid phenomena are distinguished. These mechanisms are a motion of the single-particle density due to the presence of ground-state vacancies, and motion of the single-particle density due to the cooperative tunnelling of pairs of particles. Contemporary nuclear magnetic resonance data on solid ^{3}He [33] and ^{3}He-^{4}He [34] mixtures is then provided as strong evidence for there being no ground-state vacancies in solid ^{4}He. Thus, BEC due to the presence of ground-state vacancies is ruled out. If BEC due to cooperative tunnelling occurs, the density of the superfluid component is estimated to be on the order of 10^{-6} of the bulk density, and close to the edge of observational range.

(Modern x-ray diffraction measurements [35] of thermal vacancies place an upper limit of $x_{vac} \sim 0.1\%$ for single crystals of hcp ^{4}He (grown at constant pressure) and even more recent experiments [36] still do not give evidence for vacancies at low temperature (but new measurements seem needed to put a stringent bound on groundstate vacancies). Presumably, x_{vac} would increase in disordered ^{4}He solids (grown at constant volume or quench-cooled), unfortunately no such information exists for samples of this sort.)

2.4.1.2 Experiment

While the theoretical works are free to speculate on what exactly is going inside of quantum solid ^{4}He, it will be experiment that ultimately gives us the definitive answer. With that, considerable effort has been undertaken by the experimental

community to solve the mystery of solid ^{4}He. This is no easy task, however, as the number of variables to control for are many, and the specific effects for which physicists are looking are largely unknown.

This section describes some of the major experimental searches for the supersolid phase of the 20th century.

Of course, there are several systems which potentially might possess a supersolid state under the proper conditions (e.g., BEC of vacancies in a pure ^{4}He crystal; BEC of interstitial or substitutional ^{4}He impurities in a ^{3}He crystal; a Cooper-paired superfluid state of ^{3}He impurities in solid ^{4}He; or even a transition arising from tunnelling and particle exchange in a pure ^{4}He crystal). For reasons hinted at above, however, there are a variety of reasons why nominally pure ^{4}He seems to be the system of choice (i.e., non-helium quantum crystals have smaller zero-point oscillations and are therefore less likely candidates for observing a supersolid state).

Some of the initial attempts to observe a supersolid ^{4}He phase involved the study of plastic flow in crystals through which physical objects were moved. Examples of these objects include: a magnetized sphere [37], a steel ball on a wire [38], a solid plate [39], and a porous membrane [40]. Techniques more reminiscent of superfluid helium studies were also employed. In one, it was attempted to detect mass flow through a weak link which was subjected to a chemical potential difference ($\Delta P \sim 1$ bar) between two mass reservoirs [41]. In another, a sensitive torsional oscillator searched for a change of the moment of inertia of the system [42]. Yet another searched for mass flow in a cylindric "U"-tube experiment [43]. None of these investigations resulted in a positive identification of the supersolid state.

Thermodynamic measurements possess a strong historical success rate for the discovery of new phases at low temperature, notably the discovery of superfluid ^{4}He [44], superfluid ^{3}He [45], and nuclear magnetic ordering in solid ^{3}He [46]. Taking a hint from the historical record, the principal idea of the thermodynamic measurements is to measure, for example, the entropy or pressure of the system as a function of temperature. Experiments of this sort [47, 48] also did not result in a positive identification of the supersolid state.

Finally, ultrasonic studies have been performed in solid ^{4}He at higher purity, low density, and low acoustic power [49]. Their results are rather complicated, but the authors argue that their data is consistent with the presence of a zero-point vacancy induced supersolid state. They also concede that their possible identification of the

supersolid requires additional work to solidify the validity of their arguments and interpretations.

With roughly a dozen experimental null results in the history books and theoretical uncertainty in the existence of the supersolid state, dedicated experimental searches quickly became significantly fewer and further between. Things picked up, though, in 2004.

2.4.2 The Kim and Chan renaissance

In 2004, Kim and Chan reported on a torsional oscillator technique to study solid ^{4}He confined in the pores of Vycor glass as a function of temperature [10]. As described above, a torsional oscillator is a mechanical resonator which is used as a very sensitive micro-balance. As they say at Cornell, "if you've got it, oscillate it". With their high quality factors (Q is 2π times the ratio of the total energy stored divided by the energy lost in a single cycle) at low temperatures ($Q \sim 10^6$), torsional oscillators have a low noise bandwidth and, consequently, a very high period and amplitude stability ($\delta P/P \sim 10^{-9}$ and $\delta\theta/\theta \sim 10^{-4}$, respectively).

The basic experimental configuration, shown in Figure 2.4, is a torsion rod with some sample cell attached to one end of it. Torsional oscillators typically differ from one another primarily in the design of the sample cell, but the one used by Kim and Chan to study solid helium in Vycor was cylindrical in shape (with the Vycor sample sitting snugly within), shown in Figure 2.5. The oscillator was driven by a capacitive transducer and its response was detected by another capacitive transducer.

Ideally (and to re-iterate some of what was covered earlier), torsional oscillators are modelled as simple harmonic oscillators, with a resonant period given by $P = 2\pi(I/\kappa)^{1/2}$. Here, I is the moment of inertia and κ is the torsional spring constant of the torsional oscillator, with its amplitude given by $\theta = Q\tau/\kappa$, where τ is the amplitude of the sinusoidal drive torque.

The central result of the Kim and Chan experiment is a drop in the period (ΔP) of their torsional oscillator that begins at 175 mK, shown in Figures 2.6 and 2.7. Their system fails to undergo rotation as classically predicted; specifically, they observe NCRI. Kim and Chan state that the most likely interpretation of the inertia drop is an entry of solid ^{4}He into a supersolid phase; namely, that there exists a superfluid-like phase in the solid state. (Leggett's proposal [30] to probe for NCRI is very similar to the experiments performed by Kim and Chan, but with one clear

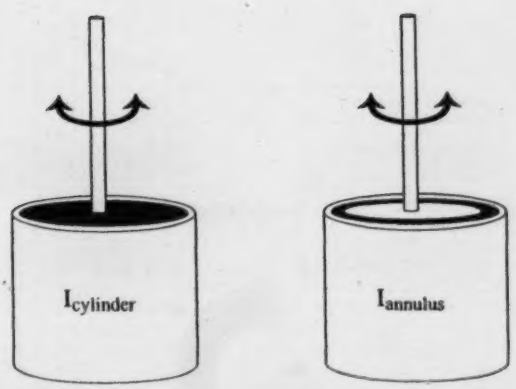

Figure 2.4: Schematic of a torsional oscillator. The cartoon on the left shows a cylindrical cavity, on the right an annular cavity. Other internal geometries may be used, giving each torsional oscillator its own unique moment of inertia I.

distinction: Kim and Chan oscillated, rather than rotated, the solid sample.)

Later that same year, Kim and Chan reported on the observation of NCRI in bulk solid ^{4}He confined to an annular channel in a sample cell under torsional motion [9]. As in their previous experiment, the effect shows up as a drop in the resonant oscillation period as the sample cell is cooled, this time to below 230 mK. Clearly, the effect is not connected to restricted geometries. They performed measurements on 17 solid samples, allowing them to map out the boundary of this superfluid-like solid or supersolid phase from the melting line up to 66 bar, as in Figure 2.8. With that, they conclude that superfluid behavior is found in all three phases of matter. And what a conclusion that is!

While they have since studied literally hundreds of samples, the principle results from Kim and Chan may be summarized by a few general statements:

- The inferred fractional supersolid density is $\rho_s/\rho \sim 0.01$.
- The transition temperature is $T_c \sim 200$ mK, with a gradual onset.
- The inferred critical velocity is $v_c \sim 10$ μm/s.
- The effect is non-existent in the bcc phase of ^{3}He, and is suppressed (in magnitude and to higher temperature) with increasing ^{3}He impurity concentrations.
- The effect is non-existent in a blocked annulus, strongly suggesting that the effect is not local.

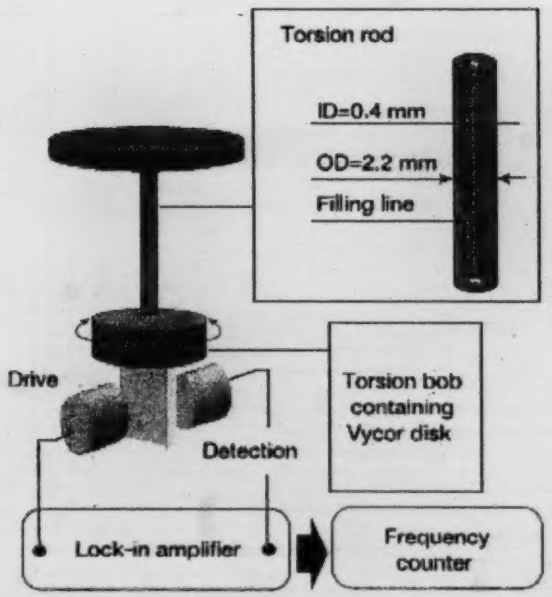

Figure 2.5: Torsional oscillator used with Vycor disk used by Kim and Chan [10]. The Vycor glass disk has a diameter of 15 mm and a thickness of 4 mm. The cylindrical drive and detection electrodes are aligned off-centre from, and are capacitively coupled to, the central electrode attached to the torsion bob. The signal from the detection electrode (proportional to the amplitude) is sent to the lock-in amplifier through a current preamplifier. The lock-in provides a driving voltage, which controls the amplitude of oscillation, to complete the phase-locked loop and keep the oscillator in resonance.

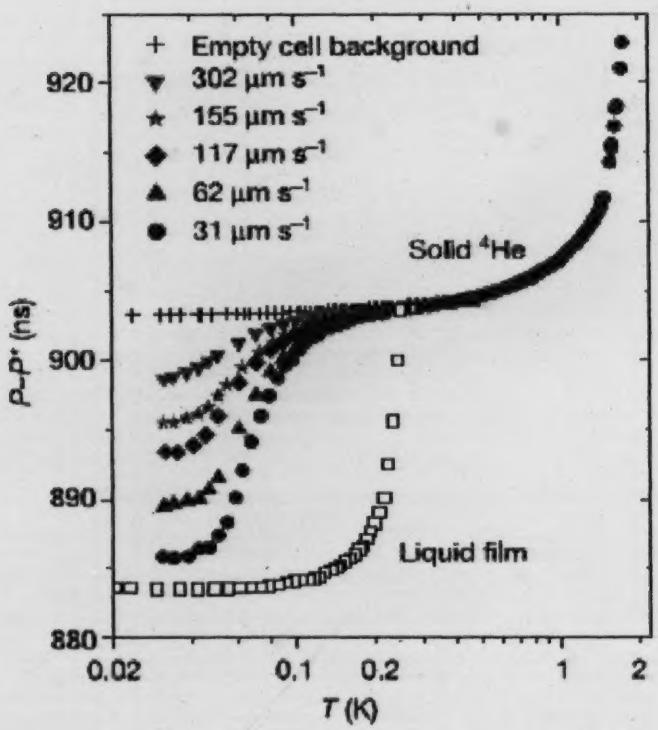

Figure 2.6: Torsional oscillator resonant period as a function of temperature of solid ^{4}He in Vycor glass [10]. The resonant period for different oscillation amplitudes (and hence different velocities of the rim of the Vycor disk, v rim) is shown. A drop in the period (ΔP), signifying the transition into the supersolid phase, is seen below 175 mK. Although the magnitude of ΔP depends strongly on the rim velocity, no such dependence of the period is seen above the transition temperature. For comparison, the empty (without helium) cell period, and the period of an atomically thin liquid film adsorbed on the walls of the internal pore space of Vycor, are also shown. The film measurement, showing a superfluid transition at 250 mK, is carried out with the same torsion cell. Data has been shifted for clarity.

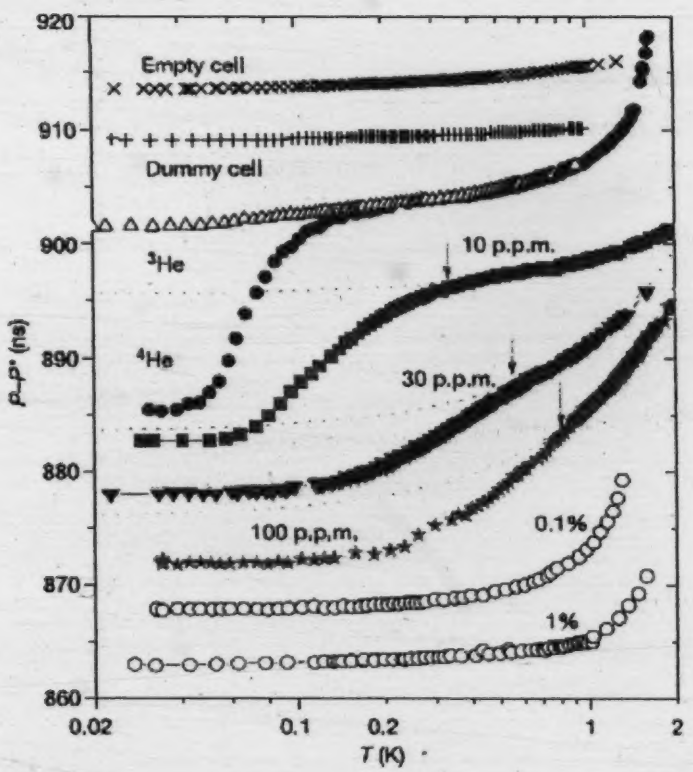

Figure 2.7: Torsional oscillator resonant periods as a function of temperature for a variety of solid helium samples [10]. The period scale shown corresponds to that for solid hcp ^{4}He and the period data for other samples are shifted for clarity and easy comparisons. All measurements were made with the rim velocity of the Vycor disk near 30 μ/s. The plots show that the period drop effect is not related to the stiffening of bulk solid helium in the torsion rod. The effect is not seen in pure bcc ^{3}He, and is not seen in solid mixtures with ^{3}He concentration exceeding 0.1%, nor is it seen in empty or dummy cells. A period drop is found for mixtures with 10, 30 and 100 ppm of ^{3}He. As in pure hcp ^{4}He, the size of the drop in these samples with low ^{3}He concentrations is also rim-velocity dependent. The dotted lines extrapolated smoothly from high temperature are the expected background period in the absence of period drops. The vertical arrows mark the transition temperatures of these samples.

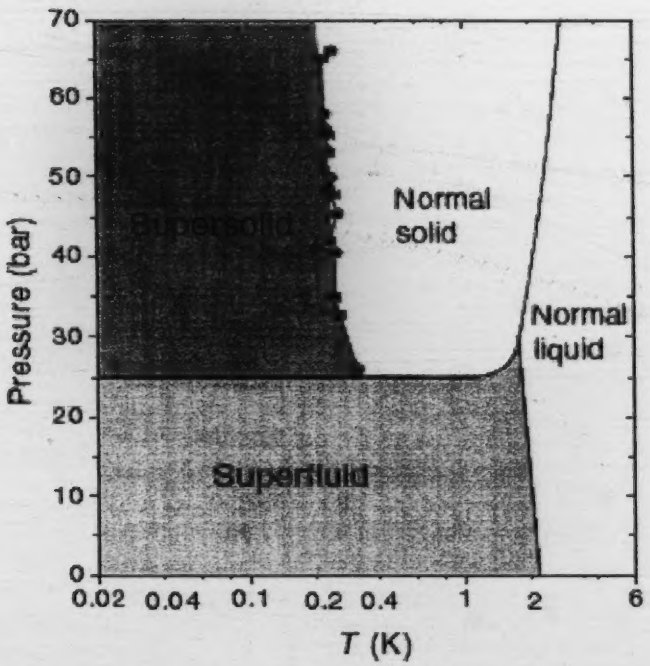

Figure 2.8: Newly proposed phase diagram of liquid and solid ^{4}He [9]. A supersolid phase is added, based on observations of NCRI in torsional oscillator experiments.

2.4.3 The later years

With the observation of NCRI in solid ^{4}He by Kim and Chan in 2004, the pace of theory and experiment quickened. Experiments were devised and executed at an accelerated pace, and theory papers were published at a near furious rate.

2.4.3.1 Other torsional oscillator measurements

One of the most important types of experiment remained the torsional oscillator, largely because a torsional experiment two decades earlier had yielded a null result [42]. It was important to first duplicate the Kim and Chan results.

Kim and Chan performed the original torsional oscillator experiments which motivates the work presented in this thesis. As a summary, NCRI was observed in solid ^{4}He in their torsional oscillator experiment. The phenomenon was first reported for solid ^{4}He embedded in a porous matrix [10], and was extended to the system embedded in a matrix of porous gold [50] (with a characteristic pore size two orders of magnitude greater than in Vycor), and also in the bulk crystal [9]. The bulk experiments were extended to high pressures [51] and to low ^{3}He impurity concentrations [52]. In all cases, the observed NCRI at low temperature was identified as the onset of supersolidity in ^{4}He. Upon discovering that the NCRI was not a confinement effect, all subsequent torsional oscillator studies were performed on bulk crystals.

The torsional oscillator findings by Kim and Chan are noteworthy not simply because of their supersolid interpretation, but also because an essentially identical experiment was performed 23 years earlier and obtained a null result [42]. Because of this discrepancy, it was quickly agreed upon by the low temperature community that the experiment needed to be triplicated. NCRI has since been observed in commercially pure (0.3 ppm ^{3}He) solid ^{4}He by four other groups [53, 54, 55, 56]. Qualitatively, all five groups observe reproducible phenomena; specifically, NCRI with a temperature dependence characterized by saturation in the low temperature limit and a gradual decay to zero at higher temperature. Quantitatively, however, these experiments do not quite agree on the onset temperature of NCRI (which varies between $\sim$ 200 mK and $\sim$ 400 mK), nor do they agree on the magnitude of the NCRI (which varies between $\sim$ 0.1% and $\sim$ 1.5%). It should be noted that these variations exist not only between groups, but also from sample to sample within the same cell. Of all groups that have studied NCRI in solid ^{4}He with torsional

oscillators, the group led by Moses Chan has studied hundreds more than anyone else (quite literally).

While there are many details within the torsional oscillator results that could be discussed, only those most pertinent to this thesis will be touched upon:

- The normalized NCRI fraction is unity when the speed of the torsional oscillator annulus is ≤ 10 μm/s, and decreases monotonically to zero as the speed of the torsional oscillator annulus approaches ~ 500 μm/s [51].
- The NCRI fraction at low and high temperature of the identical cylindrical solid ^{4}He was studied at 496 and 1173 Hz by a double resonance torsional oscillator and was found to be frequency independent [56]. However, the crossover (transition) is frequency dependent; this is the most direct evidence in torsional oscillator experiments that the transition shifts/sharpens at low frequency.
- The effect is limited by a critical velocity v_c (rather than a critical stress σ_c) in the torsional oscillator probes [56].
- The magnitude of the NCRI displays relative insensitivity to pressure [51].
- There exists "zero-field cooled" versus "field cooled" hysteresis. If the sample is cooled while under high amplitude drive, then the observed NCRI will be relatively small. If the sample is cooled while under low amplitude drive, then the observed NCRI will be relatively large; however, subsequently increasing the amplitude of the drive will not decrease the magnitude of the NCRI.
- The magnitude of the NCRI fraction and the onset temperature are highly sensitive to the ^{3}He isotopic impurity concentration (at the ppb level) in the solid ^{4}He sample [10, 52]. Specifically, the onset of NCRI is broadened and shifts monotonically to higher temperature with increasing ^{3}He concentration.
- There exists a dissipation peak in the torsional oscillators in the vicinity of where the NCRI fraction is changing most rapidly [9, 51, 54, 57].
- Annealing and disorder in the solid sample also appear to play a significant role in the NCRI fraction. In one study, annealing was found to essentially eliminate the NCRI signal [54], reducing it from $\sim 0.5\%$ to $<0.05\%$. In another study, annealing was found to increase the NCRI signal [55] by $\sim 10\%$. It has

also been reported that quench cooling the solid sample, as opposed to slow freezing, and which results in a highly disordered solid sample, gives a greatly increased NCRI fraction [57], upwards of 20%.

- The effect persists even in single crystals grown at constant pressure [58].
- A wide range of NCRI (from order 0.1% to order 10% (and almost order 100%) has been observed in different cells (e.g., cylinders versus annuli, of various surface area to volume ratios, in narrow gaps, and even within the same cell!)

2.4.3.2 Supersolid/solid ^{4}He theory

This unexpected experimental result quickly caught the attention of theorists: solid ^{4}He was, once again, worth devoting some effort to. The overview presented here is far from comprehensive.

A natural starting point for theoretical endeavours would be to determine the groundstate of solid ^{4}He, to see if it explicitly displays superfluidity.

2.4.3.2.1 Questions on the groundstate In the earliest of theoretical treatments, the variational method (an analytical approach) seemed to be the only technique capable of providing, from first principles, information on the groundstate properties of liquid ^{4}He. Understanding that the physical origin of the superfluid properties of bulk ^{4}He lay in the phenomena of Bose-Einstein conednsation (BEC), it was soon after confirmed [59] that the trial pair-product wave functions (WFs) used in these variational calculations for ^{4}He - the Jastrow wave function (JWF) - also possessed BEC (i.e., possessed off-diagonal long-range order (ODLRO) [60] - ODLRO tells us whether atoms at one end of the solid are in phase with atoms at the other end of the solid, and would supply a mechanism for NCRI).

On the heels of this theorem, it was conjectured [29] that, for a wide class of potentials, the JWF will exhibit crystalline ordering at sufficiently high densities (and fluid ordering at low densities). The combination of the above theorem with this conjecture is that BEC can occur in a state which exhibits crystalline ordering (i.e., that both diagonal and off-diagonal long-range order are possible in a single system). It is also found, however, that a crystal will have BEC only if there exists groundstate vacancies - an argument which has since been elaborated upon [61].

It has recently been shown, however, that no JWF can describe solid ^{4}He near melting, nor can it describe a quantum crystal without an intrinsic population of point defects [62]. A much better description of solid ^{4}He is obtained by multiplying the JWF by a localization term, centered around the lattice sites and summed over a permutation of atoms to lattice sites. This new WF, the Jastrow-Nosanow form [63], is very good description of the ground states, however the solid order is put in by hand, rather than appearing spontaneously. This variational WF has been considered in solid ^{4}He calculations, and it has been shown that there is no off-diagonal long-range order in these trial WFs, for both an infinite sample and that confined in a cylindrical annulus [62].

An alternate trial WF may be obtained by multiplying by a localization function which is independent of the lattice site, but still having lattice symmetry [64]. With this function, vacancies will be locally attracted to interstitials but they are not bound as pairs; as a result the WF has both BEC and NCRI. (However, calculations [65] and experiments [35] on solid ^{4}He suggest that there are no unbound vacancies or interstitials at low temperatures.)

The dilemma, then, is that a number of satisfactory trial functions exists, all of them capable of good descriptions of solid ^{4}He, but some give BEC and some do not. A more direct, reliable method than such straight-forward analytical approaches is required to determine whether the ground state of solid ^{4}He will possess BEC. Numerical methods might be the cure for what ails us.

Galli *et al.* [66] remind us that the variational theory is very useful to describe strongly interacting systems, such as liquid ^{4}He, but that it is always open to debate how much the results depend on the ansatz on the WF, especially for quantities other than the energy. They use an advanced variational theory (shadow wave function variational technique), the accuracy of which has been tested with a projector method on the exact groundstate. This projector method is an exact computation based on the projection algorithm SPIGS (shadow path integrated ground state), a path integrated ground state method which uses a SWF as the starting point. They show that solid ^{4}He at T = 0 K has BEC at melting density and above, at least up to 54 bar. The condensate fraction is quite small (5×10^{-6} at the melting density). The key process giving rise to off-diagonal long-range order is the formation of vacancy-interstitial pairs. Such defects have a finite probability to be present in the ground state of the system; they are not permanent excitation but simply rare

fluctuations of the perfect crystal induced by the large zero-point motion. In other words, the number of atoms is equal to the number of lattice sites (i.e., the crystal is commensurate) and, at the same time, atoms are delocalized.

The nature of the ground state, whether commensurate or incommensurate, is a very important point, and a phenomenological theory [67] has shown that the low temperature properties of crystalline ^{4}He would be strongly modified should the ground state be incommensurate. There is no fundamental reason why crystals should necessarily be commensurate (i.e., that the number of atoms equals the number of lattice sites). With such a high degree of delocalization in its atoms, it is possible that the groundstate of solid ^{4}He be incommensurate. This issue is not completely resolved, and is central to some theoretical efforts exploring the possibility of a superfluid state within the solid phase (although, there now exists strong theoretical [2] and experimental [1] evidence that ^{4}He is indeed a commensurate crystal).

Novel PIMC simulations have also been performed by Boninsegni and collaborators, in which a new worm algorithm [68] is employed, enabling the accurate computation of thermodynamic properties of quantum many-body systems in continuous space, at finite temperature. The computational scheme allows for efficient calculations of the superfluid fraction and off-diagonal correlations in space-time, for system sizes which are orders of magnitude larger than those accessible to conventional PIMC. Their consistent observation is of a commensurate hcp crystal, found to be insulating [69].

In the language of path integrals, the question of whether supersolidity is possible in a commensurate solid was addressed, as well as what the necessary conditions are for this to happen [61]. It is proven that the necessary condition for a solid to be also a superfluid is to have zero-point vacancies, or interstitial atoms, or both, as an integral part of the groundstate. However, they also find that the supersolid groundstate in commensurate solids have a zero probability to be found in nature, because of the asymmetry that exists between the activation energies of vacancies (15 K at the melting curve [65] and 30 K at 50 bars [70]) and interstitials (48 K [71]). (Recall that for a solid to be commensurate, the number of vacancies must equal the number of interstitials.) There is an overwhelming bulk of experimental work which indicates that vacancies and interstitials are activated. They also conclude that such crystals made of a single species of particles obeying Bose statistics (e.g., ^{4}He

atoms) are always insulating (more precisely, the commensurate supersolid phase has zero probability of being observed).

Simulation computations of energy cannot (to date) be used to decide if the groundstate of solid ^{4}He has the number of lattice sites equal to the number of atoms (commensurate state) or if it is different (incommensurate state). The best variational WF, a shadow wave function (SWF), gives an incommensurate state, but the equilibrium concentration of vacancies remains to be determined. By means of an exact groundstate projector method [72], researchers have computed the one-body density matrix in solid ^{4}He for the incommensurate state in which incommensurability occurs spontaneously.

Returning to attempts to provide an unbiased answer (e.g., one that does not rely on a starting WF), Clark and Ceperley [62] use path integral Monte Carlo (PIMC) simulations, a numerical method that calculates integrals over the many body density matrix. It is ideally suited for this calculation since it can be done at finite temperature (under conditions where an experimental signature of NCRI has been observed), and is, in principle, exact, and has been validated on many properties of liquid and solid ^{4}He [73]. Most importantly, it is independent of a trial WF bias or any assumption of lattice. Only the He-He interaction enters: a semi-empirical form [74] is known to be accurate; in any case, results suggest that supersolid behaviour is a robust phenomena insensitive to fine details of the interaction. One drawback of the PIMC technique is that finite size effects are common since it is difficult to simulate large systems (eg., greater than several hundred atoms). The results of these PIMC calculations are that off-diagonal long-range order (equivalent to BEC) does not exist in a defect-free hcp ^{4}He crystal at the melting density. Recall that PIMC does not make a variational ansatz, and has the sole assumption that the results at low temperature smoothly approach the ground state values. They only performed PIMC calculations at the melting density but do not expect different behavior at higher density, since difficulty of exchange grows rapidly with density. Furthermore, they conclude that the solid ^{4}He WF has correlations which suppress both vacancies and BEC. This result, together with the finding of zero superfluid density in a perfect ^{4}He crystal (the superfluid fraction ρ_s at T = 0.2 K is zero [71] and there is no off-diagonal long range order (off-diagonal long-range order) at T = 0.2 and 0.5 K [75, 62]), suggests that the mechanism for the observations of Kim and Chan involves more than equilibrium properties of a

commensurate ^{4}He crystal.

2.4.3.2.2 Possible supersolid mechanisms Some effort has gone into exploring possible supersolid mechanisms involving lattice vacancies. Simulation computation, for example, can investigate whether there is a BEC induced by vacancies. Based on variational Monte Carlo methods with SWFs [76], it was found that a finite concentration of vacancies does induce BEC of the atoms in solid ^{4}He at a density close to the absolute zero melting where vacancies are delocalized. However, no BEC was present in the perfect crystal and in the defected solid at higher densities.

Also within the framework of variational theory [72], vacancy induced BEC has been confirmed, with a predicted onset temperature of $T_c = 200$ mK for $x_{vac} = 0.23\%$. However, this does not explain the large range of NCRI fractions associated with this single T_c. Moreover, $x_{vac} = 0.23\%$ is beyond empirically imposed bounds.

Using quantum Monte Carlo methods [69], the subject of vacancy-induced superflow has also been investigated. Results from this numerical technique show that vacancies are unstable in a ^{4}He crystal. Simulations were performed at 200 mK with 800 and 2016 atoms in the crystal under different pressures up to 65 bar, with vacancies created by explicitly removing a number of atoms. Various initial configurations with randomly located, remote, and clustered vacancy positions were considered, with vacancy concentrations ranging from 0.5% up to 6%. Specifically, it was found that the vacancies form clusters and the system phase separates into a vacancy-rich phase and a perfect, insulating crystal. (The annealing results of Rittner and Reppy [54] are in good agreement with the conclusion that the ground-state of solid ^{4}He is a commensurate crystal.) Other recent efforts [77] on the vacancy-vacancy interaction in solid hcp ^{4}He, due to the mutual strain field of the two vacancies, also conclude that the interaction between them is attractive (within the basal plane). This provides strong evidence that a ^{4}He crystal does not conform to any standard supersolid scenario.

With theoretical arguments in place against the existence of commensurate supersolids [61] and the experimental fact of commensurability of the equilibrium solid ^{4}He at $T = 0$ supported by extensive experimental work over the past several decades (for review, see, e.g., [1]), as well as by the most recent experimental [78, 79] and

numeric studies [71], consensus is emerging that the earlier microscopic depictions of supersolidity involving vacancies are not practical to explain the increasing bulk of experimental data; the commensurability of solid ^{4}He seems to rule out NCRI based on BEC of vacancies [28, 29]. It becomes reasonable, then, to consider whether the NCRI might be due to quantum behaviour of some higher-dimensional defect.

The worm algorithm PIMC method has been used to study interfaces in quantum solids and, less generally, grain boundaries in solids ^{4}He. In the former, and on the basis of the most simple model of quantum crystals - the checkerboard lattice solid - it is shown [80] that the superfluidity of interfaces between solid domains can exist over a wide range of parameters. In the latter, it is shown [81] that grain boundaries in ^{4}He crystals are generically superfluid at low temperature, with a transition temperature of the order of about 0.5 K at the melting pressure. (Non-superfluid grain boundaries are also found but only for special orientations of the grains.) Furthermore, proximity to the melting curve is not a necessary condition for superfluid grain boundaries, a grain boundary in direct contact with the superfluid liquid at the melting curve is mechanically stable, and the observation of grain boundary superfluidity [82] is not just a crack filled with superfluid.

While it is noted that the onset temperatures do not agree, it is even harder to reconcile the amount of grain boundary surface area required to account for a 1% NCRI effect with the experimentally quantified value. If superfluid grain boundaries are the answer, then the average crystallite sizes in solid ^{4}He are 2-3 orders of magnitude smaller in their characteristic dimension than experimentalists would say. Grain boundaries aren't the answer.

Again with the worm algorithm PIMC method, the cores of screw dislocations have been studied [83], finding that the screw dislocation along the hexagonal axis of an hcp ^{4}He crystal features a superfluid (at $T \rightarrow 0$) core.

The worm algorithm PIMC method has also been used to observe a metastable disordered supersolid (a superglass phase of ^{4}He) [75]. Specifically, the term glass is taken to mean a spatially disordered (metastable) phase, indistinguishable from a solid (by which is meant a state with broken translational symmetry, immediately implying shear rigidity) on short enough time scales. The term superglass is the term used for such a phase that also displays superfluidity. It is discovered that the low temperature properties of the system crucially depend on the initial states. For example, an ideal hcp crystal is a clear-cut insulator, while the disordered system

freezes into a superglass (a metastable amorphous solid featuring off-diagonal long-range order and superfluidity).

In any case, all of the above proposals suggest that the solid samples grown in the laboratory contain these sorts of disordered regions (something experimentalists already know). The existence of NCRI then depends on whether or not the defect-rich, superfluid portions of the solid percolate throughout the sample.

2.4.3.2.3 Non-supersolid mechanisms An alternate explanation is that of slippage of the solid [84], due to grain boundary pre-melting between the solid and the dense adsorbed layers at the container wall (as opposed to between ordinary grain boundaries). A range of film thickness is calculated, and a viscosity is determined that accounts for the missing rotational inertia. However, mechanical effects are neglected when the equation for the total excess interfacial free energy of the solid-solid interface is written; as a result, their treatment relates to grain boundary pre-melting along the melting curve, whereas the phenomena of NCRI happens deep within the solid phase.

A dislocation-induced glass has also been proposed on more than one occasion. Using a quantum lattice gas model to describe essential aspects of the motion of ^{4}He atoms and of ^{3}He impurities in solid ^{4}He, one of which suggests that ^{3}He impurities bind to defects and promote ^{4}He atoms to interstitial sites which can turn the bosonic quantum disordered crystal into a metastable supersolid [85]. It is suggested that defects and interstitials are produced during the solid ^{4}He nucleation process where the role of ^{3}He impurities (in addition to the cooling rate) is known to be important even at very small concentrations. It is also proposed that such defects can form a glass phase during the ^{4}He solid growth by rapid cooling.

Motivated by a recent entropy analysis of solid ^{4}He [86], the possible role of a dislocation-induced glass was again considered [87]. It was proposed that a glassy state develops at low temperatures and is caused by a distribution of tunnelling systems in the crystal, produced by small scale dislocation loops. It was then argued that the reported mass decoupling is consistent with an increase in the oscillator frequency, as expected for a glasslike transition. This concept was subsequently more fully developed [88], noting that the decrease in the rotation period is also consistent with a solidification of a small liquid-like component into a low-temperature glass. Such a solidification may occur by a low-temperature quench of topological defects

(e.g., grain boundaries or dislocations), as explained above. The low-temperature glass can account for not only a monotonic decrease in the rotation period as the temperature is lowered but also explains the peak in the dissipation occurring near the transition point. Unlike the non-classical rotational inertia scenario, which depends on the supersolid fraction, the dependence of the rotational period on external parameters, e.g., the oscillator velocity, provides an alternate interpretation of the oscillator experiments.

Another recent model for the NCRI is one pertaining to dislocation vibrations [89]. It is argued that a novel vibrational mode of edge dislocation in hcp ^{4}He, excited by the shear stress in the torsional oscillator, can be the origin of the NCRI; namely, that they can cause period shift and dissipation of torsional oscillation. Dislocation theory predicts that the dynamics of the dislocations in bcc crystals differs from that of the dislocations in hcp crystals (the only structure probed by torsional oscillators so far). Ultrasonic experiments on hcp ^{4}He indicate that basal dislocations are mobile so that they can cause sound attenuation and large velocity change, whereas similar experiments on bcc ^{3}He indicate that dislocations are not mobile at low stress amplitude. In this respect, the absence of NCRI in ^{3}He crystals [10] may not be a result of the difference of quantum statistics between the two isotopes. The author of Reference [89] rightly states that the decisive experiment would be a torsional oscillator measurement on hcp ^{3}He.

2.4.3.2.4 Others Several semi-phenomenological attempts have also been put forward. These begin with the assumption that the supersolid phase exists, around which a theory is then constructed. The microscopic origin of the supersolid state seems to be almost anyone's guess.

In one theory [90], rotons condense, expand, and fuse into an ordered hexagonal lattice of vortex and anti-vortex filaments, described by a single macroscopic WF and presented as a supersolid. In another [91], it is suggested that the atomistic explanation involves a coherent translation of delocalized point defects which carry the "missing" angular momentum in the torsional oscillator experiments. In yet another [92], Leggett's idea [30] of "phase flow" is strongly supported. In another, zero-point vacancies condense and lead to the formation of a supersolid state [93]. This theory predicts that x-ray scattering intensity from the supersolid ought to have an additional modulation over that of the normal solid, and that the modula-

tion amplitude is proportional to the NCRI in the torsional oscillator experiments. In others still [94, 95], no discussion of the microscopic origin of the supersolid behaviour is given, as the result is model-independent or robust and insensitive to the details of a microscopic model for the supersolidity. In another [96], thermally excited, fluctuating, quantized vortex tangles are the mechanism.

The microscopic mechanism will really truly only be confirmed through experiment.

2.4.3.3 Other experiments

There is a need for other types of experiments to confirm (or not) the supersolid interpretation of the torsional oscillator period shifts.

2.4.3.3.1 Thermodynamic measurements Initial measurements of the specific heat of solid ^{4}He were performed [86] down to 80 mK, with no sharp feature at the onset temperature of the NCRI observable to within 1%. These samples were grown with the blocked capillary technique, were not annealed, and contained 0.3 ppm, 30 ppm, and 760 ppm ^{3}He. A re-analysis [87] of this very same data, however, does indicate a departure from the conventional T^3 specific heat behaviour expected at low temperatures, and that the measured entropy excess is several orders of magnitude smaller than the entropy expected from the BEC or λ transition of a 1% superfluid fraction. This re-analysis also claims that the absence of the entropy released at the claimed supersolid transition is puzzling, and that it is consistent with their picture of a dislocation induced glassy state in ^{4}He crystals.

These measurements were then followed by an extremely careful heat capacity study [97] on solid ^{4}He samples containing 1 ppb, 0.3 ppm, and 10 ppm ^{3}He. These samples were also grown by the blocked capillary technique but were treated with substantial annealing. A broad peak in the specific heat was observed, centered near 75 mK. The authors understand this peak to be the thermodynamic signature of the supersolid phase.

The pressure of the solid phase and of solid-liquid mixtures has also been re-examined recently. High-precision pressure measurements in hcp solid ^{4}He containing 0.3 ppm of ^{3}He, grown by the blocked-capillary technique, have been made in temperatures range from 50 to 500 mK [98]. The temperature dependence of pressure indicates that aside from the usual T^4 phonon contribution, there is an

additional contribution T^2 which becomes dominant below 300 mK, and where an abnormal behavior attributed to supersolidity has been observed. The authors take the data to suggest the appearance of a glassy phase (that might be responsible for the anomalous behaviors observed previously) which can be eliminated by substantial annealing. Although, the wider temperature range and greater accuracy of the Lin [97] measurements (who used an un-doped Si cell for its small heat capacity and high thermal conductivity at low temperature) seems to rule out the existence of such a phase.

Others have measured the melting curve of ^{4}He ($\leq$ 0.1 ppm ^{3}He) in the temperature range from 10 to 400 mK with the accuracy of about 0.5 μbar [99]. Crystals of different quality (annealed and un-annealed) showed the expected T^4 dependence (due to phonons) in the range from 80 to 400 mK without any sign of the supersolid transition. Below 80 mK, they observed a small deviation from T^4 dependence, but this was later found [100] to be an anomaly in the elastic modulus of Be-Cu, from which their pressure gauge was made. Thus, the melting pressure of ^{4}He follows the T^4 law in the whole temperature range from 10 mK to 400 mK without any attribute of a supersolid transition.

2.4.3.3.2 Neutron scattering Neutron scattering measurements of the atomic momentum distribution $n(\mathbf{k})$ have been performed on solid ^{4}He at temperatures between 80 and 500 mK [101], the aim being to determine whether there is BEC below the critical temperature, T_c = 200 mK, where a superfluid density has been observed. Assuming BEC appears as a macroscopic occupation of the k = 0 state below T_c, they find that there is a condensate fraction of n_0 = (-0.10 $\pm$ 1.20)% at T = 80 mK, and n_0 = (0.08 $\pm$ 0.78)% at T = 120 mK, consistent with zero. The shape of $n(\mathbf{k})$ also does not change on crossing T_c within measurement precision.

The single atom kinetic energy of solid hcp ^{4}He has also been measured by neutron scattering [102], but no change was observed from 0.4 K down to 70 mK (within statistical error of $\sim$2%). Furthermore, values of the single atom kinetic energy were unaffected between single crystal and polycrystalline samples, and by the addition of ^{3}He impurities (from 0.3 ppm to 10 ppm). Additionally, the lattice constant was also found to be independent of temperature to within 0.05%. These results suggest that if the supersolid transition in ^{4}He exists, it has a different microscopic origin to the superfluid transition in the liquid.

Other recent neutron diffraction experiments [103] have looked for traces of a supersolid transition via the Debye-Waller factor. The principal result here is that the mean-square atomic displacement in hcp solid ^{4}He does not change between 1 K to 140 mK. Specifically, there is no indication that the supersolid transition, if it exists, affects the crystalline lattice or zero-point fluctuations. Depending on the model used to describe supersolidity, this quantity is liable to change in the supersolid state.

2.4.3.3.3 First-sound It is expected that ultrasound should be sensitive to mass decoupling caused by superfluid-like behaviour, and if a superfluid component exists, the sound velocity of a porous material filled with solid ^{4}He could increase. Such ultrasonic measurements have been made for a porous Vycor glass filled with solid ^{4}He [104], in which they have adopted a continuous wave resonance technique that realizes an oscillating velocity of less than 1 x 10^{-7} m/s (since the reported critical velocity from torsional oscillator measurements is very low). The resolution of their sound velocity is 10^{-5} for small oscillating velocities and is enough to detect the expected mass decoupling, although no signature of supersolid was observed.

An investigation of the response of solid ^{4}He to low-frequency, low-level mechanical excitation [105] has revealed several anomalous low frequency, non-linear resonances with highly sample-dependent onset temperatures (all below $\sim$ 0.8 K). Additionally, these features are absent in ^{3}He. However, based on conversations with the authors, it is uncertain whether these measurements are actually in the solid phase or at coexistence.

2.4.3.3.4 Second-sound (heat pulse propagation) Heat pulse propagation has also been studied in solid ^{4}He between 40 and 500 mK [106]. According to theoretical studies [27, 107, 28] of the hydrodynamics of a supersolid state, a fourth sound-like mode emerges and the velocities of elastic propagating modes becomes modified in the supersolid state. Crossover behaviour from second sound in normal solid above 500 mK to ballistic propagation below 200 mK is observed. Detailed study is made to search for possible modification of this propagation behaviour by the appearance of supersolidity. It is found that the ballistic phonon propagation velocity remains constant, within 0.3%, below 100 mK. The temporal evolution of the detected pulse shape also does not reveal an anomaly below 200 mK. As

possible reasons for a null result, the authors suggest that their bolometer might have insufficient sensitivity, that the critical velocity is exceeded during heat pulse drive, or that heat pulses simply do not couple well to fourth sound.

2.4.3.3.5 Flow In one experiment, a superflow of mass was observed through a solid ^{4}He sample at solid-liquid coexistence [82]. This superfluid flow was along grain boundaries between solid faces, however, and not through the lattice of the crystal. Of the thirteen samples studies, three showed this behaviour; two of these samples were at 50 mK, but the third was at 1.13 K, suggesting that the phenomena is likely not connected to NCRI in the solid.

2.4.3.3.6 Persistent currents Measuring persistent currents in a solid ^{4}He sample is the smoking-gun experiment. It is also, very likely, the most difficult to perform. As of the writing of this thesis, two such experiments are under development, but no results have yet been published [108, 109]. A measurement of persistent currents in a solid ^{4}He sample would undoubtedly end the supersolid debate.

2.5 Current state of the field

Although much work has already been done in an attempt to unravel the mystery associated with the torsional oscillator measurements, the puzzle is far from complete. And, so, this is where we come in. In order to get to the bottom of things, there are fundamental questions that still need to be asked. Those addressed in this thesis may be divided into three categories.

First, there are questions relating to the solid ^{4}He confined in Vycor. Could the torsional oscillator NCRI be due to incomplete freezing or a mass re-arrangement within the system (both of which could mimic superfluid-like behaviour)? Does the solid ^{4}He in Vycor flow when a pressure difference is applied (as it would with confined superfluid ^{4}He)?

Second, there are questions relating to bulk solid ^{4}He. Does bulk solid ^{4}He flow when a pressure difference is applied (similarly, as it would with bulk superfluid ^{4}He)? We concede that this question has been asked before, but felt that it was imperative to answer it with a higher degree of sensitivity than previous measurements (as in Reference [41]) and off of liquid-solid coexistence (as in Reference [43]).

Furthermore, we were interested in probing the effects of extremely small pressure gradients, in both the ac and dc sense.

Third, there are questions about what the elastic properties of solid ^{4}He are doing at low temperature. Any mechanical measurement, such as in a torsional oscillator or an acoustic probe, involves mass/density/inertia effects and/or the elastic moduli. Is the frequency change in torsional oscillator entirely due to ρ_s/ρ, as assumed? Does ρ_s decouple from the lattice (i.e., from ρ) in acoustic/2^{nd}/4^{th} sound? There is great need to directly measure , for example, the shear modulus of solid ^{4}He in the same temperature range, amplitude range, frequency range, ^{3}He impurity concentration range, etc., of the torsional oscillator experiments.

Chapter 3

Experimental Methods

This chapter contains the relevant information on all of the equipment and procedures used that are common to the set of experiments described in the following chapters of this thesis.

3.1 Gas handling system

To admit clean gas to the experimental cells in a controlled manner and to the desired pressure, a gas handling system was constructed (Figure 3.1). Its features are described below.

Incoming gas from the cylinder to the cell may be run through a standard LN_2 cold trap (27.1 cm^3) filled with a molecular sieve (Union Carbide; Type 13X). The molecular sieve is a synthetic, crystalline, activated alumino-silicate having a precisely controlled pore size of about 10 Å) and is used to remove condensable gases before they reach the coldest parts of the fridge, blocking fill lines and wreaking general havoc.

The gas handling system is also equipped with a room temperature pressure gauge (Setra Model 205-2, 0-5000 psig). For pressures less than about 7 bar (e.g., measurements on liquid helium at saturated vapour pressure), gas may be admitted to the cell in a controlled manner via a flow controller (MKS Instruments; PR 4000), at rates as low as 0.2 sccm. This flow controller is on temporary loan from Dr. Mark Freeman, as the one we initially planned on using (Sierra Instruments, Inc.; Model 810C Mass-Trak Mass Flow Controller) gave us some unexpected problems. The model 810C is made with nylon components and is a few hundred dollars less expensive than its 810S stainless steel counterpart. What you gain in monetary savings, you apparently sacrifice in the outgassing from the nylon components of

whatever chemicals were used by the manufacturer to clean the controller before shipping.

Adjustable safety relief valves (R3A Relief Valves; Swagelok) were also installed to protect the important parts of the system. The system also includes a 66.9 cm^3 ballast volume, machined to accommodate pressures up to 200 bar.

3.2 Dilution refrigeration

Cooling power was provided to the cell by way of dilution refrigeration. The concept of the dilution refrigerator is about 55 years old, and a detailed explanation of its operation and physical basis may be found elsewhere (e.g., [11]). Here, I will simply introduce the subject of dilution refrigeration, on account of its importance in all aspects of this work.

Cooling from room temperature down to 4.2 K is easily achieved by keeping the cryostat immersed in a bath of liquid helium, surrounded by an outer bath of liquid nitrogen. Further cooling to about 1 K is achieved by pumping on a container (the "1 K pot") of liquid helium. As the helium refrigerant evaporates, it absorbs energy from its surroundings, cooling the cryostat. Pumping on the 1 K pot removes the gaseous helium, thereby allowing the liquid-gas phase transition to continue.

Cooling far below 1 K is not possible using conventional refrigeration techniques; however, through dilution refrigeration one can cool as low as 2 mK in continuous operation.

The underlying principle behind dilution refrigeration is that at sufficiently low temperatures (about 0.8 K), a mixture of ^{3}He and ^{4}He will spontaneously phase separate, as shown in Figure 3.2. The lighter, ^{3}He-rich fraction (actually, pure ^{3}He at absolute zero) floats on top of the heavier, ^{4}He-rich fraction (typically containing roughly 94 % ^{4}He and 6 % ^{3}He).

All helium atoms are attracted to one another by van der Waals forces; however, as a ^{3}He atom is much lighter than its ^{4}He counterpart, it has a much more rumbustious zero point motion. As a result, ^{3}He atoms keep further apart from each other than ^{4}He atoms do; in fact, the molar volume of liquid ^{3}He is about 26% greater than that of liquid ^{4}He. As the atoms in the ^{4}He-rich fraction can pack together more closely, the forces between the atoms are greater. Accordingly, all helium atoms prefer to be surrounded by ^{4}He atoms. Conveniently, this means that the heavier fraction will attract ^{3}He atoms. These two fractions are generally

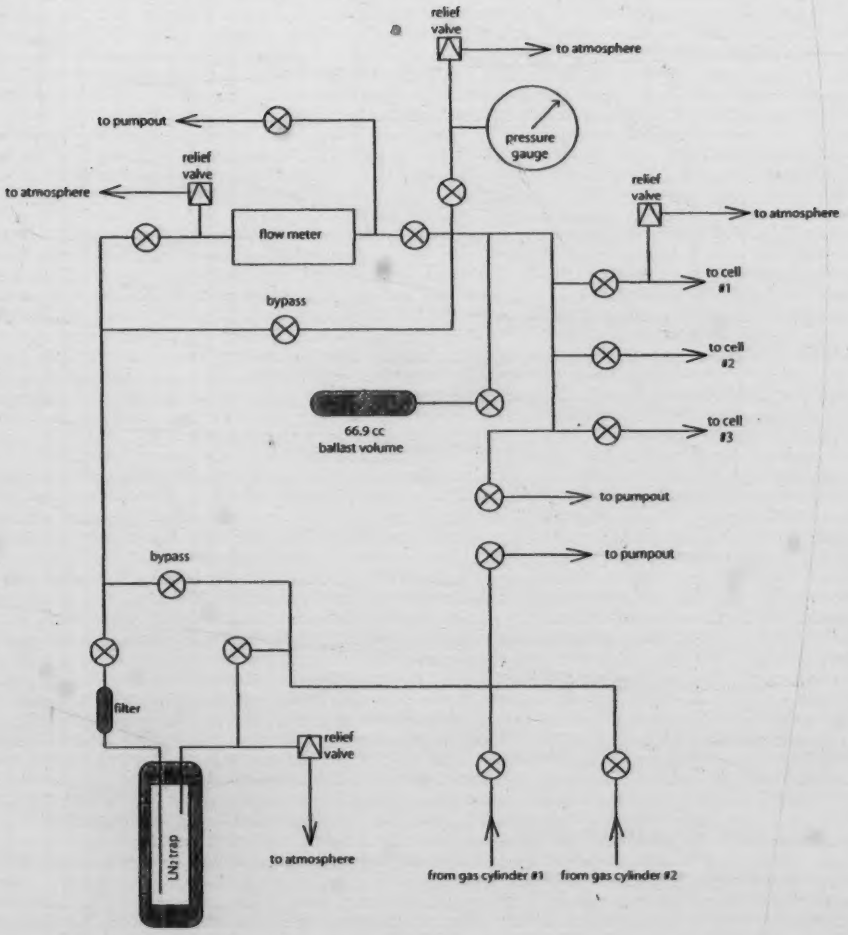

Figure 3.1: Schematic diagram of the gas handling system used in all experiments.

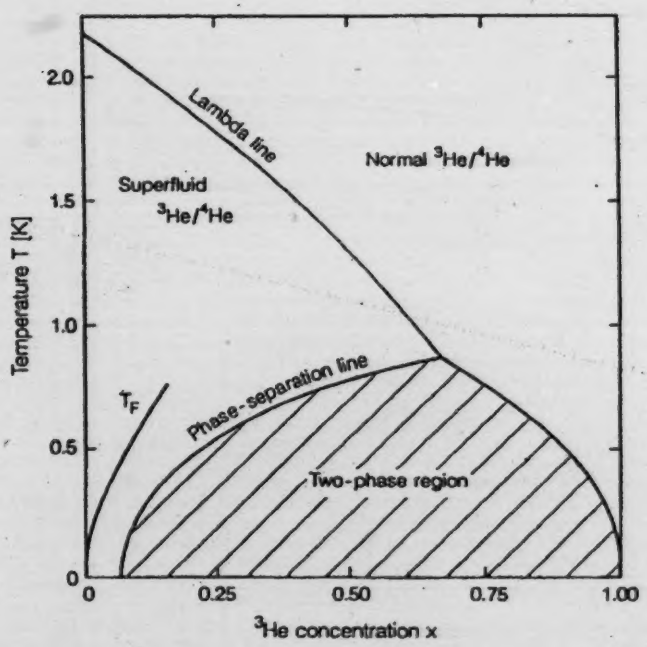

Figure 3.2: The phase diagram for a mixture of ^{3}He-^{4}He as a function of temperature [11].

referred to by their relative proportions of ^{3}He atoms; specifically, the lighter, pure ^{3}He fraction is known as the concentrated phase, while the heavier, ^{4}He-rich mixture is known as the dilute phase.

Now, if a ^{3}He atom can be persuaded to move from a relatively weakly bound state in the concentrated phase (surrounded only by other ^{3}He atoms) across the phase boundary to a more strongly bound state in the dilute phase (with few other ^{3}He atoms), then it must absorb heat from its surroundings in the process (explicitly, absorption of the latent heat of mixing). It is this very transport of ^{3}He atoms across the concentrated-dilute phase boundary that cools the dilution refrigerator and provides accessibility to the millikelvin temperature range. This cooling process dilutes the ^{4}He-rich fraction, which is how the term dilution refrigeration gets its name.

In order to take advantage of the latent heat of mixing of the two helium isotopes and achieve these low temperatures for extended periods of time, it is necessary to

continuously remove ^{3}He atoms from dilute phase. Figure 3.3 demonstrates this concept by showing the main components of a working dilution refrigerator and a flow diagram for its liquids.

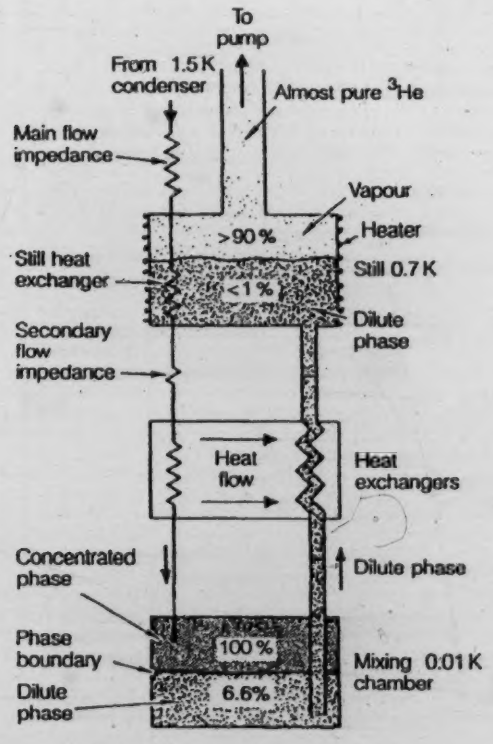

Figure 3.3: Schematic of a ^{3}He-^{4}He dilution refrigerator, with its main components and a flow diagram for its liquids [11].

The ^{3}He begins its tour at the exit of a room temperature pump by moving into the refrigerator and through its first stage of pre-cooling, a bath of liquid ^{4}He at 4.2 K. From there, the ^{3}He is condensed as it moves through a second liquid ^{4}He bath, kept at about 1 K by evaporation of ^{4}He (labelled "From 1.5 K condenser" in Figure 3.3. Appropriate flow impedances are put in place here to establish sufficient pressure for the incoming ^{3}He to actually condense (and to prevent re-evaporation

further down the line) at these temperatures. The now liquid ^{3}He will flow through heat exchangers (one of which is in thermal contact with the still, described below, at 0.7 K) and into the upper, concentrated phase in the mixing chamber. Recall from Figure 3.2 that the fluid is in a two-phase region at these temperatures. A wider tube leaves the lower, dilute phase of the mixing chamber and passes through the heat exchangers to pre-cool the incoming ^{3}He. It flows into the dilute liquid phase in the still, where the liquid ^{3}He concentration is typically less than 1%, while the vapour above this dilute liquid phase has a ^{3}He concentration of about 90%. This is due to the high vapour pressure of ^{3}He (as compared to ^{4}He) at these temperatures (as shown in Figure 3.4). The ^{3}He concentration gradient between the mixing chamber and the still results in an osmotic pressure that drives the fluid along the line.

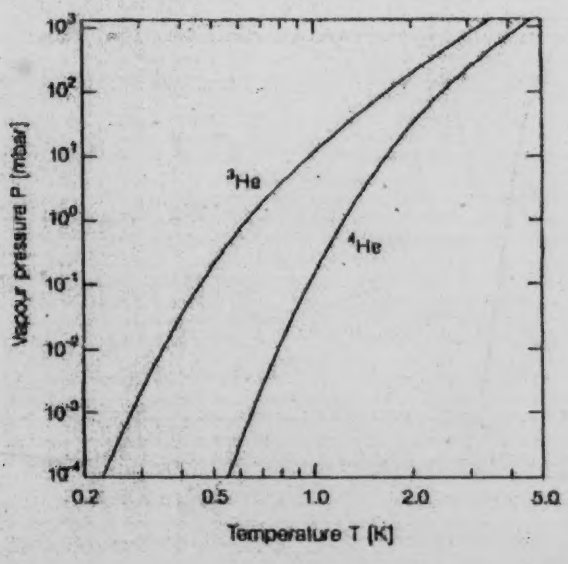

Figure 3.4: The vapour pressures of ^{3}He and ^{4}He as a function of temperature [11].

By pumping on the still and re-supplying this vapour to the condensation line continuously with ^{3}He, we achieve a closed circuit! ^{3}He is forced down the conden-

sation line, then, again, after liquefaction and pre-cooling, it enters the concentrated phase in the mixing chamber. Here it will cross the phase boundary (because we are preferentially removing ^{3}He atoms at the phase liquid-vapour phase boundary in the still), giving rise to cooling (the latent heat of mixing). It will eventually leave the mixing chamber and be driven up to the still via osmotic pressures, where it will be forced to evaporate. As mentioned before, the circulation of ^{3}He is maintained by a pumping system at room temperature.

3.3 Pressure measurements

In the study of solid (or liquid) helium, a knowledge of the pressure on the sample is often desirable. Using the known relationship between the molar volume or density and pressure, a measurement of pressure provides a rather convenient means for determining the density of a sample. Furthermore, the pressure can provide key fundamental information. Its usefulness in studying first-order transitions, such as the melting curve or crystallographic phase transitions, is obvious. As the partition function Z contains all the thermodynamic information, and recalling that the pressure is related to Z by

$$p = kT(\partial lnZ/\partial V)_T, \tag{3.1}$$

a study of the pressure versus temperature of a system at constant volume can provide an abundance of knowledge.

When studying liquids, the pressure of the system can be measured readily by some room temperature gauge in the external sample line. This is not possible in solids, however, as the solid plug in the sample line fill results in a pressure inhomogeneity between the sample cell at low temperature and the rest of the experimental system. In this case (and for constant volume measurements in the liquid) the pressure must be measured *in situ*. To this end, the Straty-Adams [110] capacitive pressure gauge was developed. The gauges are highly sensitive, extremely stable, have essentially no hysteresis, and are affected very little by changes in temperature below 4.2 K. Additionally, they have been operated at temperatures as low as about 10 mK, producing negligible heating at these low temperatures.

All of our *in situ* pressure measurements were made using homemade Straty-Adams gauges.

The body of the Straty-Adams gauge is constructed out of beryllium cooper (BeCu) and consists of a thin diaphragm (usually between 0.2 - 0.4 mm thick, depending on the pressures at which the gauge will be used) machined inside of an otherwise hollow cylinder (typically 9.5 mm o.d. and ~1 cm long), as shown in Figure 3.5. The body of the gauge is soft-soldered into a seated hole in the cell wall. The active part of the strain gauge faces the inside of the sample chamber, whose pressure is to be determined; on the other side of the diaphragm, there is a small post onto which a brass capacitor plate is fixed with epoxy. All epoxy used was BIPAX Tra-Bond BA-2151 [111], which has proven to provide reliable contact, even upon repeated thermal cycling between room and low temperatures. A second capacitor plate, fixed to a brass lid with epoxy, sits above the first, forming a parallel plate capacitor. As the pressure in the sample chamber is increased, the diaphragm of the Straty-Adams gauge is forced upwards, decreasing the separation between the capacitor plates and thereby changing their capacitance. Each capacitor plate includes, of course, a wire which runs from the inside of the gauge to the outside, so that we can measure the capacitance of the plates. Capacitances were measured using an automatic bridge operating at 1 kHz (Andeen-Hagerling 2550 A). The leads from the gauge to the bridge are coaxial cables. The plate separation is set by pressurizing the cell to the absolute maximum working pressure of the cell (typically about 100 bar) and then fixing the lid (with the affixed top capacitor plate) to the outer circumference of the Straty-Adams gauge body with epoxy (in this scenario, the plates are in contact and the capacitor is shorted). Once the epoxy has cured, the pressure in the cell is reduced leaving a plate separation on the order of 0.01 mm. A simple capacitance versus pressure calibration at 4.2 K against a room temperature pressure gauge (e.g., we use a Mensor Model 4040 pressure gauge, for the 0-70 bar range) is then all that remains to be done before we can use the gauge at low temperatures.

Pressures may be reported with one of any of an overabundance of possible units. At some point in their studies, a student of low temperature physics typically encounters the Pascal, the bar, the torr, the atmosphere, the p.s.i. (absolute, differential, and gauge), the mmHg, and the kg/cm^2. In this thesis, I will keep the pressures I report in units of bars (which is the SI Pascal [N/m^2] reduced by a factor of 10^5) - the most sensible unit, in my opinion.

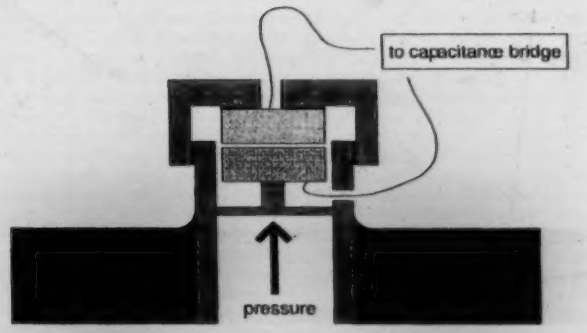

Figure 3.5: Schematic of our homemade Straty-Adams pressure gauges.

3.4 Temperature measurements

Thermodynamically speaking, temperature is the quantity in two systems which takes the same value in both systems when they are brought into thermal contact and allowed to come to thermal equilibrium. The temperature of a system is related to the average energy of microscopic motions in the system. This energy occurs as, for example, the translational motion of a particle or as internal energy of a particle, such as a molecular vibration or the excitation of an electron energy level. The process of cooling, generally speaking, involves removing energy from a system. When there is no more energy available to be removed, the system is said to be at absolute zero: the point on the thermodynamic (absolute) temperature scale where all kinetic motion in the particles comprising matter ceases and they are at complete rest in the classical (i.e., non-quantum mechanical) sense. Emphasis must be put on the word classical. By definition, absolute zero is a temperature of precisely 0 K (-273.15 °C or -459.67 °F).

3.4.1 Thermometry

At the most basic level, a thermometer is a device with a measurable output that changes with temperature in a reproducible manner. If an equation of state can be written for a thermometer without introducing any unknown, temperature-dependent quantities, then such a thermometer is called a primary thermometer. These include gas thermometers, acoustic thermometers, noise thermometers, and total radiation thermometers, to name but a few. A secondary thermometer is one whose output must be calibrated against defined fixed temperature points.

Primary thermometers are typically impractical (usually because of their size, speed, and/or expense), and so secondary thermometers are used for most applications. The standard practice is to use secondary thermometers that have first been calibrated to an internationally recognized temperature scale based on primary thermometers and fixed points. The most recent efforts in defining a temperature scale have resulted in the International Temperature Scale of 1990 (ITS-90) [112], whose lower limit is 0.65 K, and the Provisional Low Temperature Scale of 2000 (PLTS-2000) [113], which extends all the way down to 0.9 mK.

Even if a thermometer is properly calibrated, problems can arise for any number of reasons; for example, if the thermometer is not in sufficient thermal contact with the object whose temperature is to be measured, if the currents used to excite it cause self-heating (which is exceedingly an easy thing to do at the lowest temperatures, where even a few picowatts can cause a temperature error), or if its internal thermal response time is inconveniently long. It is essential to choose appropriate thermometers for the planned measurements, to mount and use them properly, and to view the temperature they report with a hint of skepticism. Whenever possible, more than one thermometer should be used so that you may check for consistency.

3.4.1.1 Germanium thermometers

Germanium resistance thermometers are the most convenient choice for measuring temperatures above 100 mK. They are sensitive, they respond rapidly, their calibrations are very stable, and they work directly with our digital temperature controllers (Conductus LTC-21 and Neocera LTC-21). Temperature dependent semiconductor resistance is exceptionally sensitive to doping during the manufacturing process, and so germanium resistance thermometers are secondary thermometers which must always be individually calibrated. Sensor resistance varies from several ohms at its upper useful temperature to several tens of kilo-ohms at its lower temperature. Device sensitivity increases rapidly with decreasing temperature, meaning that a high degree of resolution is achieved at lower temperatures: these resistors are very useful for sub-millikelvin control at 4.2 K and below. The germanium resistance thermometers sensors have excellent stability, $\pm$ 0.5 mK reproducibility at 4.2 K, and 200 ms thermal response time at 4.2 K.

Germanium resistance thermometers are measured in a standard 4-terminal resistance assembly, as the leads include part of the germanium chip itself and so

have resistance and temperature dependence comparable to that of the actual thermometer. Our germanium resistance thermometers are purchased commercially, hermetically sealed into little copper cans with a small dose of ^{4}He gas for thermal contact (or ^{3}He for the lowest temperature gauges). We customarily insert the sensor into a cylindrical copper mounting block, with the chip's electrical leads wrapped around the circumference (which serve as the thermometer's main thermal contact below a few hundred millikelvin), as shown in Figure 3.6.

Figure 3.6: One of our germanium resistance thermometers, mounted into a cylindrical copper mounting block, next to a dime for scale.

In general, resistance thermometers are quite susceptible to self-heating and electrical noise pick-up at temperatures below 1 K. At the lowest temperatures, the sensor excitation is reduced to keep ohmic heating of the thermometer below about 10 fW. If we consider, for example, a 25 kΩ sensor (a typical resistance at 50 mK), the excitation voltage should be kept below about 15 μV or the excitation current kept below about 0.6 nA. Our temperature control bridges can operate at fW levels, but electrical noise pickup (i.e., Joule heating, mostly radio frequency) often results in substantially larger thermometer readings. To reduce this noise, we install an L-C radio frequency filter box between the feedthrough at the top of our cryostat and the cable to the temperature control bridge. Even with these precautions, germanium resistance thermometers on their own should only really be trusted down to about 100 mK.

3.4.1.2 ^{3}He melting curve thermometers

Possessing a pressure-temperature relation with high sensitivity down to millikelvin temperatures, the ^{3}He melting curve (Figure 3.7) provides an excellent low temperature standard. Gauges can easily be constructed which very accurately measure the melting pressure of ^{3}He (as discussed in section 3.3), meaning that for accurate temperature measurements much below 100 mK, the ^{3}He melting curve thermometer [114] is the way to go. It is the basis of the current PLTS-2000 [113] below 700 mK, has high sensitivity, operates down to 1 mK, and doesn't suffer from self-heating. The thermal response time can also be relatively short (although ours is rather longer, at 10's of minutes below 50 mK).

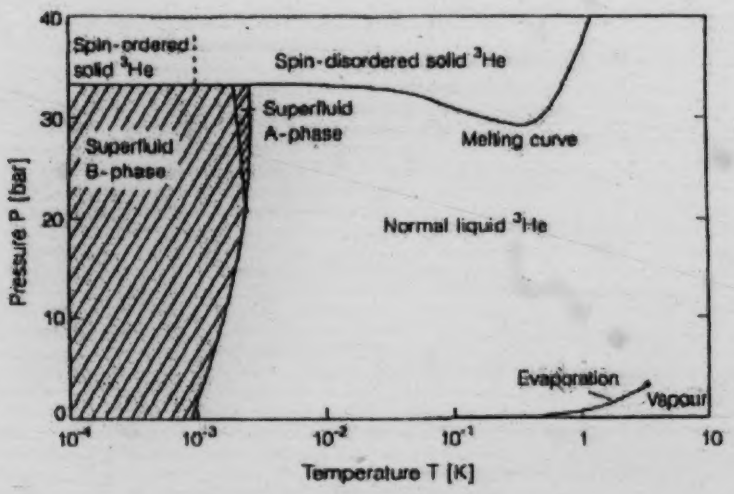

Figure 3.7: ^{3}He pressure-temperature phase diagram [11].

It has the significant advantage of having several fixed points incorporated into the scale: the temperature at the minimum of the melting pressure (T_{min}); the superfluid transition (T_A); the A-B transition (T_{AB}); and, the solid ordering transition (T_{SO}). The fixed points are given in Table 3.1. Of course, only T_{min} is accessible with our dilution refrigerator.

The polynomial which describes the ^{3}He melting curve is given by

	Pressure (bar)	T_{2000} (mK)
T_{min}	29.3113	315.24
T_A	34.3407	2.444
T_{AB}	34.3609	1.896
T_{SO}	34.3934	0.902

Table 3.1: The fixed points of the ^{3}He melting curve, used for the PLTS-2000.

Coefficient	PLTS-2000
a_{-3}	$-1.3855442 \times 10^{-12}$
a_{-2}	4.5557026×10^{-9}
a_{-1}	$-6.4430869 \times 10^{-6}$
a_0	3.4467434
a_1	-4.4176438
a_2	1.5417437×10^{1}
a_3	-3.5789853×10^{1}
a_4	7.1499125×10^{1}
a_5	-1.0414379×10^{2}
a_6	1.0518538×10^{2}
a_7	-6.9443767×10^{1}
a_8	2.6833087×10^{1}
a_9	-4.5875709×10^{0}

Table 3.2: The fixed points of the ^{3}He melting curve, used for the PLTS-2000.

$$P = \sum_{n=-3}^{+9} a_n T^n \tag{3.2}$$

where P is in MPa and T is in Kelvin. The coefficients, a_n, are given in Table 3.2. To obtain temperature in terms of the measured pressure requires inversion of the Equation 3.2. The simplest method, and the one we used, is to generate tables of T(P) and use a standard fitting package (Microsoft Excel will suffice) to fit short lengths of the curve.

With our digital capacitance bridge (Andeen-Hagerling 2550 A, operating at 1 kHz), using a ^{3}He melting curve thermometer is quite convenient; although, the thermometer must be calibrated against a room temperature pressure standard (we used a room temperature Mensor Model 4040 pressure gauge, 0-100 bars) at the beginning of each run (and it likely requires re-calibration if warmed above 700 mK). For optimal operation, the ^{3}He melting curve thermometer (like all thermometers) must be well thermally anchored to the system of interest.

The initial pressure versus capacitance calibration can be conveniently done at

around 1 K, before starting circulation in the dilution refrigerator. The gauge is first filled to about 35 bar; starting circulation in the refrigerator causes the capillary to block at about 0.75 K, with a suitable ^{3}He density in the gauge (i.e., so that it contains a solid/liquid mixture at all lower temperatures). During cooling, the capacitance at the ^{3}He melting curve minimum (315.24 mK) needs to be measured, since the pressure calibration must be corrected for the hydrostatic head in the fill capillary. With the pressure versus capacitance calibration available, the measured capacitances can be converted into pressures and subsequently into temperatures using the PLTS-2000 temperature scale.

Figure 3.8: Our (broken) ^{3}He melting curve thermometer, next to a dime for scale.

3.4.1.3 ^{60}Co nuclear orientation thermometers

This technique relies on the magnetic ordering of nuclear spins and the general theory of nuclear orientation has been formulated by several authors (see, for example, [115]). The principle is that when a radioactive nucleus decays by emitting a γ quantum (more specifically, β^- decay feeds a short-lived excited state, which then decays by emission of γ-rays) there is a certain anisotropic angular emission probability depending on the initial nuclear spin direction and characteristic of the decay (i.e., the emission is less probable along the axis of the spin). A collection of nuclei also shows anisotropic properties in the intensity of radiation, provided

that the nuclear spins are oriented (polarized or aligned). Assuming that a magnetic field is somehow applied (discussed below), the anisotropy of this radiation is temperature dependent and the absolute temperature is thus a function of the measured intensity. Specifically, the emission rate is lower in the directions parallel and antiparallel to the field than in other directions. By warming up the spin system, the overall emission becomes isotropic as the nuclear alignment/magnetization is destroyed. Comparing the emission rate along the axis at low temperatures with that at high temperatures (really, anything much over 50 mK) allows the low temperature to be readily deduced. By taking this ratio many experimental factors cancel and the result can be related directly to the temperature of the nuclei, thus forming a primary thermometer.

The advantage of using γ emitters is that detection can be from outside the cryostat with no wiring necessary inside the cryostat. In a typical setup (such as ours) the radioactive nuclei are ^{60}Co atoms, which have a half-life of 5.26 years. These are arranged to be in a single crystal of ordinary ferromagnetic ^{59}Co, so that the macroscopic orientation axis does not have to be provided by an externally applied field. Our sample is in the shape of a needle (parallel to the crystallographic c-axis) so that domains are aligned in opposition. This provides a well-defined orientation axis, but no net external field. The strength of this field defines the temperature range within which the nuclei polarize, being roughly between 100 mK and 1 mK.

The ^{60}Co nuclear orientation thermometer provides a very reliable way to make sure that other thermometers are reading correctly, since there is virtually nothing that can go wrong with it. It is a primary thermometer, requires no electrical or capillary connections, is immune to electrical noise, has negligible self-heating at dilution refrigeration temperatures, and has maximum sensitivity at the fridge's base temperature. Also, the high-energy γ rays are very penetrating, so no special windows are needed in the cryostat. On the downside, it requires the use of a (relatively) large scintillator and associated counting electronics, is insensitive to temperatures above about 50 mK, and requires long count times for accurate temperature measurements.

Typical count rates are less than 100 γ/second, so about 100 seconds are required to get a 1% accuracy, which still corresponds to a fairly large temperature uncertainty. We usually count for 1000 seconds at the most interesting spots in our

experiments.

As a millikelvin thermometer, it requires a clean, flat mounting surface and substantial clamping forces. Count rates must be measured along the cobalt crystal's c-axis. Our cobalt crystal is soft-soldered onto a copper wedge for easy mounting. The direction of the cobalt needle is recorded (height and position) so that the scintillator may be properly positioned once the dewar is raised. Given its simplicity and compactness, it is a thermometer worth mounting whenever you might even possibly consider cooling down to 50 mK.

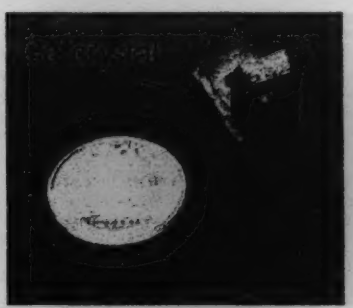

Figure 3.9: Our ^{60}Co nuclear orientation, next to a dime for scale.

3.5 Computer control

Data transcription was all but fully automated for the experiments. Various LabVIEW programs were either cannibalized from previous students and re-organized into the desired format or plainly written from scratch. LabVIEW software was also employed to communicate with the temperature bridge (for temperature control) and with the capacitance bridge (for example, to set the excitation voltage). Lastly, a LabVIEW program was occasionally used simply to display real-time data in chart format (which offers significant advantages over watching LED numbers change when trying to determine when a signal has stabilized).

Chapter 4

Dielectric Measurements of Helium Freezing in Vycor

The observation of NCRI in solid ^{4}He confined in porous Vycor was the first of the NCRI papers published by Kim and Chan. The supersolid interpretation of these results is quite extraordinary. Extraordinary claims require extraordinary evidence, which is what Kim and Chan continue to work on; equally important, though, is that the ordinary explanations be eliminated from the pool of possible solutions to the problem if the extraordinary claim is to gain acceptance in the scientific community.

It is important to recall from Chapter 3 that a torsional oscillator measures the moment of inertia of an added sample (and not simply the mass!). For example, migration of solid ^{4}He out of the porous glass would change the moment of inertia of a torsional oscillator cell and mimic superfluid decoupling. This turned out to be the case with molecular hydrogen [116].

A torsional oscillator technique was used to measure the H_2 mass inside of porous Vycor glass as a function of temperature and initial H_2 filling. At a certain temperature T_c, the resonant frequency of the torsional oscillator began to increase sharply: there seemed to be less H_2 contributing to the moment of inertia of the torsional oscillator at $T \leq T_c$ than was originally condensed into the Vycor, as shown in Figure 4.1. In other words, below T_c some of the H_2 seemed to no longer be participating in the oscillations. Could it be that the hydrogen had undergone a phase transition, becoming supersolid and thus unwilling to rotate with its container? In short: no. The same group independently determined with a capacitor filled with Vycor that H_2 molecules once adsorbed in Vycor leave it when the temperature is decreased. Their capacitance measurements indicate that at $T \leq T_c$ H_2 starts to leave the Vycor (apparently there is a de-wetting transition here that results in an

expulsion of mass from the Vycor sample), in good agreement with their torsional oscillator experiment.

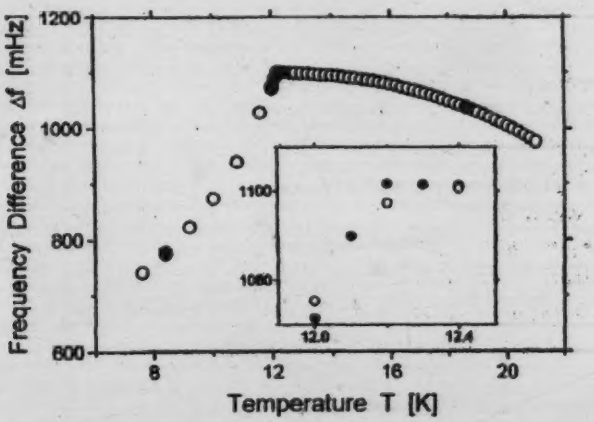

Figure 4.1: Frequency difference Δf(T) (equal to the resonant frequency of the empty oscillator minus the mass loaded frequency) in cooling (o) and warming (•) for n = 1.1 mmole H_2. The inset shows the data near T_c = 12.2 K. No hysteresis can be seen [116].

Structural transitions have also been seen in a number of adsorbates in Vycor. For example, a de-layering was observed in an argon layer near the pore surface [117] and crystallographic phase transitions exist for oxygen and argon at low temperatures [118, 119]. Also, solid argon and krypton have been seen [120] to migrate out of the pores well below their freezing temperatures. The well of alternative explanations is deep.

When ^{4}He is confined in the pores of Vycor, a number of measurements [121, 122, 123] have shown that the freezing curve is shifted upward by about 15 bar and to the left by about 0.6 K, as is shown in Figure 4.2.

Adams *et al.* [121, 122] have performed a series of experiments on the freezing of ^{4}He in Vycor and have inferred a density change substantially smaller than in bulk. It is not expected that the first monolayer or two of adsorbed atoms would experience an increase in density when freezing occurs in the pores (which is not unreasonable,

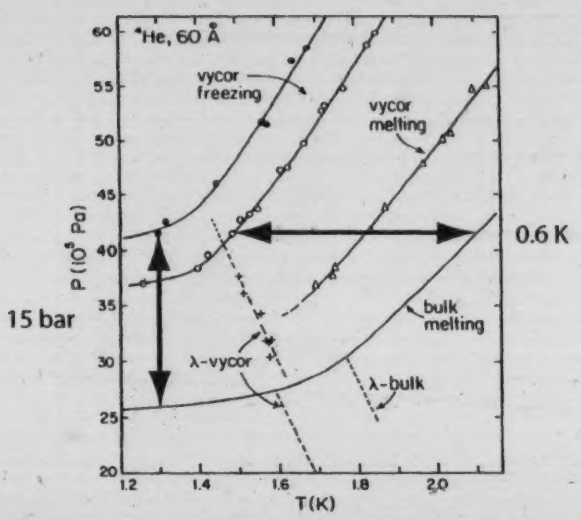

Figure 4.2: The pressure-temperature phase diagram of ^{4}He confined in 60-Å Vycor glass [122] and of bulk ^{4}He. Points shown are: (+) λ transition; (○) onset of freezing; (•) completion of freezing; (△) completion of melting.

since the van der Waals force on the ^{4}He near the surface will produce a liquid with a density that is likely already near that of the solid). They assume that no change in density occurs in a 6-Å-thick layer immediately next to the pores wall (i.e., does not participate in freezing), resulting in a remaining effective volume of the pore equal to roughly half that of the empty pore (i.e., only half of the pore volume is involved in freezing). This reasoning is consistent with their observations of the change in molar volume on freezing in the pores of Vycor, as shown in Figure 4.3.

The average latent heat of freezing in the pores was also determined by using the time interval required for freezing to take place and the measured heat current from the cell. The latent heat of freezing of the ^{4}He confined in the Vycor is shown in Figure 4.4, where that of bulk is included for comparison. The latent heat of the pore ^{4}He is greater than for bulk (and has a weaker temperature dependence). This is not unreasonable, as most of the entropy in the bulk liquid has been removed by the λ-transition at 1.8 K, while the superfluid transition in the freezing Vycor liquid does not occur until the reduced temperature of 1.4 K.

If Figures 4.3 and 4.4 are a reflection of incomplete freezing in the pores, then the decoupling seen in the torsional oscillator experiments could be occurring in a liquid

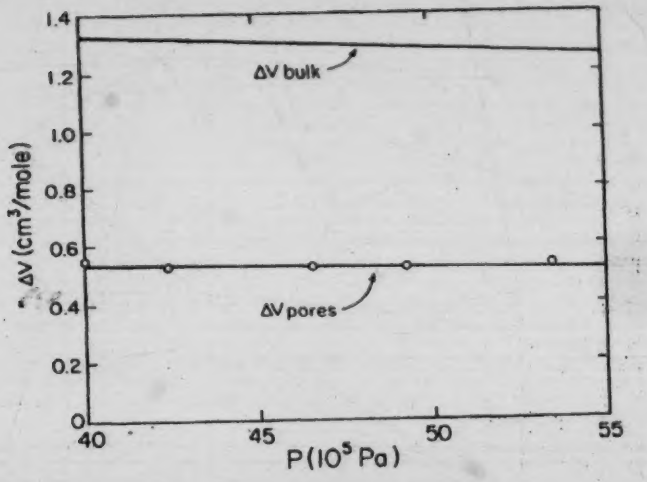

Figure 4.3: Molar volume change on freezing in the pores of Vycor versus pressure. The bulk volume change is shown for comparison [122].

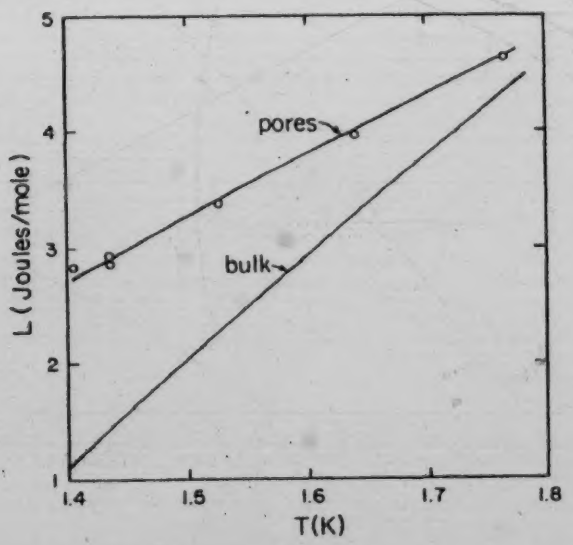

Figure 4.4: Latent heat of freezing in the pores of Vycor versus temperature. Bulk values are shown for comparison [122].

layer up against the pore wall, rather than in the solid ^{4}He. It is also important to rule out explanations based on a redistribution of mass.

4.1 Experimental design

The motivation behind the experiment described below is that alternative explanations to the NCRI observations exist and must be investigated. We have used a capacitive technique to study the density changes associated with freezing of ^{4}He in Vycor and at lower temperatures where Kim and Chan observed NCRI.

4.1.1 Cell construction

The density, pressure, and temperature measurements were performed simultaneously in one cell. A schematic and true picture of the cell are shown in Figures 4.5 and 4.6, respectively. The sample was sealed into an oxygen-free high conductivity copper pressure cell with a volume of 1.2 cm^3, much larger than the 0.018 cm^3 volume in the Vycor pores. The bulk ^{4}He, therefore, acted as a reservoir which kept the pressure essentially constant when ^{4}He in the pores froze. Crystals were grown using the blocked capillary technique. The cell incorporated an *in situ* Straty-Adams pressure gauge, soft-soldered into the side of the cell, and was mounted onto the bottom of the mixing chamber of our dilution refrigerator. A 0.004" i.d. capillary, thermally anchored at several points on the fridge, was used to introduce ^{4}He to the cell. Temperatures were measured with a calibrated germanium thermometer above about 50 mK, with a ^{60}Co nuclear orientation and/or ^{3}He melting curve thermometer for lower temperatures. A spring loaded clamp arrangement held the thin Vycor parallel plate capacitor inside the cell.

4.1.2 Vycor sample

Vycor, a Corning product, is a porous glass that is mechanically hard and strong, non-dusting, non-flaking, and chemically inert, distributed by BES Optics [124]. Vycor is 96% silica, but unlike pure fused silica it can be readily manufactured in a variety of shapes.

Vycor products are made by a multi-step process. First, a relatively soft alkali-borosilicate glass (75% SiO_2, 20% B_2O_3, and 5% Na_2O) is melted and formed by typical glass-working techniques into the desired shape. Second, the glass is heat treated, which causes a slow liquid-liquid diffusion to occur, resulting in separation

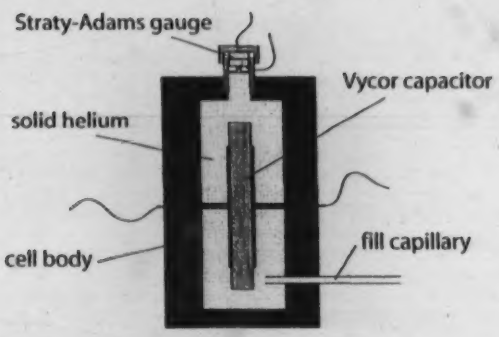

Figure 4.5: Schematic of the freezing cell.

Figure 4.6: Image of the freezing cell, next to a Canadian quarter for scale.

into a SiO_2-rich phase and a B_2O_3-alkali-oxide-rich phase. Third, after the glass has been heat treated and annealed, it is then soaked in a hot acid solution, which leaches away the soluble boron-rich phase, leaving an almost pure silica skeleton.

The resulting Vycor glass (code 7930) is an opalescent, open-cell, porous glass which exhibits excellent absorbing properties. Due to its porosity, this material has an internal surface area of approximately 200 m^2/g. Even a small bead of "thirsty" glass presents a very large adsorbing surface.

Figure 4.7 shows a TEM image of Vycor. In general, such images of Vycor show a material with a homogeneous distribution of mass and a disordered network of randomly and multiply interconnected cylindrical pores 3.5 nm in radius and roughly 30 nm in length [125]. The pore interface roughness has an upper cutoff of less than 2 nm. Our Vycor sample was a thin disc with a diameter of 12.7 mm and a thickness of 0.52 mm. The porosity of the Vycor sample is $\phi = 0.28$, defined as the ratio of open spaces (pores) to the volume of solid matter.

Figure 4.7: TEM image of porous Vycor glass [126]. Pores are shown in black, glass in shown in white.

4.2 Measurements in Vycor

The capacitor plates were copper thin films deposited directly onto the Vycor disc by thermal evaporation, as shown in Figure 4.8 (deposited at $\sim$ 3-4 Å/sec to a thickness of $\sim$ 100 nm) and a circular area of 0.71 cm^2. Before depositing the electrodes, we

dusted the Vycor with a 40 μm cobalt powder (held in place by a magnet placed behind the sample).

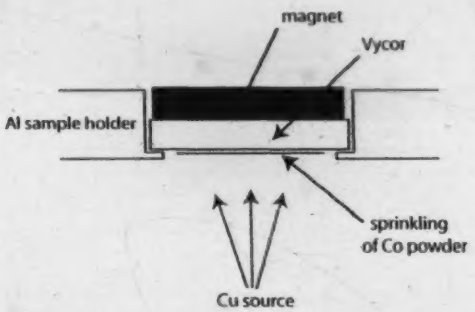

Figure 4.8: Schematic of electrode deposition onto Vycor.

After deposition the powder was removed, leaving an electrically continuous electrode with perforations (about 10 % of the area) to allow the ^{4}He easy access to the pores, as shown in Figure 4.9 and, schematically, in Figure 4.10. At 4.4 K the empty sample had a capacitance C_{vycor} = 3.7257 pF, roughly what would be expected from the manufacturer's quoted dielectric constant for Vycor ($\varepsilon_{vycor} = 3.1$ at 25 μC and 100 Hz).

(For the sake of future students, it is well worth noting that the room temperature capacitance of a Vycor-filled parallel-plate capacitor can change by as much as a factor of two(!) due to the dielectric contribution of adsorbed water. Recall that Vycor has hundreds of square meters of surface area per gram of mass. To be confident with your capacitance measurement, the Vycor should first be baked and under vacuum to minimize its moisture content.)

4.2.1 Capacitance as a measure of density

When ^{4}He is admitted to the pores of Vycor, the capacitance increases due to the change in dielectric constant (ε_{He} - 1) within the pore volume. Note that the dielectric constant of liquid ^{4}He is quite small, $\varepsilon_{(T=0)} = 1.0572$ [127]. The Clausius-Mosotti equation relates the dielectric constant ε to the mass density ρ, the molar mass M, and the molar polarizability α of a non-polar medium. The equation takes

Figure 4.9: Image of the Vycor capacitor.

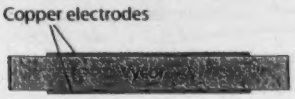

Figure 4.10: Schematic image of the Vycor capacitor.

the form

$$(\varepsilon - 1)/(\varepsilon + 2) = (4\pi/3M)\rho\alpha. \tag{4.1}$$

If the ^{4}He acted as a uniform dielectric, we would expect the capacitance change in our setup, ΔC, to simply be proportional to the porosity of the Vycor capacitor, ϕ, as

$$\Delta C = \phi(\varepsilon_{He} - 1)C_o, \tag{4.2}$$

where

$$C_o = \varepsilon_o \frac{A}{d} \tag{4.3}$$

is the geometric capacitance of our Vycor capacitor. Given our sample thickness (d $\approx$ 0.52 mm) and effective electrode area (A $\approx$ 0.78 cm^2, which includes an additional 10 % effect from fringe fields), $C_o \approx$ 1.33 pF. There will be a contribution to the capacitance increase from compression (and density increase) of the solid ^{4}He surrounding the capacitor, but our Vycor sample extends well beyond the edge of the capacitor electrodes and so this contribution is assumed to be zero. The inter-

ested reader is directed to the thesis of Herman [128], who took a closer look at the effect of fringe fields for a similar aerogel capacitor.

Using the dielectric constant of bulk liquid ^{4}He at 4.4 K ($\varepsilon_{He} = 1.048$, obtained by extrapolating the data in [129] from 4.21 K out to 4.4 K) and the porosity of Vycor ($\phi = 0.28$), Equation 4.2 predicts $\Delta C = 0.018$ pF. However, tightly bound layers on the Vycor pore walls increase the average ^{4}He density by about 25 % [130] and so we expect a proportional increase in ΔC, to 0.022 pF. Also, the contribution of a pore fluid to the dielectric constant depends on pore geometry through depolarization effects [131] and atoms on the surface of the glass likely have a different polarizability. Measurements with Ar and CO in Vycor have shown [132] that this can be accounted for by including a geometric parameter so that capacitance change is still proportional to the change in adsorbate density, giving

$$\Delta C \approx \frac{e_P}{(1-\phi)+\phi e_P}\phi(\varepsilon_{He}-1)C_o \approx 1.21\phi(\varepsilon_{He}-1)C_o, \tag{4.4}$$

where $e_P = 1.32$ for spherical pores or a mixture of perpendicular cylindrical pores. The Ar and CO measurements also showed that, except for the first monolayer, the changes in the Vycor's capacitance are directly proportional to the total density of the adsorbate.

We have confirmed this linear dependence for liquid ^{4}He via a 1.8 K adsorption isotherm, shown in Figure 4.11: for fillings greater than the first monolayer, the Vycor capacitance increased linearly with the amount of ^{4}He adsorbed. The isotherm measurements were made in the same cell shown in Figures. 4.5 and 4.6, attached to the 1 K pot of a simple ^{4}He cryostat. Temperatures were measured with a calibrated germanium thermometer and capacitances was measured using GR1615A bridge operating at 1 kHz. Small amounts of gas (less than 50 mbar) were let into the cell from a 66.9 cm^3 ballast volume and allowed to equilibrate for tens of minutes before a capacitance measurement was made and the process repeated.

The first six data points in grey in Figure 4.11 shows that the dielectric behavior of the first monolayer is different from the rest of the pore filling. The dielectric response attributed to the monolayer likely includes both the direct contribution of the monolayer molecules as well as the changes of the response of the terminating polar groups of the silica matrix brought forth by adsorption. The final three data points in black in Figure 4.11 deviate from the linear trend at a filling fraction of 1.0,

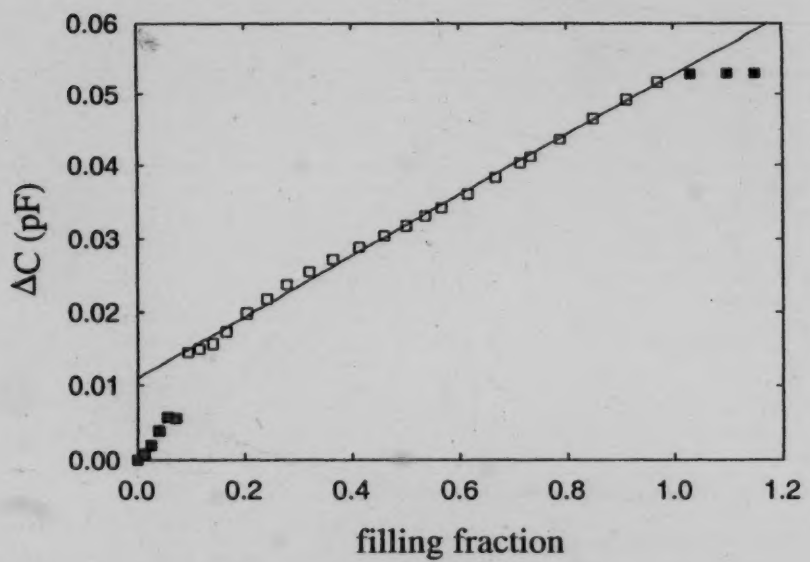

Figure 4.11: The 1.8 K ^{4}He adsorption isotherm in Vycor, confirming that capacitance change varies linearly with adsorbate density.

as expected. This is the point at which the pores of the Vycor are completely full and any ^{4}He further admitted to the cell will settle in the "dead volume" (outside of the Vycor) and therefore not contribute to the capacitance across the Vycor sample. Finally, the data wavers from perfect linearity in the [0.1 - 0.5] filling fraction regime because of insufficient equilibration time between measurements.

Using Equation 4.4, and accounting for the tightly bound layers on the Vycor pore walls which increase the average ^{4}He density by about 25 %, we now expect a capacitance increase $\Delta C = 0.027$ pF. The capacitance of our evacuated Vycor was 3.7257 pF, which increased by 0.029 pF when it was filled at 4.4 K. This is in very good agreement with the change calculated from Equation 4.4, confirming that our capacitance measurements directly probe the ^{4}He density in the pores.

(In the interest of being completely transparent, it should be noted that Equation 4.4 predicts a capacitance change $\Delta C = 0.032$ pF for the 1.8 K isotherm, whereas the observed change is actually 0.052 pF. This discrepancy cannot be explained.)

4.2.2 Freezing and melting under confinement

It is well-known that ^{4}He [133] in confined geometries remains liquid at temperatures considerably below bulk freezing and at pressures considerably above bulk freezing (for a very nice review on confinement effects on freezing and melting, see[134]). It has also been well-established that freezing occurs at a lower temperature than melting (i.e., there is a hysteresis) and that both freezing and melting are spread over a range of temperatures.

When confined in pores, liquid ^{4}He may be considered to form two components. The first is a dense solid-like layer of a few atomic thickness that contacts the pore wall. Strong van der Waals attraction with the amorphous glass make this film very tightly bound and highly disordered. The second is what remains in the pore and it acts nearly like a bulk fluid, not significantly influenced by the glass and with nearly bulk density.

The usual interpretation of the depressed freezing temperature is based on the homogeneous nucleation theory of droplet formation (i.e., the spontaneous solid formation as a result of density fluctuations, without benefit of nucleation at contact surfaces or impurities). It has been shown that the liquid phase preferentially wets the surface of glass [135]; namely, that the solid-glass interfacial energy, σ_{sg}, is greater than the liquid-glass interfacial energy, σ_{lg}. The mismatch between the interatomic spacing of ^{4}He adsorbed on the walls and that of the solid within the pore is commonly invoked to explain non-wetting of the walls by the solid and the subsequent lack of inhomogeneous nucleation.

Upon nucleation of a droplet of radius r, the change in the Gibbs free energy is given by

$$\Delta G = 4\pi r^2 \sigma_{ls} - \frac{4\pi r^3}{3v_s}(g_l - g_s), \tag{4.5}$$

where the first term is the free energy of the surface of the droplet and the second term is the change in free energy of the volume of the solid droplet. Here g_l and g_s are the molar free energies of the liquid and the solid, respectively, and v_s is the solid molar volume. The general form of Equation (4.5) is shown in Figure 4.12. The expression has a maximum at

$$r_b = \frac{2\sigma_{ls} v_s}{(g_l - g_s)}, \tag{4.6}$$

where droplets of $r < r_b$ are unstable and decrease in size, while droplets of $r > r_b$ grow.

If the freezing is assumed to take place at constant pressure, there is a depression of the freezing temperature, ΔT, from the bulk freezing temperature, T_B, given by

$$(g_l - g_s) = \left(\frac{\partial g}{\partial T}\right)_P dT = -(s_l - s_s)\Delta T = \frac{l_F}{T_B}\Delta T, \tag{4.7}$$

where s_l and s_s are the molar entropies of the liquid and solid, respectively, and l_F is the molar latent heat of freezing.

Substituting for (g_l - g_s) in Equation (4.6) allows us to write

$$\Delta T = \frac{2\sigma_{ls} v_s T_B}{r l_F}, \tag{4.8}$$

which further allows us to write Equation (4.5) as

$$\Delta G = 4\pi r^2 \sigma_{ls} - \frac{4\pi r^3}{3 v_s}\frac{l_F \Delta T}{T_B}. \tag{4.9}$$

Now consider that inside the pores of Vycor, ^{4}He nuclei of various radii are continually forming via local density fluctuations in the liquid. In a bulk system, nuclei with $r > r_b$ overcome the energy barrier and continue growing in size until the entire sample is frozen. Under confinement, however, nuclei may form but obviously cannot grow any larger than the confining pore. For a given undercooling, a pore-sized droplet may overcome the energy barrier yet still be left with positive free energy due to growth restriction imposed by the pore walls. Fluctuations similar to those which initiated freezing will eventually drive the droplet back into the liquid state. A critical radius, r_c, for freezing in pores is defined as one with zero change in Gibbs free energy,

$$r_c = \frac{3\sigma_{ls} v_s T_B}{l_F \Delta T}. \tag{4.10}$$

Stable solidification then occurs when the critical radius is equal to (or less than)

the pore size, r_p. So, a freezing point depression may be predicted if a pore size is given by

$$\Delta T = \frac{3\sigma_{ls} v_s T_B}{r_p l_F}. \tag{4.11}$$

With ^{4}He, it becomes equally useful to express solidification in pores in terms of elevated pressures at constant temperature (rather than depressed temperatures at constant pressures), as there exist a range of pressures in which the bulk ^{4}He of a system freezes while the confined ^{4}He remains liquid down to 0 K. This is done by writing

$$(g_l - g_s) = \left(\frac{\partial g}{\partial P}\right)_T dP = (v_l - v_s)\Delta P. \tag{4.12}$$

Substituting for (g_l - g_s) in Equation (4.6) this time allows us to write

$$\Delta P = \frac{2\sigma_{ls} v_s}{r}\left(\frac{v_s}{v_l - v_s}\right). \tag{4.13}$$

And by using the same line of reasoning above, we can say that solidification in pores (which, in Vycor, are connected and not independent) requires a pressure increase given by

$$\Delta P = \frac{3\sigma_{ls} v_s}{r_p (v_l - v_s)}. \tag{4.14}$$

For the reasons discussed above, the melting curve is shifted from bulk values as shown in Figure 4.13.

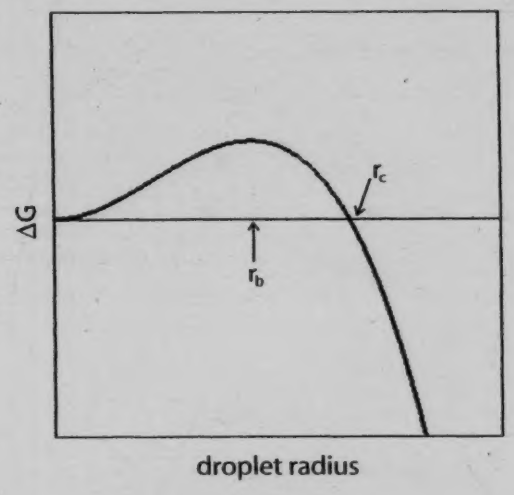

Figure 4.12: Gibbs free energy of a nucleating spherical droplet.

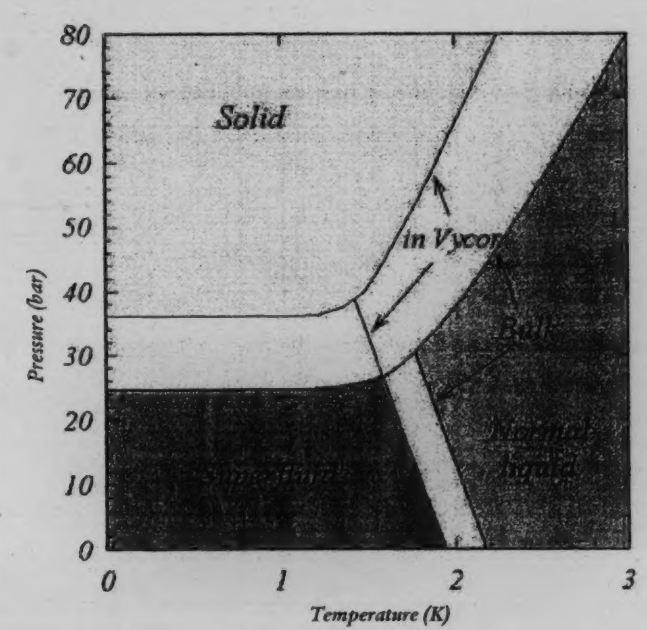

Figure 4.13: Phase diagram of ^{4}He confined in Vycor. Figure created from the data of Reference [122]

4.2.3 Typical thermodynamic path

Figure 4.14a shows the thermodynamic path during a typical measurement, as we cool our cell from about 4 K to low temperature.

The cell and Vycor sample are initially filled with ^{4}He to a high enough pressure at 4.4 K to ensure that everything (bulk and confined ^{4}He) solidifies at low temperature. Recall that the fill line blocks at the 1 K pot on the dilution fridge (at essentially the start - before any freezing in our cell takes place) and so the total amount of ^{4}He in the cell during a measurement is fixed (i.e., the thermodynamic path we are following are isopycnals).

As we decrease the temperature of our cell, there is an associated decrease in pressure within our sample. The decrease in pressure is a result of an increasing fluid density of a fixed amount of ^{4}He in a constant volume. As we reach point A (2.8 K, 68.4 bar), the bulk ^{4}He in the cell begins to freeze. Here, the pressure drops more rapidly as bulk ^{4}He around the Vycor sample begins to freeze. This time, the decrease in pressure is a result of the solid's greater density and the fixed amount of ^{4}He in a constant volume. The bulk melting curve is followed down until point B (2.1 K, 41.6 bar), which indicates the conclusion of freezing of ^{4}He in bulk. Below point B the pressure is very nearly constant since the thermal expansion of solid ^{4}He is small (and the compressibility is large, to be precise). Note that the ^{4}He confined to the Vycor pores does not begin to freeze until sufficient undercooling is achieved, as previously discussed in section 4.2.2, at point C (1.7 K, 40.8 bar). There is a small decrease in pressure associated with the freezing in the pores, but it is too small to be visible in Fig 4.14a. The bulk ^{4}He in the cell and around the Vycor sample acts as a reservoir so that freezing in the pores occurs essentially at constant pressure. After the initial cool-down, the cell could be warmed and cooled, re-tracing the thermodynamic path and confirming that the plug in the fill line had not slipped. Once the ^{4}He in the pores was frozen, the pressure in the cell is essentially constant as we approach absolute zero.

Figure 4.14b shows the Vycor capacitance, C_{vycor}, corresponding to the pressure of Figure 4.14a. Recall that the capacitance is a reflection of the ^{4}He density in the pores. The decrease between point A and point B is due to liquid ^{4}He leaving the pores as the pressure in the cell drops as the bulk ^{4}He freezes. Below point B, the pressure and the liquid density in the pores is nearly constant; the slope of C_{vycor} is

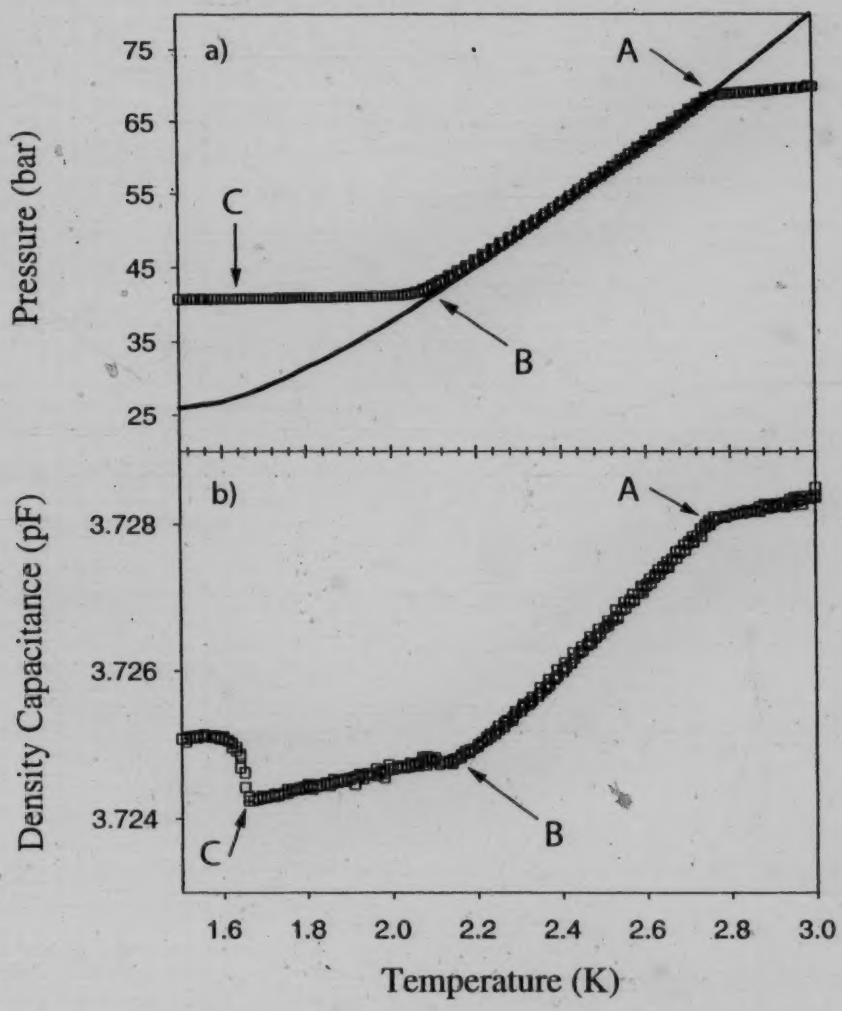

Figure 4.14: a) the thermodynamic path followed during a typical measurement, with b) the associated density capacitance. See text for meaning of letters. The solid line is the accepted melting curve for ^{4}He, taken from [151].

just the background temperature dependence of the dielectric constant of the Vycor glass itself (details in section 4.5). Freezing in the pores begins at point C, where C_{vycor} rises suddenly due to the larger density of solid ^{4}He. This requires that ^{4}He be drawn into the pores from the surrounding bulk solid bath (i.e., that pressure equilibrium is maintained at melting on this time scale). Not all of the ^{4}He in the pores will freeze at once: there exists a narrow freezing band (because of the narrow pore radius band in the Vycor) over which gradually more and more of the liquid is converted into solid as the temperature is lowered. Once the ^{4}He in the pores has completely frozen, C_{vycor} follows the background temperature dependence of the dielectric constant of the Vycor glass.

4.3 Onset of freezing

Despite the background temperature dependence of C_{vycor} (due to "two levels systems" in the glass, to be discussed in section 4.5), we can extract the jump in capacitance, ΔC_f, associated with freezing.

The jumps in Fig 4.15a-f ($\Delta C_f = 0.0011$ pF) are about 2.8 % the total change due to filling and pressurizing with liquid to 38.1 bar ($\Delta C = 0.0395$ pF). This is significantly smaller than the 6 % density increase when bulk ^{4}He freezes at this temperature [136]. This could be due to a large fraction of the ^{4}He (i.e., the dense surface layer) which is already highly localized and so would not participate in freezing and melting. However, it is also possible that some of the ^{4}He simply remains liquid at these pressures. We would expect the amount of liquid remaining at low temperatures to decrease with increasing pressure, but Figure 4.15 shows that this isn't the case. The increases in capacitance associated with freezing are essentially the same at all pressures in the 35-55 bar range, in contrast to what would be expected if the ^{4}He was only partially frozen at some lower pressures. Figure 4.16 shows the density change $\Delta\rho$ for ^{4}He in Vycor as we measure it, along with the ^{4}He in Vycor results obtained by Adams *et al.* [122]. In their experiment, they are able to measure the pressure in the pores of a Vycor powder on freezing and melting while simultaneously obtaining the volume change and latent heat on freezing. The density change for bulk freezing [136, 137] in the same temperature range is also included, for comparison.

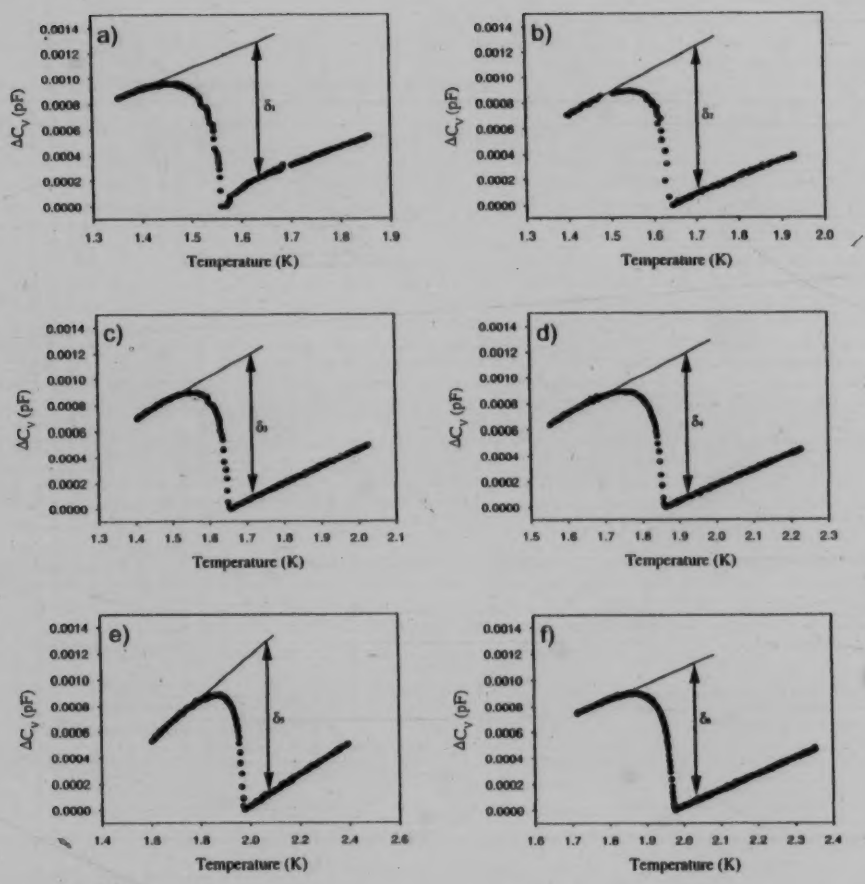

Figure 4.15: The sudden increase in density capacitance associated with the onset of freezing in the pores of Vycor: a) $\delta_1 = 0.00105$ pF at 36.2 bar, b) $\delta_2 = 0.00110$ pF at 36.8 bar, c)$\delta_3 = 0.00107$ pF at 39.3 bar, d) $\delta_4 = 0.00108$ pF at 48.3 bar, e) $\delta_5 = 0.00113$ pF at 53.8 bar, f) $\delta_6 = 0.00108$ pF at 54.0 bar.

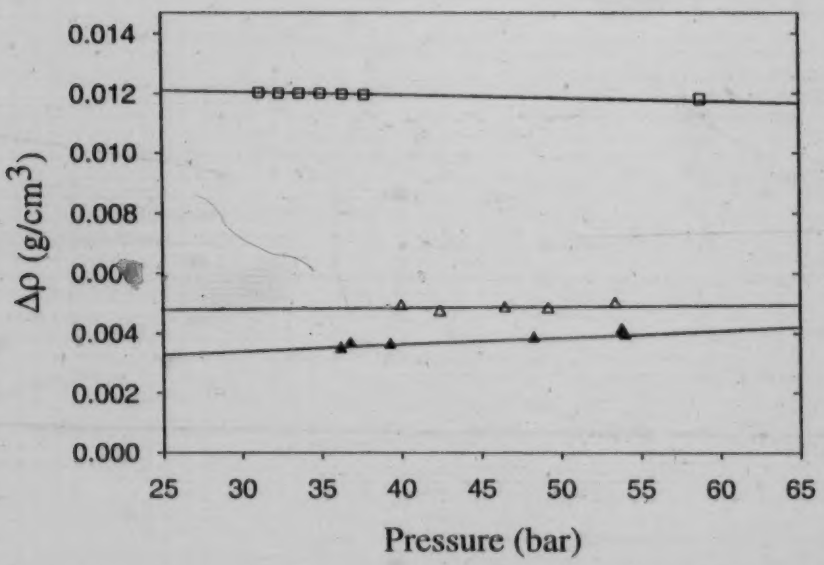

Figure 4.16: Solid-liquid density change associated with freezing. □'s are for bulk values, as measured by Grilly *et al.* [137, 136]; △'s are for ^{4}He confined in Vycor, as measured by Adams *et al.* [122]; ▲'s are for ^{4}He confined in Vycor, as reported in this thesis. Solid lines are guides to the eye. The reason for the difference in the data between that reported in this thesis and of [122] is not known.

4.4 Hysteresis between freezing and melting

When the sample was later warmed, the ^{4}He in the pores melted at higher temperature and over a narrow temperature range, as shown in Figure 4.17. The hysteresis between freezing and melting is a common feature of adsorbates in small pores [134]. The hysteresis arises from the energy barrier associated with surface formation that must be overcome to form disconnected blobs of solid within the pore network.

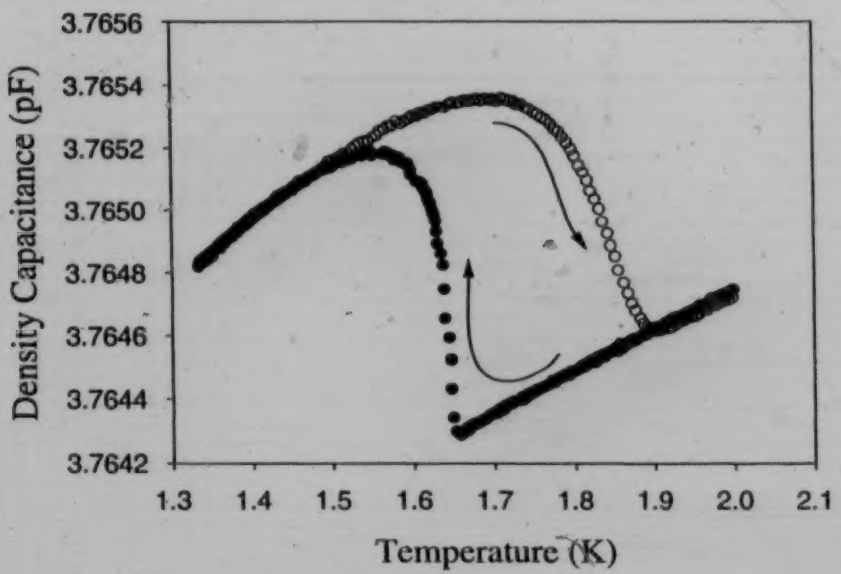

Figure 4.17: Hysteresis between freezing and melting, at 39.3 bar. The •'s are cooling and the o's are warming.

4.5 At lower temperatures

While the goings-on near melting are interesting, it was an observation at low temperature that motivated this study. Following solidification of the ^{4}He within the pores, we then cooled the solid ^{4}He-filled Vycor sample to look for any changes in ^{4}He density that might mimic superfluidity in a torsional oscillator. Possible scenarios of mimicking behaviour could include de-wetting transitions or crystallographic

phase transitions. For example, were the ^{4}He to leave the hcp phase (assuming that the ^{4}He is indeed in the hcp phase), then the density of the solid within the pores would change, thereby altering the system's moment of inertia and showing up as a period change in a torsional oscillator experiment. Figure 4.18 shows the capacitance data over the full range of the temperatures investigated for a 36.6 bar sample, where the letters A, B, and C were defined in subsection 4.2.3.

The dielectric (and thermal and acoustic) properties of amorphous materials, such as Vycor, exhibit different behaviours from those of crystalline substances at very low temperatures and the smooth capacitance minimum, located at ~85 mK in Figure 4.18, is typical of dielectric glasses. The minimum reflects coupling to "two level systems" and not changes in the ^{4}He density (e.g., the effect would be present in empty Vycor). For a nice short review of two level systems [138, 139], see chapter 3 of Mulders' doctoral dissertation [140].

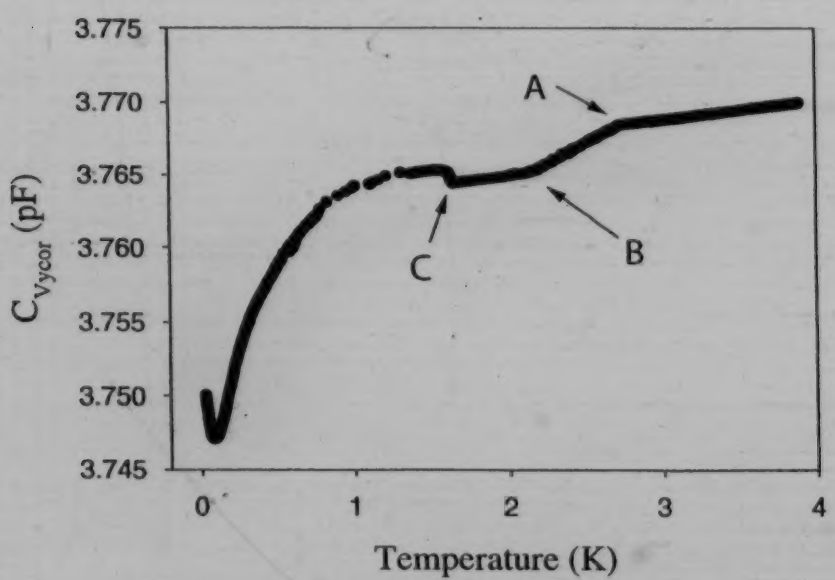

Figure 4.18: Vycor capacitance, from 4 K to 30 mK.

Experimentally, such behaviour has been observed in various amorphous ma-

terials. (In fact, the temperature dependence is sharp enough that several glasses prove useful as a thermometer!) Figure 4.19, displaying measurements made on an OH-doped vitreous silica called Suprasil, provides an example of how the dielectric properties of amorphous glass change with temperature, as a function of frequency. The minimum that we observe at ~85 mK and with a 1 kHz measurement is not inconsistent with the dielectric measurements shown in Figure 4.19.

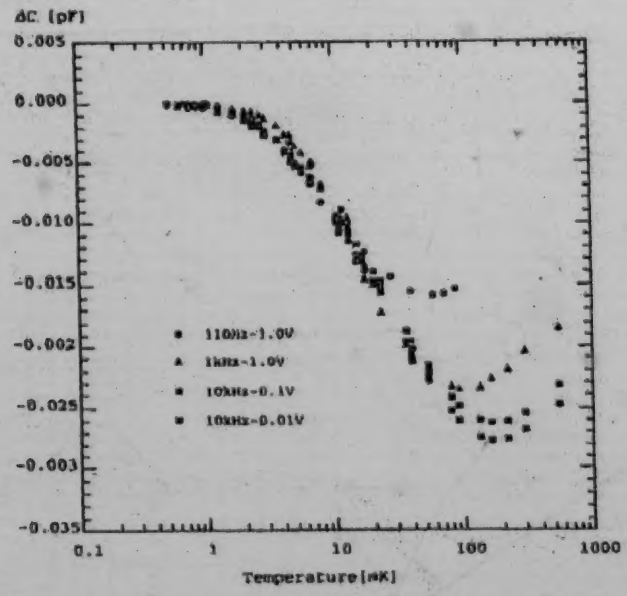

Figure 4.19: Variation of the capacitance in Suprasil glass as a function of temperature [141]. The negative slope of ε(T) on the low temperature side of the minimum is due to resonant interactions and is frequency independent provided $\hbar\omega \ll$ kT. At higher temperatures, where the slope is positive, relaxation interactions becomes dominant.

To further confirm that the minimum in our capacitance was in no way related to the solid ^{4}He, we took an analogous measurement of liquid ^{4}He at saturated vapour pressure confined in the pores of Vycor, where the superfluid transition is at around 2 K, at low temperature. As is shown in Figure 4.20, the minimum in capacitance remains: it is an effect of the porous Vycor glass and not of the ^{4}He.

(Without question, capacitance measurements of our empty Vycor sample should have been performed. Unfortunately, the significance of this measurement only became apparent after ^{4}He had been adsorbed onto the cold Vycor pores.)

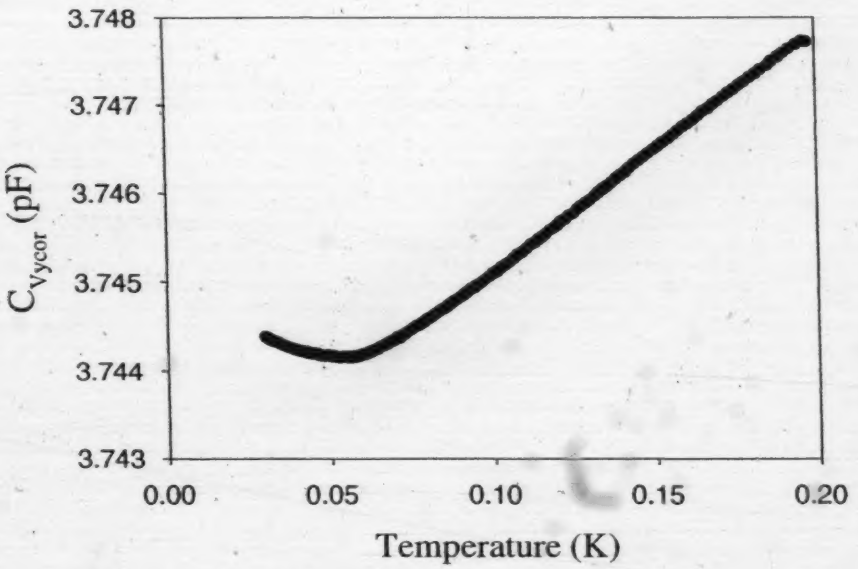

Figure 4.20: Vycor filled with liquid ^{4}He at saturated vapour pressure.

Figures 4.21 and 4.22 show the capacitance data at low temperature and in the region of greatest interest (i.e., where Kim and Chan observe NCRI). If there was a low temperature transition which resulted in ^{4}He being expelled from the pores of the Vycor, then it would show up as a sudden decrease in capacitance, but we saw no such change in the range below 200 mK where Kim and Chan saw decoupling in their torsional oscillator. The arrow in Figures 4.21 and 4.22 show the magnitude of the change that would be expected if 1% of the ^{4}He were to leave the pores.

Since movement of ^{4}He out of (or into) the pores might occur very slowly (Kim and Chan observed time constants on the order of one hour for their oscillator period to stabilize), we waited overnight at our lowest temperature (about 30 mK) and then warmed up our sample. Figure 4.23 shows our density capacitance data on cooling through the minimum at ~85 mK down to base temperature and then on

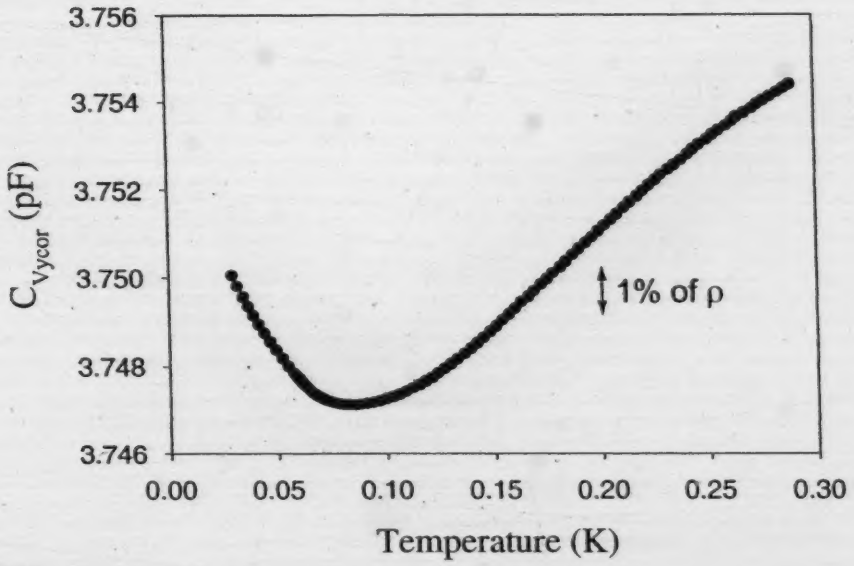

Figure 4.21: Density change of solid ^{4}He in Vycor at low T and at 36.6 bar. The arrow indicates the size of change we'd expect to see for a 1% density effect.

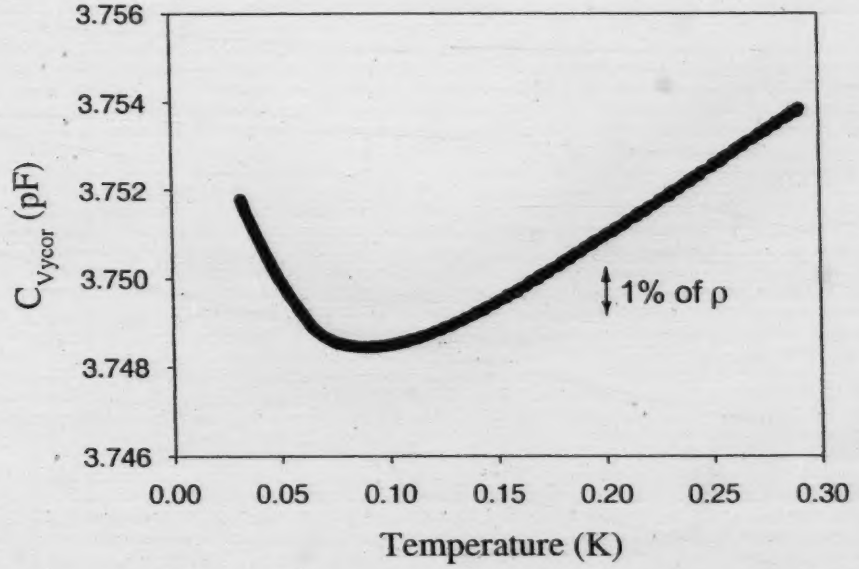

Figure 4.22: Density change of solid ^{4}He in Vycor at low T and at 53.6 bar. The arrow indicates the size of change we'd expect to see for a 1% density effect.

warming back through the minimum, about 20 hours later. The measured difference in density capacitance is about 5 ppm, which is a change in density equal to 0.05%. Figure 4.24 shows the same measurement made in a different experimental cell. Here, the measured difference in density capacitance after cooling to base temperature and then waiting overnight is about 3 ppm, which is a change in density equal to 0.03%. Both measurements support the claim that ^{4}He does not move out of (or into) the pores, even very slowly.

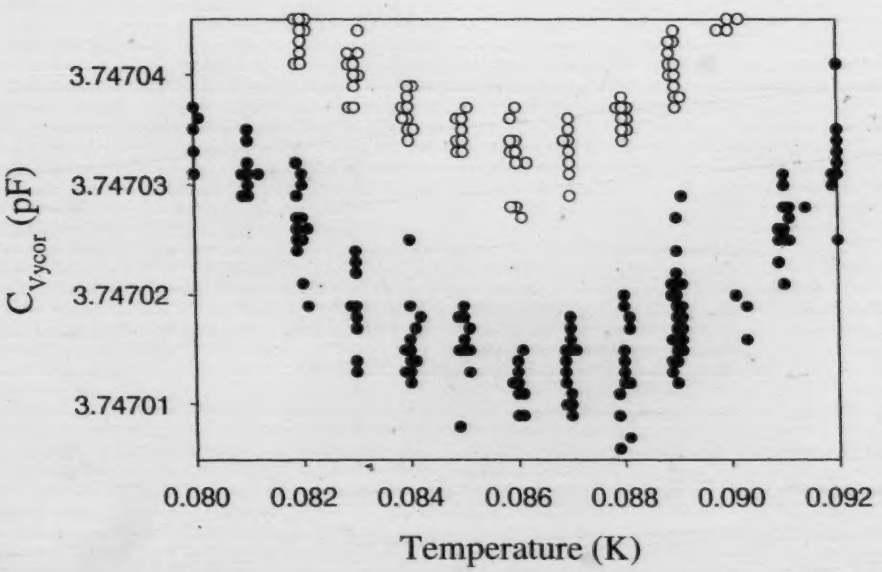

Figure 4.23: Low temperature stability of the confined ^{4}He density at 36.6 bar (i.e., the minimum from Figure 4.21). •'s show cooling and o's show warming.

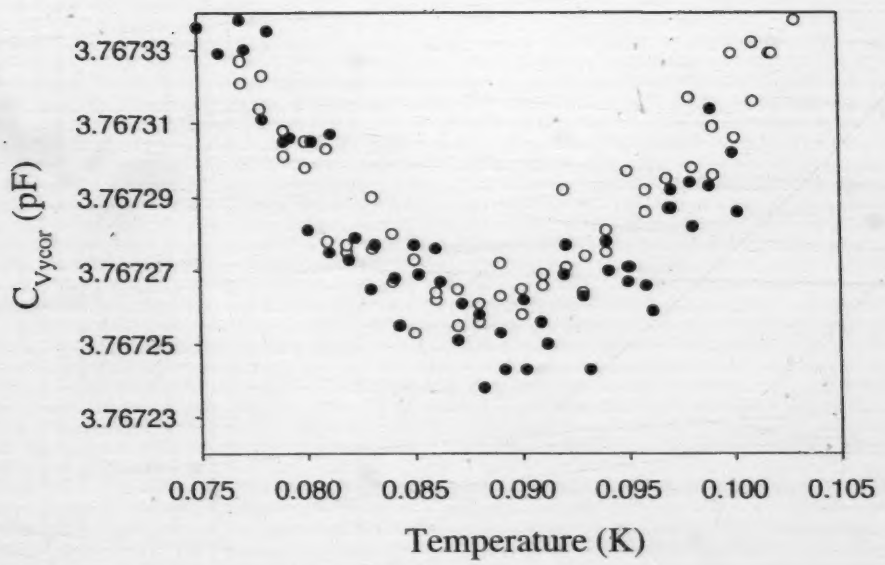

Figure 4.24: Low temperature stability of the confined ^{4}He density at 57 bar (the data shown in this plot was taken in the Vycor squeezing cell, to be described in Chapter 6, which did not have an *in situ* pressure gauge). •'s show cooling and ○'s show warming.

4.6 Conclusions

Motivated by claims of a supersolid phase in ^{4}He, we have taken some dielectric measurements of ^{4}He freezing in the pores of Vycor. We have confirmed that the density change associated with freezing is substantially smaller than in bulk, telling us that not all of the ^{4}He in the pores is actually participating in solidification. Or, although unlikely, that it all does freeze, but the volume change associated with freezing is small in the pores of Vycor (for reasons unknown). If some of the confined ^{4}He remained liquid (say, as some thin film that lines the pore), then it is entirely possible that the superfluid-like behaviour observed by Kim and Chan in their torsional oscillator experiment is actually superfluidity in that thin film. However, we expect that the thickness of this film (i.e., the amount of ^{4}He that remains liquid) would be dependent on pressure. Our measurements, though, strongly suggest that the amount of ^{4}He that solidifies in the pores is independent of pressure. We cannot rule out the presence of a persistent liquid layer. What we can say is that there likely exists an amorphous ^{4}He film strongly adsorbed to the pore wall, having a density already near that of the solid phase and thereby not really contributing to the change in density upon complete solidification. The properties of such a film are unknown, but it is conceivable that it could display superfluid-like behaviour. In fact, Path Integral Monte Carlo (PIMC) simulations [142] support the persistent liquid layer model to explain the NCRI observations, as it is found that ^{4}He forms a distinct layered structure. The first layer is solid-like and highly localized; the second layer is disordered (some atoms are not localized and they could give rise to the observed superfluid response); higher layers are then nearly perfect crystals and only participate in the superfluidity in so far as they are close to the second layer. Variational Monte Carlo simulations [143] further support the persistent liquid layer model. Those "experiments" conclude that the layer in contact with the pore is always solid. For their narrow pore radius (R = 1.3 nm, roughly half that of Vycor), as the density is increased, solidification takes place layer by layer, starting from the pore wall. Their pore radius is too small to allow a bulk-like solid to nucleate in the liquid region at the center of the pore, and in order to have a complete crystalline order in all the layers a pressure greater than 200 bar was required.

Figure 4.16 suggests that about 70% of the ^{4}He confined in the pores of Vycor does not participate in freezing. If this were the case, and taking a spherical pore

radius of 3.5 nm, then it would be an outer shell 1.2 nm thick that remains "unfrozen". This thickness corresponds to 3-4 layers of adsorbed ^{4}He not participating in a phase change, which seems plausible and is not inconsistent with the theoretical results mentioned above.

We also find no evidence of any sudden density changes, such as a crystallographic phase transition, nor any signs of the solid ^{4}He leaving the Vycor, such as a de-wetting transition, at low temperatures. Anything of this sort would have altered the moment of inertia in a torsional oscillator and could have looked like mass decoupling (or, perhaps, it would have increased the moment of inertia). Our results leave no doubt that the ^{4}He stays put at low temperatures.

This first set of measurements described rule out some of the most obvious alternative explanations to the NCRI observed for solid ^{4}He in Vycor, thus strengthening the supersolid claims. It then becomes interesting, however, to see whether solid ^{4}He exhibits any of the other unusual flow properties of a superfluid. If we naïvely assume that a supersolid behaves in an analogous way to a superfluid, there are other experiments one could do to help solve this mystery. Some of these experiments are described in the following chapters.

Chapter 5

Pressure Induced Flow of Solid Helium (Vycor)

Other than the torsional oscillator experiments, there has not (yet) been a direct observation of supersolid behavior of ^{4}He, either in bulk or under confinement. However, the small critical velocities implied and the apparent sensitivity to ^{3}He impurities may affect dc flow (or other properties) even more strongly than the decoupling in the torsional oscillator measurements. It is important to recall that solids have many properties not shared by liquids (e.g., a lattice with shear rigidity) and a supersolid may not exhibit all of the effects we typically associate with superfluidity (e.g., superleaks, persistent currents, thermo-mechanical effects, quantized vortices, second sound, etc.). Below we describe an experiment to look for one such property in solid ^{4}He in Vycor: superflow in response to applied pressure.

5.1 Vycor experimental design

Since the measurements discussed in the previous chapter essentially rule out what we believe to be the most obvious alternate explanations of the decoupling observed in solid ^{4}He in Vycor, it became interesting to see whether or not solid ^{4}He exhibited any of the other unusual flow properties of a superfluid.

By suddenly increasing the pressure in a cell containing the same Vycor sample used in our freezing experiment, we were able to monitor the pressure induced flow of solid ^{4}He into the pores. It is known that thermally activated vacancies can transport mass in a pressure gradient. Beamish *et al.* [144] reported on results of ultrasonic attenuation and velocity measurements of helium freezing in Vycor, in which they observed attenuation peaks whose dependence on frequency and temper-

ature was characteristic of a thermally activated relaxation process. The mechanism responsible was identified as the relaxation of ultrasonic stresses in the solid helium via vacancy diffusion. The diffusion rates and activation energy for diffusion which they extracted were consistent with those determined in other experiments on solid helium [35]. They note that when interpreting other freezing experiments in Vycor it is imperative to consider mass transport due to this vacancy-diffusion mechanism, since it can allow for pressure equilibrium to be maintained between the helium in the pores and bulk helium outside.

Therefore, we expected to see flow at temperatures near the melting point, and further expected that this flow rate should decrease rapidly with temperature.

5.1.1 Cell construction

The density and temperature measurements were performed simultaneously in one cell. The Vycor sample (the same one that was used in the freezing experiment described in Chapter 4) was sealed into a beryllium copper pressure "squeezing" cell, with a flexible diaphragm machined into one end and an external piezoelectric actuator designed to compress the helium by up to 1%. A schematic and image of the cell are shown in Figures 5.1 and 5.2, respectively. The internal volume of the cell was 1.2 cm^3, much larger than the 0.018 cm^3 volume in the Vycor pores. A spring loaded clamp arrangement held the thin Vycor parallel plate capacitor inside the cell. Crystals were again grown using the blocked capillary technique. A 0.004" i.d. capillary, thermally anchored at several points on the fridge, was used to introduce helium to the cell. Temperatures were measured with a calibrated germanium thermometer above about 50 mK, with a ^{60}Co nuclear orientation and/or ^3He melting curve thermometer for lower temperatures.

5.1.2 Piezo-mechanics

5.1.2.1 Generation of motion by piezo-electrical devices

Piezo-actuators make use of the deformation of electro-active PZT-ceramics (PZT: lead (Pb) zirconia (Zr) titanate (Ti)) when subjected to an electrical field; the subsequent deformation may be used to produce motions and/or forces. This is complementary to the effect of piezo-electricity, where electrical charges are produced upon application of mechanical stress to the ceramic.

In the simplest case, a single PZT layer is used for piezo-mechanical conversion.

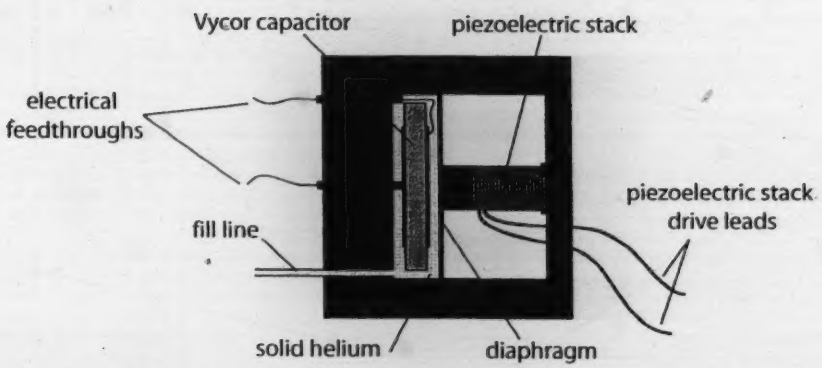

Figure 5.1: Schematic image of the Vycor squeezing cell.

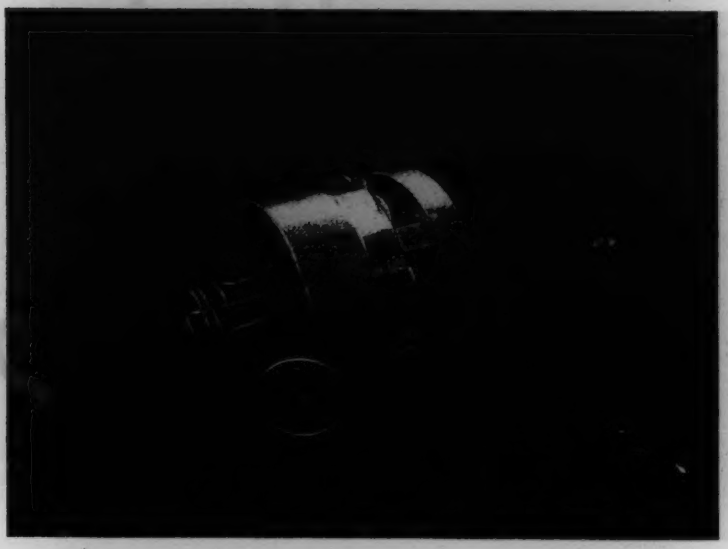

Figure 5.2: Image of the Vycor squeezing cell, next to a quarter for scale.

Such a PZT monolayer structure, as shown in Figure 5.3, behaves as a capacitive element (where the piezo-ceramic is a dielectric enclosed by two thin conductive electrode coatings). When this "piezo-capacitor" is charged by applying a voltage, a deformation is created.

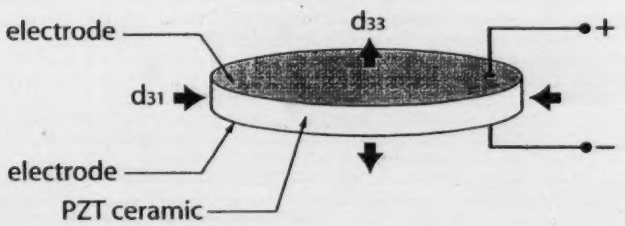

Figure 5.3: Schematic of a piezo-electric single layer element.

Stacked piezo-actuators (i.e., stacking several single layers to increase the total stroke, like the one shown in Figure 5.4) make use of the increase of the ceramic thickness in direction of the applied electrical field, known as the d_{33} effect. In practice, axial strain rates up to 2‰ of stack's length can be achieved under certain conditions. Similar to normal elastic deformation of a solid state body, the thickness expansion (d_{33}) of a PZT layer is accompanied by an in-plane shrinking, as shown in Figure 5.3. This is called the d_{31} effect, which is complementary in motion to the d_{33} effect while showing roughly half the linear strain.

5.1.2.2 Thermal properties

Piezo-actuators show self-heating proportional to the reactive power balance during dynamic operation. The self-heating is increased with drive frequency and amplitude, and is further enhanced by the poor internal heat sinking (the sole mechanical contacts of the PZT stack are its end-faces). In order to avoid measurable heating at base temperatures (e.g., 0.1 mK at temperatures below 50 mK), frequency limitations for the operation of piezo-actuators exist. In fact, normal low-voltage actuators with mid-sized diameters, like the one we used, come with the warning that they tend to overheat for frequencies in the range of about 200 Hz/full stroke

Figure 5.4: Image of the lead (Pb) zirconium (Zr) titanate (Ti) (PZT) piezoelectric stack, next to a quarter for scale. The black polymer coating around the PZT stack protects the brittle ceramic against "less skillful" handling (e.g., mechanical impact, chemical contamination) and exotic driving conditions (e.g., cryogenic temperatures, vacuum). Polymers are much more flexible than PZT-ceramics and do therefore not adversely affect the piezo-action.

operation, presumably causing irreparable damage to the stack. Near the lowest temperatures of the dilution refrigerator, for example, a 150 Vdc stroke caused noticeable transient heating (about 1 mK at 29 mK).

The piezo-mechanical (and electrical) properties of PZT ceramic are a function of temperature. When piezo-actuators are cooled down towards absolute zero, they suffer from a reduced piezo-elongation factor (d_{33}). For example, the stroke of our piezo-actuator at 4 K is about 6% its room temperature value (nominally 20 μm).

5.2 Measurements in Vycor

As discussed in Chapter 4, our measurement of capacitance across the helium-filled Vycor glass is a direct probe of the density of the helium within the Vycor pores. We started at a pressure high enough to completely freeze the helium in the pores and cooled to a temperature between near melting and 30 mK. We then suddenly (over about 10 seconds) compressed the helium by applying 150 Vdc (Regulated Power Supply, Model 71, Lambda Electronics Corp.) to the piezoelectric actuator while monitoring the helium density in the Vycor. By increasing the pressure in the reservoir around the Vycor, helium is encouraged to flow into the Vycor to

equilibrate the newly created pressure gradient.

5.3 High temperature squeezing

Figure 5.5 shows data representative of the results of such "squeezes" at five temperatures between 1.8 K and 0.5 K ($T_F = 2.05$ K at 57 bar for this data). At 1.1 K and warmer, the density capacitance responded to the pressure step in two stages. First, there was an immediate capacitance jump (an elastic response) of about 0.133 fF, which occurred within the measurement time of our capacitance bridge (i.e., during the 10 seconds taken to increase the pressure). Second, there followed a slower, temperature-dependent increase (a plastic response). The time constant associated with the slower increase varied from less than 30 seconds at 1.8 K to well over an hour at 1.1 K. At temperatures below 700 mK (e.g., the 500 mK data in Figure 5.5) there was no measurable density capacitance change following the initial jump.

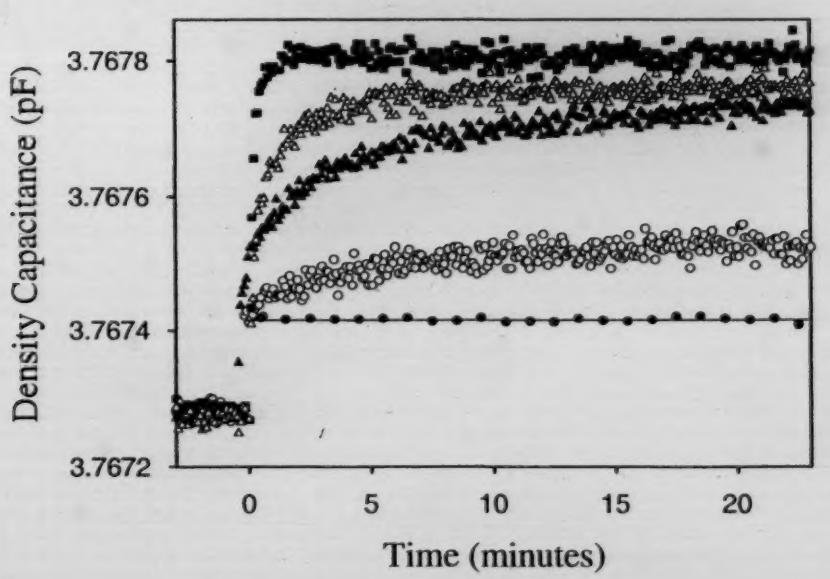

Figure 5.5: Density capacitance response of helium-filled Vycor to a rapid compression of the surrounding helium by 0.1 bar. From top to bottom, the curves correspond to temperatures 1.8 K (■), 1.5 K (△), 1.3 K (▲), 1.1 K (○), and 0.5 K (●). Horizontal line through the 0.5 K data is a guide to the eye.

5.3.1 Elastic response of Vycor to ΔP

The initial 0.133 fF jumps in Figure 5.5 are due to the elastic compression of the Vycor capacitor. Even if no helium flows into the pores, a pressure change, ΔP, will nonetheless elastically compress the capacitor and produce a geometric change in the density capacitance, ΔC_{vycor}, relative to the initial density capacitance, C_{vycor}. Such a change is temperature independent, immediate, and can be calculated from Vycor's dielectric and elastic constants. If subjected to a change in pressure, ΔP, then our Vycor capacitor will experience a change in volume, ΔV, relative to its uncompressed volume, V, the magnitude of which is a function of its bulk modulus, K_{vycor}. This change may be written as

$$\frac{\Delta V}{V} = -\frac{\Delta P}{K_{vycor}}. \tag{5.1}$$

Strictly speaking, we require the bulk modulus of the Vycor/helium system, but for all intents and purposes this is equal to the bulk modulus of the Vycor alone.

The volume of our Vycor capacitor (of radius r and thickness t) is given by

$$V = \pi r^2 t, \tag{5.2}$$

and so it follows that

$$\frac{\Delta V}{V} = 2\frac{\Delta r}{r} + \frac{\Delta t}{t}. \tag{5.3}$$

Assuming isotropy (for the sake of simplicity), Equations 5.3 and 5.1 together imply

$$\frac{\Delta r}{r} = \frac{\Delta t}{t} = \frac{-1}{3}\frac{\Delta P}{K_{vycor}}. \tag{5.4}$$

The capacitance of our Vycor capacitor (with dielectric constant ε_{vycor}) is given by

$$C_{vycor} = \varepsilon_{vycor}\frac{\pi r^2}{t}, \tag{5.5}$$

and so it follows that

$$\frac{\Delta C_{vycor}}{C_{vycor}} = \frac{\Delta \varepsilon_{vycor}}{\varepsilon_{vycor}} + 2\frac{\Delta r}{r} - \frac{\Delta t}{t}. \tag{5.6}$$

The change in the dielectric constant is due to the change in density of the helium-filled Vycor system. Recalling the Clausius-Mosotti equation (Equation 4.1), it follows that

$$\frac{\Delta \rho}{\rho} = \frac{\Delta(\varepsilon - 1)}{(\varepsilon - 1)} - \frac{\Delta(\varepsilon + 2)}{(\varepsilon + 2)} = \frac{\Delta \varepsilon}{(\varepsilon - 1)} - \frac{\Delta \varepsilon}{(\varepsilon + 2)}$$

$$= \frac{3\Delta \varepsilon}{(\varepsilon - 1)(\varepsilon + 2)}. \tag{5.7}$$

So, for our Vycor sample,

$$\frac{\Delta \varepsilon_{vycor}}{\varepsilon_{vycor}} = \frac{\Delta \rho_{vycor}}{\rho_{vycor}} \frac{(\varepsilon_{vycor} - 1)(\varepsilon_{vycor} + 2)}{3\varepsilon_{vycor}}. \tag{5.8}$$

And, as

$$\frac{\Delta \rho_{vycor}}{\rho_{vycor}} = -\frac{\Delta V}{V} = \frac{\Delta P}{K_{vycor}}, \tag{5.9}$$

we may write

$$\frac{\Delta \varepsilon_{vycor}}{\varepsilon_{vycor}} = \frac{(\varepsilon_{vycor} - 1)(\varepsilon_{vycor} + 2)}{3\varepsilon_{vycor}} \frac{\Delta P}{K}. \tag{5.10}$$

Inserting Equations 5.4 and 5.10 into Equation 5.6 yields

$$\frac{\Delta C_{vycor}}{C_{vycor}} = \left(\frac{(\varepsilon_{vycor} - 1)(\varepsilon_{vycor} + 2) - \varepsilon_{vycor}}{\varepsilon_{vycor}} \right) \frac{\Delta P}{3K_{vycor}}. \tag{5.11}$$

If we then take Vycor's dielectric constant ($\varepsilon_{vycor} = 3.1$) as well as its bulk modulus ($K_{vycor} = 1.0 \times 10^{10}$ Pa), we expect $\Delta C_{vycor}/C_{vycor} = (8.2 \times 10^{-11}\ \text{Pa}^{-1})\ \Delta P$. The 0.133 fF jump, therefore, implies a pressure increase of about 4.3 bar.

5.3.2 Plastic response of Vycor to ΔP

If solid helium subsequently flows into the Vycor to equalize the pressures after compression, then the density capacitance will increase further, but at a slower rate which depends on the flow velocity. This density capacitance change depends on the compressibility of the helium in the pores, which can be estimated from the data of Figure 5.6.

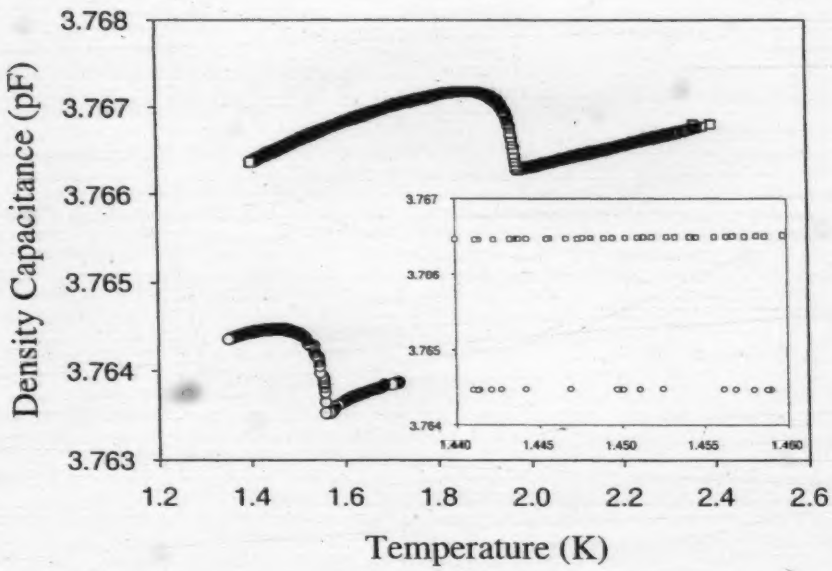

Figure 5.6: Density capacitance during cooling at 36.2 bar (○) and 54.0 bar (□). The inset shows the same two plots over a smaller temperature range.

The compressibility of a solid is given by

$$\beta = -\frac{1}{V}\left(\frac{\Delta V}{\Delta P}\right). \tag{5.12}$$

And as $-\Delta V/V = \Delta\rho/\rho$, we can write

$$\beta = \frac{1}{\Delta P}\frac{\Delta \rho}{\rho}. \tag{5.13}$$

Inserting Equation 5.7 brings us to

$$\beta = \frac{1}{\Delta P}\frac{3}{(\varepsilon+2)}\frac{\Delta\varepsilon}{(\varepsilon-1)}. \tag{5.14}$$

Recalling that the capacitance of the ^{4}He in the pores of Vycor is given by

$$C = \phi(\varepsilon_{He}-1)C_0, \tag{5.15}$$

we find that

$$\frac{\Delta C}{C} = \frac{\Delta(\varepsilon_{He}-1)}{(\varepsilon_{He}-1)} = \frac{\Delta\varepsilon_{He}}{(\varepsilon_{He}-1)}, \tag{5.16}$$

which finally leads us to

$$\beta = \frac{1}{\Delta P}\frac{3}{(\varepsilon_{He}+2)}\frac{\Delta C}{C}. \tag{5.17}$$

Looking at the 36.2 bar and 54.0 bar data at 1.45 K of Figure 5.6 (i.e., a difference in pressure of ΔP = 17.8 bar = 1.78 x 10^6 Pa), the density capacitance difference between the two is ΔC = 0.002 pF. The adsorption isotherm of Figure 4.11 showed that helium's contribution to the density capacitance is 0.052 pF at 1.8 K. This allows us to estimate the solid's compressibility (a measure of the relative volume change of a fluid or solid as a response to a pressure change) as 2.1 x 10^{-8} Pa^{-1} (at 1.45 K), slightly less than the corresponding value for bulk helium (2.3 x 10^{-8} Pa^{-1} at 54.5 bar [145]).

For a 4.3 bar pressure step, equilibrating the pressure inside and outside the pores would produce a change of about 4.8 x 10^{-4} pF, roughly what we observe (about three times the magnitude of the elastic response).

The observed change in capacitance after the initial jump is a combination of two factors. There is an increase in capacitance due to the helium flowing into the pores and equilibrating the pressures, and there is a decrease resulting from the Vycor glass springing back into its original dimensions.

The flow-induced density capacitance changes in Figure 5.5 occurred more slowly as the temperature was reduced. This is consistent with mass transport via a thermally activated process, presumably the diffusion of vacancies in the solid helium

or in a disordered layer at the pore walls. Vacancy diffusion in solid ^{4}He has been studied under confinement [144] and in bulk [146]. Such a stress-induced migration of vacancies is often referred to as vacancy creep or self-diffusion. The diffusion of vacancies within the interior of the crystal cannot alter its external shape; however, the migration of vacancies to or from the surfaces of a crystal or discontinuities in a polycrystalline solid (e.g., grain boundaries, dislocations) does induce shape change. For example, the arrival or departure of a vacancy at a surface causes matter to be subtracted or added. This is the very basis of vacancy creep: a slow, diffusion-controlled change in shape at elevated temperatures in response to a constant applied stress. Nabarro-Herring creep [147] is a form of diffusion-controlled creep, in which atoms/vacancies diffuse through the lattice causing grains to elongate along the stress axis.

Above 1.3 K, the capacitances approached similar final values within the time shown; at 1.1 K the changes continued for much longer (e.g., many hours) and we did not wait long enough to determine the asymptotic value. (It should be noted that the flow behavior depended slightly on the thermal history of the sample and differences between the final capacitance values may reflect defect creation associated with deformation of the bulk solid and annealing at the higher temperatures. This will be discussed in the section 5.5). At 0.5 K we saw no flow at all.

Even though the results of Figure 5.5 are not systematic enough to provide a precise activation energy for the pressure induced flow (an empirical parameter characterizing the exponential temperature dependence of the rate coefficient), it is possible to determine an approximate value. If τ is the time constant associated with the flow and E_a is the activation energy for the quasi-particles participating in the flow at a temperature T, then we can write the rate of the observed flow as

$$\frac{1}{\tau} = Ae^{-E_a/k_BT}, \tag{5.18}$$

where A is a pre-exponential factor. By writing Equation 5.18 for two different temperatures and taking the ratio, we obtain a relation for the activation energy

$$\frac{E_a}{k_B} = \frac{ln(\tau_2/\tau_1)}{1/T_2 - 1/T_1}, \tag{5.19}$$

Physically, the time constant represents the time it takes the system's step re-

sponse to reach 63.2% of its final asymptotic value (i.e., [1 - e^{-1}] times its final value). From the data in Figure 5.5 (as well as data from a squeeze at 1.7 K, not shown in Figure 5.5 to avoid clutter), and assuming that the 1.8 K data had reached the asymptotic value after about 20 minutes, we obtain time constants of $\tau_{1.8} \approx 10$ s, $\tau_{1.7} \approx 15$ s, $\tau_{1.5} \approx 30$ s, $\tau_{1.3} \approx 60$ s. Through application of Equation 5.19, we obtain activation energies of $(\frac{E_a}{k_B})_{1.8\rightarrow1.7} \approx 12.4$ K, $(\frac{E_a}{k_B})_{1.8\rightarrow1.5} \approx 9.9$ K, $(\frac{E_a}{k_B})_{1.8\rightarrow1.3} \approx 8.4$ K, $(\frac{E_a}{k_B})_{1.7\rightarrow1.5} \approx 8.8$ K, $(\frac{E_a}{k_B})_{1.7\rightarrow1.3} \approx 7.7$ K, $(\frac{E_a}{k_B})_{1.5\rightarrow1.3} \approx 6.8$ K. Again, our results are not systematic enough to provide a precise activation energy, but the data between 1.3 and 1.8 K indicate a value around 9 K.

Alternatively, we could take Equation 5.18 and plot $\ln(1/\tau)$ against (1/T), as shown in Figure 5.7. The negative slope of this line gives us an activation energy of 8.2 K.

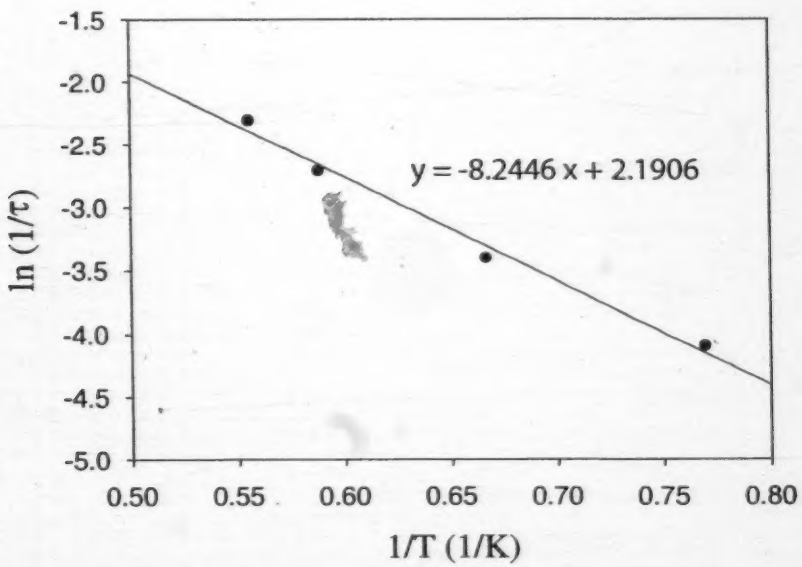

Figure 5.7: The determination of the activation energy of the quasi-particles in the pressure-induced flow of solid ^{4}He in Vycor.

The essential result is that solid helium near its melting point flows in Vycor

when an external pressure is applied, but this flow is negligible at temperatures below about half the melting temperature of the sample.

5.4 Low temperature squeezing

The most interesting question is whether or not the solid helium in the Vycor responds to a pressure difference when cooled below 200 mK (where Kim and Chan saw decoupling). Figure 5.8 shows our density capacitance results at 88 mK when the pressure was raised (by an estimated 4.3 bar), held for over four hours, and then returned to its original value. By taking data at the capacitance minimum of Figure 4.22 (88 mK), we eliminated potential background effects of the small temperature changes caused by heating in the piezoelectric actuator. As can be seen, there is no indication of any density change within the Vycor following the initial capacitance jump. This measurement was also taken at 13 mK above (101 mK, shown in Figure 5.10) and below (75 mK, shown in Figure 5.9) the capacitance minimum, yielding the same result within the resolution of our system.

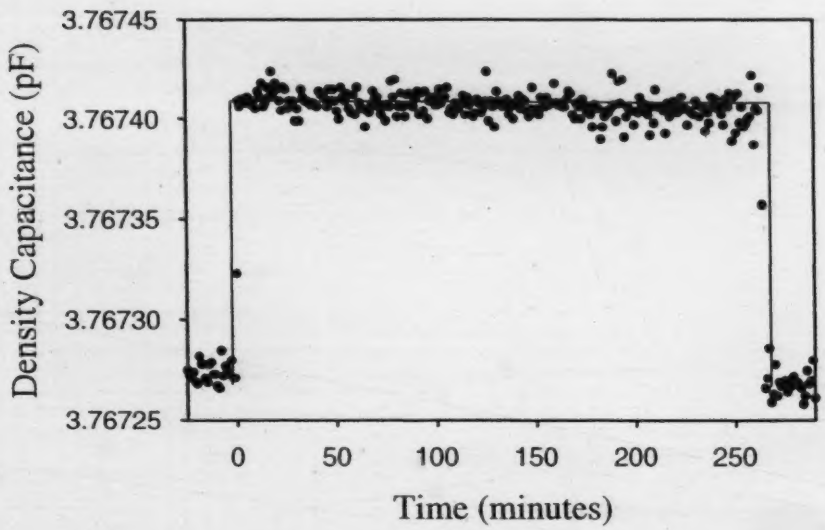

Figure 5.8: Density capacitance change for a compression at 88 mK, followed by a decompression 260 minutes later. Lines are a guide to the eye. The ever-so-slight negative slope in the data is attributed to instrumental drift.

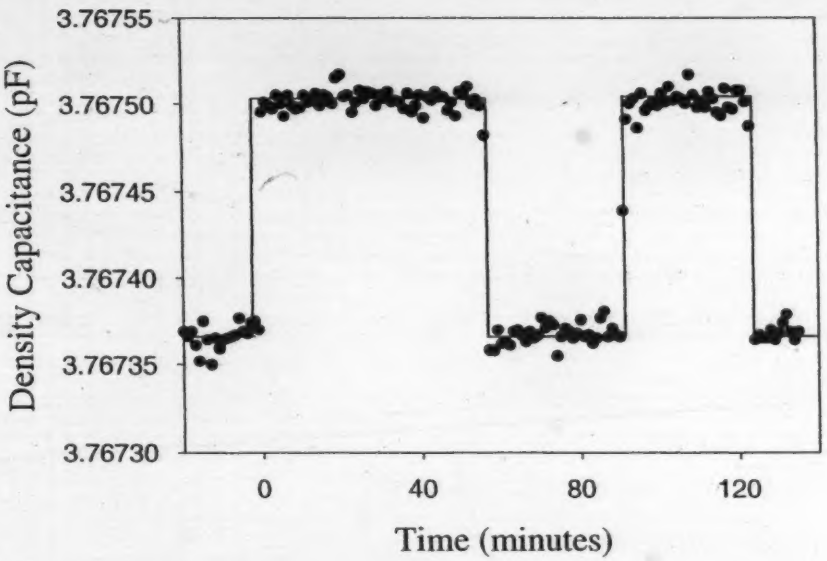

Figure 5.9: Density capacitance change for a compression at 75 mK, followed by a decompression 55 minutes later, a second compression 30 minutes later, and a second decompression 30 minutes later. Lines are a guide to the eye.

About 0.5% of the helium was shown to decouple in Kim and Chan's Vycor measurements. If this fraction were to flow from the surface to the center of our sample at their critical velocity ($\sim 10\ \mu$m/s), then a 1% density change outside the pores would be transmitted throughout the pores within a few seconds. Figure 5.8 shows that any pressure-induced helium flow in our experiments must occur at much lower speeds. Assuming that helium does flow into the Vycor through the perforations in the electrodes and its edges (totalling about 30% of the sample's outer surface), we can put a limit on the flow velocity of the helium into the pores by looking at the noise in our signal. Note that an increase in measured density capacitance (beyond the elastic compression of the Vycor) must be due to an increase of the helium density within the pores; such an increase in helium density would be the result of a movement of helium mass from the surrounding solid helium reservoir to inside the Vycor, and may be expressed as

$$\Delta M = At\phi\Delta\rho = \rho v_{av}(0.3A)\tau, \tag{5.20}$$

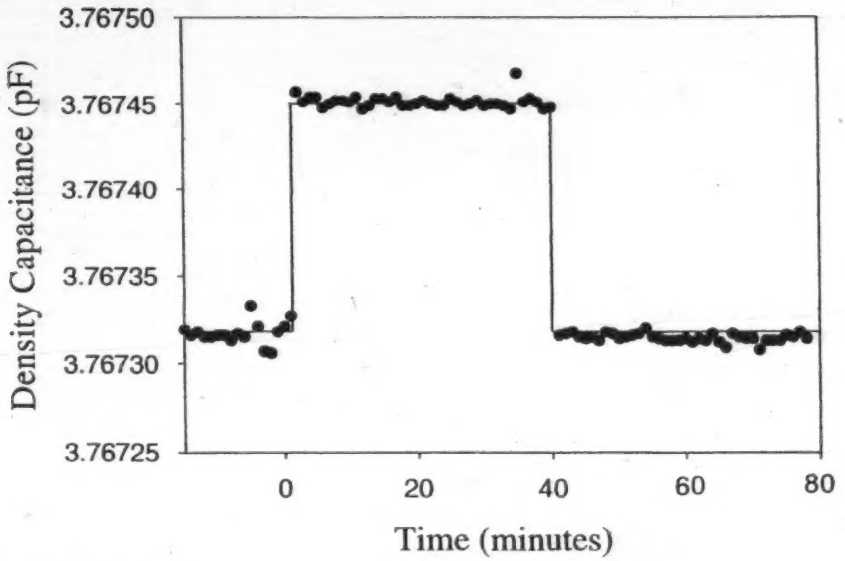

Figure 5.10: Density capacitance change for a compression at 101 mK, followed by a decompression 40 minutes later. Lines are a guide to the eye.

where ΔM is the amount of mass that moves into the Vycor sample (of area A, thickness t, and porosity ϕ), $\Delta\rho$ is the resulting density change within the Vycor, ρ is the density of the helium, v_{av} is the average velocity at which the helium flows, and τ is the time interval over which the helium is allowed to move into the Vycor. This permits us to write

$$v_{av} = \frac{t\phi}{(0.3)\tau}\frac{\Delta\rho}{\rho}. \tag{5.21}$$

Recalling that

$$\Delta C = \phi(\varepsilon_{He} - 1)C_o, \tag{5.22}$$

it follows that

$$\frac{\Delta C}{C} = \frac{\Delta(\varepsilon_{He} - 1)}{(\varepsilon_{He} - 1)} = \frac{\Delta\varepsilon_{He}}{(\varepsilon_{He} - 1)}. \tag{5.23}$$

And recalling that

$$\frac{\Delta\rho}{\rho} = \frac{3\Delta\varepsilon}{(\varepsilon-1)(\varepsilon+2)}. \tag{5.24}$$

we get

$$\frac{\Delta C}{C} = \frac{(\varepsilon_{He}+2)}{3}\frac{\Delta\rho}{\rho}, \tag{5.25}$$

which finally allows us to write Equation 5.21 as

$$v_{av} = \frac{t\phi}{(0.3)\tau}\frac{3}{(\varepsilon_{He}+2)}\frac{\Delta C}{C}. \tag{5.26}$$

As a reminder, our Vycor was 0.52 mm in thickness and had a porosity equal to 0.28; the noise in our density capacitance reading (see Figure 5.8) is 0.00002 pF and the density capacitance of the helium itself is 0.052 pF. With that, we find that the average flow velocity, v_{av} must be less than or equal to 0.012 nm/s. If we further consider that the helium that flows into the Vycor is a supersolid component, which is of the order 0.5% of the total helium density, then we can put an upper limit on the critical velocity, v_c, of this supersolid component of 3 nm/s (i.e., $\rho v_{av} = \rho_s v_c$). We extended our squeezing measurements down to 48 mK with no indication of mass flow. Below this temperature, dissipation in the piezoelectric actuator would heat the cell slightly ($\sim$ 1 mK) and prevented accurate measurements.

5.5 Sensitivity to sample history

Not surprisingly, the measured response to deformation was sensitive to both the thermal history (whether it had been annealed, or if its current temperature had been reached from above or below, etc.) and the mechanical history (whether it had been previously deformed) of the polycrystalline sample. Figure 5.11 provides an example of how simple mechanical history of a sample (T_F = 1.46 K at 34 bar, with bulk melting at $\sim$ 1.9 K) can affect the measurement. Here, the sample was solidified and cooled directly to 0.5 K, where it was then compressed. The first compression results in an immediate increase in the density capacitance (due to the elastic compression of the Vycor), followed by a slower increase in the density

capacitance (cause unknown). Decompression results only in an immediate decrease of the density capacitance, equal in magnitude to the initial immediate increase following compression. Subsequent compressions and decompressions result solely in this elastic response.

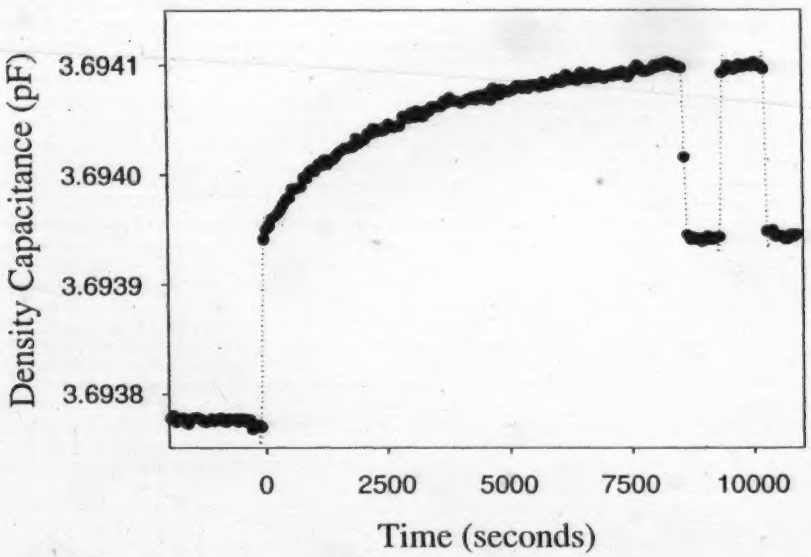

Figure 5.11: Deformation history dependence of pressure-induced flow at 0.5 K. The first squeeze is for a crystal that has not been annealed, nor previously compressed. The magnitude of the elastic response for both compression/decompression sets is the same.

Figure 5.12 shows measurements on a sample (T_F = 2.12 K at 57 bar, with bulk melting at $\sim$ 2.5 K) with a more involved thermal and mechanical history. The crystal was grown slowly, 2.55 K to 2.10 K at 1 mK per 120 seconds, and then cooled to 2.06 K and compressed twice. Once the density capacitance had equilibrated, the sample was cooled to 2.0 K and compressed again (top curve). We then repeated this process at 1.9 K, 1.8 K, and 1.5 K, before returning to 2.0 K for another compression (bottom curve). The curves have not been offset. The difference in shape and absolute value of the density capacitance curves serves to remind us that

returning to the same temperature is not at all equivalent to returning to the same thermodynamic state of the sample.

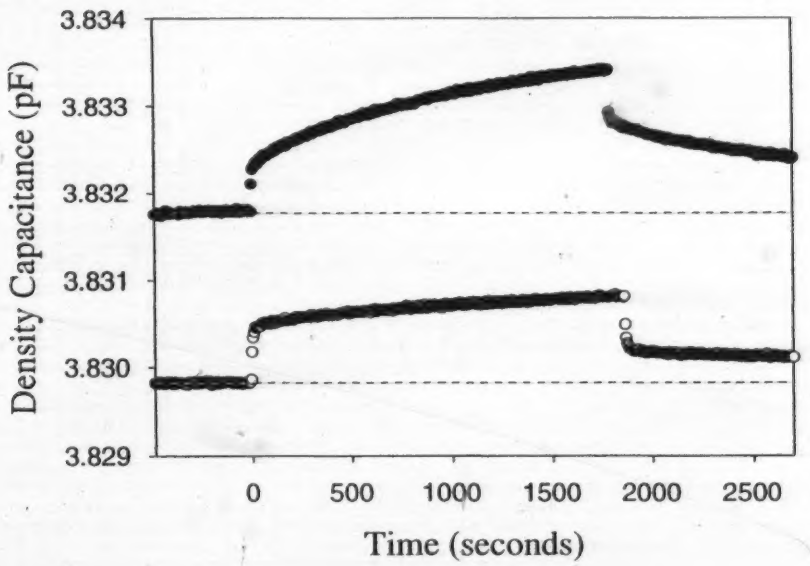

Figure 5.12: Thermal history dependence of pressure-induced flow at 2.0 K. The top curve (•) is the pressure-induced flow response in a crystal at 2.0 K, reached from cooling from warmer temperatures, and with minimal mechanical history. The bottom curve (○) is the pressure-induced flow response in a crystal at 2.0 K, reached from warming from cooler temperatures, with significant mechanical history. The offset between the curves is real.

A further complication to these measurements (which was not fully understood at the time of their collection) was the common occurrence of a background drift. Figure 5.13 shows an example of this drift as the sample sat for 6 hours overnight at a constant temperature of 0.5 K, at 57 bar.

Figures 5.14, 5.15, and 5.16 show examples of this drift occurring as we were applying the pressure difference. The dashed lines in each are guides to the eye, and are intended to show how the thermally activated background drift slows as the temperature is reduced (i.e., the slope of the dashed line is steepest in Figure 5.14 at 1.9 K and gentlest in Figure 5.16 at 1.5 K).

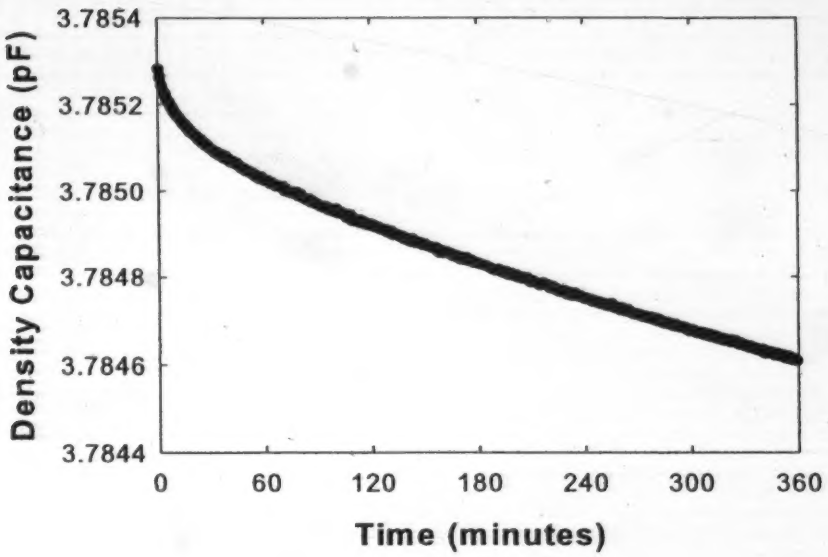

Figure 5.13: Overnight (6 hour) background drift as the sample sits at 0.5 K.

These background drifts are likely caused by a shifting of the Vycor sample inside our cell, as extended defects re-organize themselves within the strained crystal. Recall that the initial squeeze to which the sample is subjected is uniaxial and so the initial sample compression is certainly not isotropic: pressure gradients will exist between the volume directly below the diaphragm and the regions near the cell wall. This sort of compression may relax by bulk flow to a more isotropic compression, and such bulk flow could shift the position of the Vycor sample. The capacitance we measure includes an effect from fringe fields (about 10% of the total capacitance), and such fields are sensitive to the precise geometry of the of the capacitor within its immediate environment. Shifting the Vycor capacitor's position will result in a change of the density capacitance we measure even though the density of the helium within the Vycor is unchanged. Admittedly, we held a poor understanding of the pressure response of bulk ^{4}He at the time of these experiments (a good motivation for the bulk flow experiments that follow, and the subsequent care we took to always start from the same "pressure-annealed" state).

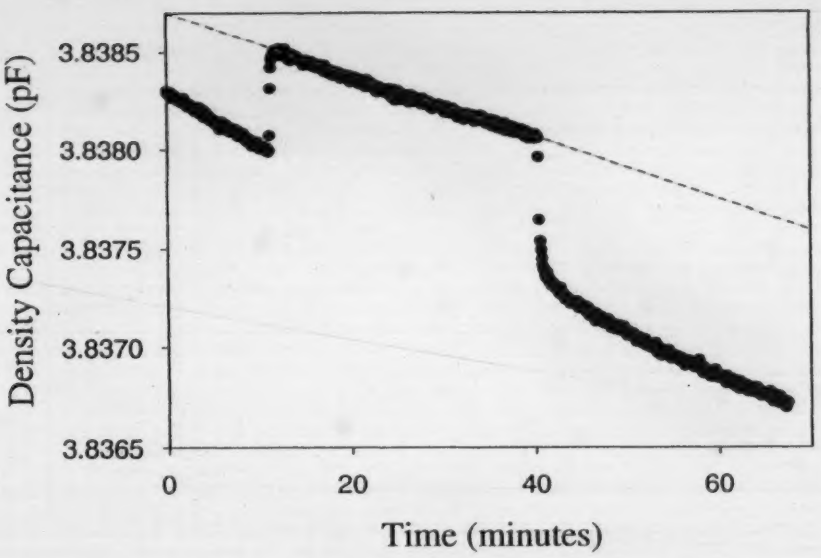

Figure 5.14: Squeezes during the background drift at 1.9 K. The rate at which the (downward) background drift occurs is a function of temperature.

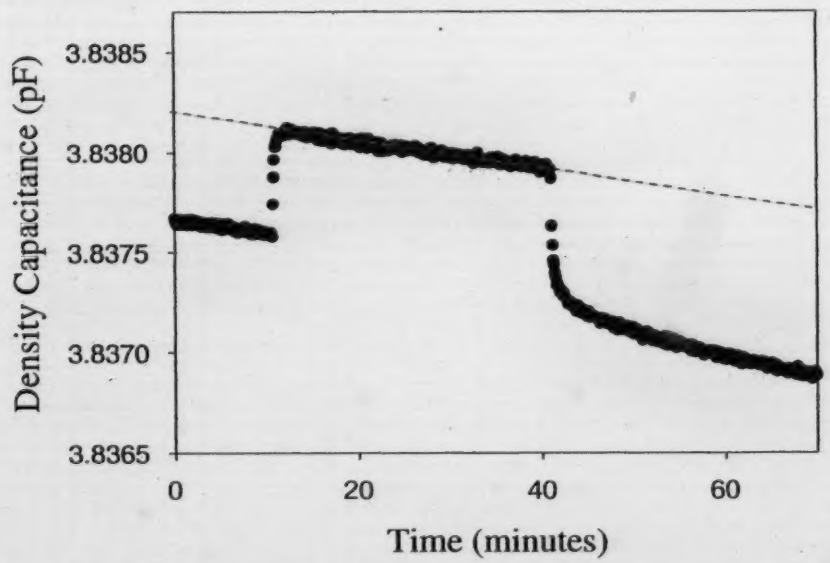

Figure 5.15: Squeezes during the background drift at 1.8 K. The rate at which the (downward) background drift occurs is a function of temperature.

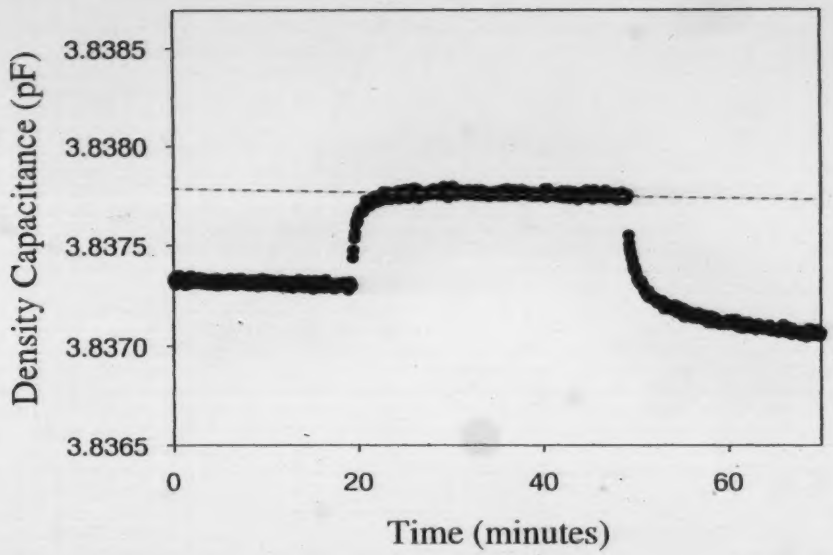

Figure 5.16: Squeezes during the background drift at 1.5 K. The rate at which the (downward) background drift occurs is a function of temperature.

5.6 Conclusions

The NCRI observed in Kim and Chan's torsional oscillator measurements appears to be a fundamental property of solid helium at low temperatures. Our measurements rule out alternative explanations of their results based on redistribution of mass in Vycor rather than supersolid decoupling. However, we do not see any evidence of pressure induced flow in the temperature range where they observed supersolidity. This is consistent with previous experiments by Greywall[41] in which a small pressure difference ($\sim$ bar) between two sample chambers filled with solid ^{4}He and joined by fine capillaries was measured as a function of temperature. For temperatures greater than 30 mK and for pressures between 25 and 50 bar there were no indications (i.e., a similar limit of 0.002 μm/s, using Kim and Chan's bulk supersolid fraction of 1.5%, on pressure-induced flow of bulk solid helium through capillaries) of "superfluid flow" in the capillary.

If a supersolid exists, then this experiment shows that its flow properties must be quite different from that of superfluids, since the chemical potential difference created by a pressure change does not appear to produce superflow.

Chapter 6

Pressure Induced Flow of Solid Helium (Bulk)

The observation of NCRI in bulk solid ^{4}He [9] suggests that the superfluid-like behaviour is a general property of solid helium and not the result of confinement in any particular medium. It should be made clear, however, that this discovery does not diminish the importance of the Vycor torsional oscillator results [10]. In fact, the problem arguably becomes more difficult to solve as possible explanations for the NCRI should apply to both systems (confinement and bulk). While it is entirely possible that two separate mechanisms act for each system, it seems unlikely. As an example, recall that mass can be transported in bulk crystals via the motion of extended defects like dislocations or grain boundaries. Some have noted [18, 61] that such defects may be essential for supersolidity. But these very same defects would be pinned in small pores and would not explain the observed NCRI in Vycor. Therefore, it seems unlikely (although, certainly not impossible) that such defects are required for supersolidity. All the same, in discovering that the NCRI was not a result of confinement, the more pertinent experiments became those which investigate the properties of bulk solid ^{4}He.

6.1 Bulk experimental design

The motivation behind the experiment described here is that, other than the torsional oscillator experiments, there had not to date been any direct observations of supersolid behavior, either in bulk or in small pores. However, the small critical velocities (μm/s) and the sensitivity to ^{3}He impurities (at the ppb level) may affect dc flow (or other properties) even more strongly than the torsional oscillator mea-

surements. Also, and more fundamentally, we must keep in mind that solids have properties not shared by liquids (e.g., a lattice with shear rigidity) and a supersolid simply may not exhibit all of the effects we associate with superfluidity (e.g., superleaks, persistent currents, thermo-mechanical effects, quantized vortices, second sound, etc.). Here we describe a set of experiments to look for one such property in solid ^{4}He: superflow in response to pressure differences. We have used a piezoelectrically driven diaphragm to study the pressure-induced flow of solid ^{4}He through an array of capillaries at low temperatures. We applied small pressure differences (3 to 100 mbar) at low temperatures (down to 35 mK) and used both isotopically purified ^{4}He (1 ppb ^{3}He concentration [148]) and ^{4}He with the natural isotopic composition (typically 0.3 ppm ^{3}He). We made both dc and low frequency ac (below 1 Hz) measurements, but did not see any evidence of flow below about 1 K.

6.1.1 Glass capillary array sample

Glass capillary arrays [149] (GCAs) consist of tens of thousands of precision glass capillary tubes fused together to produce a uniform and mechanically rigid structure (see Figures 6.1,6.2,6.3).

Figure 6.1: SEM image of our GCA.

The manufacture of these arrays begins with the fusion of drawn and clad glass

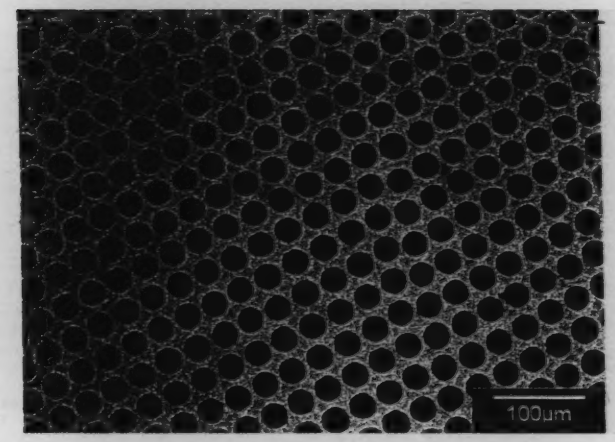

Figure 6.2: Close-up SEM image of our GCA.

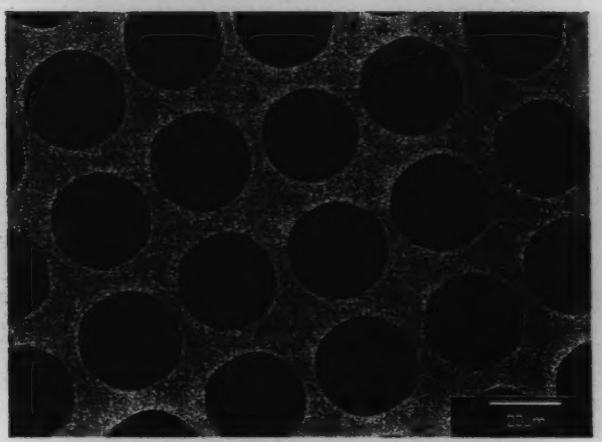

Figure 6.3: Even closer-up SEM image of our GCA.

fibres. The holes of the capillaries are created via a chemical etching process, producing a smooth interface between the polished surfaces of the cladding and the etch-able core. After the chemical removal of the etch-able core element, few defects larger than 1/100th of a capillary diameter remain. The etched holes are individually straight and parallel, and the diameters in a close-packed array typically vary by less than 5% from one to another, and by less than 2% along their length.

6.1.2 Cell construction

The pressure and temperature measurements were performed simultaneously in one cell (the "squeezing" cell). A schematic of the cell is shown in Figure 6.4, with a magnified view of the central part of the cell shown in Figure 6.5, and an image of the cell is shown in Figure 6.6. Our beryllium copper cell consisted of two cylindrical chambers connected by a GCA porous barrier (roughly 36,000 parallel glass capillaries, 25 μm in diameter, and 3 mm long). The porous barrier had an open cross-sectional area A = 0.18 cm^2. The outer wall of the larger chamber (diameter = 25 mm, height $\approx$ 1 mm, volume $V_1 = 0.49$ cm^3) included a flexible diaphragm which could be moved with an external piezoelectric actuator (APC International, model PSt 150/10 x 10 x 18 [150]) to compress the helium. The smaller chamber (diameter = 7 mm, height $\approx$ 0.3 mm, $V_2 = 0.01$ cm^3) included an *in situ* Straty-Adams capacitive pressure gauge which, when used with a 1 kHz automatic bridge (Andeen-Hagerling 2550A), had a resolution and stability better than 0.2 mbar. A simple block diagram of the electronics used to make our measurements is shown in Figure 6.7. Data collection (i.e., automatic capacitance bridge readouts) was automated by a computer.

The cell, which had a total volume (including the GCA channels and fill line) $V_{total} = 0.79$ cm^3, was mounted onto the bottom of the mixing chamber of our dilution refrigerator. A 0.004" i.d. capillary, thermally anchored at several points on the fridge, was used to introduce ^{4}He to the cell. Temperatures were measured with a calibrated germanium thermometer above about 50 mK, with a ^{60}Co nuclear orientation and/or ^{3}He melting curve thermometer for lower temperatures.

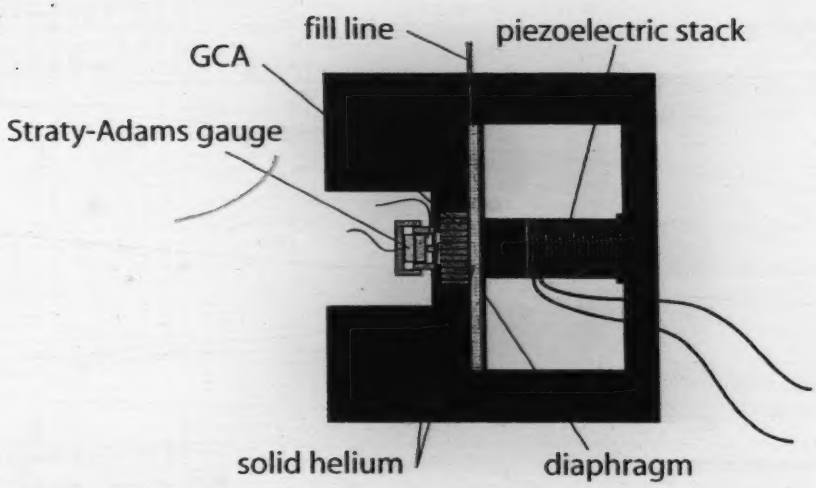

Figure 6.4: Schematic image of the bulk squeezing cell, with the GCA in place.

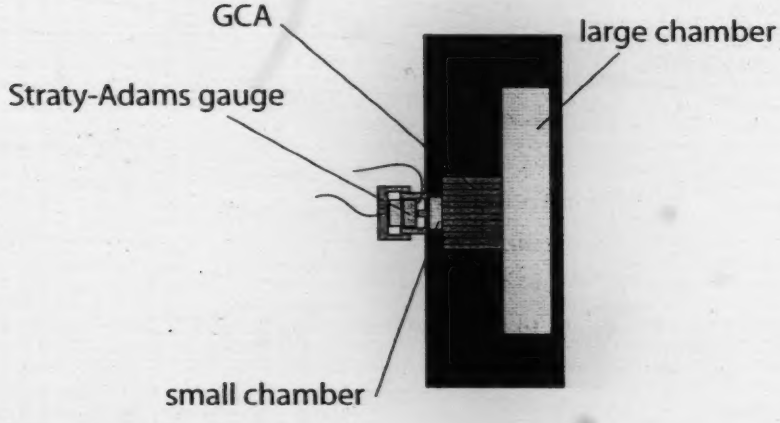

Figure 6.5: Close-up schematic image of the bulk squeezing cell, with the GCA in place.

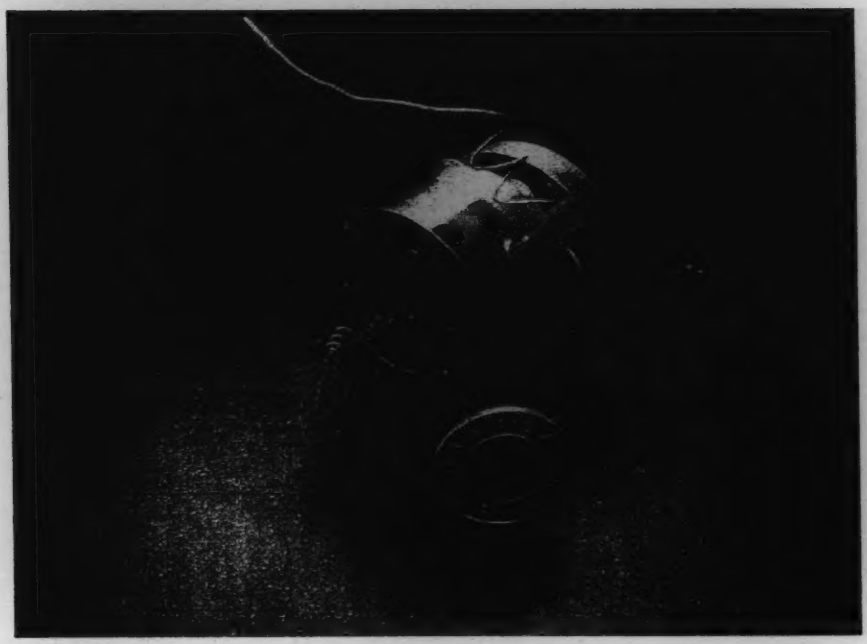

Figure 6.6: Image of the bulk squeezing cell, next to a Canadian twoonie coin for scale.

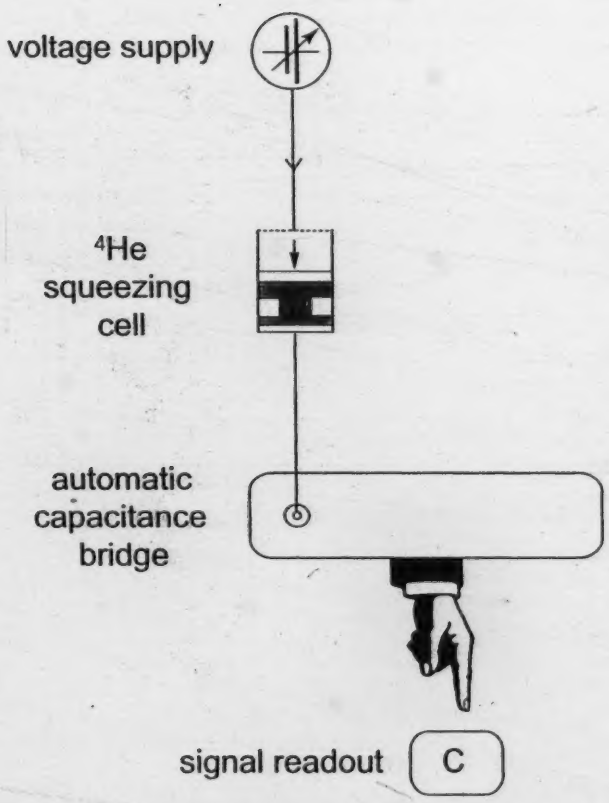

Figure 6.7: Block diagram for the bulk squeezing experiment.

6.2 Measurements in bulk (without GCA)

Before studying the pressure-induced flow of solid ^{4}He across the GCA porous barrier, we performed a few simple measurements in our cell without the GCA porous barrier. This involved growing a solid ^{4}He sample in the open volume (see Figure 6.8 for a schematic) between the diaphragm and the pressure gauge, and then squeezing the sample (by flexing the diaphragm) while measuring how the pressure was transmitted across the sample to the pressure gauge.

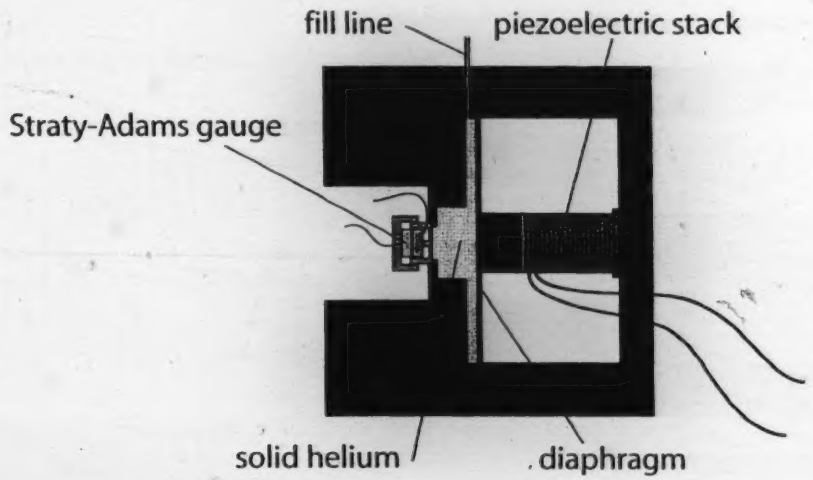

Figure 6.8: Schematic image of the bulk squeezing cell, without the GCA installed.

First, the Straty-Adams capacitive pressure gauge was calibrated against a room temperature Mensor pressure gauge. This involved filling the cell at low temperature with liquid helium to known pressures (measured by the Mensor pressure gauge on the gas handling system) and recording the capacitance of the Straty-Adams gauge. This was done at 5 bar intervals, for pressures between about 25 and 75 bar. The pressure is plotted against the capacitance, and a second-order polynomial is fit to the data; it is this polynomial, then, which is used to convert our capacitive read-outs to a pressure.

The cell was then filled with high-pressure, commercially purified, liquid ^{4}He

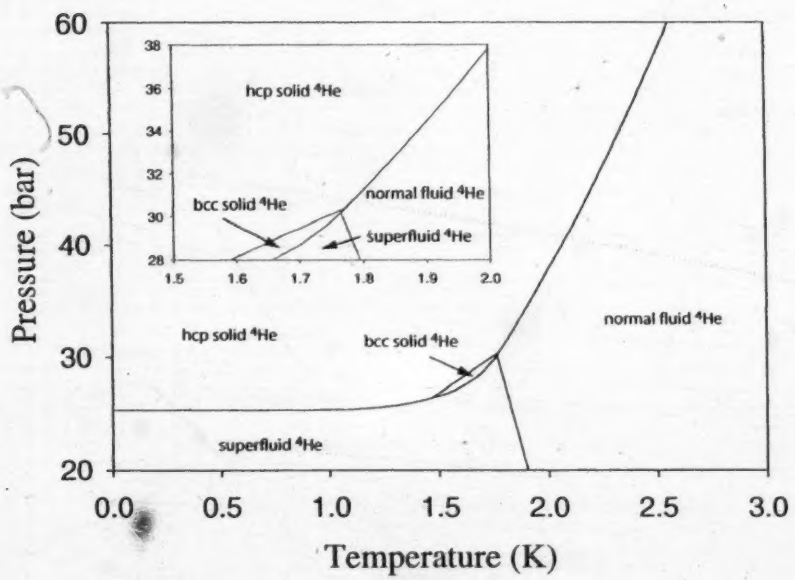

Figure 6.9: The ^{4}He melting curve [151].

(0.3 ppm ^{3}He impurities) at 4.2 K and a solid sample was grown in the open volume of the cell using the blocked capillary technique. The melting curve of ^{4}He is shown in Figure 6.9, with a focus on the thermodynamic phase space in which our crystals are grown. Subsequent phase diagrams showing the measured thermodynamic path do not include the lambda line (dividing the normal fluid from the superfluid phase), as none of the solid samples presented in this thesis ever passed through the superfluid phase. For this sample, freezing began at T = 2.39 K and P = 53.2 bar and was complete at T = 1.76 K and P = 29.9 bar (the sample subsequently passed along the bcc/hcp phase line upon further cooling, before entering the pure hcp phase at 1.70 K and 29.3 bar). This thermodynamic path is shown in Figure 6.10. It must be made clear that the path shown here (and all others) is measured data of pressure versus temperature.

The cell was then cooled to 1.60 K and the linearity of the compressions was tested. Figure 6.11 shows the pressure capacitance C_P increase which results from the application of a voltage to the PZT stack, thus compressing the sample. The left side of the plot shows the C_P increase (and subsequent decrease) resulting from the application (and subsequent removal) of 140 Vdc to the PZT stack. The

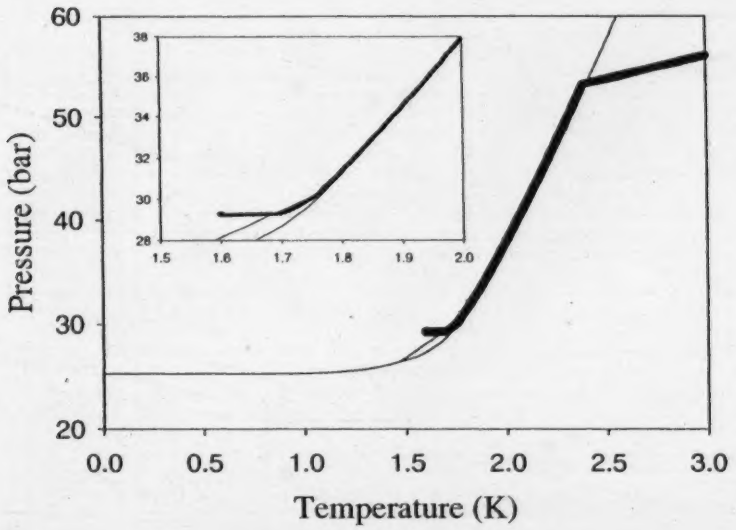

Figure 6.10: The thermodynamic path for the solid ^{4}He sample in open squeezing cell. Inset shows a close-up of the end of freezing. This data is the pressure versus temperature as we measured it.

compression(decompression) results in a positive(negative) capacitance change of 2.8 fF, corresponding to a pressure change of 0.08 bar within the sample, about 0.3% of the initial pressure. This change in pressure occurs effectively immediately. The right side of the plot shows the C_P increase (and subsequent decrease) resulting from the stepwise application (and subsequent removal) of five 25 Vdc and one 15 Vdc increases to the PZT stack. The total pressure change (0.08 bar) after the stepwise application of 140 Vdc is equal the total pressure change after the single application of 140 Vdc to the PZT stack, confirming the linearity of our compressions and decompressions.

This measurement was also made at 750 mK and is shown in Figure 6.12. Here, 140 Vdc compressions result in pressure changes of 0.1 bar. Given the solid's reduced compressibility at lower temperatures [145], a larger pressure change was expected for this measurement. What was unexpected, however, was that the pressure change deeper within the solid phase at 750 mK be $\sim$ 20% greater than what was observed near melting (the solid's compressibility only changes by only a few percent with decreasing temperature). In hindsight, we suspect that at 1.6 K there may be some "flow" of solid to equilibrate the pressure over the entire volume of the cell. At lower

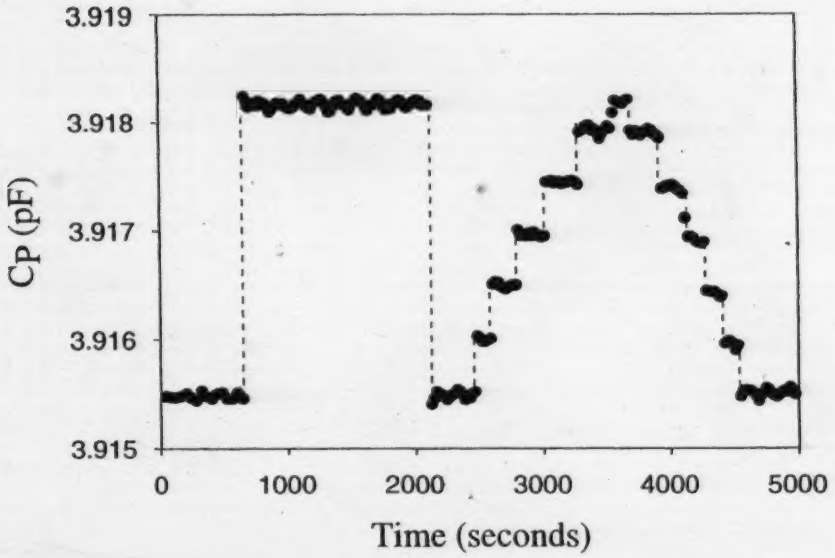

Figure 6.11: Pressure response to squeezes in open bulk cell containing solid ^{4}He at 1.60 K. Lines are guides to the eye.

temperatures, pressure gradients would instead remain.

Finally, this measurement was made at 50 mK and is shown in Figure 6.13. There is no discernable difference between the 750 mK and the 50 mK pressure changes, as expected given that the solid's compressibility is constant below $\sim$ 1 K [145].

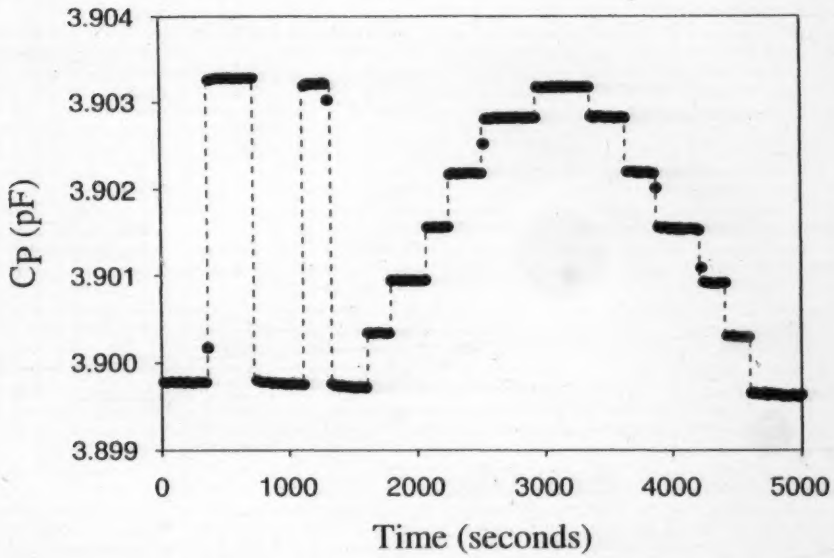

Figure 6.12: Pressure response to squeezes in open bulk cell containing solid ^{4}He at 750 mK. Lines are guides to the eye.

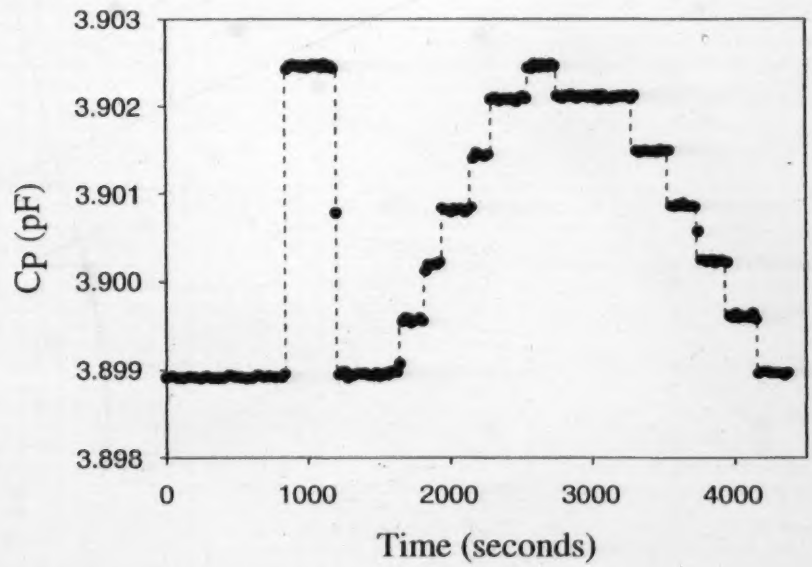

Figure 6.13: Pressure response to squeezes in open bulk cell containing solid ^{4}He at 50 mK. Lines are guides to the eye.

6.3 Measurements in bulk (with GCA)

The GCA was then epoxied into the cell, dividing the inner volume into two separate chambers, as previously described. If helium moves a distance dx through the capillaries, the resulting pressure change is given by

$$dP = \frac{A}{\kappa_{He} V_2} dx, \tag{6.1}$$

where κ_{He} is the helium's compressibility. With a resolution on our capacitive pressure gauge equal to 0.2 mbar, we typically could detect a 0.3 nm displacement of solid ^{4}He through the GCA.

A back-of-the-envelope calculation of the elastic energy of the system suggests that we should not expect to see any elastic displacement of solid ^{4}He across the entire 3 mm length of the capillaries in our GCA. Imagine one single channel, as shown in Figure 6.14, of radius r, which is filled with solid ^{4}He, elastically compressed from the top by δl, where l characterizes the distance over which a deformation from equilibrium exists.

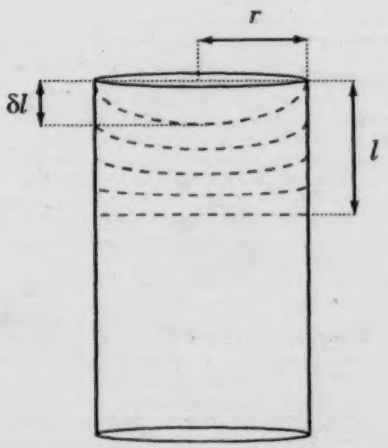

Figure 6.14: Elastic deformation of solid helium in a channel.

This system is subject to compressional strain

$$\varepsilon_c \sim \frac{\delta l}{l} \tag{6.2}$$

and to shear strain

$$\varepsilon_s \sim \frac{\delta l}{r}. \tag{6.3}$$

The total elastic energy, E_{el} of this system at fixed δl and r, then, is

$$E_{el} = E_c + E_s = \frac{1}{2}(\kappa + \frac{4}{3}\mu){\varepsilon_c}^2 V + \frac{1}{2}\mu{\varepsilon_s}^2 V, \tag{6.4}$$

where κ and μ are the bulk and shear modulus of the solid helium, respectively. We use the longitudinal modulus $(\kappa + \frac{4}{3}\mu)$ in this expression rather than just the bulk modulus κ as we are only compressing in one direction (as in a longitudinal plane wave). We may then write

$$E_{el} = \frac{1}{2}\kappa\frac{\delta l^2}{l^2}\pi r^2 l + \frac{2}{3}\mu\frac{\delta l^2}{l^2}\pi r^2 l + \frac{1}{2}\mu\frac{\delta l^2}{r^2}\pi r^2 l \tag{6.5}$$

$$= \frac{1}{2}\kappa\frac{\delta l^2}{l}\pi r^2 + \frac{2}{3}\mu\frac{\delta l^2}{l}\pi r^2 + \frac{1}{2}\mu\delta l^2 l\pi. \tag{6.6}$$

Minimizing Equation 6.6 with respect to the characteristic penetration depth of the deformation l gives us

$$0 = \frac{dE_{el}}{dl} = -\frac{1}{2}\kappa\frac{\delta l^2}{l^2}\pi r^2 - \frac{2}{3}\mu\frac{\delta l^2}{l^2}\pi r^2 + \frac{1}{2}\mu\delta l^2\pi, \tag{6.7}$$

which simplifies to

$$l = r\sqrt{\frac{\kappa}{\mu} + \frac{4}{3}}. \tag{6.8}$$

As $\kappa \approx \mu$, we can conclude that $l \approx 1.5r$; that is to say, the deformation only penetrates the length of the channel to a depth roughly equal to its diameter. So, we do not expect to see any elastic deformation at the opposite end of the GCA channels (which have length 120 times greater than their diameter).

Computer modelling was initiated to confirm that we should not expect such an elastic deformation to span the length of our channels. Specifically, a deformation analysis of low temperature bulk solid ^{4}He within a GCA channel was done using a 3-D solid, stress-strain structural mechanics module within the COMSOL Multiphysics [152] simulation environment. Preliminary models predict that the application of 100 mbar in the direction of the length of the ^{4}He-filled channel results in a maximum compressional displacement of the order of the channel diameter ($\sim 25\mu$m), and that the characteristic depth to which the deformation exists does not extend beyond a few channel diameters (~ 75 μm). This is consistent with the back-of-the-envelope calculation presented above.

What we might expect to see, however, is plastic flow of solid ^{4}He along the channels. Helium is a relatively soft solid, often likened to butter. Mass may be transported in bulk crystals via the motion of extended defects like grain boundaries or dislocations (e.g., the glide of dislocations on parallel sets of crystal planes). Mass may also be transported by vacancy motion. If a vacancy moves one lattice spacing to the left, a helium atom moves one lattice spacing to the right. Mass can be moved and crystals can be deformed through a mechanism called diffusional flow [147] (or vacancy creep), the stress-induced migration of vacancies. Because of the lattice mismatching between the helium crystals in the GCA pores and that which is strongly adsorbed to the GCA pore wall, a higher-than-usual density of such defects might be expected near the walls of the GCA.

With an idea of what we might expect to see, we began by filling and pressurizing the cell at 4.2 K, using a room temperature gauge to calibrate our capacitive pressure gauge (as described earlier). The actuator and diaphragm were then calibrated in the liquid phase at 1.95 K and 36.4 bar, just below the melting curve. Figure 6.15 shows the pressure response of the liquid in the small chamber when the full voltage (150 Vdc) was applied to the actuator, thus compressing the liquid in the large chamber. It should be pointed out that the capillary was blocked (by a closed needle valve) higher up along the fill line. As expected, the pressure increased immediately (within the few seconds the capacitance bridge took to respond), and returned to its original value when the diaphragm was released after about half an hour. The pressure change due to the compression was $\Delta P_{liquid} \approx 84$ mbar. Using the liquid's compressibility ($\kappa_{liquid} \approx 3.6 \times 10^{-3}$ bar^{-1} [151]) gives a volume change $\Delta V/V_{total} \approx 0.03\%$, corresponding to a diaphragm deflection of about 1 μm. This is

consistent with the manufacturer's statement [150] that the full stroke ($0 \rightarrow 150$ Vdc) at low temperature is 6% of its room temperature value of 20 μm.

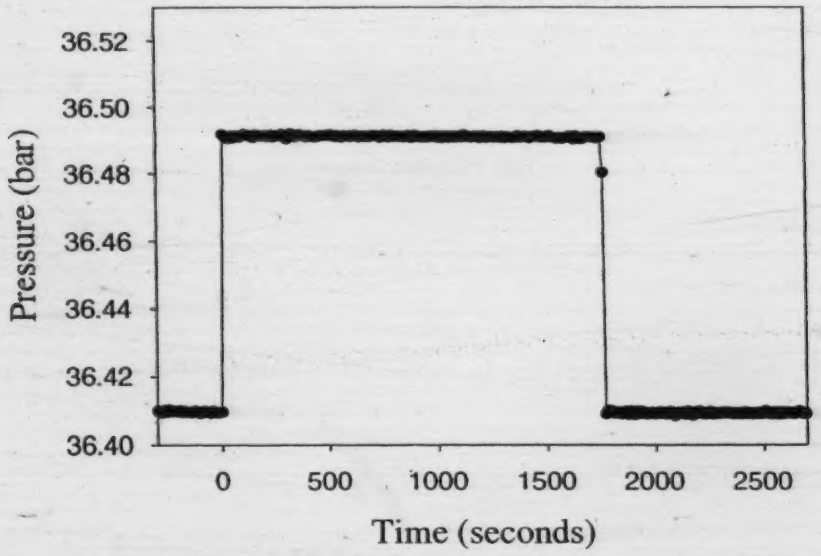

Figure 6.15: Pressure response to squeezes in liquid ^{4}He, at 1.95 K and 36.4 bar. Lines are guides to the eye.

Crystals were then grown using the blocked capillary, constant volume technique, with isotopically purified ^{4}He (nominally 1 ppb ^{3}He impurity concentration). This is the same gas used in Kim and Chan's torsional oscillator experiments [52]. We started with liquid at high pressure and monitored the cell pressure as it was cooled. At a pressure of 61.7 bar, freezing began at 2.60 K and was complete at a final pressure of 36.8 bar. This thermodynamic path is shown in Figure 6.16.

We then annealed the solid by keeping it within 50 mK of its melting temperature for at least 2 hours, thereby eliminating many of the pressure gradients created during freezing and thus producing a sharp melting onset (at $T_m = 1.96$ K), characteristic of a uniform density crystal, and as shown in Figure 6.17.

Our basic flow measurement was made at temperatures below T_m by quickly

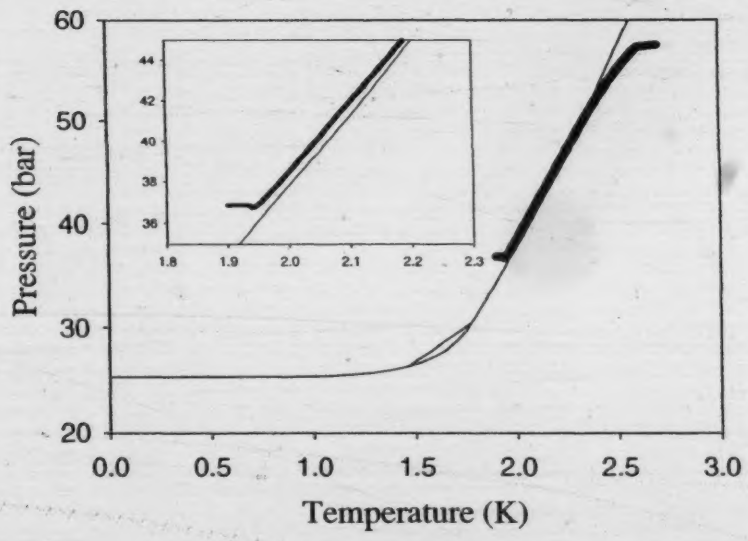

Figure 6.16: The thermodynamic path for solid ^{4}He sample in open squeezing cell with GCA. Inset shows a close-up of the end of freezing. This data is the pressure versus temperature as we measured it.

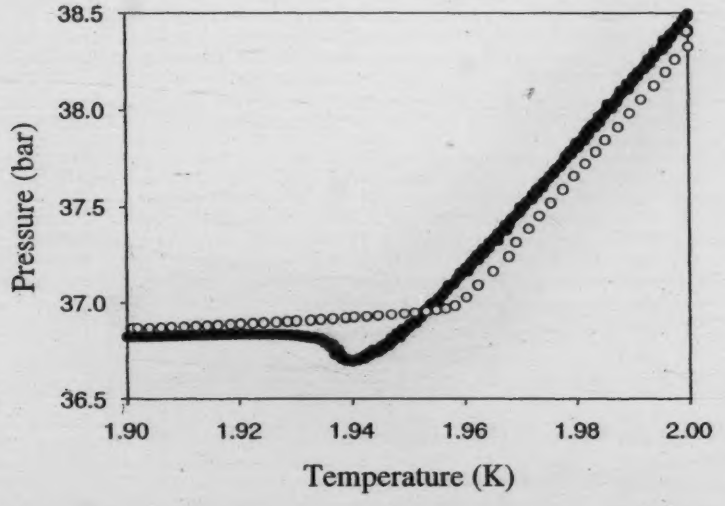

Figure 6.17: The elimination of pressure gradients through annealing. Pressure is measured *in situ* during blocked capillary freezing of ^{4}He (•) and subsequent melting (○). Annealing essentially eliminates the initial pressure gradients ($\sim$ 200 mbar).

(over about 5 seconds) applying a dc voltage to the actuator to squeeze the solid ^{4}He, thus increasing the pressure in the large chamber. In contrast to the case where the cell contained liquid, the solid helium may flow through the GCA channels slowly, or not at all, and so the pressures in the two chambers may not equilibrate. However, even without flow, some pressure is transmitted to the second chamber, since a pressure difference will cause the GCA plate separating the chambers to flex elastically. This small deflection appears as an immediate pressure step in the other chamber. Any subsequent flow through the channels will further increase the pressure, but more slowly.

The data in Figures 6.18 and 6.19 show the response to a pressure step when the cell contains isotopically purified solid ^{4}He (1 ppb ^{3}He impurity concentration). At 0.5 K (Figure 6.18) the pressure in the second chamber immediately changed by 38 mbar, corresponding to the GCA flexing by about 30 nm. Above about half the melting temperature, this initial jump was followed by a slower, temperature-dependent change due to flow. The curve in Figure 6.19 shows the response at 1.95 K, very close to melting. After the initial jump, the pressure continued to increase due to flow of solid through the channels, but stabilized within about half an hour. During this time, the GCA presumably relaxes to its original position. The total increase of 105 mbar is slightly larger than the corresponding change with liquid helium, as expected given the solid's smaller compressibility ($\kappa_{solid} \approx 3.1 \times 10^{-3}$ bar^{-1} [151]), and indicates that, near melting, flow through the channels can maintain pressure equilibrium between the two chambers.

For all three sets of data, we confirmed the linearity of the response (i.e., the pressure changes were proportional to the voltage applied to the diaphragm actuator). Figure 6.20 shows these results.

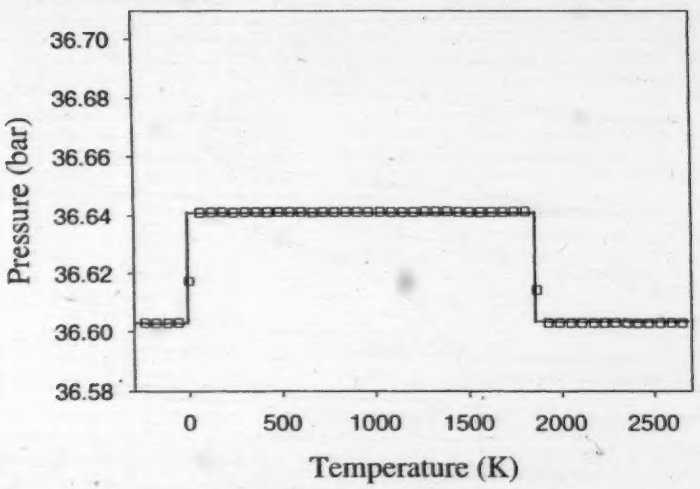

Figure 6.18: Pressure response to squeezes in solid ^{4}He, at 500 mK and 36.6 bar. The magnitude of the vertical scale is the same as on Figure 6.15. Lines are guides to the eye.

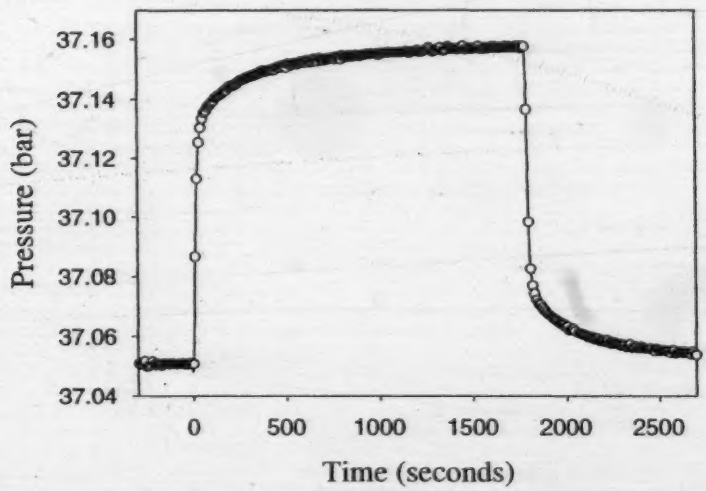

Figure 6.19: Pressure response to squeezes in solid ^{4}He, at 1.95 K and 37.1 bar. The magnitude of the vertical scale is the same as on Figure 6.15. Lines are guides to the eye.

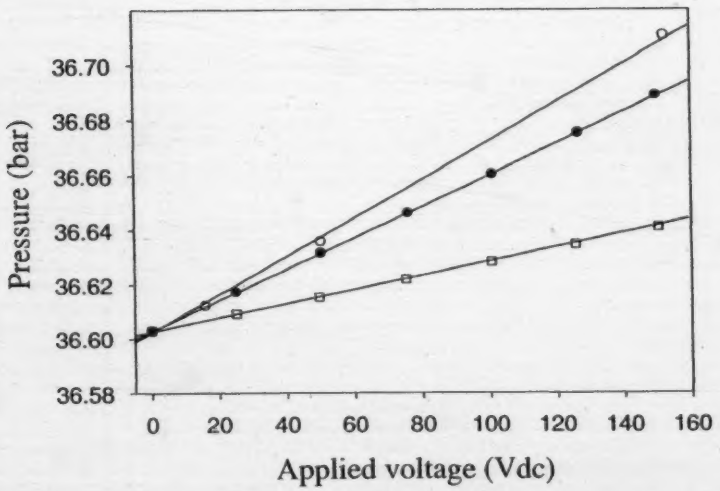

Figure 6.20: The linearity of the pressure response to the compressions as a function of applied voltage. Data sets for the solid at 1.95 K (○) and for the liquid at 1.95 K (●) have been shifted vertically by a constant amount to agree with the data set for the solid 0.5 K (□) at 0 Vdc. Lines are guides to the eye.

6.4 High temperature squeezing

Figure 6.21 shows the response of a 42.0 bar sample of commercially purified solid ^{4}He (0.3 ppm ^{3}He impurity concentration), with a melting temperature $T_m = 2.12$ K, when the larger chamber was suddenly compressed by about 0.1 bar and then decompressed 300 seconds later. The pressure in the smaller chamber responded in two stages. First, there was an immediate pressure increase caused by the GCA flexing elastically due to the pressure difference, thus compressing the helium in the smaller chamber. Second, there followed a slower, temperature-dependent pressure increase as solid helium flowed through the 25 μm channels in response to the pressure gradient across the GCA.

At 2.10 K (i.e., 20 mK below melting), the pressure stabilized within a minute following a compression and returned to its original value just as quickly after decompression. This confirms that both chambers experienced essentially the same compression (i.e., that flow of solid through the GCA equilibrated the pressures in the two chambers within a minute). We studied the response at lower temperatures, but between squeezes we always warmed the crystal to 2.10 K to ensure we started each measurement from a state of pressure equilibrium.

The response of solid helium changed rapidly as the temperature was lowered. At 2.08 K the pressure increase after squeezing was essentially unchanged but after decompression the pressure did not return quite to its original value. At 2.04 K the pressure increase was smaller (by about 5%) and after decompression the pressure remained even higher, indicating that flow in the solid was no longer sufficient to completely eliminate the pressure difference between the two chambers. By 1.96 K the decompression produced only a small pressure drop and below 1.92 K there was almost no flow through the GCA after squeezing. This irreversible behavior due to flow is characteristic of plastic deformation, as are the stress gradients that remain after compressing and decompressing. As can also be seen, the flow slowed as the temperature was lowered, but the complicated behavior we observed (e.g., note the small bump developing at the beginning of compression as early as 1.98 K) cannot be described simply with a thermally activated time constant. Instead, it appears to reflect the creation of defects (dislocations) and stress gradients during pressure-induced flow and the subsequent partial annealing of these defects near the melting temperature.

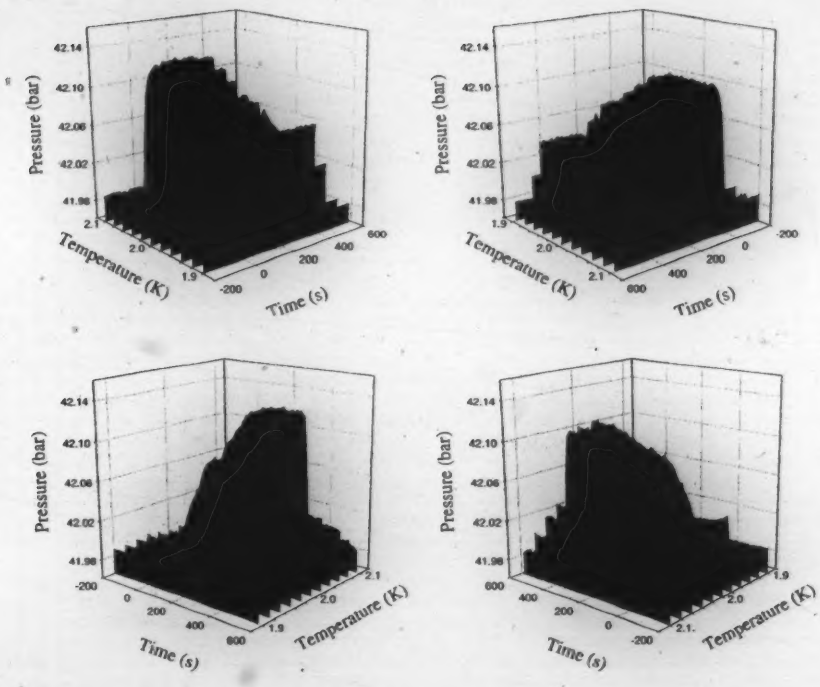

Figure 6.21: Bulk ^{4}He: Temperature dependence of pressure response to a compression/decompression near the melting point of a 42.0 bar sample with a 0.3 ppm ^{3}He impurity concentration.

Figure 6.22 shows the response of a 41.2 bar sample of commercially purified solid ^{4}He (0.3 ppm ^{3}He impurity concentration), with a melting temperature $T_m = 2.08$ K, for the same type of compression/decompression procedure as above. The behaviour is extremely similar to that shown in Figure 6.21.

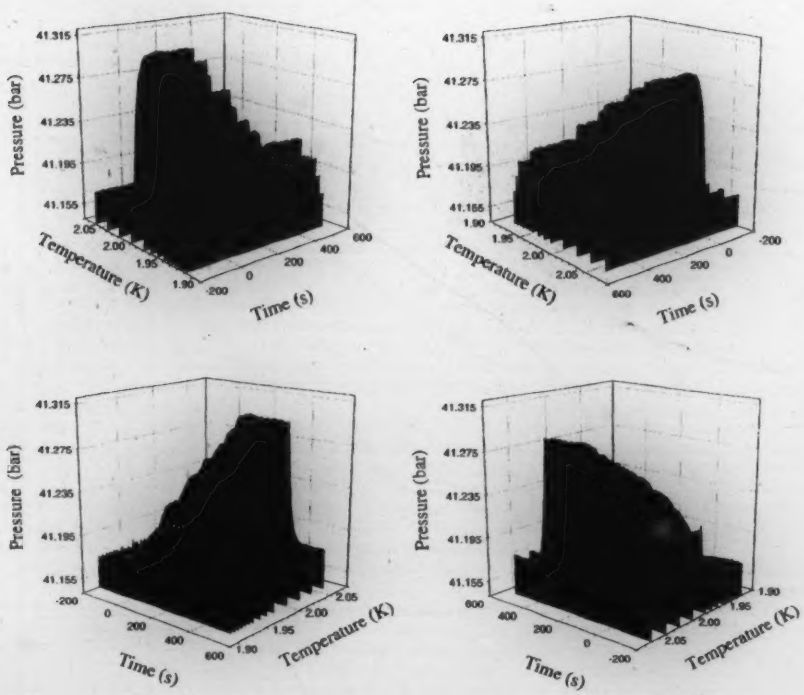

Figure 6.22: Bulk ^{4}He: Temperature dependence of pressure response to a compression/decompression near the melting point of a 41.2 bar sample with a 0.3 ppm ^{3}He impurity concentration.

6.5 Low temperature squeezing

The most interesting question is whether solid helium will flow through the channels in the temperature range where Kim and Chan saw decoupling. Figure 6.23 compares the pressure response at 35 mK to that at 500 mK in a sample of isotopically purified solid ^{4}He (1 ppb ^{3}He impurity concentration). They are offset for clarity and are essentially identical, with no indication of flow over a period of about 20 hours.

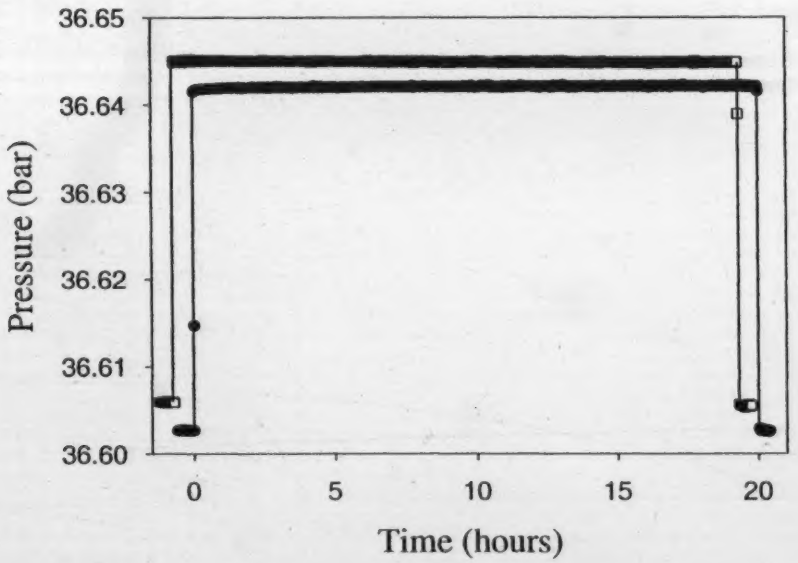

Figure 6.23: Solid ^{4}He response at 500 mK (upper curve, □'s) and 35 mK (lower curve, •'s). Lines are guides to the eye and the curves are offset for clarity. Note the time scale, which is much longer than in Figures 6.21 and 6.22.

The rate of pressure change, set by the noise in our data, is given by

$$\frac{dP}{dt} = \frac{\sigma A v_{av}}{\kappa_{solid} V_2} < \frac{0.5 \text{ mbar}}{20 \text{ hours}}. \tag{6.9}$$

. With A $\approx$ 0.18 cm^2, V$_2$ $\approx$ 0.01 cm^3, and $\kappa_{solid} \approx$ 3.1 x 10^{-3} bar^{-1}, this provides a

limit on the average flow velocity of the solid,

$$v_{av} = \frac{\rho_s}{\rho} v_c < 1.2 \text{ x } 10^{-14} \text{ m/s.} \qquad (6.10)$$

Taking Kim and Chan's value of $\frac{\rho_s}{\rho} \approx 0.01$, we conclude that any supersolid fraction present in the helium moves at a velocity of $1.2 \text{ x } 10^{-12}$ m/s. This is seven orders of magnitude below the supercritical velocities inferred from the Kim and Chan torsional oscillator experiments.

For completeness, we also show Figure 6.24, which compares the pressure response at 75 mK to that at 500 mK in a sample of commercially pure solid ^{4}He (0.3 ppm ^{3}He impurity concentration). They are offset for clarity and their magnitudes are essentially identical. There is no indication of flow over a period of about 12 hours in the 75 mK sample.

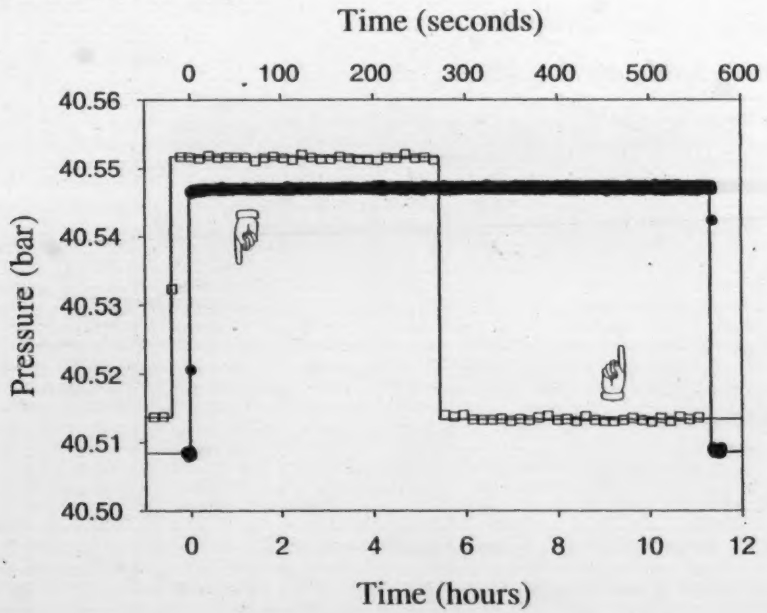

Figure 6.24: Solid ^{4}He response at 500 mK (upper curve, □'s) and 75 mK (lower curve, •'s). Lines are guides to the eye and the curves are offset for clarity. Note the different time scales.

6.6 AC pressure induced flow

A common point raised in response to the pressure-induced flow results presented above is that while these experiments measure a dc effect, the torsional oscillators are an ac probe (i.e., they oscillate back-and-forth). Therefore, we also made low frequency ac measurements using the piezoelectric actuator to produce smaller pressure oscillations (± 4 $V_{peak-to-peak}$, corresponding to ± 3 mbar). The pressure was measured using a manual capacitance bridge (General Radio 1615-A, operating at 10 kHz) with an analog lock-in amplifier, and the ac response was monitored with a digital lock-in amplifier(Stanford Research SR830 DSP). A simple block diagram of the electronics used to make our measurements is shown in Figure 6.25. Sample heating from the piezoelectric actuator limited these measurements to frequencies below 1 Hz, and so we were not able to make direct comparisons to the Kim and Chan torsional oscillator measurements at 1 kHz.

At 0.5 K the amplitude of the pressure oscillations was independent of frequency up to about 1 Hz, as expected since the GCA can flex very rapidly. Close to melting, the frequency dependence was considerably more complicated since, as Figures 6.21 and 6.22 remind us, the solid can flow through the capillaries even on a time scale of a few seconds. We looked for ac flow at low temperatures by cooling a 34.3 bar sample of isotopically purified solid ^{4}He (1 ppb ^{3}He impurity concentration) below 0.5 K. Figure 6.26 shows the amplitude of the pressure oscillations at a frequency of 0.1 Hz. It also shows 0.01 Hz data at 35 mK and at 0.5 K, illustrating the frequency independence over this temperature range. The resolution is better than for dc flow and the pressure amplitude is constant within ± 0.02 mbar. No evidence of temperature dependence is seen that could be attributed to the onset of flow through the capillaries.

6.7 Conclusions

For a supersolid fraction $\rho_s/\rho = 1\%$, our dc flow limit (obtained from Equation 6.10) implies a critical velocity $v_c \leq 1.2 \times 10^{-12}$ m/s, seven orders of magnitude smaller than the critical velocity inferred from Kim and Chan's torsional oscillator measurements and more than three orders of magnitude smaller than the limits set by previous flow experiments [41, 43]. Flow in solids often involves dislocations or grain boundaries, which can be immobilized by small concentrations of impurities. Our

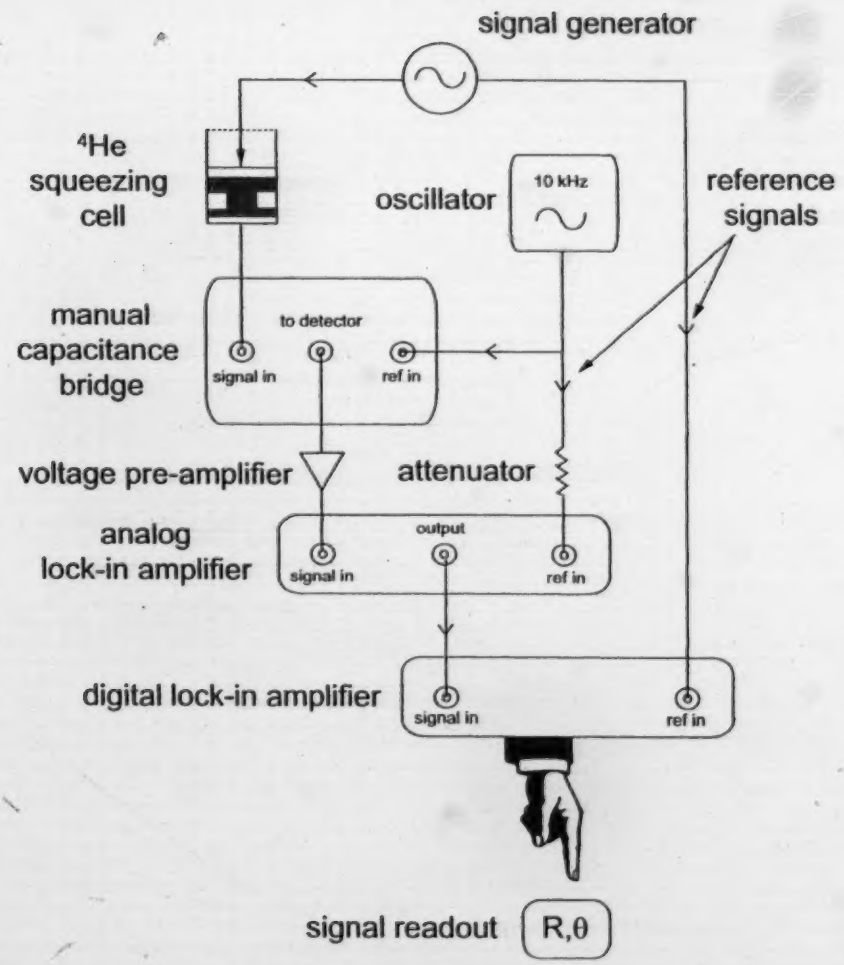

Figure 6.25: Block diagram for the ac squeezing experiment.

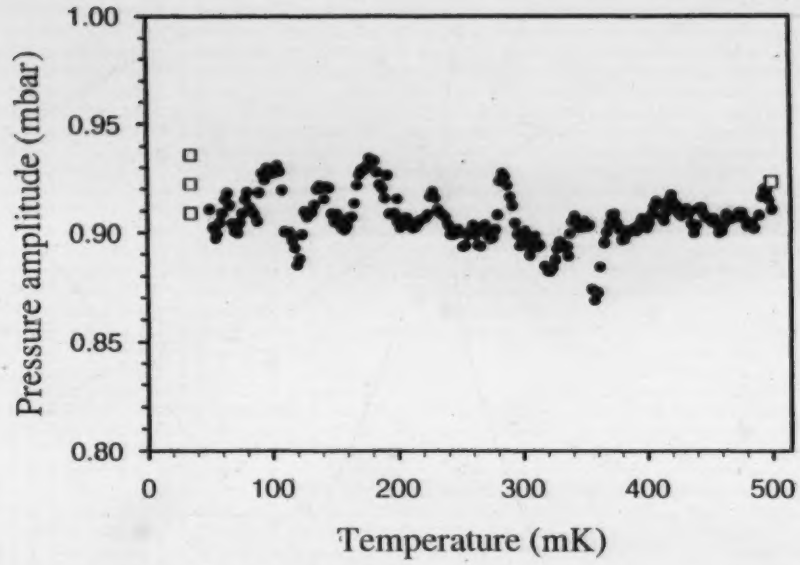

Figure 6.26: AC pressure response in solid ^{4}He at low temperatures. Solid symbols are taken at 0.1 Hz during cooling. Open squares at 35 mK and 500 mK were taken at 0.01 Hz.

measurements using isotopically purified ^{4}He were essentially identical to our results with commercially purified ^{4}He, so the absence of pressure-induced superflow seems not to be due to impurity pinning of such defects (although it possible that such effects are sensitive to impurities even at the ppb level). There has also been a suggestion [84] that a surface melted layer could allow solid helium in a torsional oscillator to slip, providing an alternative, non-supersolid explanation of the bulk ^{4}He decoupling. Our measurements appear to rule out such behavior at low temperatures, although it may occur near melting. The torsional oscillator results were also consistent with the displacement, rather than the velocity, being limited to a critical value. We can put limits on possible displacements of the solid helium at low temperatures from the data in Figures 6.23 and 6.26.

Recall that the bulk modulus K is given by

$$K = -V\left(\frac{\partial P}{\partial V}\right)_T. \tag{6.11}$$

Solid ^{4}He has a bulk modulus of $\sim$ 325 bar, while the volume of the chamber is

11 mm^3. A pressure increase in this chamber will result if its volume is decreased. We can correspond this decrease to some volume of solid ^{4}He moving a distance h along the 36,000 GCA channels of radius r and into the chamber (i.e., $\Delta V = 36000\ \pi r^2 h$). Since the pressure jumps at 35 and 500 mK of Figure 6.23 agree within 1 mbar, the corresponding displacements (i.e., the distance that solid ^{4}He can travel along the length of our GCA capillaries) cannot differ by more than 2 nm.

Our ac measurements are less sensitive to flow, but more sensitive to displacements, and rule out movements of solid helium through the channels larger than 0.03 nm. If we again assume that only a 1% supersolid fraction moves, this would imply supersolid displacements less than 3 nm, comparable to the amplitude of Kim and Chan's torsional oscillator at their critical velocity (for their 1 kHz oscillator, $v_c \approx 10\ \mu m/s$ corresponds to an amplitude $v_c/\omega \approx 2$ nm). These experiments show that static or low frequency pressure differences do not produce either superflow or unusual displacements at low temperatures in solid ^{4}He. If the helium forms a supersolid, then its flow properties must be quite different from those of a superfluid, in which the chemical potential difference created by a pressure change would cause superflow.

Chapter 7

Shear Modulus Study of Solid Helium

The first, and so far only, evidence for supersolidity comes from torsional oscillator measurements in which the frequency increased at temperatures below about 200 mK, suggesting that some of the solid helium decoupled from the oscillator. This behaviour has been interpreted in terms of the nonclassical rotational inertia which characterizes a supersolid. The behaviour has been replicated by several groups [53, 55, 54, 57, 56]; however, no clear signature has yet been seen in other properties (although a recently reported heat capacity peak supports the existence of such a new phase [97]). Persistent currents would provide definitive proof of supersolidity, but this challenging experiment has not yet been performed. Other experiments (i.e., Chapters 5 and 6) put extremely small bounds on possible pressure-driven DC mass flow [78, 79].

Although the amount of helium which decouples in different torsional oscillators varies widely, the measurements have many common features. Decoupling occurs below about 200 mK, with a gradual onset accompanied by a dissipation peak. It decreases at large oscillation amplitudes, which is interpreted in terms of a superflow critical velocity ($\dot{v}_c \sim 10$ μm/s). The magnitude of the decoupling is frequency independent, although its onset shifts with frequency. Its amplitude dependence appears to scale with velocity [56], but depends on the oscillation amplitude during cooling and is hysteretic. A crucial feature of the decoupling is its sensitivity to ^{3}He. Most measurements used commercial ^{4}He gas (with ^{3}He concentration $x_3 \sim 0.3$ ppm) but experiments [52, 58] with isotopically pure ^{4}He (1 ppb ^{3}He) show a sharper onset at a lower temperature, around 75 mK. Decoupling is usually larger in narrow annuli than in open cylinders [57] but begins at similar temperatures. Its magnitude

also depends on how the solid helium was grown and annealed, indicating that defects are important. Most samples were grown at constant volume under blocked capillary conditions, a procedure which involves substantial plastic deformation and is expected to produce a polycrystalline solid with many defects. Theoretical work also suggests that supersolidity does not occur in a perfect crystal [71, 61] and that vacancies [67], grain boundaries [80, 81], glassy regions [75] or dislocations [83, 153] are involved. Superflow associated with grain boundaries has been seen in solid ^{4}He coexisting with liquid [82], but solidification at constant pressure (producing single crystals with fewer defects) still gives significant decoupling [58].

7.1 Experimental design

Dislocation networks are an important defect to consider. Since their main effect is on mechanical behavior, we have made a detailed study of the elastic properties of solid ^{4}He. This required a completely new method to measure the shear modulus μ at extremely low frequencies and amplitudes. Embedding piezoelectric transducers in the helium allowed us to measure μ of the ^{4}He within the gap separating the transducers directly at strains (stresses) as low as $\varepsilon = 2.2 \times 10^{-9}$ ($\sigma = 0.03$ Pa). This is two to three orders of magnitude lower than in previous ultrasonic [154, 155, 156], internal friction [157] and torsional [158] measurements and is comparable to inertial stresses in torsional oscillator measurements. A low noise current amplifier allowed us to measure μ at frequencies down to 20 Hz, far lower than in any other measurements. These low amplitude and low frequency features proved crucial to our experiments. We could also excite and detect acoustic modes of solid ^{4}He outside of the gap separating the transducers and within the surrounding solid ^{4}He. The first such acoustic resonance was near 8000 Hz and had a quality factor $Q \sim 2000$ at our lowest temperature.

7.1.1 Cell construction

The shear and acoustic resonance measurements were performed in the same cell. A schematic of the cell is shown in Figure 7.1 and an image of the cell is shown in Figure 7.2. Our OFHC cell consisted of a large inner volume (≈ 25 cm^3) into which our shear transducers were installed. The transducers were epoxied onto solid brass backing pieces, which were themselves rigidly mounted onto a solid brass support arm, ensuring that the faces between the transducers were parallel. The

cell also included an *in situ* Straty-Adams capacitive pressure gauge which, when used with a 1 kHz automatic bridge (Andeen-Hagerling 2550A), had a resolution and stability better than 0.2 mbar. The cell was mounted onto the bottom of the mixing chamber of our dilution refrigerator. A 0.004" i.d. CuNi capillary, thermally anchored at the 1 K pot of the fridge and at the 0.6 K step heat exchangers, was used to introduce ^{4}He to the cell. The ^{4}He used in these experiments ranged in isotopic purity from $\sim$ 0.3 ppm ^{3}He isotopic impurities down to nominally pure 1 ppb ^{3}He isotopic impurities [148]. All crystals were grown using the constant volume, blocked capillary technique. Temperatures were measured with a calibrated germanium thermometer above about 50 mK, with a ^{60}Co nuclear orientation thermometer for lower temperatures.

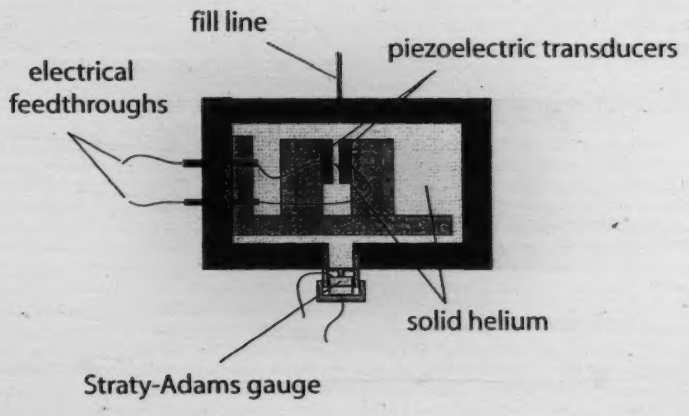

Figure 7.1: Schematic of the shear cell. The front faces of the transducers are grounded to the body of the cell.

7.1.2 PZT transducers

Displacements were generated and stresses were detected by two parallel-aligned shear transducers [159] with a helium-filled gap (D $\approx$ 180 μm) between their faces. The transducers were made from PZT 5A material (quoted fundamental resonance at 500 kHz, with dimensions width W = 9.6 mm, length L = 12.8 mm, thickness t = 2.1 mm).

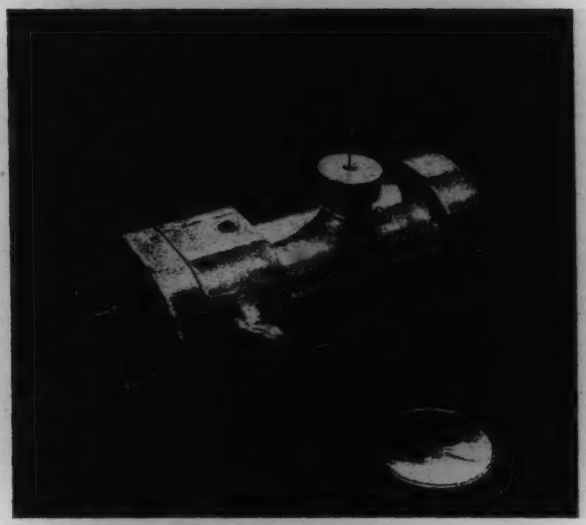

Figure 7.2: Image of the shear cell, next to a Canadian quarter for scale.

When a voltage is applied across a capacitor made of normal dielectric material, a charge results on the plates or electrodes of the capacitor. Charge can also be produced on the electrodes of a capacitor made of a piezoelectric material by the application of stress; this is known as the direct piezoelectric effect. Conversely, the application of a field to the material will result in strain; this is known as the inverse piezoelectric effect. Therefore, a piezo-ceramic is capable of acting as either a transmitting element, a sensing element, or both.

Relationships between the applied forces and the resultant responses depend upon a number of factors: for example, the piezoelectric properties of the ceramic; the size and shape of the piezo-ceramic; and the direction of the electrical and mechanical excitation. There exist double subscripted coefficients associated with piezoelectric constants that link electrical and mechanical quantities. The first subscript gives the direction of the electrical field associated with the voltage applied, or the charge produced; the second subscript gives the direction of the mechanical stress or strain.

The piezoelectric constant which relates the mechanical strain produced by an applied electric field are termed the strain constants, or the "d" coefficients (Equation 7.1). The units may then be expressed as m/m per V/m (i.e., m/V, and actual displacements (in m) are independent of transducer thickness). The subscripts in

d_{15} indicate that the voltage is applied to the electrodes which are at right angles to the original poling electrodes and that the applied mechanical stress is shear.

$$d = \frac{\text{strain developed}}{\text{applied electric field}}. \tag{7.1}$$

The piezoelectric constant which relates the electric field produced by a mechanical stress are termed the voltage constants, or the "g" coefficients (Equation 7.2). The units may then be expressed as V/m per N/m^2 (i.e., Vm/N) or V/m per Pa. The subscript in g_{15} implies that the applied stress is shear and that the resulting electric field is perpendicular to the polarization axis (and charge is collected on electrodes which are at right angles to the original poling electrodes).

$$g = \frac{\text{open circuit electric field}}{\text{applied mechanical stress}}. \tag{7.2}$$

Finally, whereas the relative dielectric constant is strictly a material property, the capacitance is a quantity which depends both on the type of material and its dimensions. At frequencies far below resonance, piezoelectric ceramic transducers are fundamentally capacitors. Consequently, the voltage coefficients g_{ij} are related to the charge coefficients d_{ij} by the dielectric constant K_i (as in a capacitor the voltage is related to the charge by the capacitance).

$$d_{15} = K_i \varepsilon_0 g_{15}, \tag{7.3}$$

7.2 Measurements in sample

A simple block diagram of the electronics used to make our measurements is shown in Figure 7.3. Data collection (i.e., lock-in amplifier readouts) was automated by a computer.

A voltage V applied to the driving transducer produces a shear displacement at its front face $\delta x = d_{15}V$. Voltages were generated using a synthesized function generator (Stanford Research Systems DS345), capable of generating many standard waveforms with a frequency resolution of 1 μHz. Sinusoidal outputs were employed for all measurements described below, the amplitude of which was adjustable from 10 mVpp to 10 Vpp. The signal was split into a driving voltage for the PZT and

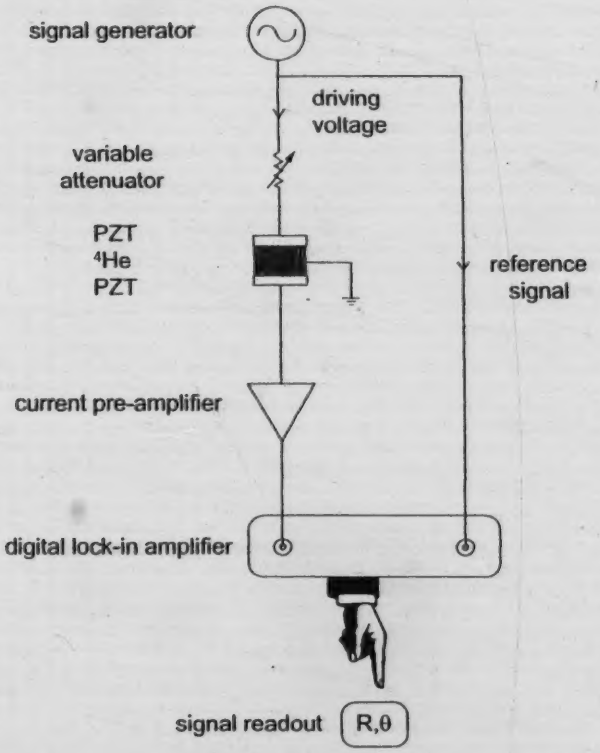

Figure 7.3: Block diagram for the shear experiment.

a reference signal for the lock-in amplifier. The minimum amplitude to which the signal generator was set was 150 mVpp, near the reference detection limit of the lock-in amplifier. The driving voltage was attenuated from 150 mVpp by a series of electronic attenuators. The actual driving voltages (used to calculate strains) were measured using an auto-ranging microvolt digital multi-meter (Keithley 197).

At room temperature, d_{15} is given by the manufacturer as 585 x 10^{-12} m/V. In order to determine the low temperature value of this coefficient, consider that the electric field generated in the detecting transducer is

$$E = g_{15}\sigma, \tag{7.4}$$

or that the voltage generated across the transducer is

$$V = Et = g_{15}\sigma t, \tag{7.5}$$

where the stress σ is related to the strain ϵ by the shear modulus of the helium in the gap D $\approx$ 180 μm ($\mu = \sigma/\epsilon$). The strain in the helium in the gap between the two transducers is

$$\epsilon = \frac{\delta x}{D} = \frac{d_{15}V}{D}, \tag{7.6}$$

so that the stress induced in the detecting transducer is

$$\sigma = \frac{\mu d_{15}V}{D}. \tag{7.7}$$

The capacitance of the piezo-ceramic is given by

$$C = \frac{K_1 \varepsilon_0 A}{t}, \tag{7.8}$$

where is A is the area of the electrodes. As q = CV, Equations 7.3, 7.5, and 7.8 allow us to write the charge generated on the face of the stressed electrode as

$$q = d_{15}\sigma A. \tag{7.9}$$

We measure this charge generated as a current I (at a drive frequency f)

$$I = \omega q = 2\pi f q = 2\pi f d_{15}\sigma A. \tag{7.10}$$

Coupled with Equation 7.7, we measure an output current from our detecting shear transducer equal to

$$I = 2\pi f \frac{A}{D} {d_{15}}^2 \mu V. \tag{7.11}$$

This output current I can be vanishingly small, and so we used an ultra-low-noise current preamplifier (Femto LCA-20K-200M) to magnify the signal. The preamplifier has an extremely low 14 fA/$\sqrt{Hz}$ equivalent input noise current, a 20 kHz bandwidth, and a gain of 2 x 10^8 V/A. This signal was then detected with a 2-phase digital lock-in amplifier (Stanford Research System SR830 DSP), as R (the amplitude of I) and θ (the phase of I). By measuring our signal in this way, back-

grounds/crosstalk could be subtracted even if they had different phases.

With that, we can write d_{15} in terms of our experimental variables at low temperature:

$$d_{15} = \left(\frac{D}{2\pi A\mu}\frac{1}{V}\frac{I}{f}\right)^{\frac{1}{2}}. \tag{7.12}$$

We must be careful to note that A is the overlapping area of the electrodes. The total area of each electrode is 1.23 x 10^{-4} m^2, but our electrodes are horizontally offset from one another by about 3 mm (see Figure 7.4), so that the overlapping area is actually $\approx 10^{-4}$ m^2. For solid ^{4}He at about 35 bar ($\mu \approx 1.5 \times 10^7$ Pa), we measured $I_{rms} \approx 25$ pA at 2000 Hz for a driving voltage $V_{rms} \approx 17.3$ mV. This means that $d_{15} = 1.2 \times 10^{-10}$ m/V for these transducers below 4 K (reduced to 21% of its room temperature value).

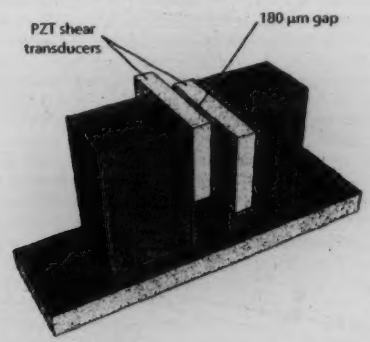

Figure 7.4: The horizontal offset in the transducers.

Returning to the original statement of this section, a voltage V applied to the driving transducer produces a shear displacement at its front face δ x = d_{15}V. Below the resonance frequency of solid ^{4}He in the gap (v_t/2D $\sim$ 830 kHz), this creates a strain, $\epsilon_t = \delta x/D$, which then produces a shear stress, $\sigma_t = \mu\epsilon_t$, on the detecting transducer. The minimum detectable stress at 2000 Hz, set by noise in our

preamplifier (14 fA/$\sqrt{Hz}$, resulting in $\sim$ 2.5 fA at 30 s averaging), is $\sigma_t \sim 10^{-5}$ Pa (which corresponds to a displacement $\delta x \sim 2 \times 10^{-16}$ m and strain $\epsilon_t \sim 10^{-12}$).

After subtracting a background due to electrical crosstalk (the signal with liquid ^{4}He in the cell, a correction of less than 15%, see Figure 7.5) from the raw signal (Figure 7.6), the solid's shear modulus ($\sim 1.5 \times 10^7$ Pa) is proportional to I/f (recall Equation 7.12). It is important to note that the small resonances in the liquid background aren't individually considered; rather, we subtract an "average" smooth background. The shear modulus is nearly frequency independent below 4000 Hz, as shown in Figure 7.7.

The 3 mm offset of the transducers (recall Figure 7.11) provided exposed surfaces which could be used to excite and detect acoustic modes of the solid helium outside the gap, surrounding the transducers. The first such resonance can be found near 8000 Hz in Figure 7.6.

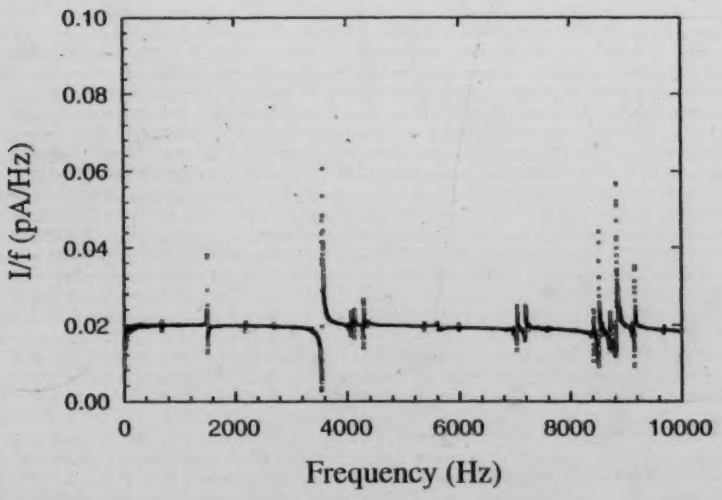

Figure 7.5: The liquid ^{4}He background signal in the shear cell. Data were collected at T = 0.5 K and P = 22.1 bar, at a 24.5 mV_{peak} sinusoidal drive.

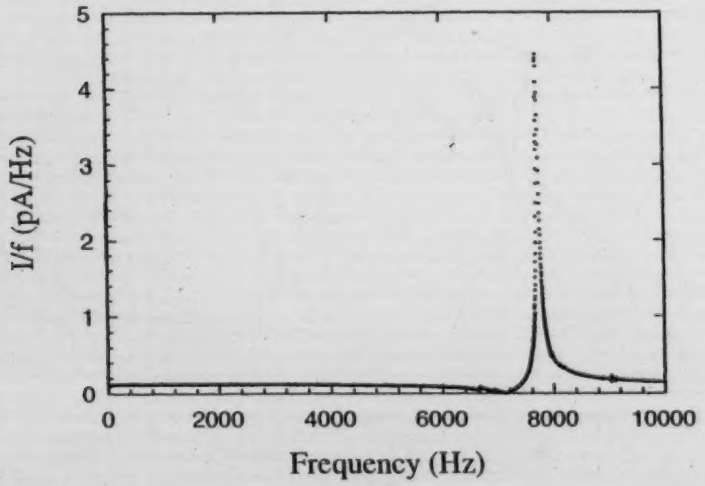

Figure 7.6: The raw signal of solid ^{4}He in the shear cell. Data were collected at T = 0.5 K and P = 33.3 bar, at a 24.5 mV_{peak} sinusoidal drive. Notice the difference in vertical scale from Figure 7.5.

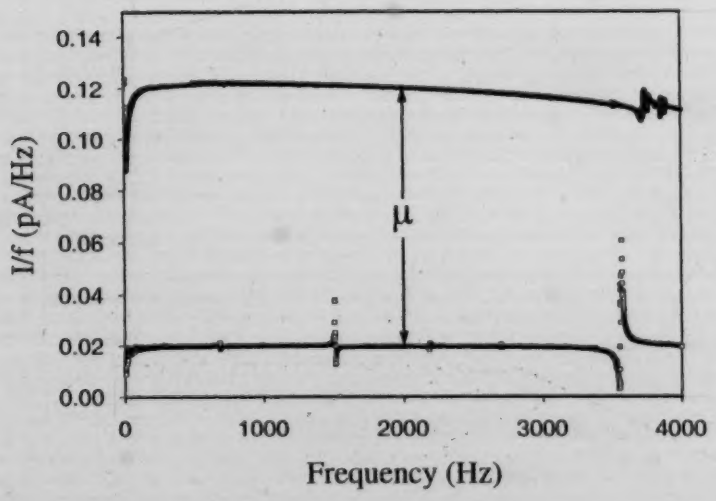

Figure 7.7: The measurement of the shear modulus of solid ^{4}He. Both sets of data were collected at T = 0.5 K (liquid P = 22.1 bar; solid P = 33.3 bar), at a 24.5 mV_{peak} sinusoidal drive.

7.3 Shear modulus in gap

The following section discusses the essential result of this experiment; namely, the anomalous stiffening of solid hcp ^{4}He at low temperatures. All solid samples are grown by first filling the cell with a high pressure liquid ($\sim$ 70 bar) at 4.2 K and then cooling. No special effort is taken to keep the fill line from the high-pressure gas cylinder to the cell open. As the dilution refrigerator is set into operation, parts of the fill line will reach temperatures near 1 K long before the cell reaches those same temperatures. As a result, a solid plug will develop in the fill line before the ^{4}He in the sample cell freezes, meaning that no more ^{4}He may enter (or leave) the cell during sample solidification (i.e., solidification occurs under constant density conditions). This is referred to as the blocked capillary technique for sample growth, and presumably results in a polycrystalline solid sample with many defects. 0.3 ppm ^{3}He was used for all samples discussed in this section (i.e. Section 7.3). Sometimes the sample was annealed before the measurement was made, other times it wasn't. Here, annealing means keeping the sample at a temperature slightly below melting for an extended period of time. We presume that this process improves the quality of the sample under study (e.g., results in fewer crystallographic defects), but we have no way of directly knowing this. The melting curve of ^{4}He was given in Figure 6.9, and the thermodynamic path followed during each particular sample growth will be overlaid in the following subsections. Following that, the shear modulus of each sample is provided and discussed. In each case, the liquid background has been subtracted.

7.3.1 Sample 300ppb29.3

Figure 7.8 shows the thermodynamic path followed during the growth of sample 300ppb29.3. As can be seen from the inset of Figure 7.8, solidification was complete at the upper bcc/hcp/liquid triple point; from there, the sample continued along the bcc/hcp line until entering the pure hcp phase at T = 1.68 K and P = 29.3 bar. The helium used for this sample had an isotopic purity of 300 ppb ^{3}He.

Figure 7.9 shows the temperature dependence of the shear modulus of a sample 300ppb29.3 (typical of all samples studied). Sample 300ppb29.3 was annealed before this measurement was taken by holding the cell temperature at 1.45 K for $\sim$ 17 hours. We annealed the sample until the shear modulus was no longer changing as a function

of time. The data was collected as the sample was cooled. The measurement was made at 2000 Hz, at a driving voltage of 32.7 mV_{peak} and a corresponding strain of 2.2 x 10^{-8}. Below 200 mK, the shear modulus μ increases by about 11% ($\Delta\mu \sim 16$ bar). As mentioned above, this anomalous stiffening is our central result. The pressure in the cell is constant within 0.2 mbar in this temperature range, which rules out local density changes (e.g., freezing of small liquid regions) as the cause of the μ increase and implies that the bulk modulus does not have a similar anomaly.

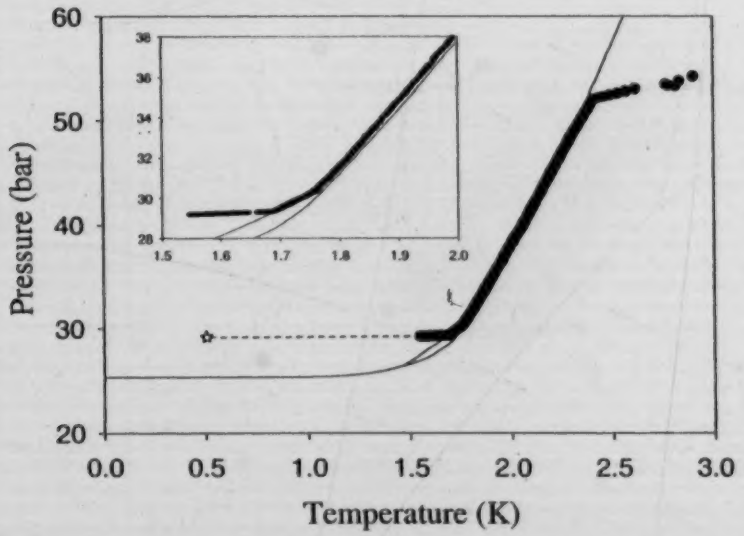

Figure 7.8: The thermodynamic path for sample 300ppb29.3. Inset shows a close-up of the end of freezing. This data is the pressure versus temperature as we measured it.

Figure 7.10 shows a typical NCRI fraction from a torsional oscillator measurement [51], at a frequency of 910 Hz. The onset and shape of the temperature dependence is essentially the same as that of shear modulus anomaly, $\Delta\mu$, shown in Figure 7.9.

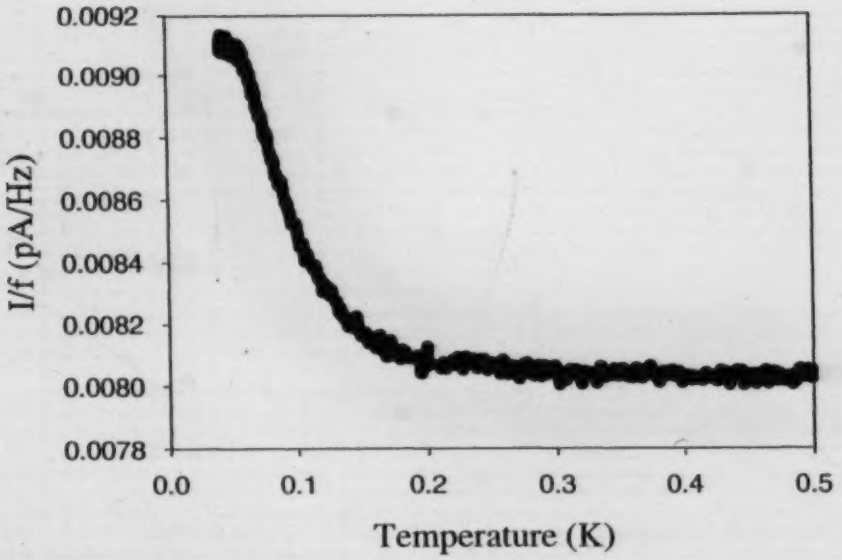

Figure 7.9: Shear modulus anomaly in sample 300ppb29.3 as a function of temperature, measured at 2000 Hz.

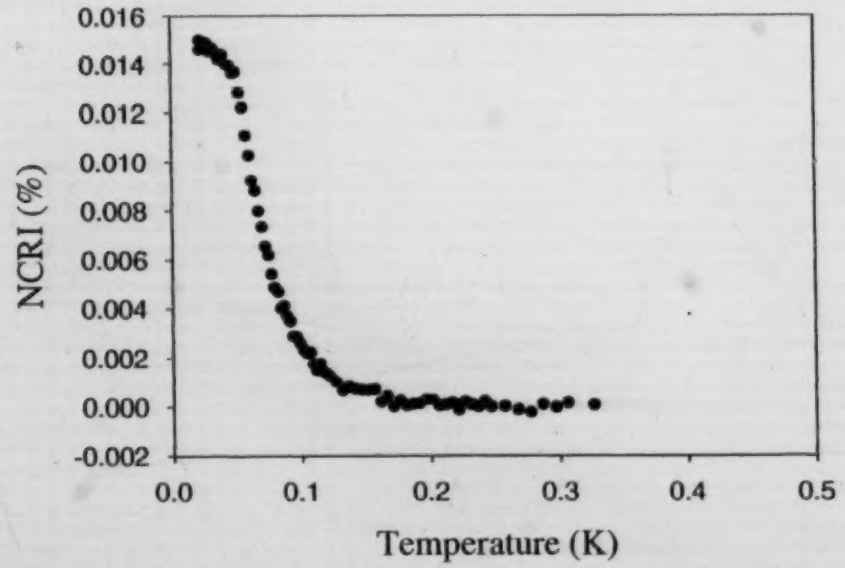

Figure 7.10: Typical NCRI fraction (65 bar) in a torsional oscillator operating at 910 Hz.

7.3.2 Sample 300ppb34.0

Figure 7.11 shows the thermodynamic path followed during the growth of another hcp solid ^{4}He sample, 300ppb34.0. As can be seen from the inset of Figure 7.11, solidification this time was complete before reaching the bcc/hcp/liquid triple point. The rounded knee, signalling the end of freezing, is commonly observed when no attempt is made to control the temperature of the cell while the dilution refrigerator is cooling and can be made sharper through annealing the sample (as was shown in Figure 6.17), or by way of a partial melt and re-freeze. The helium used for this sample also had an isotopic purity of 300 ppb ^{3}He.

Figure 7.12 shows the temperature dependence of the shear modulus μ of sample 300ppb34.0. Sample 300ppb34.0 was annealed before this measurement was taken by holding the cell temperature at 1.70 K for $\sim$ 10 hours. The data was collected as the sample was cooled. The measurement was made at 2000 Hz, at a driving voltage of 32.7 mV_{peak} and a corresponding strain of 2.2 x 10^{-8}. At low temperature, it increases by about 6% ($\Delta\mu \sim 9$ bar).

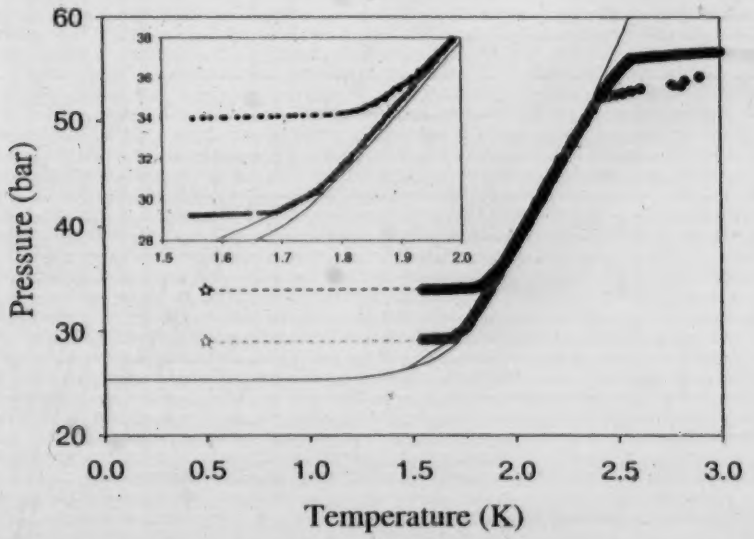

Figure 7.11: The thermodynamic path for sample 300ppb34.0. Inset shows a close-up of the end of freezing. This data is the pressure versus temperature as we measured it. Data in grey shows sample 300ppb29.3.

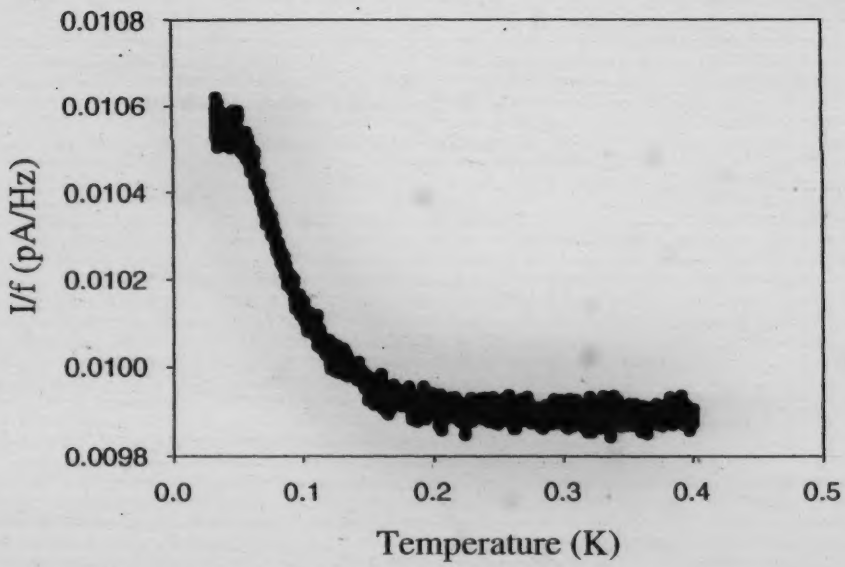

Figure 7.12: Shear modulus anomaly in sample 300ppb34.0 as a function of temperature, measured at 2000 Hz.

7.3.3 Sample 300ppb33.3

Figure 7.13 shows the thermodynamic path followed during the growth of sample 300ppb33.3. As can be seen from the inset of Figure 7.13, this sample is at only a slightly lower pressure than the previous sample 300ppb34.0. As well, it has entered the hcp phase without having first entered the mixed bcc/hcp phase. The helium used for this sample also had an isotopic purity of 300 ppb ^{3}He.

Figure 7.14 shows the temperature dependence of the shear modulus μ of sample 300ppb33.3 (and looks cleaner than the previous sets of data, as it was taken with our then-newly-acquired current pre-amplifier). Sample 300ppb33.3 was annealed before this measurement was taken by holding the cell temperature at 1.70 K for $\sim$ 12 hours. The data was collected as the sample was cooled. The measurement was made at 2000 Hz, at a driving voltage of 32.7 mV_{peak} and a corresponding strain of 2.2 x 10^{-8}. At low temperature, it increases by about 8% ($\Delta\mu \sim 12$ bar).

We observed variations in $\Delta\mu$ of up to a factor of 2 over a total of 8 samples

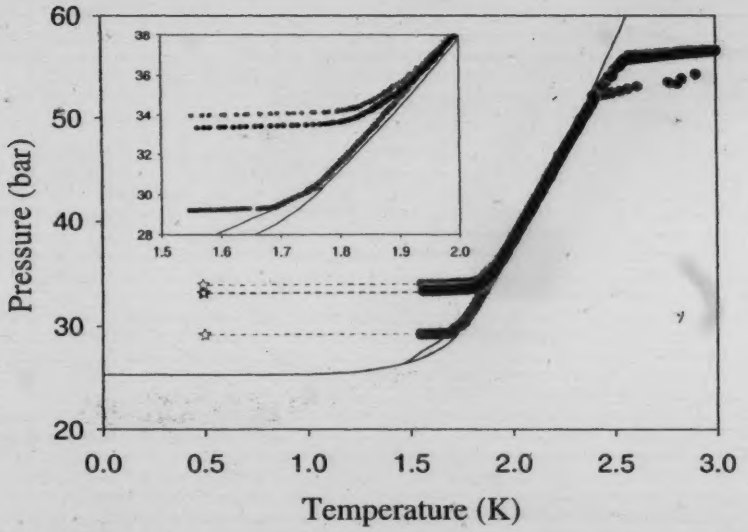

Figure 7.13: The thermodynamic path for sample 300ppb33.3. Inset shows a close-up of the end of freezing. This data is the pressure versus temperature as we measured it. Data in grey shows sample 300ppb29.3 and sample 300ppb34.0.

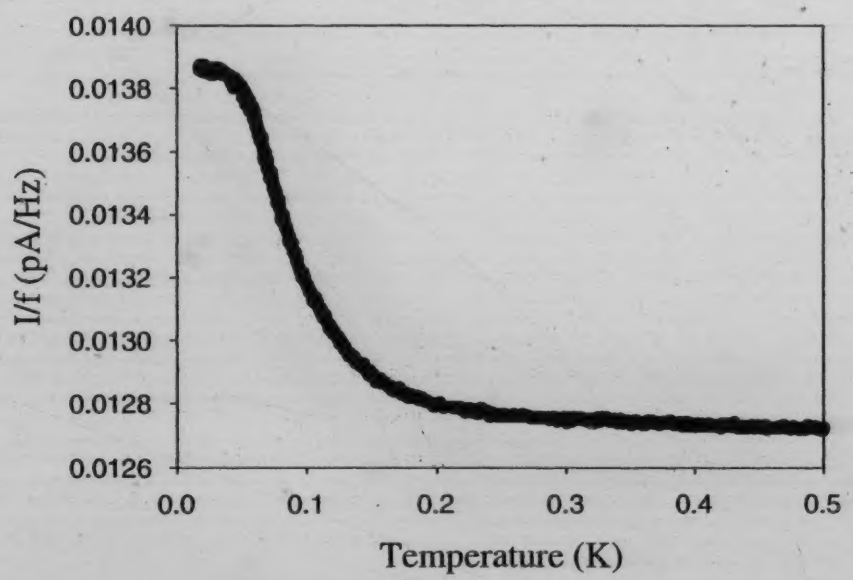

Figure 7.14: Shear modulus anomaly in sample 300ppb33.3 as a function of temperature, measured at 2000 Hz.

in the pressure range 29-34 bar, and with varying concentrations of ^{3}He impurities. This is similar to the range of NCRI seen in a single torsional oscillator.

7.3.4 Frequency dependence

Figure 7.15 shows the shear modulus anomaly at three frequencies (2000, 200 and 20 Hz), at a driving voltage of 32.7 mV_{peak} and a corresponding strain of 2.2 x 10^{-8}, in the sample 300ppb33.3 of Figure 7.14. The magnitude of the modulus increase is similar for each and is nearly independent of frequency over two orders of magnitude. This is in agreement with torsional oscillator experiments where a frequency independent NCRI fraction is measured [56]. The transition is sharper at low frequency, and appears to begin at lower temperatures.

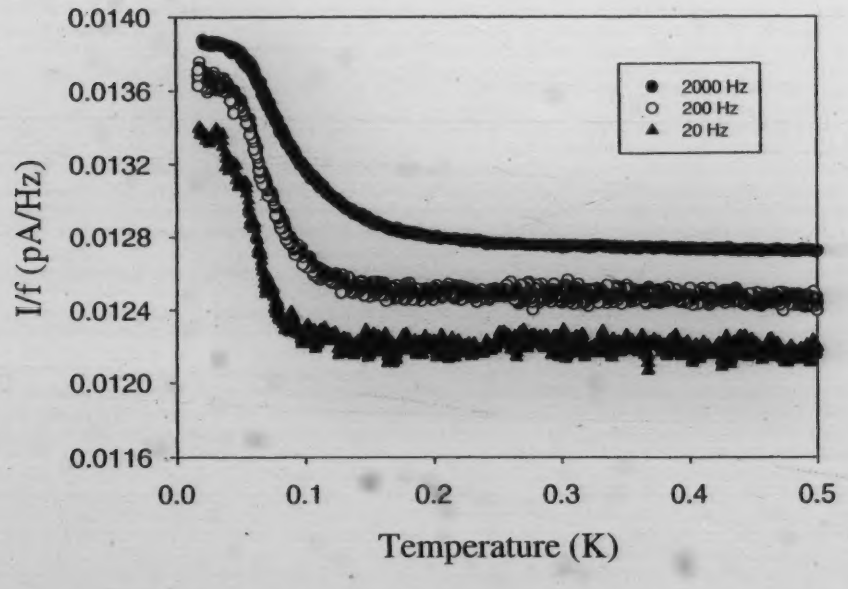

Figure 7.15: The shear modulus anomaly as a function of frequency in sample 300ppb33.3. The 200 Hz and 20 Hz data have been shifted down for clarity.

We did not measure the shear modulus μ at frequencies below 20 Hz because the low signal-to-noise ratio required painfully long averaging times with the lock-in amplifier. For example, the 200 Hz data was collected over a period of 4 hours,

whereas the 20 Hz data was collected over a period of 12 hours. Measuring the shear modulus μ at a significantly lower frequency would have taken more than a full day, which is about as long as the dilution refrigerator can run without having to re-fill the pot (a process we know can disturb the signal). Additionally, and even at temperatures above the anomaly, the shear modulus μ is not independent of frequency much below 20 Hz, as we measure it. A closer look at Figure 7.7 shows that the signal tends to roll off at the lowest frequencies, and that the effect is greater in the solid than in the liquid. The cause of this roll-off is unknown.

Also, we did not perform measurements at frequencies above 2000 Hz because the shear modulus μ becomes frequency dependent near 4000 Hz. As will later be discussed in greater detail, an acoustic resonance exists in the cell, outside of the gap. This resonance is centered near 8000 Hz, and while its Q-factor is high, it is not infinite. As a result, measurements of I/f at frequencies near to the resonance give more than just the shear modulus μ of the solid in the gap.

7.3.5 Amplitude dependence

Figure 7.16 shows $\Delta\mu$ at 2000 Hz for sample 300ppb33.3 at different strains (as calculated from the drive voltages using Equation 7.6). The shear modulus anomaly $\Delta\mu$ is independent of drive amplitude for strains up to 2.2 x 10^{-8} and then begins to decrease.

Nearly identical behavior was also observed at 200 Hz, as shown in Figure 7.17. The amplitude dependence begins at roughly the same drive level, indicating that $\Delta\mu$ scales with either stress or strain and not with velocity. That stress or strain best parameterizes the magnitude of the shear anomaly $\Delta\mu$ and how this compares to analogous torsional oscillator measurements will be discussed in the following subsection.

For an easier comparison of the data sets at 2000 Hz and 200 Hz, Figure 7.18 shows them side-by-side (with the 200 Hz data plotted on a decreasing temperature scale).

The low temperature values of the shear modulus I/fV are plotted in Figure 7.19. At the lowest strains, the shear modulus I/fV is constant; at the highest strains, the shear modulus I/fV decreases with increasing strain. These two regimes are demonstrated in Figure 7.19 by dashed lines, and are separated by a "critical strain" $\epsilon_c \sim 4.5$ x 10^{-8}, shown in grey.

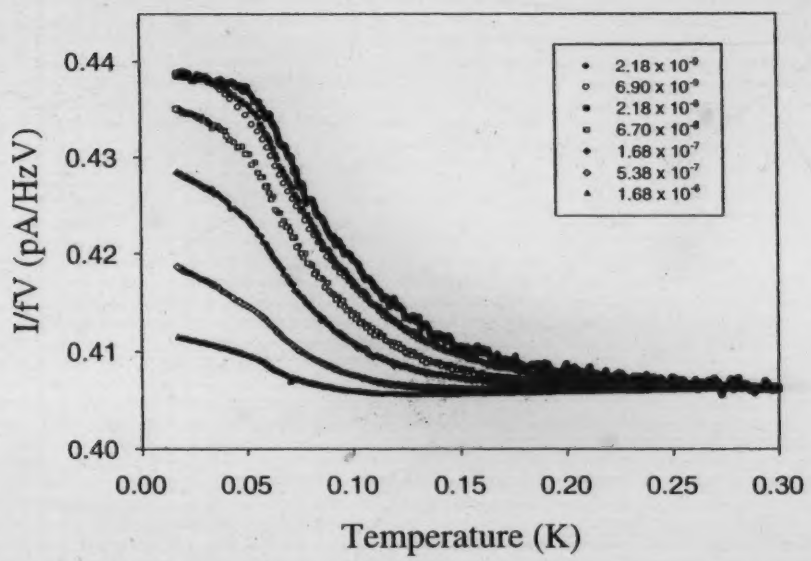

Figure 7.16: The shear modulus anomaly as a function of strain amplitude at 2000 Hz in sample 300ppb33.3. The data have been scaled by the driving voltage, have had the liquid background subtracted, and have been shifted to have equal μ at 300 mK at the lowest strain.

The corresponding velocities in Figures 7.16 and 7.17 ($v = \omega x$: $\sim$ 100 nm/s for $\epsilon = 4.5 \times 10^{-8}$ at 2000 Hz; $\sim$ 10 nm/s for the same strain level at 200 Hz) are much smaller than the critical velocity ($v_c \approx 10$ μm/s) inferred from torsional oscillator measurements. However, the stress levels (0.3 Pa) are comparable to inertial stresses in torsional oscillators.

For example, consider the stresses involved in the annular torsional oscillator of Reference [10]. The torque acting on the solid sample in such a system is given by

$$\tau = \sigma A R, \tag{7.13}$$

where σ is the shear stress at the walls, A is the area of the walls against which the solid sits, and R is the radius of the annulus. For a narrow cylindrical annulus, $A = 4\pi Rh$, where h is the height of the walls, and the extra factor of 2 comes in because there is an inner and an outer wall whose area must be considered. The torque of the oscillator acting on the solid ^{4}He may also be written as

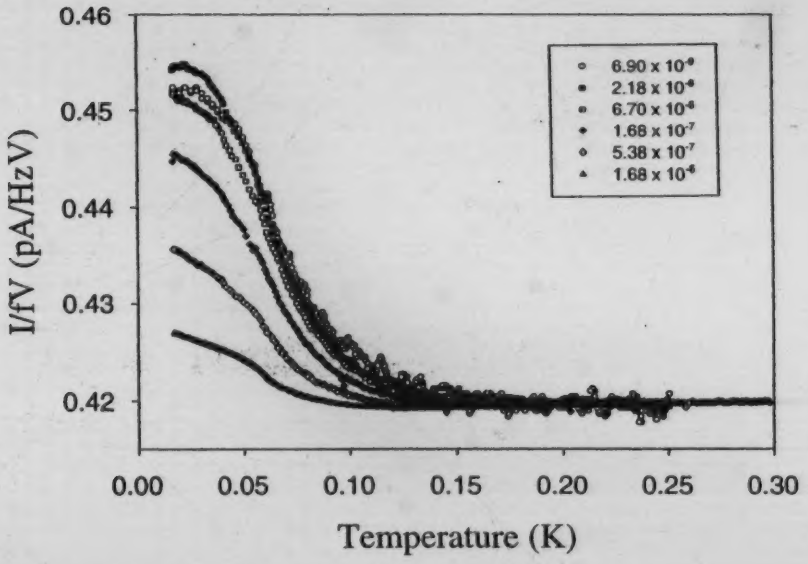

Figure 7.17: The shear modulus anomaly as a function of strain amplitude at 200 Hz in sample 300ppb33.3. The data have been scaled by the driving voltage, have had the liquid background subtracted, and have been shifted to have equal μ at 250 mK at the lowest strain.

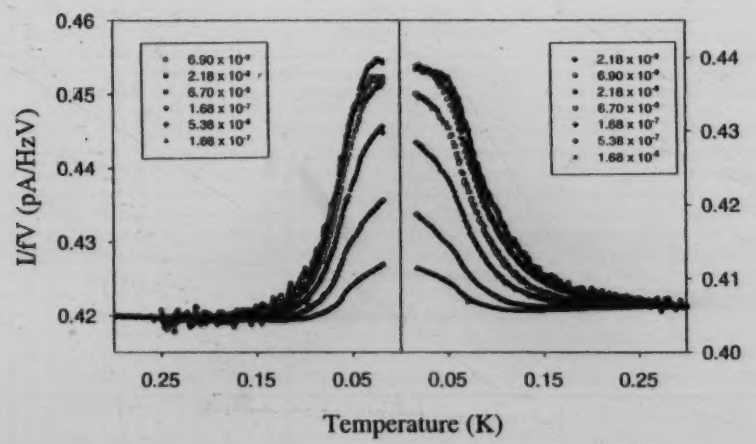

Figure 7.18: The shear modulus anomaly as a function of strain amplitude at 200 Hz (left) and 2000 Hz (right) in sample 300ppb33.3. Note that the two vertical axes span different ranges of the same scale.

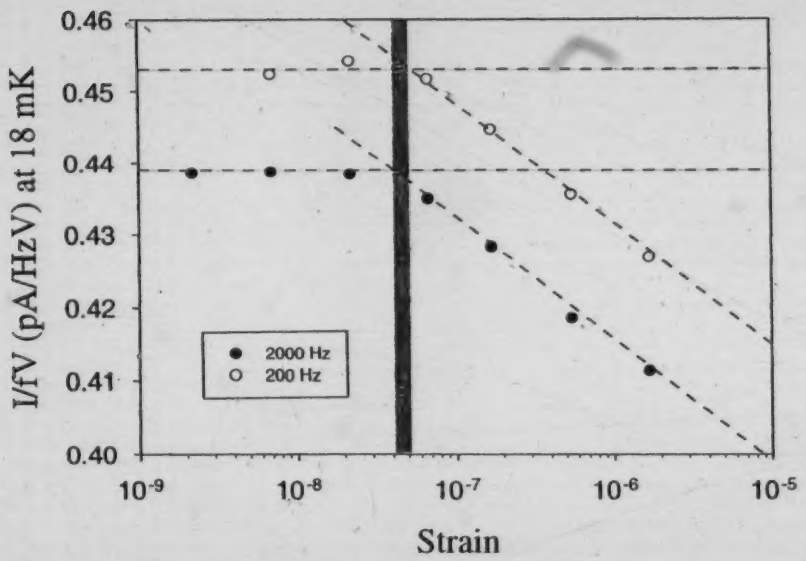

Figure 7.19: The shear modulus anomaly as a function of strain amplitude at 2000 Hz and 200 Hz in sample 300ppb33.3 at 18 mK. Dashed lines are a guide to the eye. The shaded region highlights the inferred "critical strain" ϵ_c.

$$\tau = I\alpha = Ia/R, \tag{7.14}$$

where α is the angular acceleration and $I = MR^2 = 2\pi\rho htR^3$ is the moment of inertia of the solid. The stress exerted by the walls on the solid is

$$\sigma = \frac{\tau}{RA} = \frac{Ia}{AR^2}. \tag{7.15}$$

This may be re-written as

$$\sigma = \frac{2\pi\rho htR^3}{R^2(4\pi Rh)}\omega v = \frac{\rho t}{2}\omega v, \tag{7.16}$$

where ρ is the density of the solid, t is the width of the annular channel, ω is the frequency of oscillation, and v is its linear velocity. From the 910 Hz torsional oscillator of Reference [9] at 41 bar ($\rho \approx 160$ kg/m^3), which had an annular width

of 0.63 mm, we calculate $\sigma_t \sim 0.15$ Pa at their highest velocity, 520 μm/s.

7.3.6 Hysteresis

A recurring theme to this chapter is the comparison of our shear modulus anomaly $\Delta\mu$ to the NCRI fraction measured in torsional oscillator experiments. Continuing along these comparative lines, it is important to know that hysteretic behavior has been observed in torsional oscillator decoupling in a double resonance torsional oscillator operating at 496 and 1173 Hz [56]. (In fact, this hysteretic behaviour has also been observed in single resonance torsional oscillators [160].) A torsional oscillation is initiated with a relatively high drive level at 300 mK. While keeping the drive level constant, the torsional oscillator is then cooled down and held at 19 mK, where the rim velocity of the torsional oscillator becomes 610 μm/s. (The process is likened to a field cooled procedure in the studies of superconducting materials.) As the drive level is then decreased, the NCRI fraction increases and eventually attains the low velocity limit consistent with their previous measurements. When the drive level is subsequently increased, however, the measured NCRI fraction does not diminish; specifically, the NCRI fraction remains constant up to 610 μm/s. The authors concede that it is conceivable that the high NCRI fraction would decay to the low value at the highest rim velocity given enough time, but their estimated time constant for this is greater than 100 hours. As well, if the torsional oscillation is cooled down to 19 mK with low rim velocity near 10 μm/s (as in a nearly zero-field cooled process) and the drive level is subsequently increased, then the NCRI fraction again does not diminish. The observed history dependence of the NCRI fraction on the initial state set by the rim velocity at low temperature seems to be an important characteristics of the supersolid state.

Similarly, the observed behaviour in μ is reversible at temperatures above about 100 mK and at lower drive amplitudes where there is no amplitude dependence (as shown in Figures 7.16, 7.17, 7.18, and 7.19). Figures 7.20 and 7.21 demonstrate this behaviour for sample 300ppm33.3. To be explicit, Figures 7.20 and 7.21 plot data from a completely separate measurement and are not simply the 17 and 100 mK data from Figures 7.16 through 7.19.

The lower curves in Figure 7.20 (circles) show the magnitude of μ at 2000 Hz and 100 mK, as a function of strain. The shear modulus increases as the strain is decreased from above 1 x 10^{-6} down to almost 1 x 10^{-9} (•), and then reversibly

decreases as the strain is once again increased (○). The finite slope of these curves is consistent with Figure 7.16 which shows that, at 100 mK, the magnitude of the shear modulus increases with decreasing strain. However, they also show that, at 100 mK, the magnitude of the shear anomaly is constant at strains equal to or less than $\epsilon = 2.2 \times 10^{-8}$, which is inconsistent with what we measure at the lowest strains in Figure 7.20 (i.e., the $\epsilon = 2.2 \times 10^{-9}$ data point). Unfortunately, this discrepancy cannot be explained. (A liquid background was subtracted from this data but with the assumption that it was independent of temperature and scaled perfectly with drive voltage. These assumptions might not hold and could possibly be the source of the slight upturn in the data at the lowest strains in Figure 7.20, as well as in the following Figures 7.21, 7.22, and 7.23.)

After having taken this measurement, the sample was cooled to the base temperature of the dilution fridge while driving at high strain ($\epsilon = 1.7 \times 10^{-6}$) at 2000 Hz.

The upper curves in Figure 7.20 (squares) show the resultant magnitude of the anomaly at 2000 Hz and 17 mK, as a function of strain. When the sample has been cooled at high amplitude and the drive is then reduced at low temperature from strains above 1×10^{-6} down to almost 1×10^{-9} (■), μ increases. The general shape of this curve at is expected from Figure 7.16 for reasons similar to those outlined above. However, they also show that, at 17 mK, the magnitude of the shear anomaly is constant at strains equal to or less than $\epsilon = 2.2 \times 10^{-8}$, which is inconsistent with what we measure at the lowest strains in Figure 7.20 (i.e., again, the $\epsilon = 2.2 \times 10^{-9}$ data point). As before, this discrepancy cannot be explained.

Alternatively, we could say that the anomaly increases with decreasing strain. Explicitly, the anomaly is (roughly) the difference between the 100 mK (circles) and 17 mK (squares) shear modulus, and is the analog of the torsional oscillator NCRI. This is as expected from Figure 7.16 which shows that the magnitude of the anomaly increase with decreasing strain. There is no discrepancy here, as both Figures 7.16 and 7.20 show that the shear modulus anomaly is constant at strains equal to or less than $\epsilon = 2.2 \times 10^{-8}$.

When the drive is then increased at 17 mK from strains of almost 1×10^{-9} to above 1×10^{-6} (□), μ does not decrease (with the exception, again, of the $\epsilon = 2.2 \times 10^{-9}$ data point). In terms of the shear modulus anomaly $\Delta\mu$, it does not decrease at all as the strain is increased. In fact, the 17 mK shear modulus anomaly $\Delta\mu$ actually increases slightly as the strain is increased beyond $\epsilon = 2.2 \times 10^{-8}$. The

reason for this could be one of equilibration times for the curves measured in Figure 7.16; for example, a slower cooling ramp might have resulted in a steeper curve and a greater value for the shear modulus μ at 100 mK.

These slight discrepancies aside, it is clear that the low temperature behaviour of the shear modulus μ is hysteretic. The region at which this hysteretic behaviour begins (e.g., a "critical strain" ϵ_c) is highlighted by the grey region in Figure 7.20, spanning the strains $\epsilon = (2 - 7) \times 10^{-8}$, consistent with the range $\epsilon = (4 - 5) \times 10^{-8}$ determined in Figure 7.19.

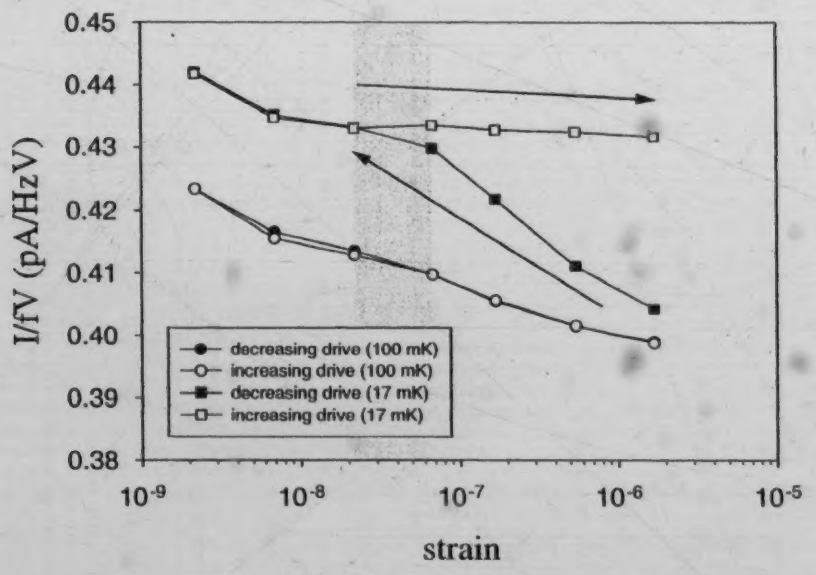

Figure 7.20: Behaviour of the shear modulus anomaly at 2000 Hz, cooled at high drive, as a function of decreasing and then increasing strain in sample 300ppm33.3. The behaviour is not reversible at 17 mK. The shaded region highlights the inferred "critical strain" ϵ_c.

Figure 7.21 is meant to show how the behaviour of the shear modulus μ changes after the sample has been cooled at low drive, rather than at high drive as in Figure 7.20.

The lower curves in Figure 7.21 (circles) show the magnitude of μ at 2000 Hz

and 100 mK, as a function of strain. The shear modulus is measured as the strain is increased from almost 1 x 10^{-9} up to above 1 x 10^{-6} (○), and then back down again (●) - essentially the same data as the lower curve in Figure 7.20, as the behaviour is reversible. The sample is then cooled to the base temperature of the dilution fridge while under low strain (ϵ = 2.2 x 10^{-9}) at 2000 Hz.

The upper curves in Figure 7.21 (squares) show the resultant magnitude of the anomaly at 2000 Hz and 17 mK, as a function of strain. When the sample has been cooled at low amplitude and the drive is then increased at low temperature from strains of almost 1 x 10^{-9} to above 1 x 10^{-6} (□), the anomaly behaves essentially as it did in Figure 7.20. The one difference appears at the highest strain ϵ = 1.7 x 10^{-6}, where the magnitude of the shear modulus anomaly does decreases slightly. When the strain is subsequently reduced (■), a small hysteresis loop is formed. We expected to observe identical behaviour as that shown in Figure 7.20, and the reason for this slight decrease in the shear modulus anomaly at this highest strain is unknown. Perhaps the dilution refrigerator was accidentally bumped at this measurement, an event that we know can cause significant shifts in the data. We believe that had we stopped increasing the strain at ϵ = 5.4 x 10^{-7}, the behaviour would have been completely reversible. So, while a small hysteresis loop does exist in this data set, we describe this behaviour as reversible.

Figures 7.22 and 7.23 show the same sort of measurement as in Figures 7.20 and 7.21 on a solid ^{4}He sample with 50 ppb ^{3}He impurity concentration, which came off the melting curve at 33.1 bar (sample 050ppb33.1, not annealed before these measurements were taken). They are intended to show the same reversible behaviour at higher temperature (150 mK), the same hysteretic behaviour at low temperature (20 mK) when the sample has been cooled at high drive amplitude, and the same reversible behaviour at low temperature (20 mK) when the sample has been cooled at low drive amplitude.

Figure 7.22 shows the same increase in μ at the lowest strains at 150 mK and the same hysteresis at 20 mK at higher strains, as in Figure 7.20. The region at which this hysteretic behaviour begins (e.g., the "critical strain" ϵ_c) is highlighted by the grey region in Figure 7.22, spanning the strains ϵ = (3 - 5) x 10^{-8}, consistent with our previous measures of this variable. There is also an increase in μ at the lowest strains which (again) cannot be explained.

Figure 7.23 shows reversible behaviour in the shear modulus at 150 mK and at

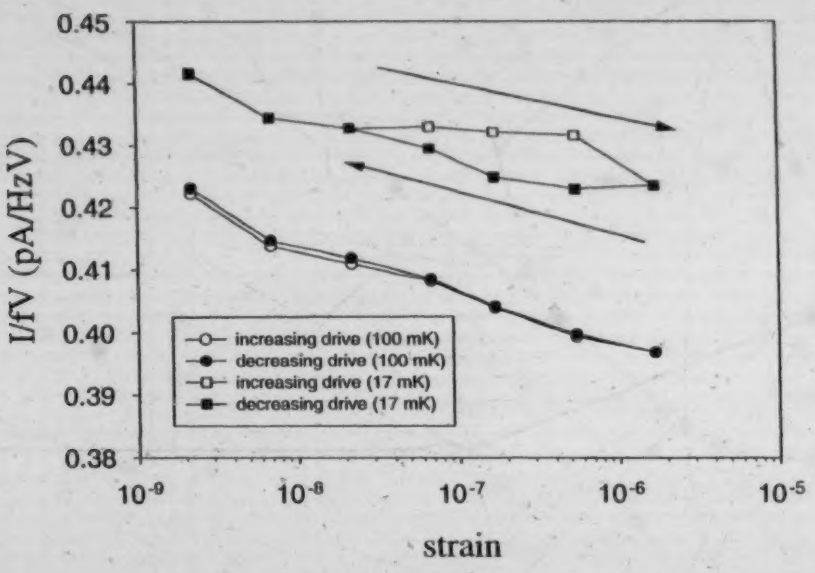

Figure 7.21: Behaviour of the shear modulus anomaly at 2000 Hz, cooled at low drive, as a function of increasing and then decreasing strain in sample 300ppm33.3. The behaviour is almost reversible at 17 mK.

20 mK, nearly identical to what was observed in Figure 7.21.

Returning now to the comparison of the shear modulus anomaly $\Delta\mu$ in our experiments to the NCRI in the torsional oscillator experiments, the reduction in the NCRI fraction as the drive level is increased was observed to be the same for both 496 and 1173 Hz when plotted as a function of cell rim velocity [56]. When the NCRI fraction is plotted against displacement amplitude or acceleration, the reduction does not coincide in the two modes. The authors take this observation as a demonstration that it is velocity, not displacement amplitude (strain) nor acceleration (stress) applied to the solid, that best parameterizes the reduction in the NCRI fraction. This contrasts our observation, as explained above, that $\Delta\mu$ scales with either stress or strain but not with velocity. It is not clear why these two observations seemingly contradict each other, but it must be kept in mind that fundamentally different properties are being studied. These torsional oscillator experiments probe inertial effects, while our shear experiments probe elastic effects.

Finally, the torsional oscillator experiments reveal no history dependence at 63 mK; the measured NCRI fraction does not depend on how the initial state is

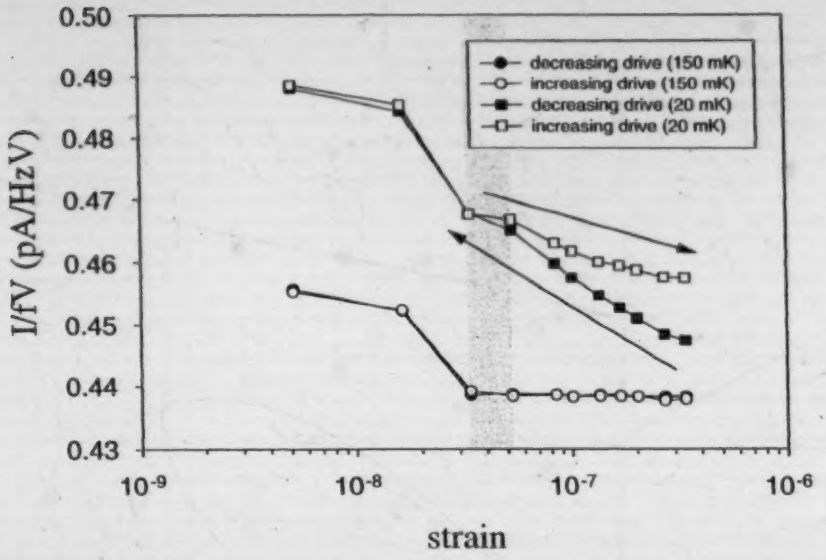

Figure 7.22: Behaviour of the shear modulus anomaly at 2000 Hz, cooled at high drive, as a function of decreasing and then increasing strain in sample 300ppm33.1. The behaviour is not reversible at 17 mK. The shaded region highlights the inferred "critical strain" ϵ_c.

reached [56]. The border between the history dependent low temperature behavior and the reversible higher temperature behavior appears to be around 40 mK, close to the temperature where the NCRI fraction begins to decrease. This is consistent with our observation that the behaviour of the anomaly as a function of strain is reversible at 100 mK but not at 17 mK in sample 300ppb33.3, and at 150 mK but not at 20 mK in sample 050ppb33.1.

7.4 Acoustic resonance in cell

The essential result of the experiments described above is the observation of a large anomalous increase in μ with the same temperature dependence as the decoupling in torsional oscillators. This effect was confirmed by simultaneously measuring the frequency f_r and damping $1/Q$ of an acoustic resonance in the cell.

A quick estimate (Equation 7.17) tells us that we should expect to observe a resonance in our shear cell around a frequency

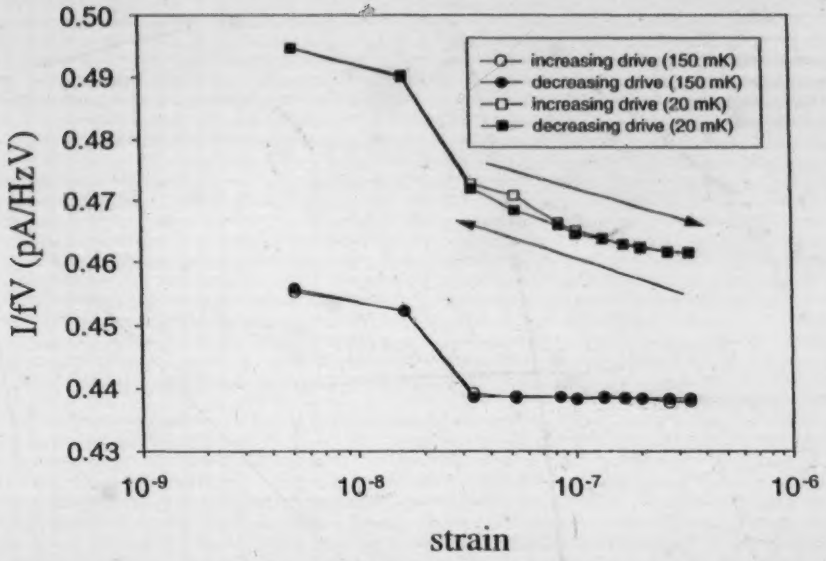

Figure 7.23: Behaviour of the shear modulus anomaly at 2000 Hz, cooled at low drive, as a function of increasing and then decreasing strain in sample 300ppm33.1. The behaviour is almost reversible at 17 mK.

$$f_r = \frac{v_{shear}}{2L}, \tag{7.17}$$

where v_{shear} is the speed of shear sound in the solid and L is the smallest relevant cell dimension. Taking the speed of shear sound in solid ^{4}He to be $\sim$ 300 m/s and the characteristic length in our shear cell to be $\sim$ 2 cm (its diameter), we predict an acoustic resonance in the shear cell near 7500 Hz. Note that this is a resonance of the helium in the whole cell and not in the gap between the piezoelectric transducers.

Computer modelling was also initiated to confirm that we should expect to find an acoustic resonance in our shear cell. Specifically, an eigenfrequency analysis of the bulk solid ^{4}He within the cell was done using a 3-D solid, stress-strain structural mechanics module within the COMSOL Multiphysics [152] simulation environment. This was done using a realistic model of the cell's internal geometry. Preliminary models predicted an acoustic resonance in the cell around 10 kHz.

7.4.1 Acoustic resonance peak position

Measurements of the low temperature (18 mK) frequency f_r and damping 1/Q of the acoustic resonance in the cell were made at drive voltages ranging from 2 μV_{peak} to 1.4 V_{peak}, with the purpose of determining a drive amplitude independent regime. For example, we discovered early on that the position of the acoustic resonance shifted to lower frequencies at higher drive amplitudes. We also noted that the shape of the acoustic resonance was asymmetric at higher drive amplitudes and that the asymmetry was a function of the direction of the frequency sweep. To best characterize the behaviour of this acoustic resonance solely as a function of temperature, we need to eliminate the effects of these other variables. So, to ensure that the acoustic resonance was measured in a drive amplitude independent regime, its amplitude and position were studied at low temperature, as a function of drive amplitude.

Figure 7.24 shows the behaviour of the acoustic resonance as a function of drive voltage in an annealed sample of isotopically pure ^{4}He (i.e., nominally 1 ppb ^{3}He isotopic impurity concentration) that solidified at 33.4 bar, hereafter referred to as sample 001ppb33.4. The data of Figure 7.24 is re-plotted (in three sets per figure) in Figures 7.25, 7.26, 7.27, 7.28, 7.29 for greater clarity. For each of the following figures, the lowest drive amplitude displayed on one is the highest drive amplitude displayed on the next. As well, each of these data sets was measured as the frequency of the drive was increased.

It is clear from Figures 7.24 through 7.29 that, for drive amplitudes greater than $\sim$ 50 μV, the position of the resonance is a function of drive amplitude. It is natural to suppose that the shift in f_r is a result of our sample heating, but a quick estimate of the power would suggest otherwise. Equations 7.3 and 7.8 allow us to calculate the capacitance of the PZT transducer. As the manufacturer quotes $d_{15} = 585 \times 10^{-12}$ m/V and $g_{15} = 38.2 \times 10^{-3}$ Vm/N, the capacitance of the PZT is $C_{PZT} \approx 7.3 \times 10^{-10}$ F. So, it has an impedance $Z = 1/\omega C \approx 28$ kΩ at 7900 Hz. Now, as an example, consider the 34.6 mV drive of Figure 7.26 - the dissipation must be (considerably) less than $P = V^2/Z = 4.3 \times 10^{-8}$ W. It seems very unlikely that such a small heat input could shift f_r by more than 125 Hz in frequency space.

Figures 7.24 through 7.29 further demonstrate that, for drive amplitudes greater than $\sim$ 50 μV, the symmetry of the acoustic resonance is governed by the drive

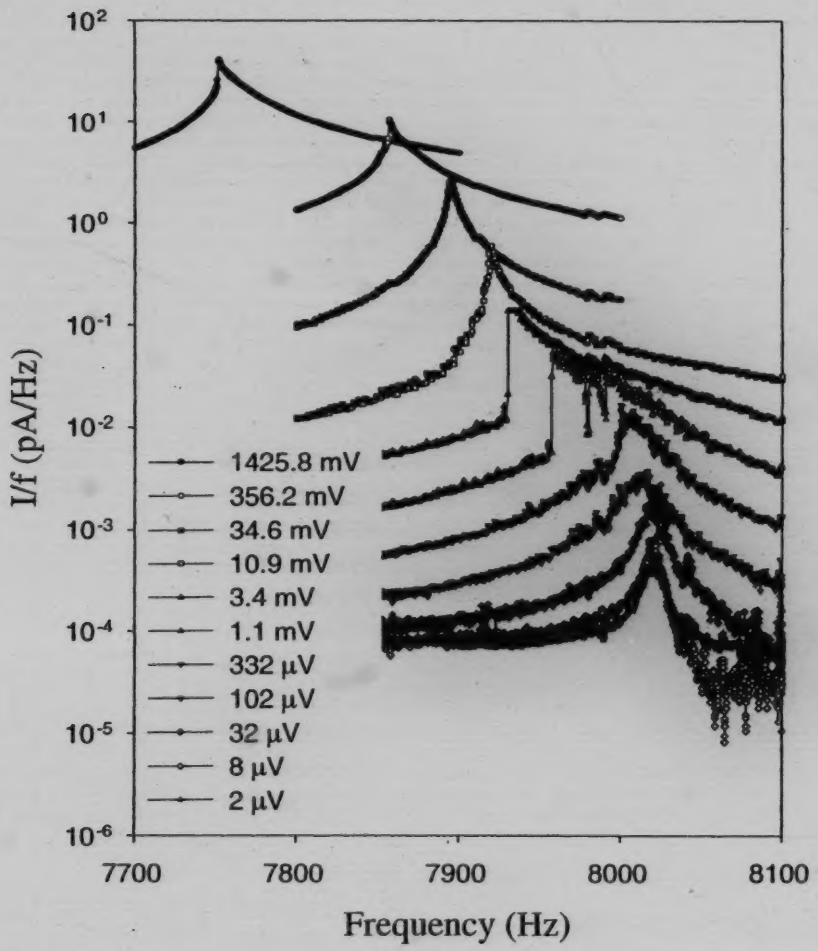

Figure 7.24: Behaviour of the resonance peak at 18 mK, as a function of drive amplitude.

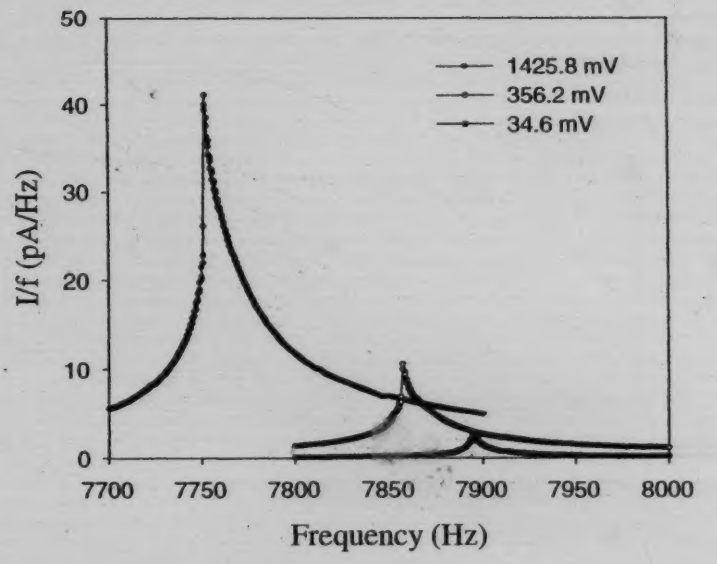

Figure 7.25: Behaviour of the resonance peak at 18 mK, at a drive amplitude of 1425.8 mV, 356.2 mV, and 34.6 mV.

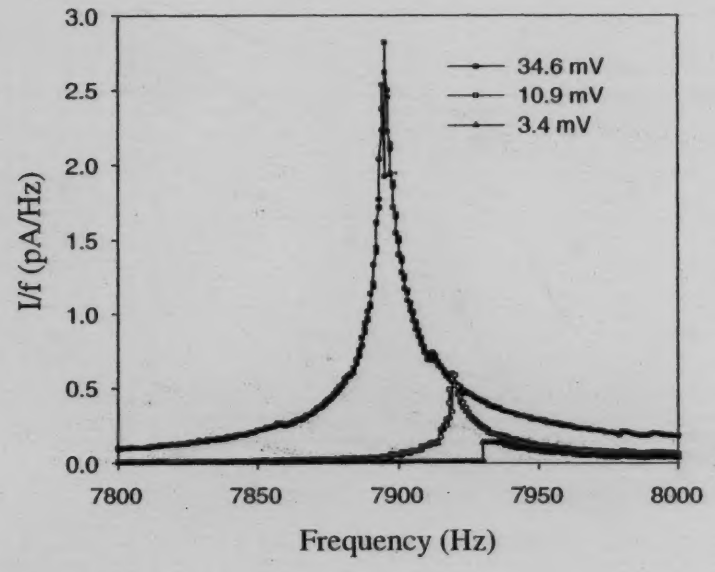

Figure 7.26: Behaviour of the resonance peak at 18 mK, at a drive amplitude of 34.6 mV, 10.9 mV, and 3.4 mV.

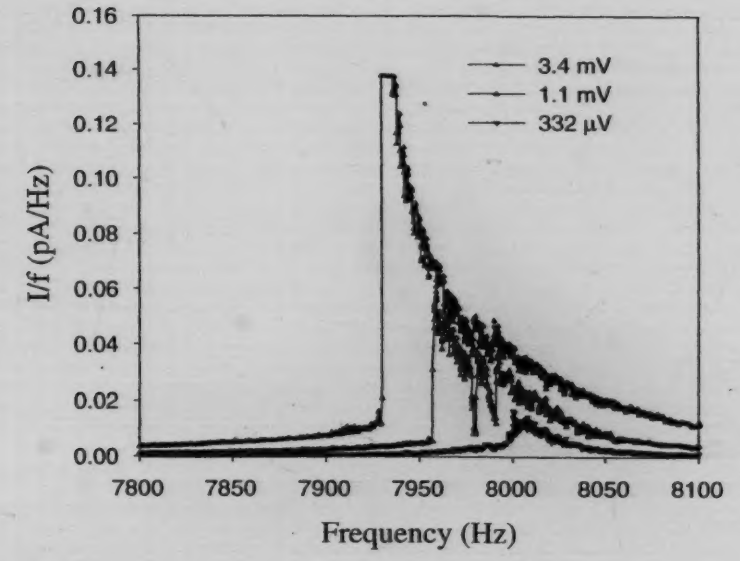

Figure 7.27: Behaviour of the resonance peak at 18 mK, at a drive amplitude of 3.4 mV, 1.1 mV, and 332 μV.

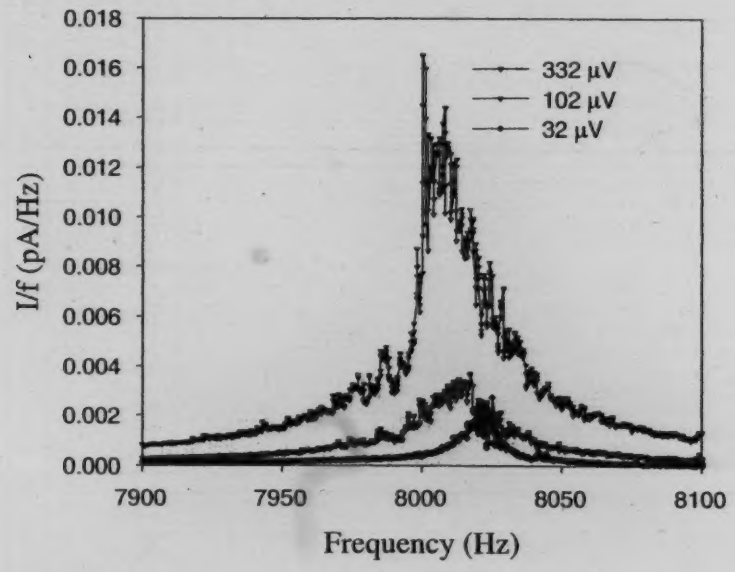

Figure 7.28: Behaviour of the resonance peak at 18 mK, at a drive amplitude of 332 μV, 102 μV, and 32 μV.

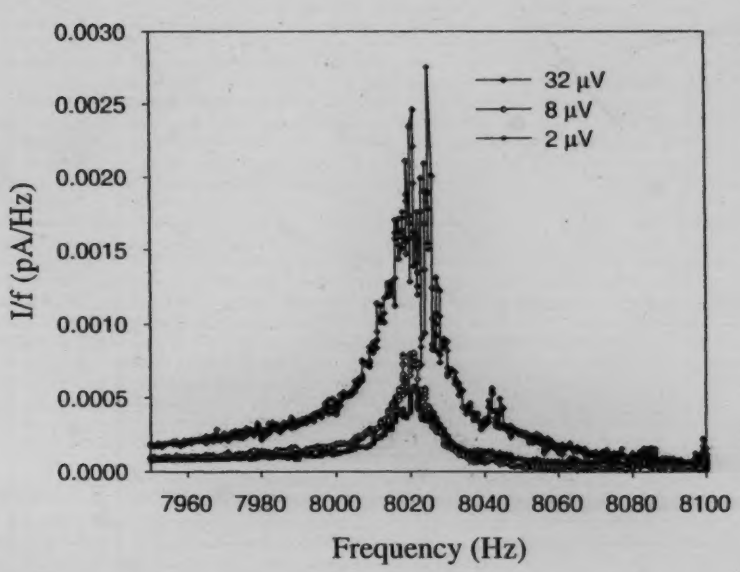

Figure 7.29: Behaviour of the resonance peak at 18 mK, at a drive amplitude of 32 μV, 8 μV, and 2 μV.

amplitude. More specifically, we observe that our acoustic resonance behaves as a nonlinear oscillator, displaying bi-stability and hysteresis for sufficiently strong driving amplitudes. That is, the nonlinear oscillator (the acoustic resonance) oscillates either with a large amplitude or a small amplitude - this behaviour is most apparent in Figure 7.27.

While certainly interesting in its own right, the nonlinearity of the acoustic resonance was beyond the scope of this experimental investigation and was therefore not studied in great detail. In fact, the nonlinearity of the acoustic resonance of sample 01ppb33.4 was not studied at all; however, a few days worth of time were spent observing the nonlinear character of the acoustic resonance in sample 300ppb29.3. Figure 7.30 shows the bi-stable and hysteretic nature of the acoustic resonance in sample 300ppb29.3 at 126 mV drive and 50 mK. The curve labelled "increasing frequency" in Figure 7.30 is comparable to the curve labelled "356.2 mV" in Figure 7.25 (i.e., they are of similar drive amplitude and were both taken as the frequency was increased).

Figure 7.31 shows a decreased bi-stable and hysteretic nature of the same acous-

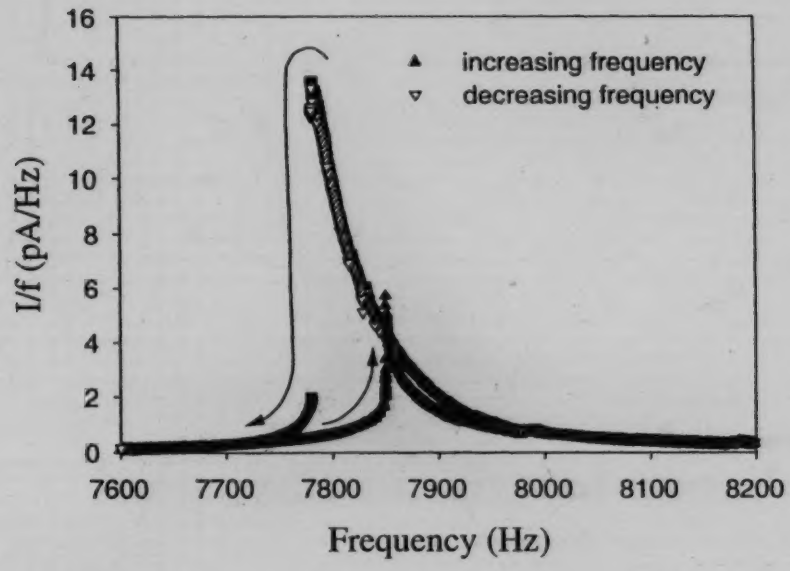

Figure 7.30: Hysteretic behaviour of the acoustic resonance at 126 mV drive amplitude and 50 mK, in sample 300ppb29.3.

tic resonance (in sample 300ppb29.3) at 760 μV drive and 50 mK. The curve labelled "increasing frequency" in Figure 7.31 is comparable to the curve labelled "1.1 mV" in Figure 7.27 (i.e., they are of similar drive amplitude and were both taken as the frequency was increased).

Figure 7.32 shows an absence of bi-stability and hysteresis of the same acoustic resonance (in sample 300ppb29.3) at 22 μV drive and 50 mK. The curve labelled "increasing frequency" in Figure 7.32 is comparable to the curve labelled "32 μV" in Figure 7.29 (i.e., they are of similar drive amplitude and were both taken as the frequency was increased).

Provided that the excitation is driven at an amplitude of less than about 50 μV, we observe no hysteresis in the acoustic resonance. Also at sufficiently low excitation, we observe that f_r and Q are independent of the drive amplitude, as shown in Figure 7.33.

With this knowledge in mind, our subsequent study of the temperature dependence of the acoustic resonance was performed at a driving amplitude of 32 μV (i.e., in the amplitude independent regime). All future plots of acoustic resonances, peak positions, Q's (or 1/Q's), etc., are in this low amplitude regime (where they are

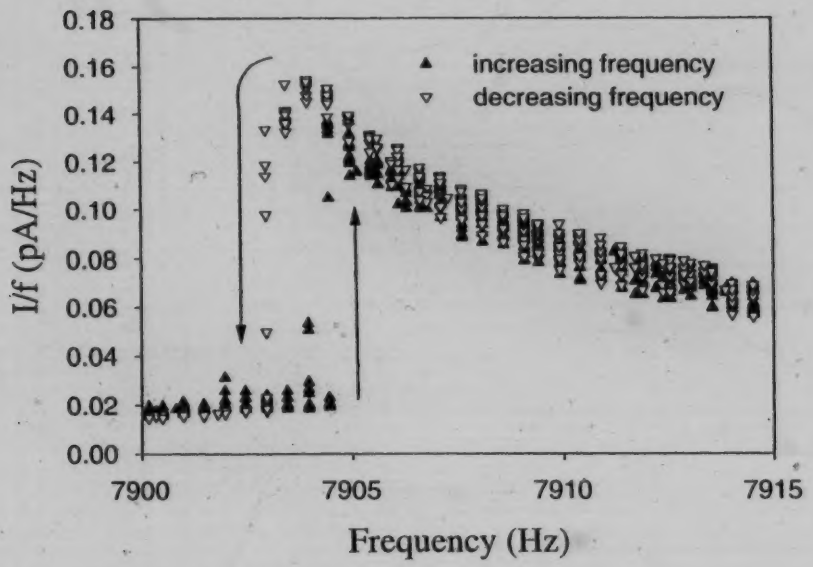

Figure 7.31: Hysteretic behaviour of the acoustic resonance at 760 μV drive amplitude and 50 mK, in sample 300ppb29.3.

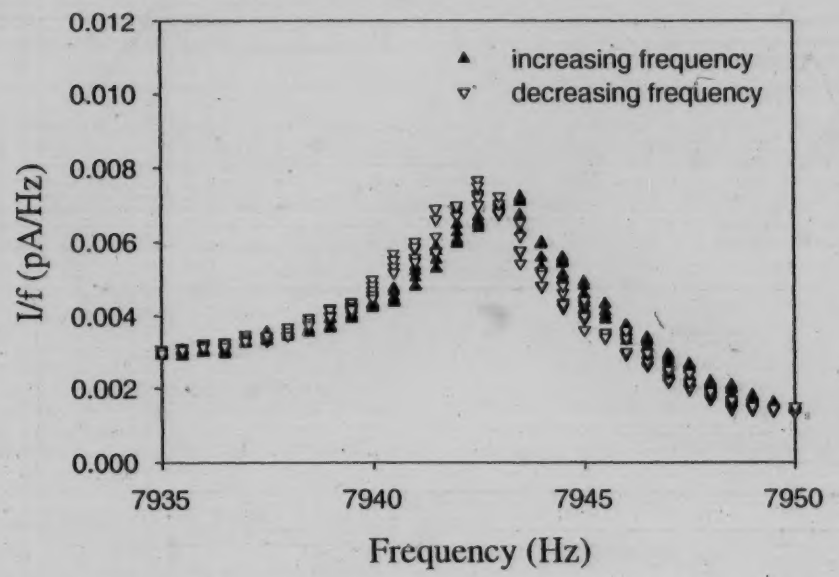

Figure 7.32: Non-hysteretic behaviour of the acoustic resonance at 22 μV drive amplitude and 50 mK, in sample 300ppb29.3.

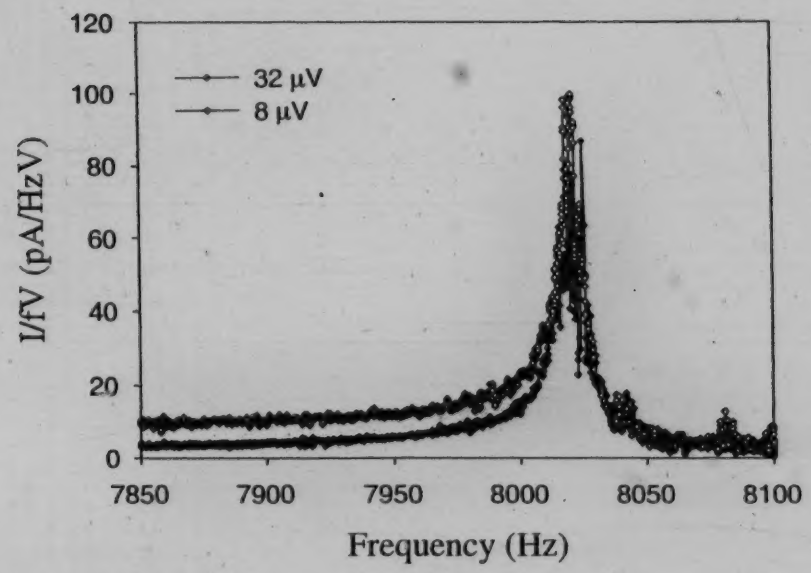

Figure 7.33: Acoustic resonance in sample 001ppb33.4 at 18 mK, scaled by its low drive amplitude.

independent of drive amplitude).

7.4.1.1 Sample 300ppb33.3

This sample is presented first because its acoustic resonance was studied in the greatest detail. Figure 7.34 shows the acoustic resonance in sample 300ppb33.3 at 300 mK (refer back to the thermodynamic path on the phase diagram of Figure 7.13). Recall that sample 300ppb33.3 had been annealed before these measurements were taken.

The resonance frequency f_r of this peak is (7782 ± 2) Hz. The amplitude of this peak is (0.00106 ± 0.00001) pA/Hz. Both of these measures are shown in Figure 7.34 (for clarity and here only). No liquid/background subtractions were made in the analysis of these acoustic resonance peaks, as the effect was on the order of 0.2% of the total signal. We can also assign a quality factor Q to this resonance peak. Physically speaking, Q is 2π times the ratio of the total energy stored divided by the energy lost in a single cycle. Equivalently (and for sufficiently large values of Q, such as in the torsional oscillator experiments), the quality factor is approximately the number of oscillations required for a freely oscillating system's

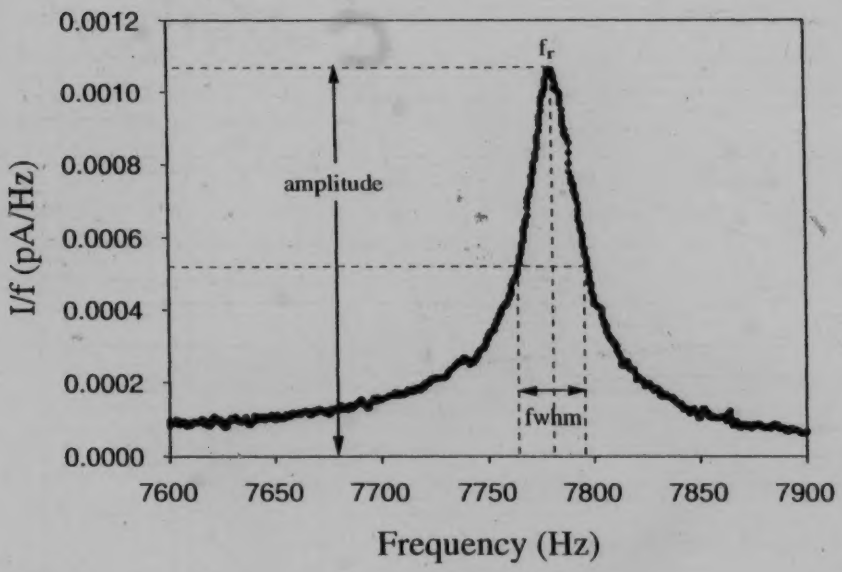

Figure 7.34: Acoustic resonance in sample 300ppb33.3 at 300 mK.

energy to fall off to $1/e^{2\pi}$ of its original energy. When the system is driven by a sinusoidal drive, its resonant behavior depends strongly on Q. Resonant systems respond to frequencies close to their natural frequency much more strongly than they respond to other frequencies. A system with a high Q resonates with a greater amplitude at the resonant frequency than one with a low Q factor, and its response falls off more rapidly as the frequency moves away from resonance. The width of the resonance is given by $\Delta f = f_r/Q$, where Δf, the bandwidth, is the width of the range of frequencies for which the energy is at least half its peak value (the full width at half-maximum). The peak shown in Figure 7.34 has a Q of ~ 250. The dissipation of the peak is defined as $1/Q$.

It should be stated that the peak f_r, amplitude, and Q were all determined manually (i.e., by eye and not by a computer peak fitting algorithm). Of course, a computer program could also be used to determine these values. Figure 7.35 shows the same data as plotted in Figure 7.34, along with a simple 4-parameter Lorentzian curve, fitted by SigmaPlot, to that same data. The equation used to fit the data is

$$y = y_0 + \frac{a}{1 + (\frac{x - x_0}{b})^2}, \tag{7.18}$$

where y_0 is a vertical offset, a is the peak amplitude, b is the full width of the peak at its half maximum, and x_0 is the resonant frequency f_r. For the fit in Figure 7.35, the resonance frequency f_r is 7780 Hz, the peak amplitude is 0.00103 pA/Hz, and the half width of the curve at half its maximum is 16 Hz, implying Q = 243. So, there is no discrepancy between the values determined by eye and those determined via a fitting program. Of course, this is a relatively "clean" peak - estimates become more difficult as the shape of the peak is distorted (as will be discussed momentarily). Still, the analysis presented here is largely qualitative in nature and the values determined by eye will suffice for our purposes.

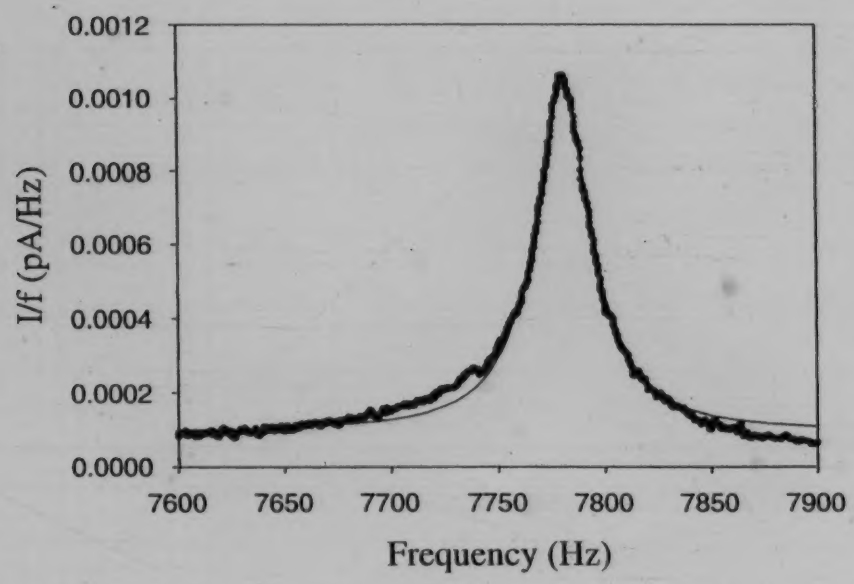

Figure 7.35: Acoustic resonance in sample 300ppb33.3 at 300 mK, with an overlaid Lorentzian fit.

Figure 7.36 shows the same acoustic resonance in the shear cell for sample

300ppb33.3 at 18 mK.

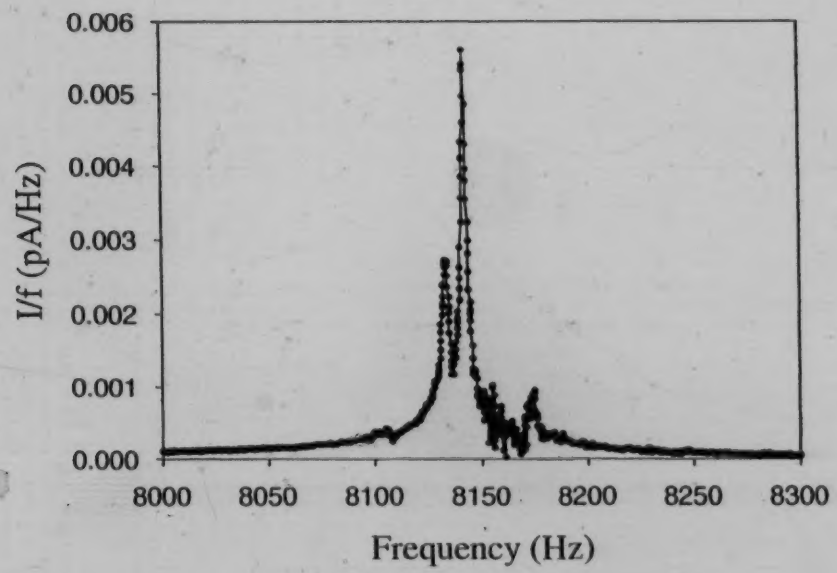

Figure 7.36: Acoustic resonance in sample 300ppb33.3 at 18 mK.

The resonance frequency f_r of this peak is (8141 $\pm$ 3) Hz. The amplitude is much more difficult to determine because of a destructive interference very near to the resonance frequency, resulting in what looks to be a double-peak. The interference likely arises from the background signal of the cell; referring back to Figure 7.5, there are a handful of smaller resonances that exist in the 8100-8200 Hz neighborhood. In principle, this background could be subtracted from our signal, but the effort is not worth the payoff (as I will soon argue). It is possible to estimate the amplitude by manually (e.g., by eye) removing the effect of the interference. Figure 7.37 demonstrates what is intended by this admittedly crude technique, where the dashed lines guide the eye along the shape of roughly where the peak (alone) sits. Using this method, the amplitude is (0.014 $\pm$ 0.002) pA/Hz, and the Q is $\sim$ 2000.

Again, we can use a computer program to fit a curve to this data. Figure 7.38 shows the same data as plotted in Figure 7.36 (minus the range which contained the

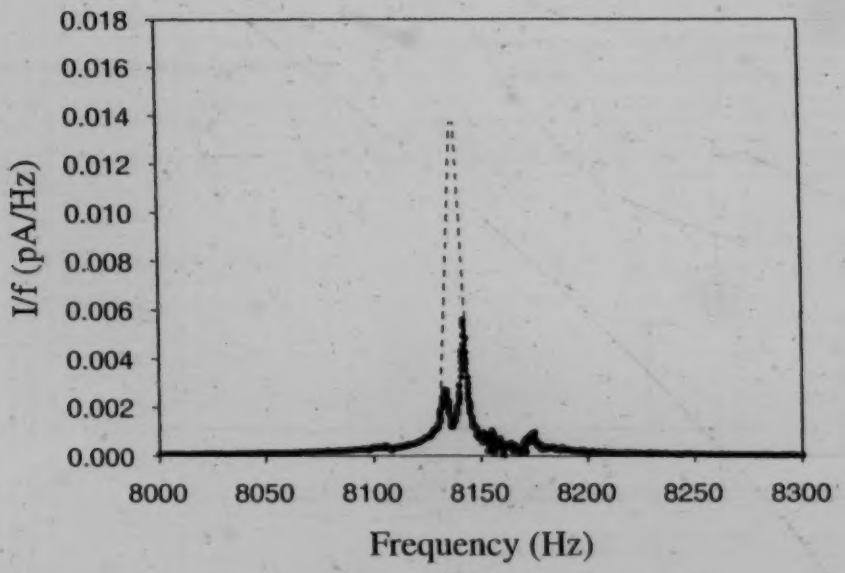

Figure 7.37: Acoustic resonance in sample 300ppb33.3 at 18 mK with a rough estimate of the true shape of the peak.

interference), along with the 4-parameter Lorentzian curve, fitted by SigmaPlot, to that same data. For the fit in Figure 7.38, the resonance frequency f_r is 8138 Hz, the peak amplitude is 0.016 pA/Hz, and the half width of the curve at half its maximum is 3 Hz, implying Q = 1356. There is very little difference between the values determined by eye and those determined via the fitting program, even though we aren't dealing with a "clean" peak.

As stated above, we will be using the values determined by eye and not those determined by a fitting program. Those extracted by eye are less time consuming to determine and, more important, our analysis is fairly insensitive to the small differences that do exist between the two techniques. For example, we will be examining the temperature dependence of the peak position of the acoustic resonance (i.e., $f_r(T)$), and the difference f_r(300 mK) - f_r(18 mK) is two orders of magnitude greater than the error in any value of $f_r(T)$. Also, we will be studying the dissipation 1/Q ($\times 10^3$) of the acoustic resonance. While it is conceivable that values determined by eye and by fitting differ by as much as a factor of 2, it is unlikely; in any case, conservative error bars have been included for every dissipation data

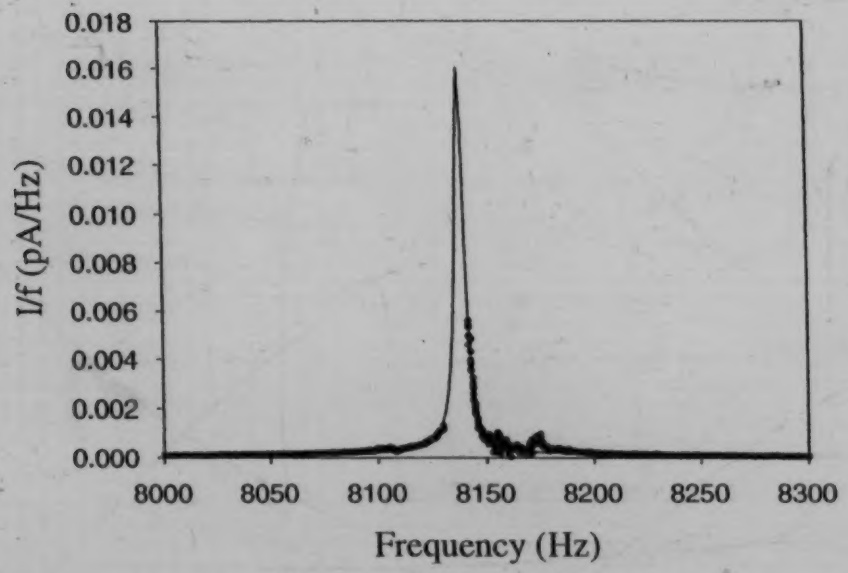

Figure 7.38: Acoustic resonance in sample 300ppb33.3 at 18 mK, with an overlaid Lorentzian fit.

point (and are largest when the peak is not "clean").

Figures 7.39 and 7.40 show how the resonance peak in sample 300ppb33.3 evolves as a function of temperature. Both plot the same data, but the latter has its temperature scale reversed.

Figure 7.41 plots the temperature dependence of the peak position of the acoustic resonance for sample 300ppb33.3 as a function of temperature. Comparing the temperature dependence of the resonance frequency f_r to that of the shear modulus μ, it is clear that the two measurements probe the same elastic changes.

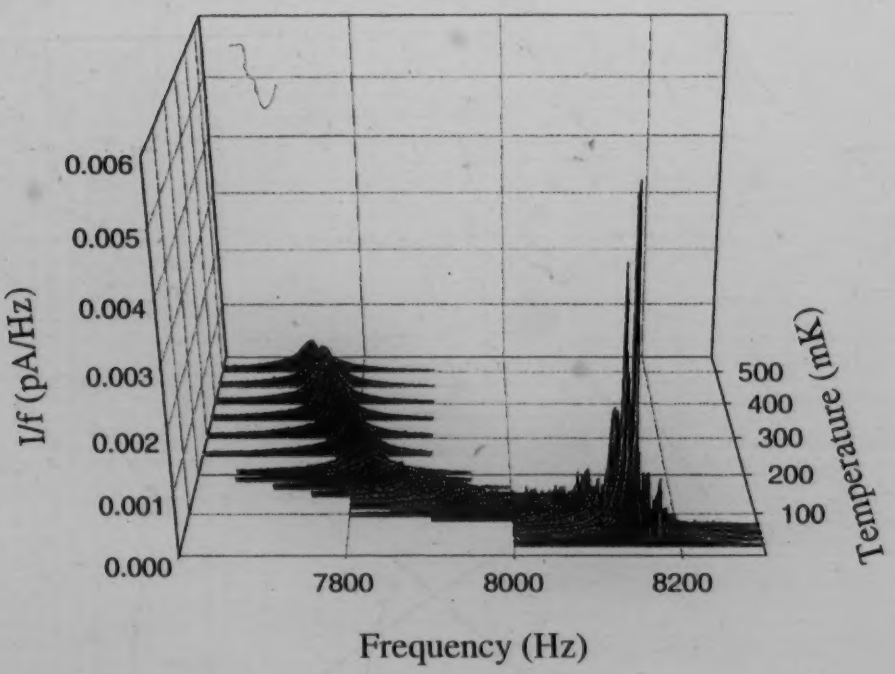

Figure 7.39: Acoustic resonance in sample 300ppb33.3 as a function of temperature (from the "front").

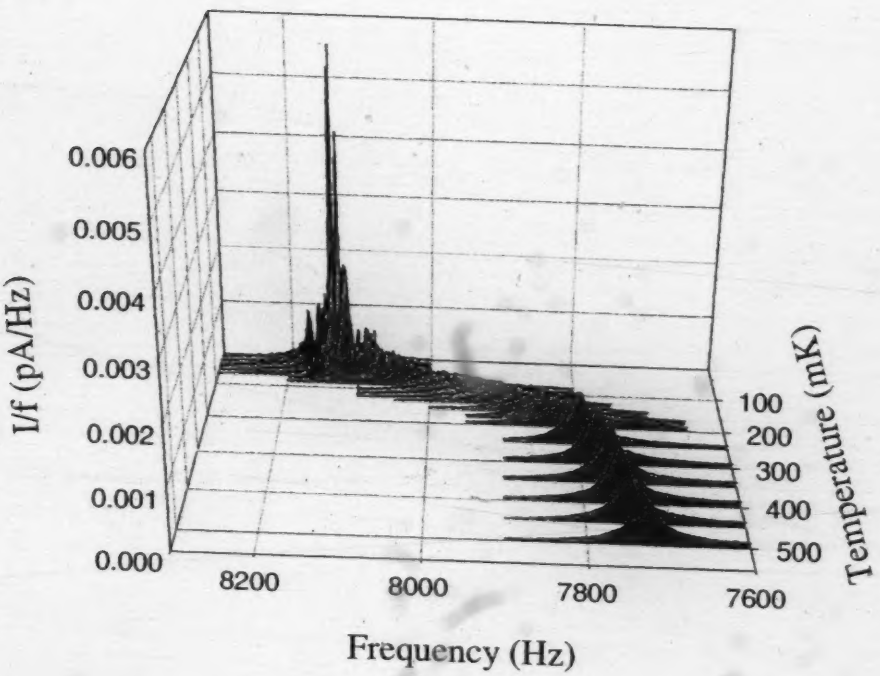

Figure 7.40: Acoustic resonance in sample 300ppb33.3 as a function of temperature (from the "back").

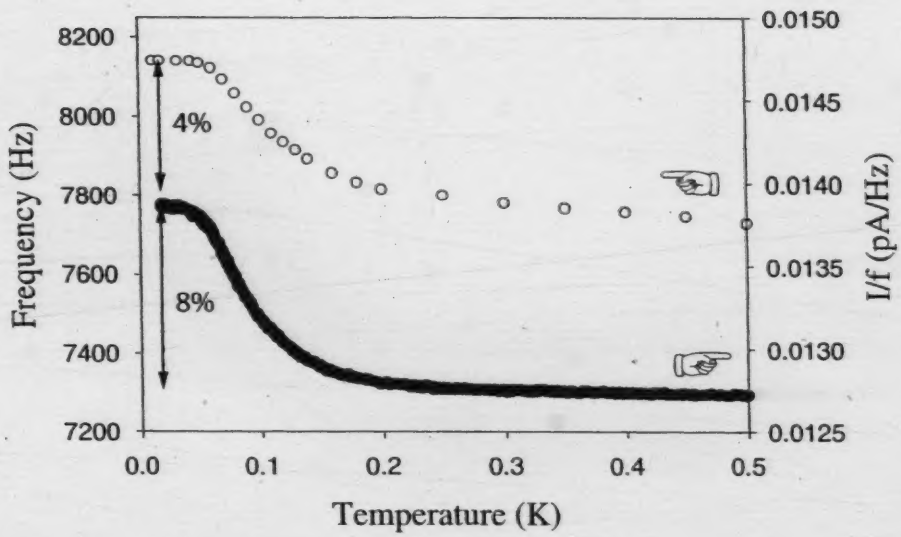

Figure 7.41: Peak position of the acoustic resonance in sample 300ppb33.3 as a function of temperature, compared to the associated shear modulus anomaly.

The changes in f_r ($\sim 4\%$) are about half as large as for μ ($\sim 8\%$), as expected since f_r varies with sound speed, as the square root of elastic moduli. As a brief aside, the computer modelling of the acoustic resonance in our cell was extended to calculate how the resonant frequency would shift given a 15% change in the shear modulus or bulk modulus of the solid ^{4}He. Table 7.1 summarizes the results of this simulation for the lowest mode, f_1. The modelling shows that f_r depends almost entirely on the shear modulus, and not the bulk modulus (otherwise, we would expect $\Delta f_r/f_r$ to be less than half of $\Delta\mu/\mu$).

Shear modulus (15.6 MPa)	Bulk Modulus (33.5 MPa)	Δf_1 (kHz)	% change
decreased 15%	fixed	-1.01	-6.4
increased 15%	fixed	+0.94	+5.9
fixed	decreased 15%	-0.22	-1.4
fixed	increased 15%	+0.20	+1.2

Table 7.1: Simulation response of the lowest resonant mode to changes in the shear and bulk modulus.

If supersolidity produces a decoupling of a supersolid fraction from the lattice which responds to shear deformation in acoustic resonances [27], we wouldn't expect our low frequency (essentially static) shear modulus measurements to agree with the acoustic resonance frequencies. (If some supersolid fraction decoupled, the sound speeds would increase even more than expected from the shear modulus increases. We wouldn't be able to separate out a $\sim 1\%$ effect due to decoupling from the $\sim 10\%$ modulus effect, but if the supersolid density were $\sim 50\%$ it would be obvious.)

The corresponding dissipation $1/Q$, shown in Figure 7.42, is largest near 140 mK, near where f_r is changing rapidly. The maximum dissipation consistently occurs at a temperature slightly above the inflection in the f_r curve (or the shear modulus μ curve). In torsional oscillator experiments, the dissipation peak typically occurs at a temperature slightly below the inflection in the NCRI fraction curve (which is analogous to our shear modulus μ curve). This may be due to their lower frequencies, which span from $\sim$ 185 Hz to $\sim$ 1500 Hz.

Figure 7.43 shows the change in dissipation versus the change in resonance frequency scaled by its low temperature value for the acoustic resonances of sample 300ppb33.3. For this sample, $\Delta(Q^{-1}) \approx 11 \times 10^{-3}$ is about a factor of five smaller

than its $\Delta f_r/f_r \approx 50 \times 10^{-3}$. A comparison of this type of measurement to torsional oscillator data is made toward the end of this section.

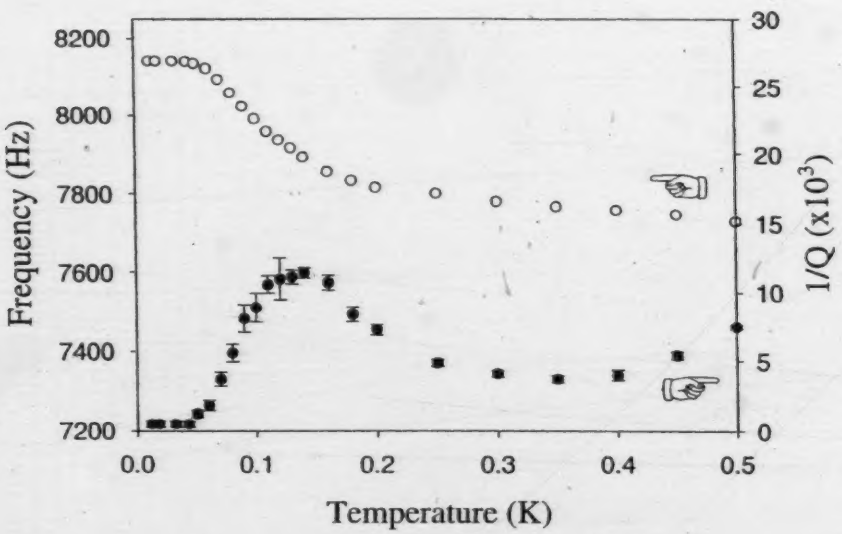

Figure 7.42: Dissipation in the acoustic resonance in sample 300ppb33.3 as a function of temperature, compared to its peak position.

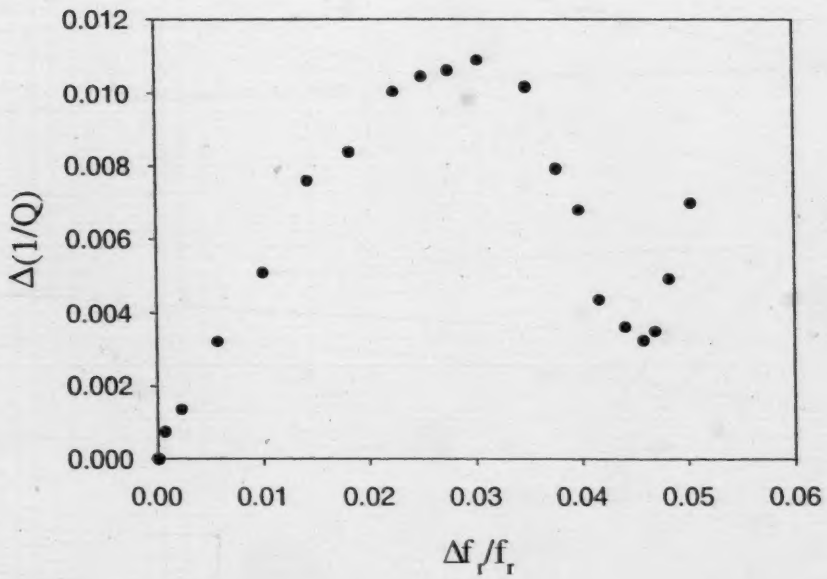

Figure 7.43: Change in dissipation of the acoustic resonance in sample 300ppb33.3 as a function of the scaled change in resonance frequency.

7.4.1.2 Sample 300ppb34.0

Figure 7.44 shows the acoustic resonance in sample 300ppb34.0 at 300 mK (refer back to the thermodynamic path on the phase diagram of Figure 7.11). Recall that sample 300ppb34.0 had been annealed before these measurements were taken. The data presented here is noisier than that of the previous section because it was collected without the current preamplifier (recall the block diagram of Figure 7.3).

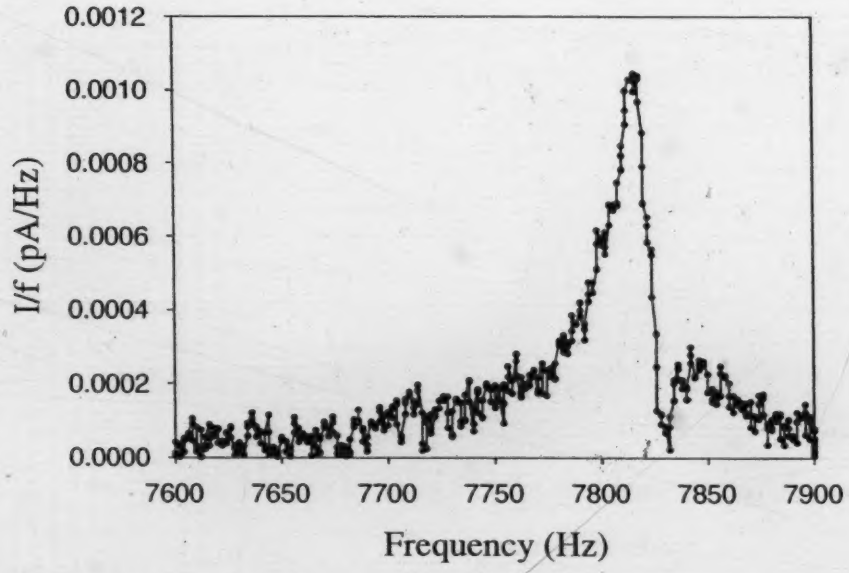

Figure 7.44: Acoustic resonance in sample 300ppb34.0 at 300 mK.

The resonance frequency f_r of this peak is (7816 ± 4) Hz; its amplitude is measured (0.00104 ± 0.00004) pA/Hz and it has a Q of ~ 300.

Figure 7.45 shows the acoustic resonance that we measure in the shear cell for the sample 300ppb34.0 at 33 mK.

The resonance frequency f_r of this peak is (8148 ± 5) Hz; its amplitude is (0.0027 ± 0.0004) pA/Hz and it has a Q of ~ 800. As explained above, these values have been determined by eye, without the aid of a fitting algorithm. For the reader who remains unconvinced that this technique will suffice, we again use

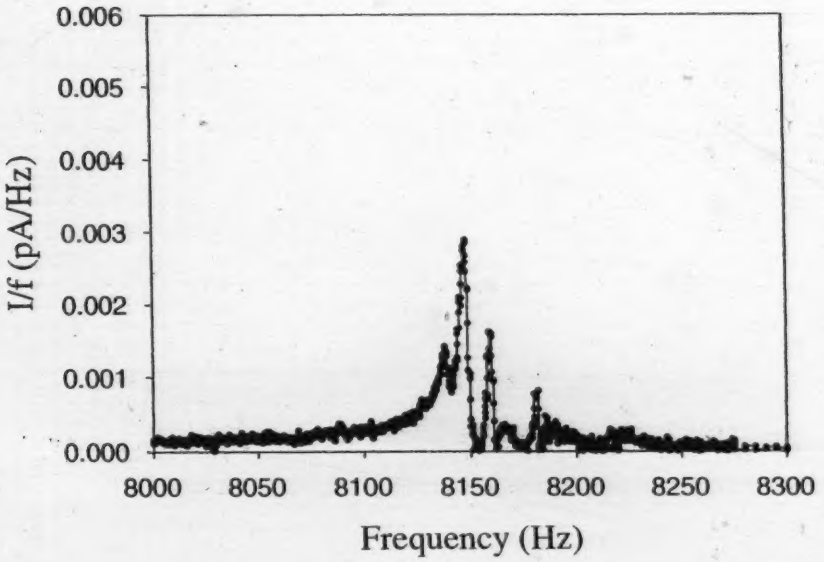

Figure 7.45: Acoustic resonance in sample 300ppb34.0 at 33 mK.

a computer program to fit a curve to this data. Figure 7.46 shows the same data as plotted in Figure 7.45 (minus the range which contained the interference), along with the 4-parameter Lorentzian curve, fitted by SigmaPlot, to that same data. For the fit in Figure 7.46, the resonance frequency f_r is 8153 Hz, the peak amplitude is 0.032 pA/Hz, and the half width of the curve at half its maximum is 10 Hz, implying Q = 408. As before, there is very little difference between the values determined by eye and those determined via the fitting program, even though we aren't dealing with a "clean" peak. As a reminder, conservative error bars have been included for the dissipation data.

Figures 7.47 and 7.48 show how the resonance peak in sample 300ppb34.0 evolves as a function of temperature. Both plot the same data, but the latter has its temperature scale reversed. As was the case in the previous sample, the peak shifts to higher frequency with decreasing temperature, experiencing a maximum in dissipation near where it moves through frequency space most quickly.

Figure 7.49 plots the resonance frequency for sample 300ppb34.0 as a function of temperature. Comparing the temperature dependence of the resonance frequency f_r to that of the shear modulus μ, it is again clear that the two measurements probe

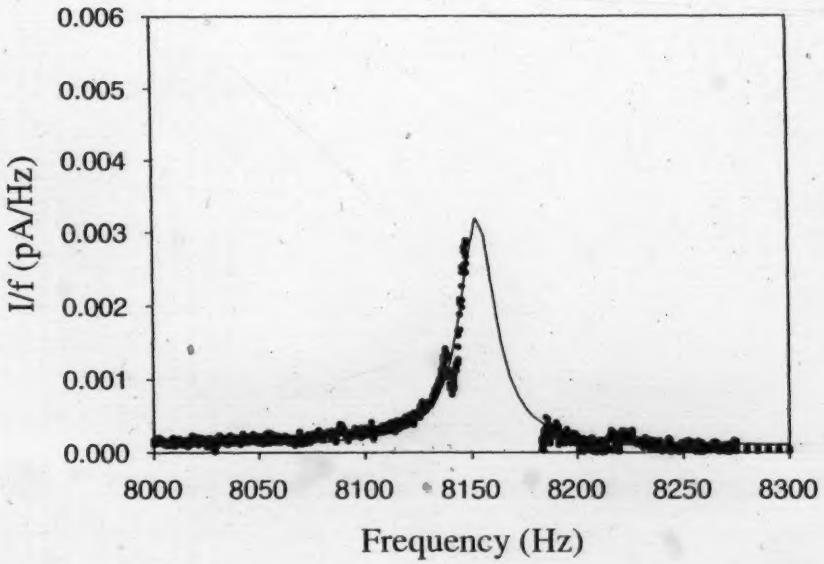

Figure 7.46: Acoustic resonance in sample 300ppb34.0 at 18 mK, with an overlaid Lorentzian fit.

the same elastic changes. The changes in f_r ($\sim 4\%$) are about half as large as for μ ($\sim 6\%$).

The corresponding dissipation $1/Q$, shown in Figure 7.50, is largest near 110 mK, near where f_r is changing rapidly. Again, the maximum dissipation occurs at a temperature slightly above the inflection in the f_r curve (or the shear modulus μ curve).

Figure 7.51 shows the change in dissipation versus the change in resonance frequency scaled by its low temperature value for the acoustic resonances of sample 300ppb34.0. For this sample, $\Delta(Q^{-1}) \approx 8 \times 10^{-3}$ is about a factor of five smaller than its $\Delta f_r/f_r \approx 42 \times 10^{-3}$.

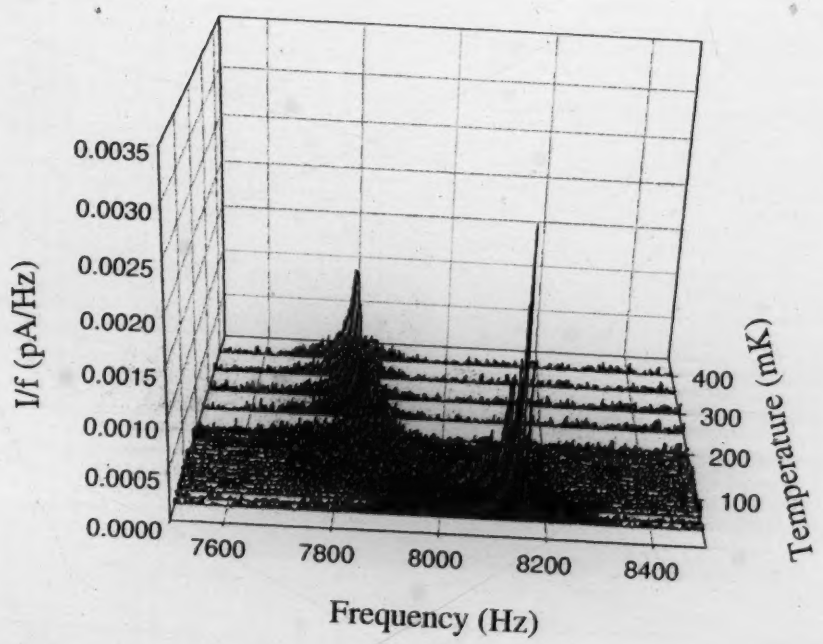

Figure 7.47: Acoustic resonance in sample 300ppb34.0 as a function of temperature (from the "front").

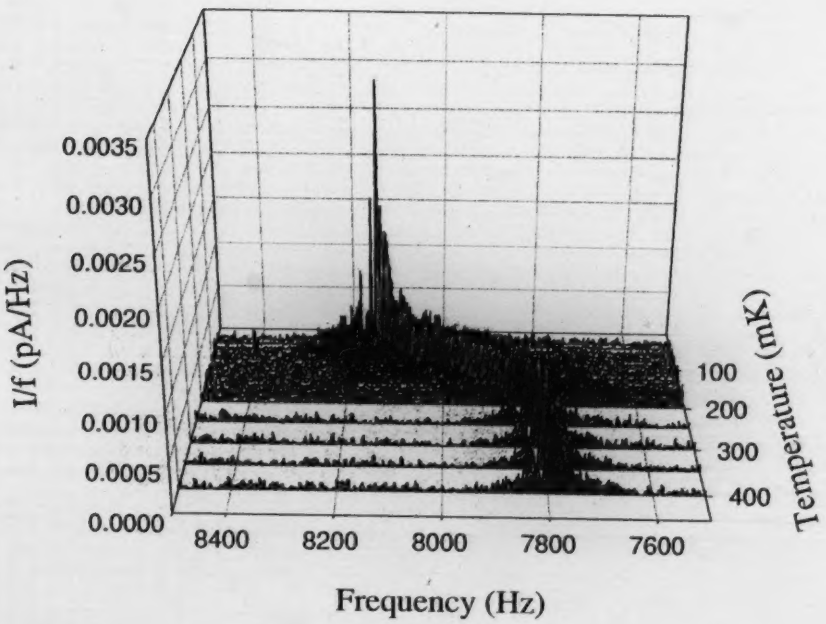

Figure 7.48: Acoustic resonance in sample 300ppb34.0 as a function of temperature (from the "back").

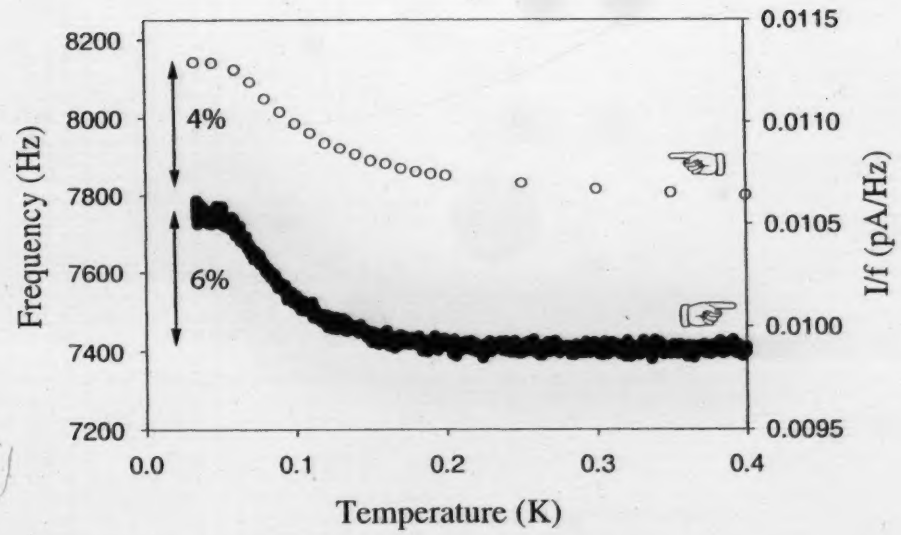

Figure 7.49: Acoustic resonance in sample 300ppb34.0 compared to shear modulus anomaly.

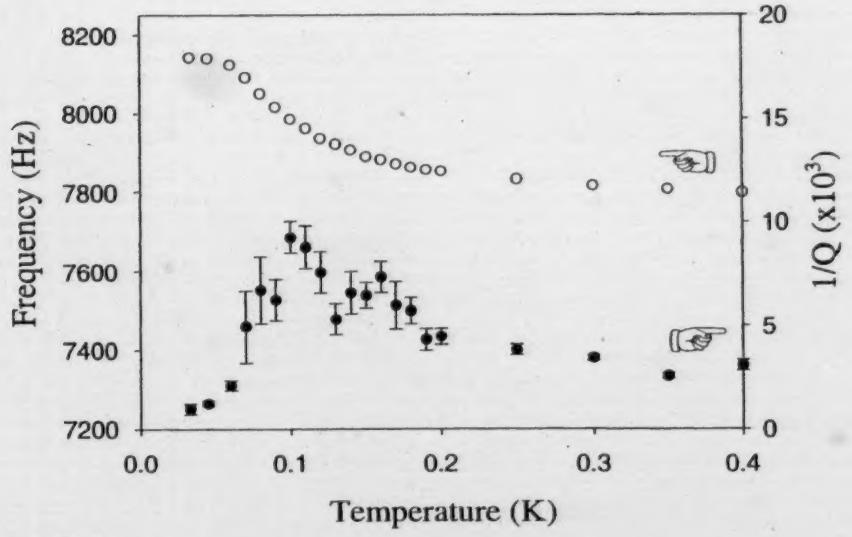

Figure 7.50: Acoustic resonance in sample 300ppb34.0 and its dissipation.

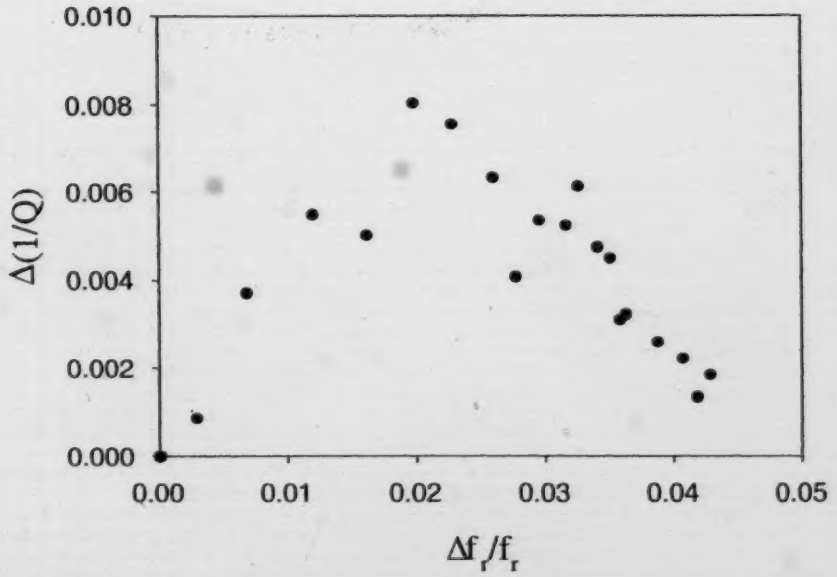

Figure 7.51: Change in dissipation of the acoustic resonance in sample 300ppb34.0 as a function of the scaled change in resonance frequency.

7.4.1.3 Sample 300ppb29.3

Figure 7.52 shows the acoustic resonance in sample 300ppb29.3 at 200 mK (refer back to the thermodynamic path on the phase diagram of Figure 7.8). Sample 300ppb29.3 had not been annealed before these measurements were taken.

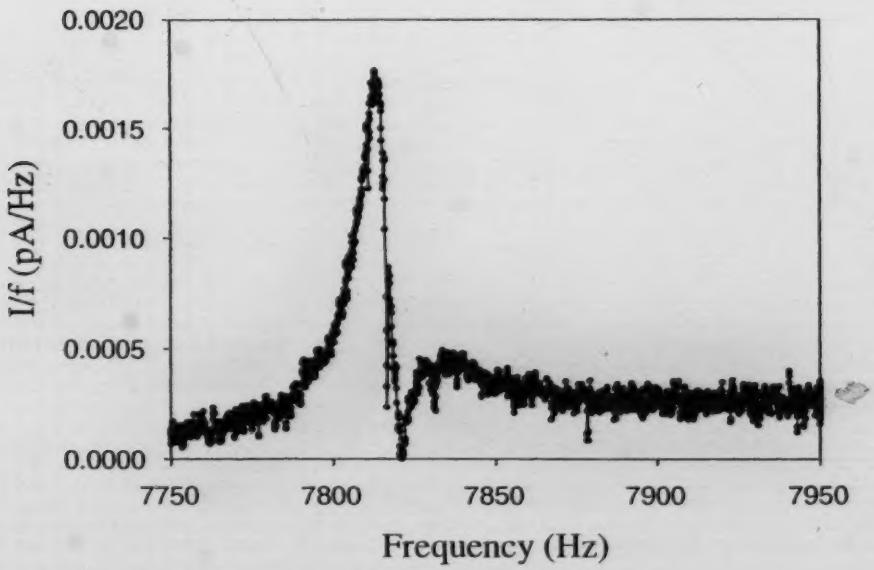

Figure 7.52: Acoustic resonance in sample 300ppb34.0 at 200 mK.

The resonance frequency f_r of this peak is (7814 $\pm$ 4) Hz; its amplitude is measured (0.00176 $\pm$ 0.00005) pA/Hz and it has a Q of $\sim$ 650.

Figure 7.53 shows the acoustic resonance that we measure in the shear cell for the sample 300ppb34.0 at 35 mK.

The resonance frequency f_r of this peak is (7943 $\pm$ 1) Hz; its amplitude is measured (0.051 $\pm$ 0.001) pA/Hz and it has a Q of $\sim$ 1750. This peak is "clean" enough that no comparison to a fitting algorithm will be provided.

Figures 7.54 and 7.55 show how the resonance peak in sample 300ppb29.3 evolves as a function of temperature. As was presented before, both plot the same data, but the latter has its temperature scale reversed. Once again, the peak shifts to higher

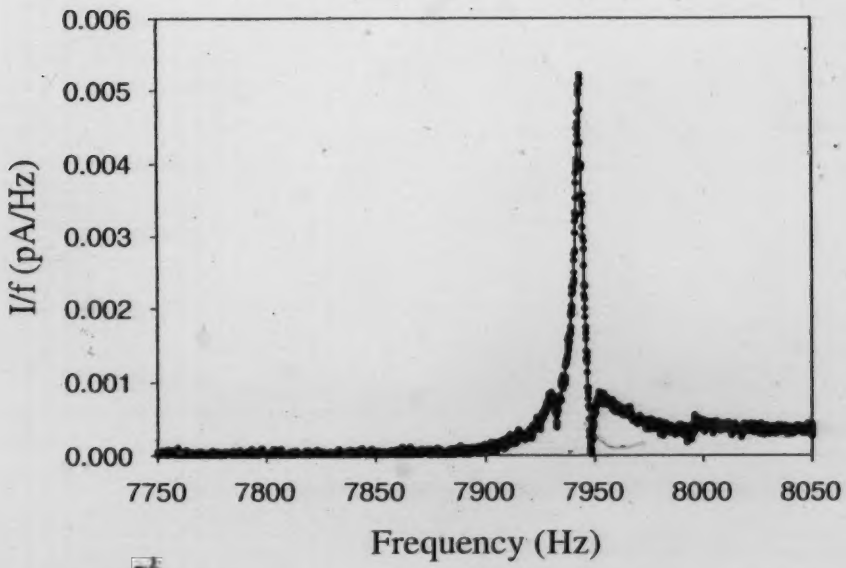

Figure 7.53: Acoustic resonance in sample 300ppb34.0 at 35 mK.

frequency with decreasing temperature, experiencing a maximum in dissipation near where it moves through frequency space most quickly.

Figure 7.56 plots the resonance frequency of sample 300ppb29.3 as a function of temperature. This was one of the first measurements made on μ and it was done before we had all of our electronics set to the proper sensitivities; therefore, the μ data plotted here shows a digitization step. μ appears to change by $\sim 4\%$; however, the digitization means that this value could be off by as much as a factor of two. Also, this measurement was made at 100 Hz (as opposed to 2000 Hz), but Figure 7.15 reminds us that $\Delta\mu$ is unaffected by the measurement frequency. The changes in f_r ($\sim 2\%$) are about half as large as for μ, as before.

The corresponding dissipation $1/Q$, shown in Figure 7.57, is largest near 150 mK, near where f_r is changing rapidly. In conformity with our previous measurements, the maximum dissipation occurs at a temperature slightly above the inflection in the f_r curve (or the shear modulus μ curve).

Figure 7.58 shows the change in dissipation versus the change in resonance frequency scaled by its low temperature value for the acoustic resonances of sample 3300ppb29.3. For this sample, $\Delta(Q^{-1}) \approx 2 \times 10^{-3}$ is a factor of eight smaller than

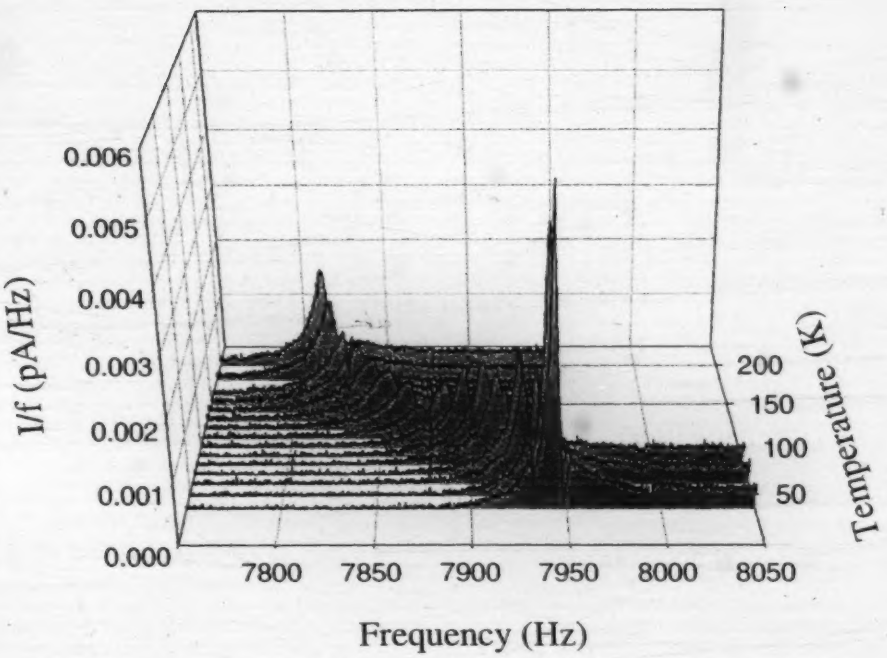

Figure 7.54: Acoustic resonance in sample 300ppb29.3 as a function of temperature (from the "front").

its $\Delta f_r/f_r \approx 16 \times 10^{-3}$.

In a simple oscillator the maximum dissipation $\Delta(Q^{-1})$ should equal the frequency shift $\Delta f_r/f_r$. Figure 7.59 shows the change in dissipation versus the change in resonance frequency scaled by its low temperature value for the acoustic resonances of all three samples discussed above. Recall that $\Delta(Q^{-1})$ was smaller than $\Delta f_r/f_r$ by a factor ranging from five to eight. Similar differences in torsional oscillator measurements have been ascribed [161] to sample inhomogeneity. For example, Fig. 2 of Reference [51] shows $\Delta(Q^{-1}) \approx 3 \times 10^{-6}$, about a factor of six or seven smaller than its $\Delta\omega/\omega \approx 20 \times 10^{-6}$. In other examples, Rittner and Reppy [54] show data very close to the homogeneous expectation (i.e., their Fig. 2 shows $\Delta(Q^{-1}) \approx 12 \times 10^{-6}$ and $\Delta\omega/\omega \approx 18 \times 10^{-6}$); conversely, Kim and Chan [9, 51] also have data in which the factor ranges up to about 100.

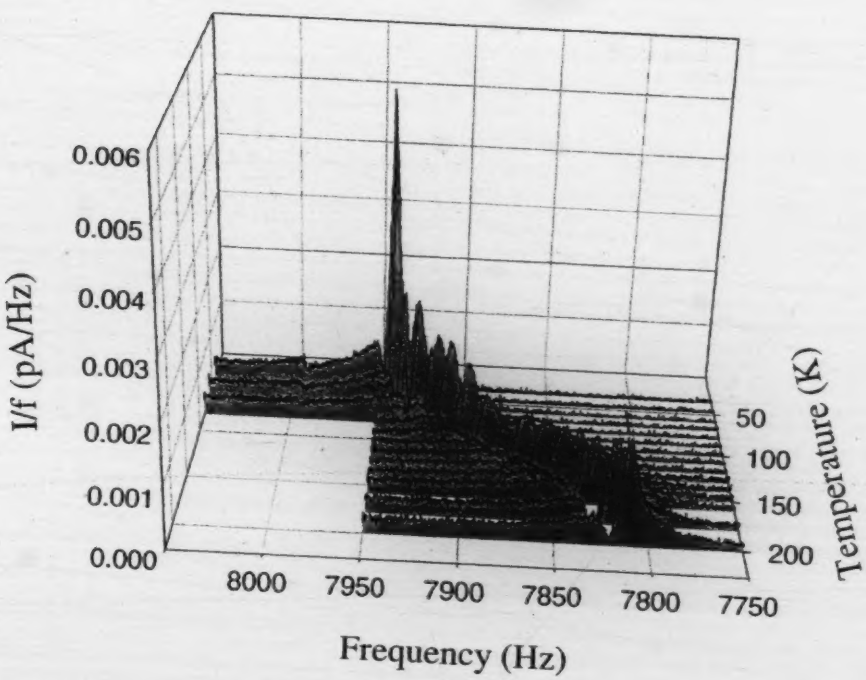

Figure 7.55: Acoustic resonance in sample 300ppb29.3 as a function of temperature (from the "back").

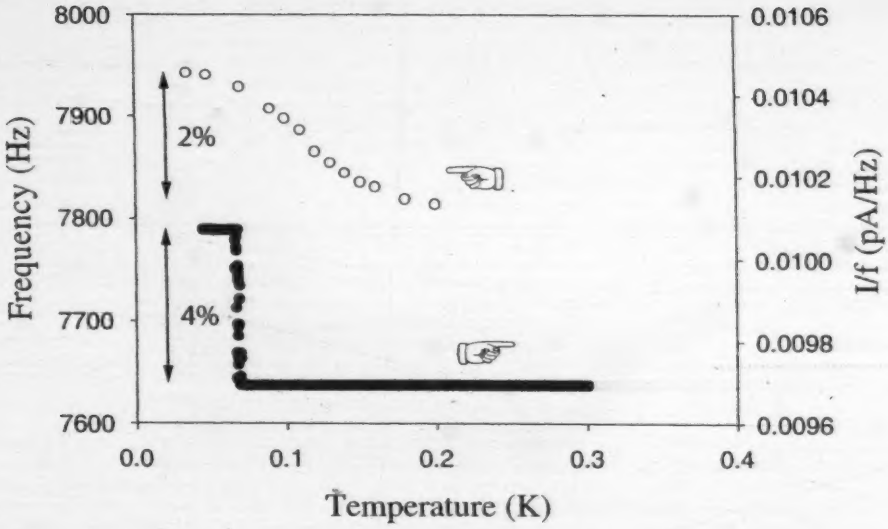

Figure 7.56: Acoustic resonance in 300ppb29.3 compared to shear modulus anomaly.

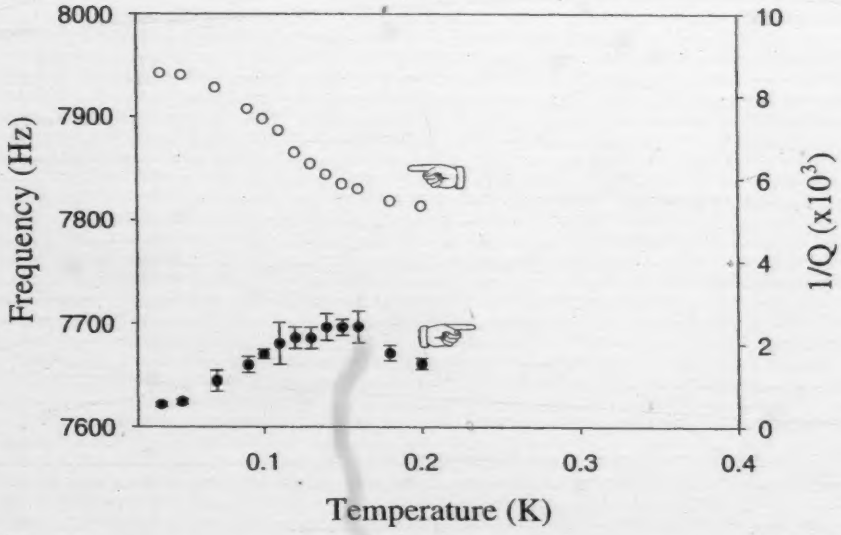

Figure 7.57: Acoustic resonance in sample 300ppb29.3 and its dissipation.

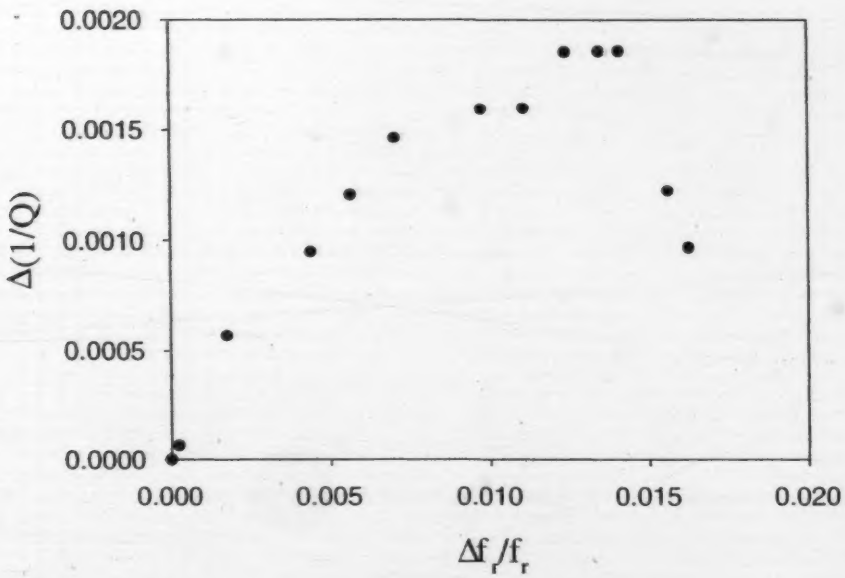

Figure 7.58: Change in dissipation of the acoustic resonance in sample 300ppb29.3 as a function of the scaled change in resonance frequency.

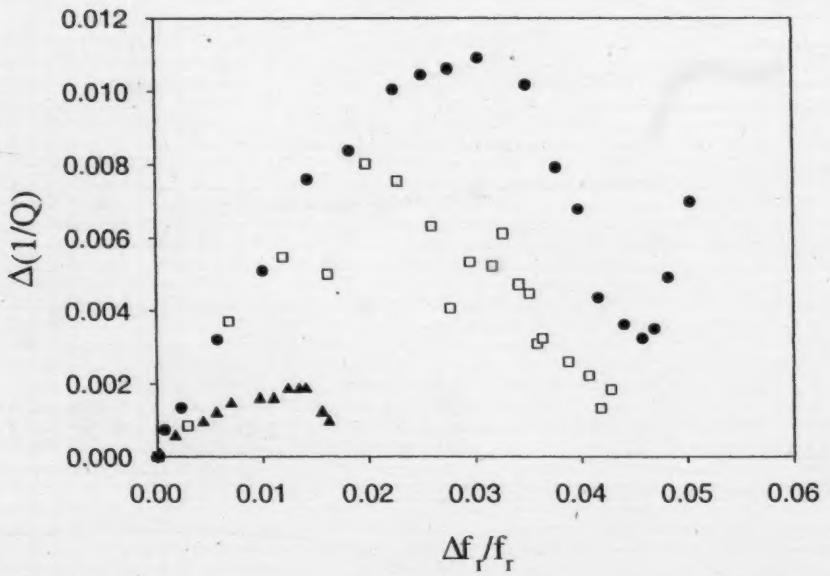

Figure 7.59: Summary of the change in dissipation of the acoustic resonance as a function of the scaled change in resonance frequency. •'s are for sample 300ppb33.3, □'s are for sample 300ppb34.0, and ▲'s are for sample 300ppb29.3.

7.5 ^{3}He dependence

A striking feature of torsional oscillator experiments is their sensitivity to ^{3}He. We grew samples from isotopically pure ^{4}He (1 ppb ^{3}He - the same gas used in torsional oscillator measurements [52]) and from intermediate concentrations made by mixing with commercial ^{4}He (0.3 ppm ^{3}He). We compare their behavior in Figure 7.60. The anomaly shifts to lower temperatures as the ^{3}He concentration decreases.

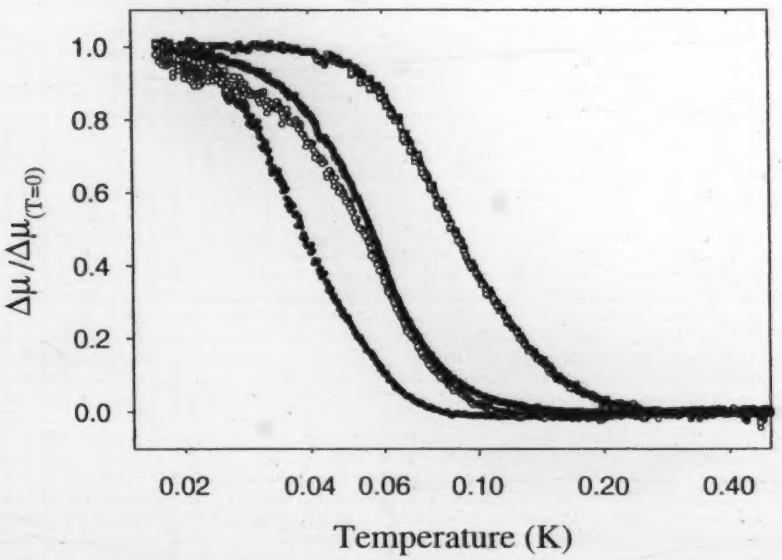

Figure 7.60: Shear modulus anomaly in solid ^{4}He at 2000 Hz, for different ^{3}He impurity concentrations: 1 ppb (33.4 bar, •), 45 ppb (33.0 bar, ○), 85 ppb (33.5 bar, ■), and 0.3 ppm ^{3}He (33.3 bar, □). Changes $\Delta\mu$ have been scaled by their values at the lowest temperature (18 mK) in order to compare temperature dependence. The sizes of the anomalies $\Delta\mu$ before scaling were: 14.9% for 1 ppb data; 7.8% for 45 ppb data; 16.6% for 85 ppb data; and 8.3% for 0.3 ppm data.

We also show similarly scaled decoupling data from torsional oscillator experiments [9, 52] on 1 ppb and 0.3 ppm ^{3}He samples in Figures 7.61 and 7.62, respectively. In reference to this borrowed data, samples were grown using two different techniques. Some samples were grown using the blocked capillary technique (BC),

which was described earlier in this thesis. This technique results in a polycrystalline sample with a relatively high level of associated disorder. Other samples were grown using the constant temperature (CT) technique. This technique involves keeping the fill line from high-pressure cylinder to experimental cell open during crystal growth. The pressure in the experimental cell is slowly increased at low temperature (around 1 K) until solidification begins, and then is kept fixed until solidification is complete. This technique results in single crystal that occupies the entire cell (or, at worst, a few large crystals), with very little presumed associated disorder. Returning to Figures 7.61 and 7.62, the onset temperatures and shapes of the curves agree very well (roughly within the sample to sample variations in torsional oscillator measurements).

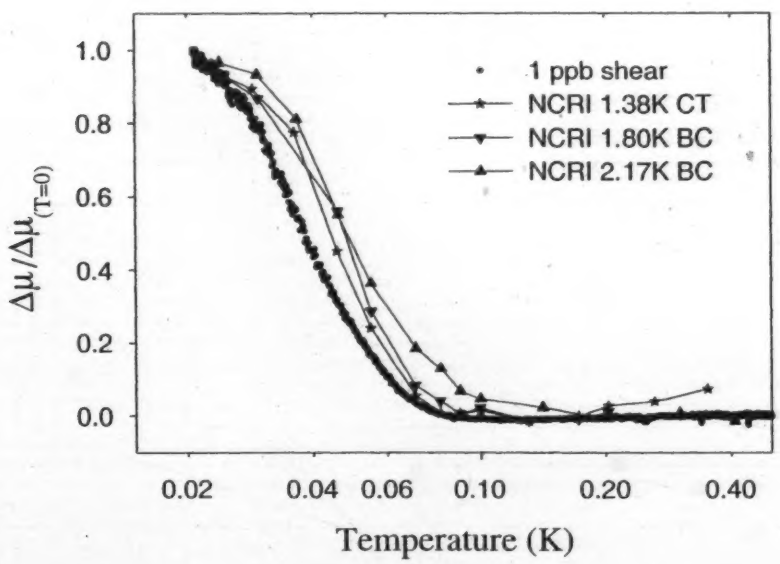

Figure 7.61: Shear modulus anomaly at 2000 Hz and NCRI at 1072 Hz in solid ^{4}He at 1 ppb ^{3}He impurity concentration. Changes $\Delta\mu$ have been scaled by the values at the lowest temperature (18 mK) and NCRI has been similarly scaled in order to compare temperature dependence. The NCRI data is that of Reference [58]; the letters CT mean that the sample was grown at a constant temperature (of 1.38 K), and the letters BC mean that the sample was grown using the blocked capillary technique (and solidification was complete at 1.80 K and 2.17 K).

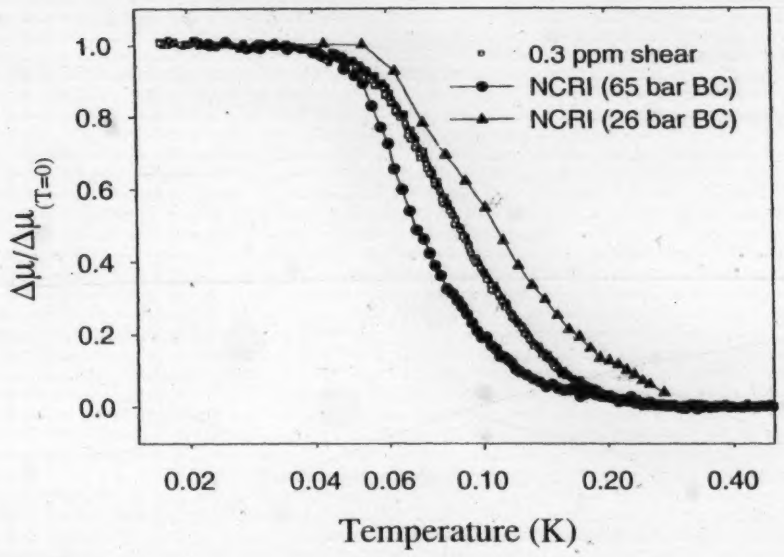

Figure 7.62: Shear modulus anomaly at 2000 Hz and NCRI at 910 Hz in solid ^{4}He at 0.3 ppm ^{3}He impurity concentration. Changes $\Delta\mu$ have been scaled by the values at the lowest temperature (18 mK) and NCRI has been similarly scaled in order to compare temperature dependence. The NCRI data is that of Reference [9]; the letters BC mean that the sample was grown using the blocked capillary technique.

Figure 7.63 shows the shear modulus anomaly at three frequencies (2000, 200 and 20 Hz), at a driving voltage of 32.7 mV_{peak} and a corresponding strain of 2.2 x 10^{-8}, in the 1 ppb ^{3}He sample at 33.4 bar of Figure 7.60. It is not possible to say whether the magnitude of the modulus increase is the same for each, as sufficiently low temperatures were not achieved to "saturate" the value for $\Delta\mu$. The transition temperature appears to decrease with frequency, but does not appear sharper at low frequency (as was the case in samples with greater ^{3}He impurity concentrations).

7.5.1 Acoustic resonance peak position at 1ppb ^{3}He

Now that the shear modulus anomaly has been examined at lower ^{3}He concentrations, we'll follow through a quick study of the acoustic resonance at lower ^{3}He concentrations.

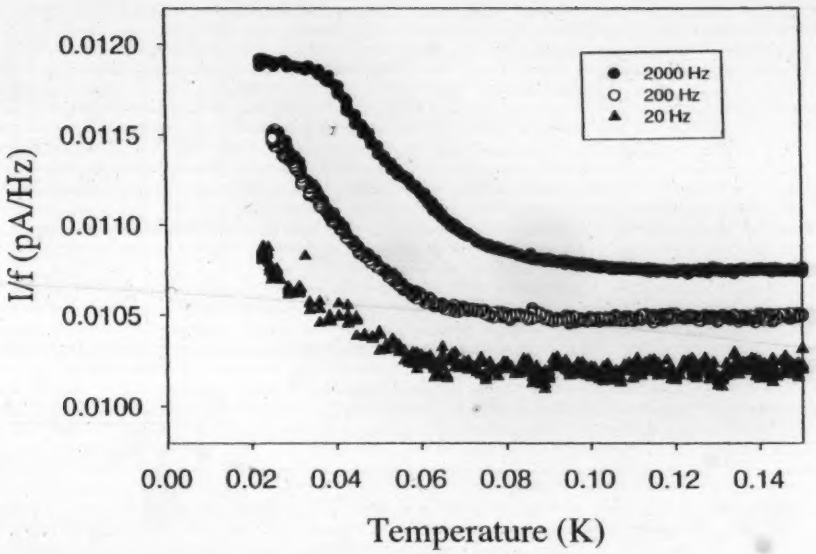

Figure 7.63: The shear modulus anomaly as a function of frequency in sample 001ppb33.4. The 200 Hz and 2000s Hz data have been shifted up for clarity.

7.5.1.1 Sample 001ppb33.4

Figure 7.64 shows the thermodynamic path followed during the growth of sample 001ppb33.4. As can be seen from the inset of Figure 7.64, this sample is at only a slightly higher pressure than the sample 300ppb33.3. Also note that it has entered the hcp phase without having first entered the mixed bcc/hcp phase. The helium used for this sample also had an isotopic purity of 1 ppb ^{3}He.

Figure 7.65 shows the acoustic resonance in sample 001ppb33.4 at 150 mK. Sample 001ppb33.4 had not been annealed before these measurements were taken.

The resonance frequency f_r of this peak is (7591 $\pm$ 2) Hz; its amplitude is (0.006 $\pm$ 0.003) pA/Hz and it has a Q of $\sim$ 1100. As before, these values have been determined by eye, without the aid of a fitting algorithm.

Figure 7.66 shows the acoustic resonance that we measure in the shear cell for the sample 001ppb33.4 at 24 mK.

The resonance frequency f_r of this peak is (8023 $\pm$ 3) Hz; its amplitude is measured (0.030 $\pm$ 0.005) pA/Hz and it has a Q of $\sim$ 1000.

Figures 7.67 and 7.68 demonstrate how the acoustic resonance peak in the sample

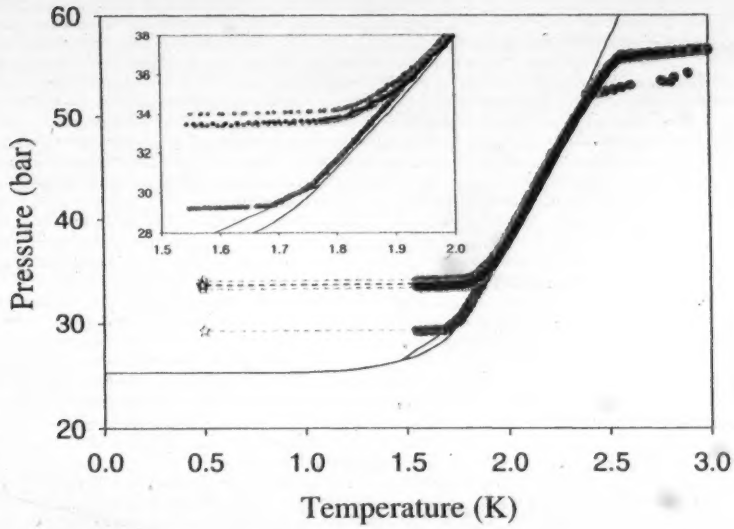

Figure 7.64: The thermodynamic path for sample 001ppb33.4. Inset shows a close-up of the end of freezing. This data is the pressure versus temperature as we measured it. Data in grey shows sample 300ppb29.3, sample 300ppb34.0, and sample 300ppb33.3.

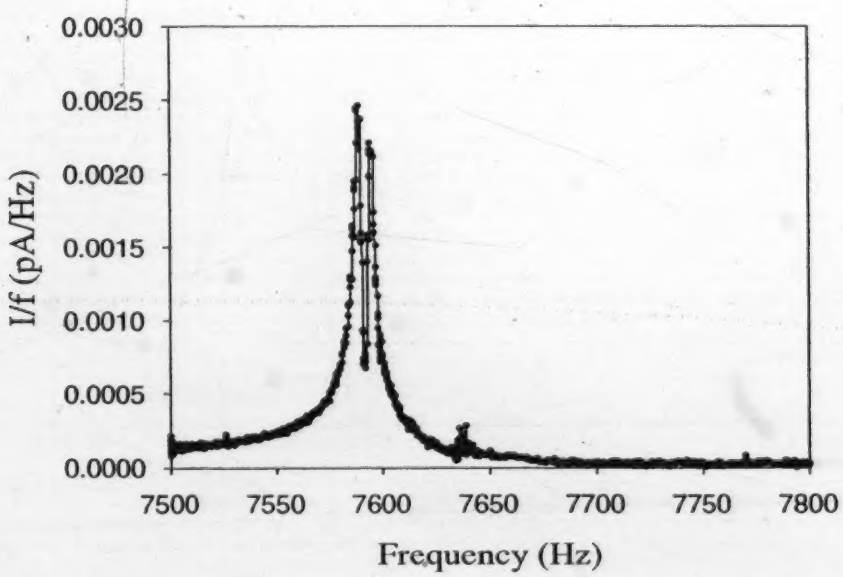

Figure 7.65: Acoustic resonance in sample 001ppb33.4 at 150 mK.

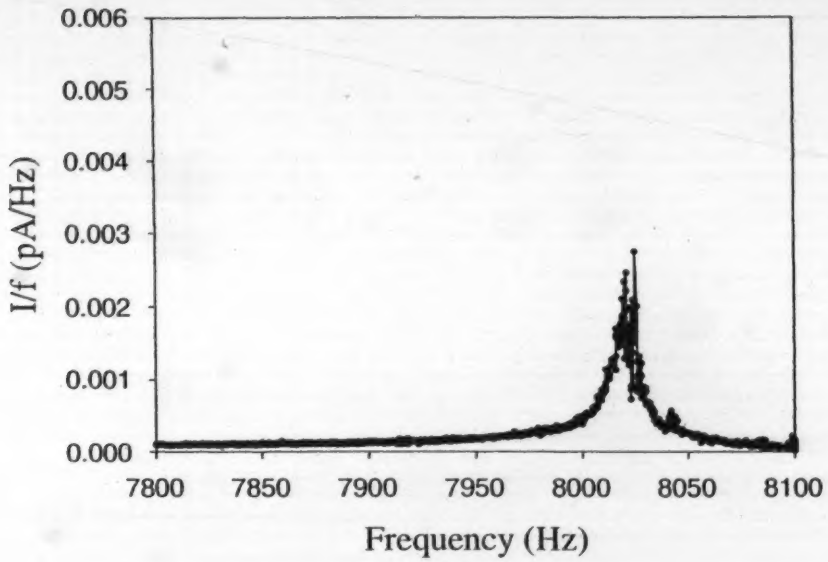

Figure 7.66: Acoustic resonance in sample 001ppb33.4 at 24 mK.

001ppb33.4 evolves as a function of temperature. Just as before, both plot the same data, but the latter has its temperature scale reversed. At the risk of sounding like a broken record, the peak shifts to higher frequency with decreasing temperature, experiencing a maximum in dissipation near where it moves through frequency space most quickly.

Figure 7.69 plots the resonance frequency for the sample 001ppb33.4 as a function of temperature. Comparing the temperature dependence of the resonance frequency f_r to that of the shear modulus μ, it is again clear that the two measurements probe the same elastic changes. The changes in f_r ($\sim$ 5%) are about half as large as for μ ($\sim$ 11%), and the corresponding dissipation 1/Q (see Figure 7.70 is largest near 70 mK, near where f_r is changing rapidly. Last, but certainly not least, Figure 7.71 shows the change in dissipation versus the change in resonance frequency scaled by its low temperature value for the acoustic resonances of sample 001ppb33.4. For this sample, $\Delta(Q^{-1}) \approx 2 \times 10^{-3}$ is about a factor of twenty-five smaller than its $\Delta f_r/f_r \approx 55 \times 10^{-3}$.

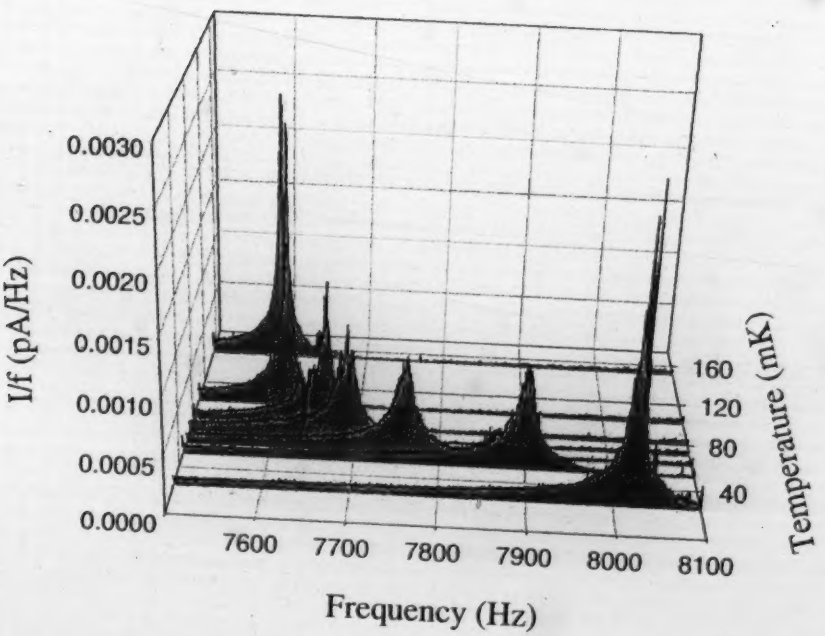

Figure 7.67: Acoustic resonance in sample 001ppb33.4 as a function of temperature (from the "front").

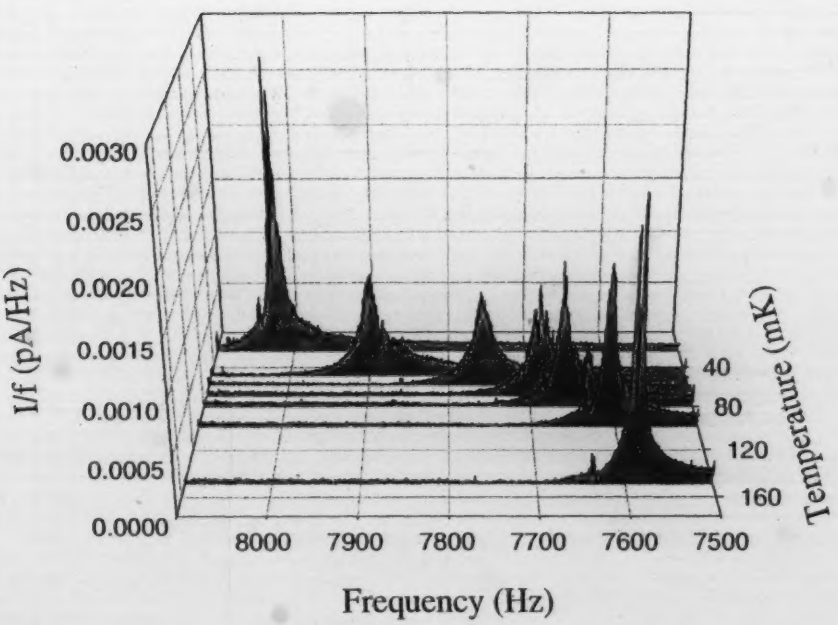

Figure 7.68: Acoustic resonance in sample 001ppb33.4 as a function of temperature ("from the back").

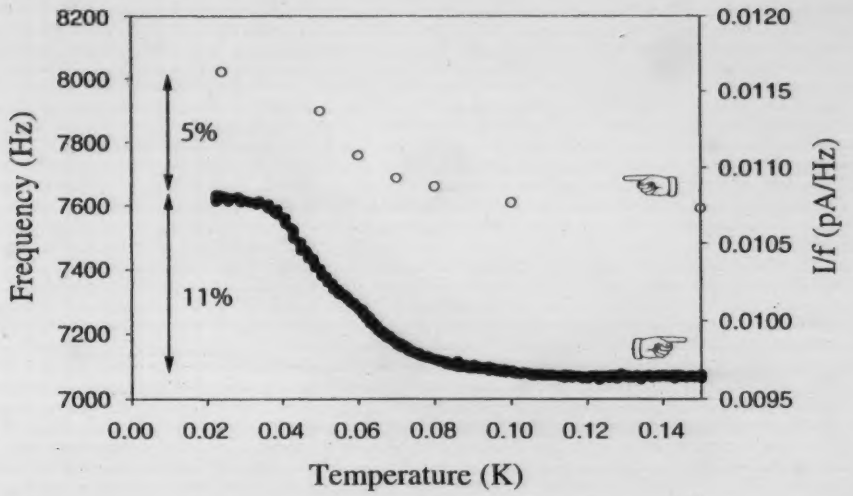

Figure 7.69: Acoustic resonance in sample 001ppb33.4 compared to shear modulus anomaly.

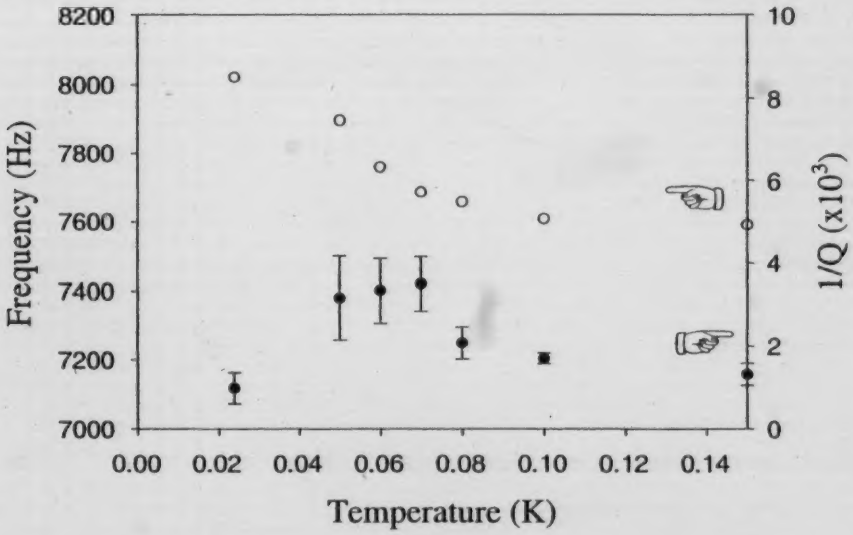

Figure 7.70: Acoustic resonance in sample 001ppb33.4 and its dissipation.

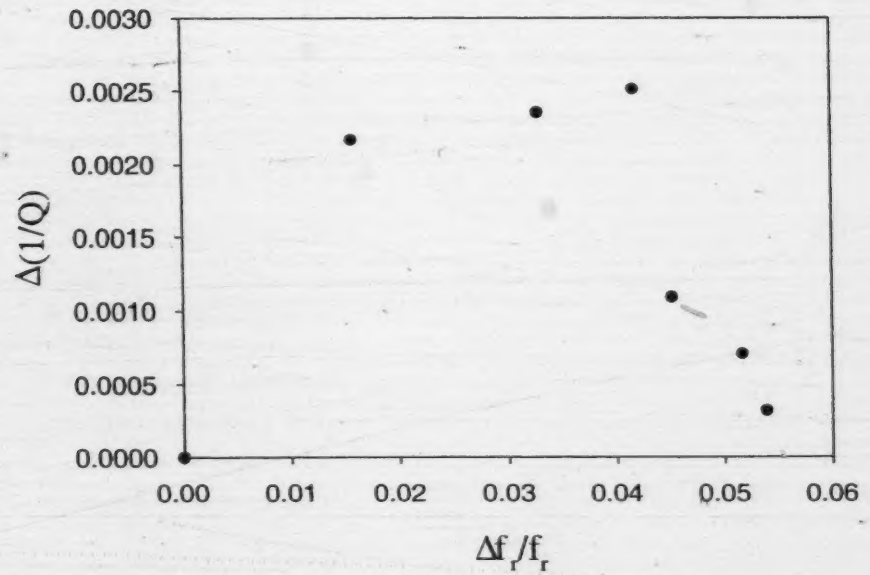

Figure 7.71: Dissipation of the acoustic resonance in sample 001ppb33.4 as a function of the scaled change in resonance frequency f_r.

7.6 Annealing and stress effects

Another fascinating feature of the torsional oscillator results is the NCRI dependence on sample history. For example, the NCRI fraction can be nearly eliminated through annealing [54] (a process which presumably results in a reduced number of crystal defects), or can be made remarkably large through quench cooling [57] (a process which results in an increased number of crystal defects). Other groups performing torsional oscillator experiments have noted similar behaviour. In order to begin to understand the role of defects, we studied some the properties of our samples before and after annealing. What follows is little more than scratching the surface of the effects of annealing and stress, although one important conclusion is drawn - it is largely the high temperature behaviour that is affected by annealing and stressing the solid, not the low temperature behaviour.

To begin, we studied some the properties of sample 001ppb33.4 (please refer back to Figure 7.64) before and after annealing. This sample was annealed for 11 hours at 1.70 K ($\sim$ 0.2 K below T_m). We continued annealing the sample until the measured shear modulus near melting no longer changed as a function of time, as shown in Figure 7.72.

As shown in Figure 7.73, the annealing process reduced $\Delta\mu$ from 11.3% to 7.4%, but it was largely the high temperature behavior which changed. The values of μ and f_r at the lowest temperature were almost unaffected by annealing. For example, at 25 mK f_r decreased by less than 0.2% (as shown in Figure 7.74). At 25 mK μ increased by only 0.3%, whereas at 0.5 K, μ increased by 2.9%. Unfortunately, the analogous measurement was not made for f_r at 0.5 K. The low temperature values appear to reflect an intrinsic shear modulus and the effect of defects is mostly to reduce μ at higher temperatures.

We also applied large acoustic stresses ($\sim$ 700 Pa) to the annealed sample at $\sim$ 20 mK in an attempt to create additional defects. These large stresses were created by applying a large driving voltage to the piezoelectric transducers ($\sim$ 1.5 V) and then sweeping the frequency over the range of the acoustic resonance. (In hindsight, this might not be relevant to the low frequency μ measurement, since the large amplitude at resonance presumably affects the solid ^{4}He outside of the gap, but doesn't necessarily have a larger effect on the solid ^{4}He in the gap than applying, for example, $\sim$ 1.5 V at 1000 Hz.) Figure 7.75 shows that the value of μ remains

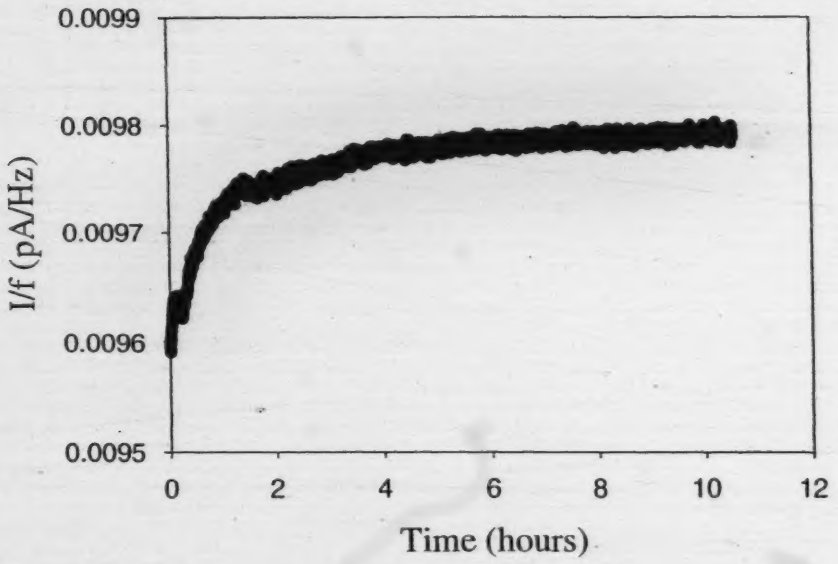

Figure 7.72: Annealing time for sample 001ppb33.4 at 1.70 K.

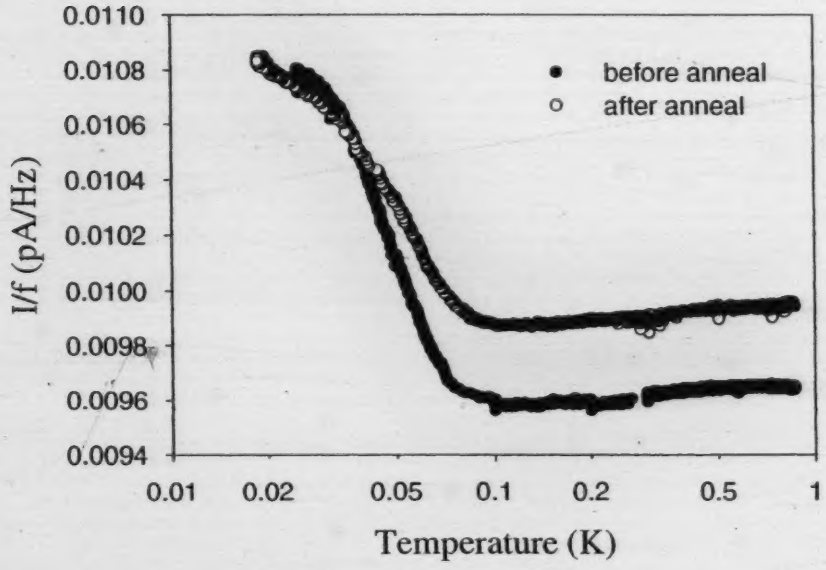

Figure 7.73: Effect of annealing shear modulus anomaly in sample 001ppb33.4. Both data sets taken on cooling.

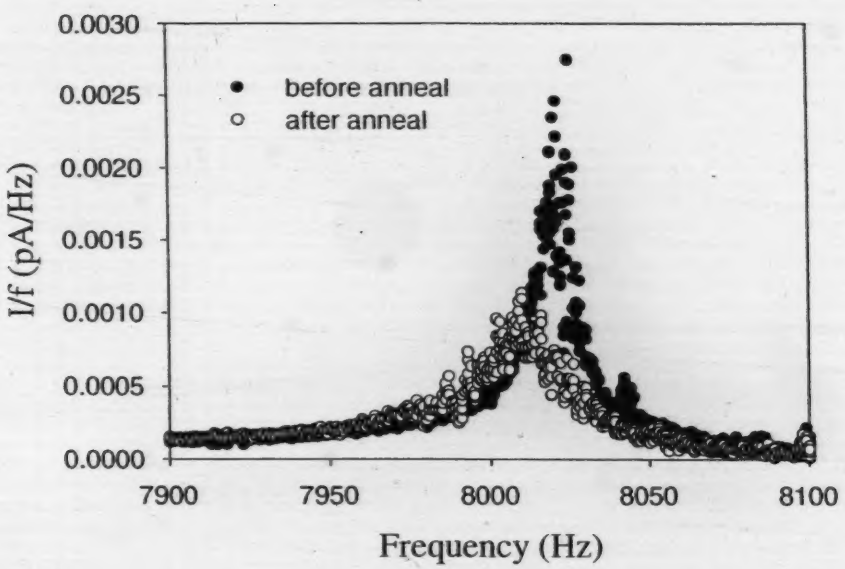

Figure 7.74: Effect of annealing on resonant frequency in sample 001ppb33.4, at 25 mK.

essentially unchanged at low temperature but does change at high temperature (which, to be clear, means above 100 mK but below 500 mK). Warming above 0.6 K undoes these effects, indicating that defects introduced by stressing the crystal are only stable at low temperatures. Ultrasonic measurements [156] on bcc and hcp ^{3}He showed similar effects of large stresses.

Figure 7.76 shows that the value of f_r remains virtually unchanged at low temperature (a 0.3% increase). There is no data showing how much f_r is affected at high temperatures by stressing. (In hindsight - which is always clearer than foresight - and knowing that μ and f_r probe different volumes of the cell, one would expect that, depending on the procedure, the large stresses would affect each of those properties differently; annealing, on the other hand, might be expected to affect μ and f_r in the same way.)

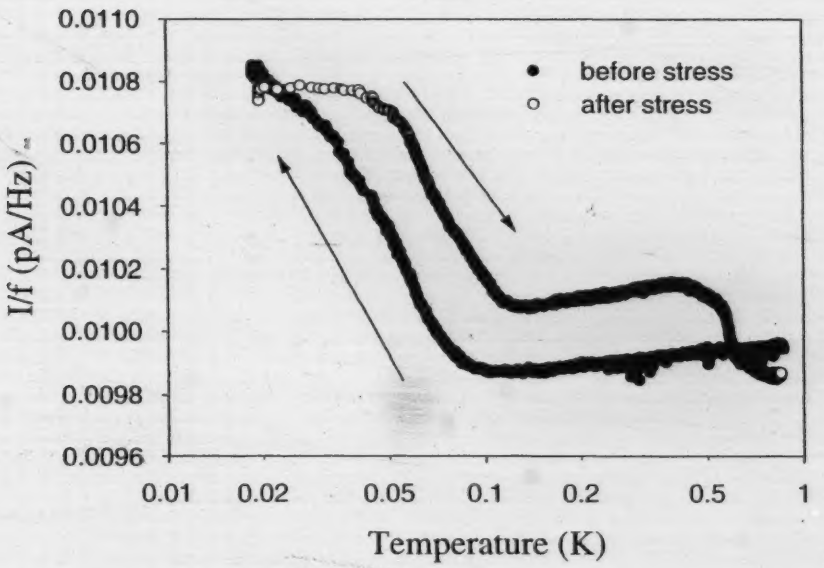

Figure 7.75: Effect of stressing on shear modulus anomaly in sample 001ppb33.4. The "before stress" data set taken on cooling, "after stress" data set taken on warming.

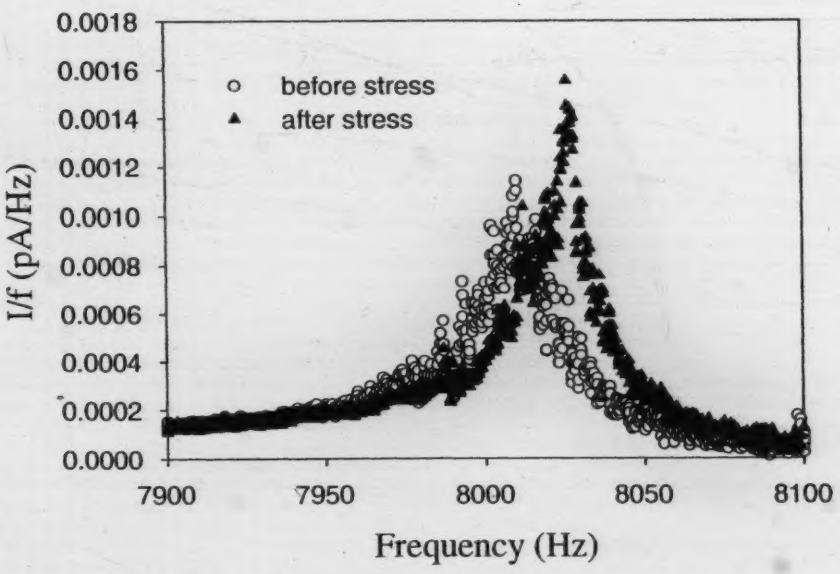

Figure 7.76: Effect of stressing on resonant frequency in sample 001ppb33.4 at 20 mK.

We also studied some of the properties of sample 300ppb33.3 (please refer back to Figure 7.13) before and after annealing. This sample was annealed for 15 hours at 1.70 K ($\sim$ 0.2 K below T_m). We continued annealing the sample until the measured shear modulus near melting no longer changed as a function of time, as shown in Figure 7.77.

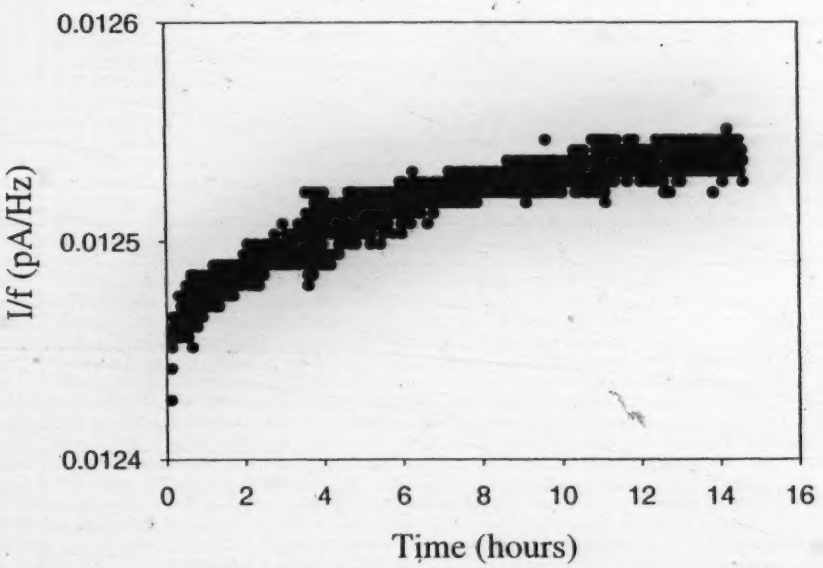

Figure 7.77: Annealing time for sample 300ppb33.3 at 1.70 K.

As shown in Figure 7.78, the annealing process reduced $\Delta\mu$ from 9.8% to 7.7%, and it was more so the high temperature behavior which changed. The values of μ and f_r at the lowest temperature were almost unaffected by annealing. For example, at 18 mK f_r increased by only 0.1% (as shown in Figure 7.79). At 18 mK, μ decreased by only 0.5%, whereas at 0.4 K, μ increased by 1.1%. At 0.4 K, f_r increased by 3.8% (as shown in Figure 7.80). Again, the low temperature values appear to reflect an intrinsic shear modulus and the effect of defects is mostly to change μ at higher temperatures.

We then, once again, applied large acoustic stresses ($\sim$ 700 Pa) to the annealed

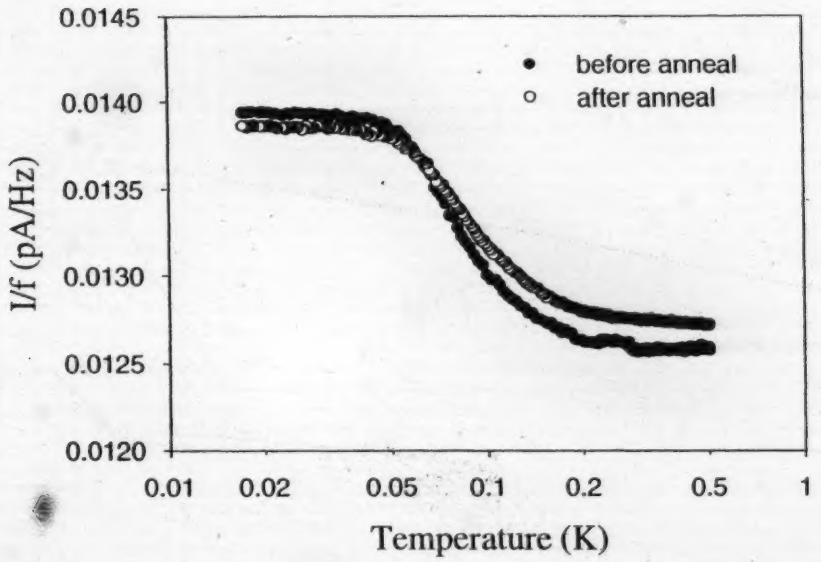

Figure 7.78: Effect of annealing on shear modulus anomaly in sample 300ppb33.3. Both data sets taken on cooling.

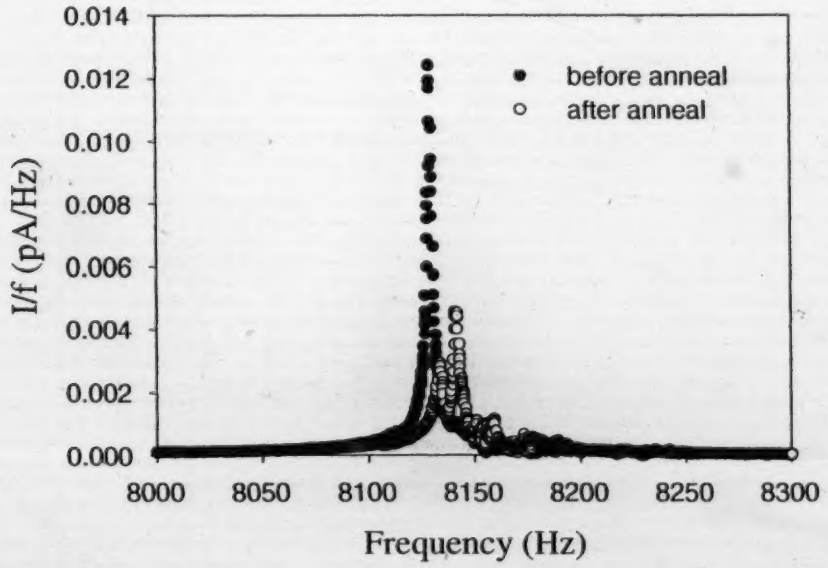

Figure 7.79: Effect of annealing on resonant frequency in sample 300ppb33.3, at 18 mK.

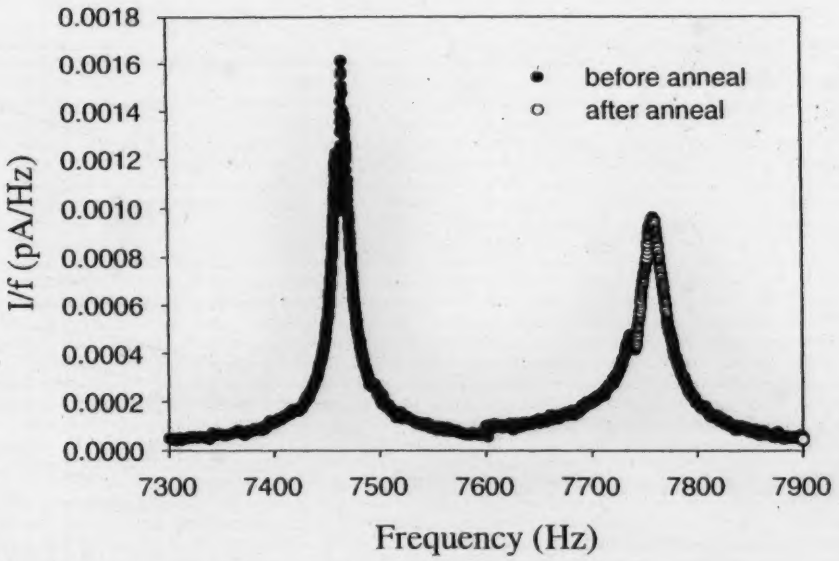

Figure 7.80: Effect of annealing on resonant frequency in sample 300ppb33.3, at 400 mK.

crystal at 18 mK in an attempt to create additional defects. Here, the values of μ changed at both low and high temperature, as shown in Figure 7.81. There is no corresponding f_r data to study. Stressing the crystal in this way caused μ to increase by 1.4% at low temperature, and by 3.8% at 400 mK. Alternatively, we could say that stressing the crystal caused the anomaly $\Delta\mu$ (as measured between low temperature and 400 mK) to decrease from 7.7% to 5.3%, as shown in Figure 7.82. Again, warming above 0.6 K undoes these effects, restoring the anomaly $\Delta\mu$ back to 7.7%.

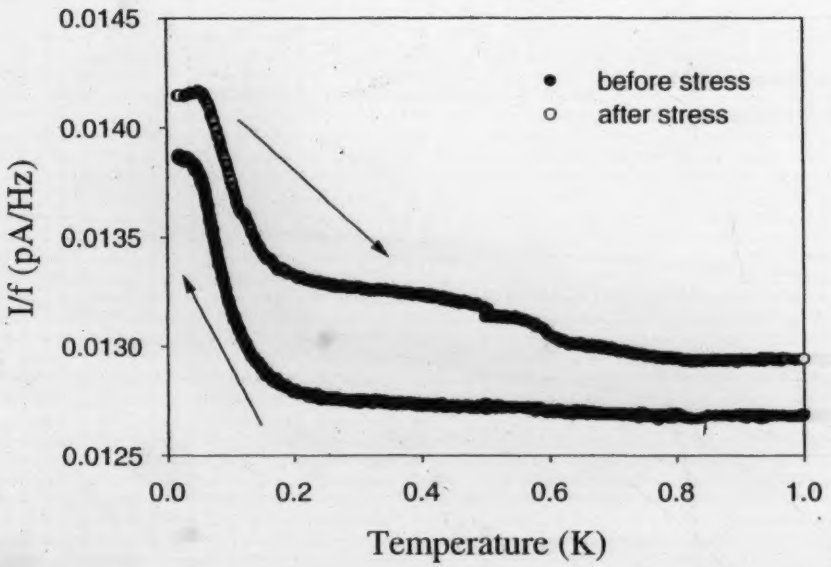

Figure 7.81: Effect of stressing on shear modulus anomaly in sample 300ppb33.3. The "before stress" data set taken on cooling, "after stress" data set taken on warming.

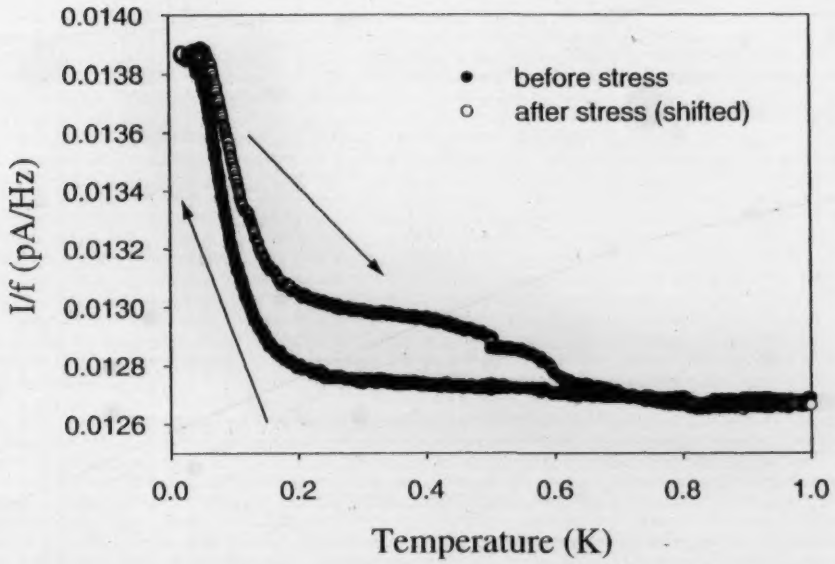

Figure 7.82: Effect of stressing on shear modulus anomaly in sample 300ppb33.3, with data shifted. The "before stress" data set taken on cooling, "after stress" data set taken on warming. Also, "after stress" data has been shifted to agree with "before stress" data at low temperature.

Finally, we consider sample 300ppb29.3 (please refer back to Figure 7.8) before and after annealing. This sample was annealed for 10 hours at 1.45 K ($\sim$ 0.3 K below T_m). As before, we continued annealing the sample until the measured shear modulus near melting no longer changed as a function of time (this data unavailable).

As shown in Figure 7.83, the annealing process enhanced $\Delta\mu$ from 6.0% to 11.1%, and it was mostly the high temperature behavior which changed. The values of μ and f_r at the lowest temperature were almost unaffected by annealing. For example, at 50 mK f_r increased by 0.1% (as shown in Figure 7.84) and μ decreased by only 4.3%. At 0.2 K, however, f_r decreased by 1.8% (as shown in Figure 7.85) and μ decreased by 10.2%. To reiterate, we conclude that the low temperature values appear to reflect an intrinsic shear modulus and the effect of defects is mostly to reduce μ at higher temperatures.

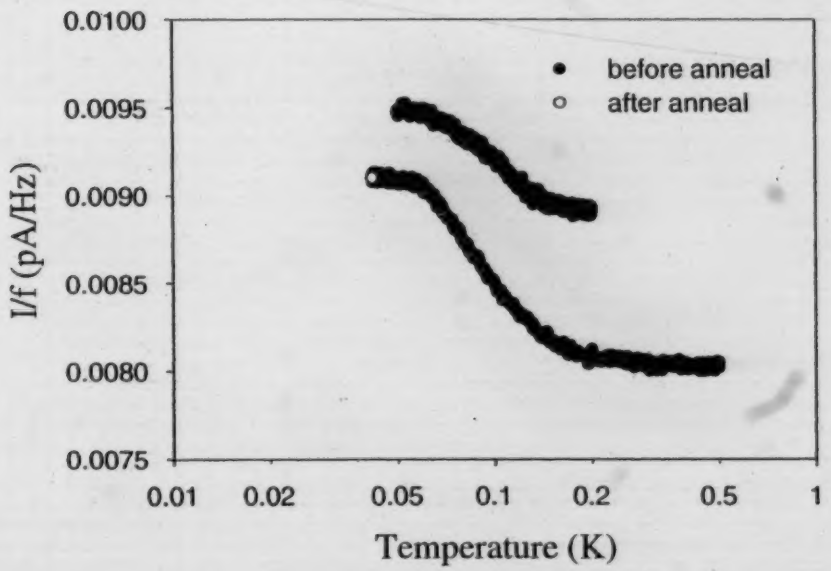

Figure 7.83: Effect of annealing on shear modulus anomaly in sample 300ppb29.3. Both data sets taken on cooling.

As before, we then applied large acoustic stresses ($\sim$ 700 Pa) at the base temper-

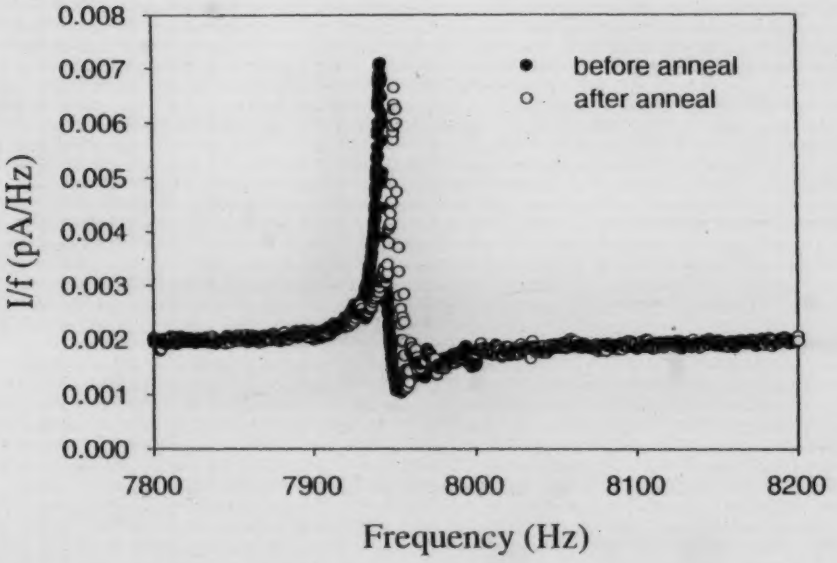

Figure 7.84: Effect of annealing on resonant frequency in sample 300ppb29.3, at 50 mK.

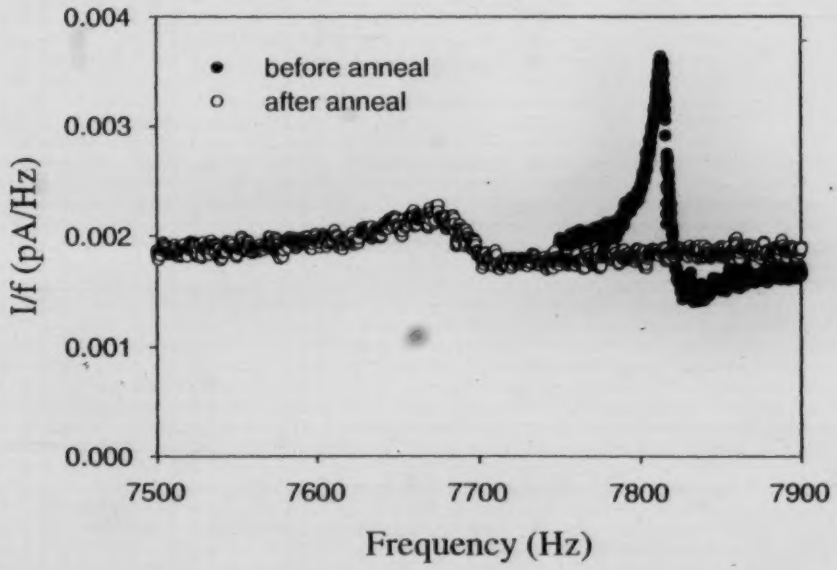

Figure 7.85: Effect of annealing on resonant frequency in sample 300ppb29.3, at 200 mK.

ature of the annealed crystal in an attempt to create additional defects. Again, the values of μ and f_r changed at high temperature but not at low temperature, as shown in Figure 7.86. One last time, warming above 0.6 K undoes these effects: the defects introduced by stressing the crystal seem to be stable only at low temperatures.

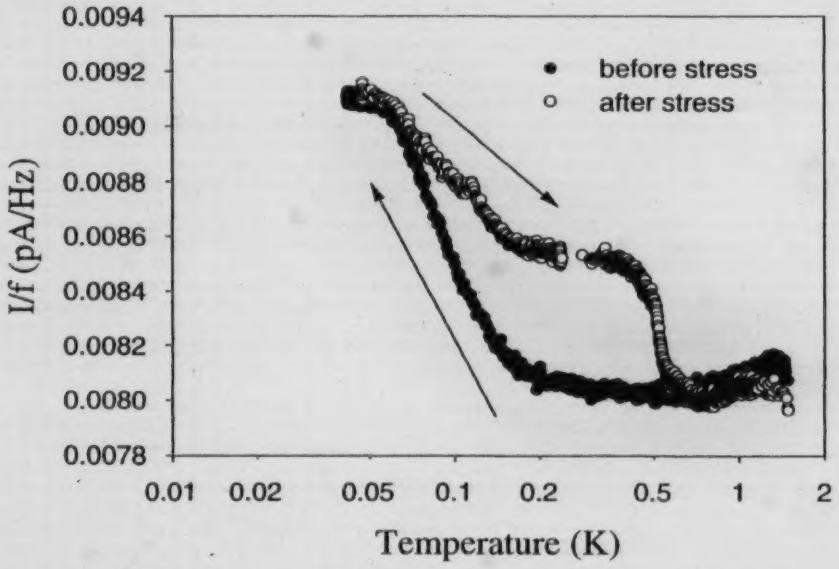

Figure 7.86: Effect of stressing on shear modulus anomaly in sample 300ppb29.3. The "before stress" data set taken on cooling, "after stress" data set taken on warming.

7.7 Discussion

The modulus changes at low temperatures are very large: orders of magnitude larger than expected in defect-free crystals (e.g., than are seen in ultrasonic measurements on single crystals [49, 154]). It is difficult to imagine small concentrations of point defects having such significant effects. Dislocations, however, can dramatically affect the elastic properties of solids and may lead to anomalous low temperature behavior in quantum crystals like helium [162].

Much of what is known about dislocations in metals has been directly confirmed through electron microscopy (and other techniques) which can monitor their motion. In solid helium, of course, direct observation isn't possible, and so what is known is much more indirect. Most dislocation information for solid helium comes from acoustic experiments [154, 155, 156, 163, 164], plastic deformation [38, 165], and internal friction [157, 158] studies, although dislocations have been shown to be important in thermal conductivity [166, 167, 168], ion motion [169], and perhaps even heat capacity of solid helium [87]. Recent synchrotron X-ray tomography on solid helium [170] has even given some pictorial confirmations that dislocations really do exist in solid helium.

7.7.1 Dislocation basics

Dislocations can be easily conceptualized in (semi-)two-dimensional structural cartoons on the atomic scale. They are typically introduced and thought of as extra lattice planes inserted into the crystal that do not extend all the way through, ending at the dislocation line. The schematic of Figure 7.87 displays a three-dimensional view of an edge dislocation in a cubic primitive lattice, and should serve as the quintessential illustration of what an edge dislocation looks like. The upside-down T is an end view of the dislocation itself and the dashed gray line is its glide plane, along which it may move. It is imperative, however, to remember that this is just a cartoon. First, such a crystal very rarely exists in nature - with the exception of polonium, all real lattices are more complicated. Second, the exact structure of real dislocations will never be so simple - edge dislocations are just an extreme form of the possible dislocation structures. A mental expansion of Figure 7.87 (no easy feat) shows that a dislocation cannot end in the interior of an otherwise perfect crystal. Dislocations must end on either: a crystal surface; an internal surface or interface (e.g., a grain boundary); at a point where other dislocations intersect, forming a dislocation node; or on itself, forming a closed dislocation loop (it is worth making the "closed" distinction, since dislocations between pinning nodes are often referred to as "loops").

Figure 7.87 should also illuminate the fact that dislocations are one-dimensional defects. Beyond the edge dislocation, a screw dislocation is the other primary type (which result in a helical nature of the lattice in its vicinity). Mixed dislocations are intermediate between these. In all cases, the crystal lattice is disturbed only along

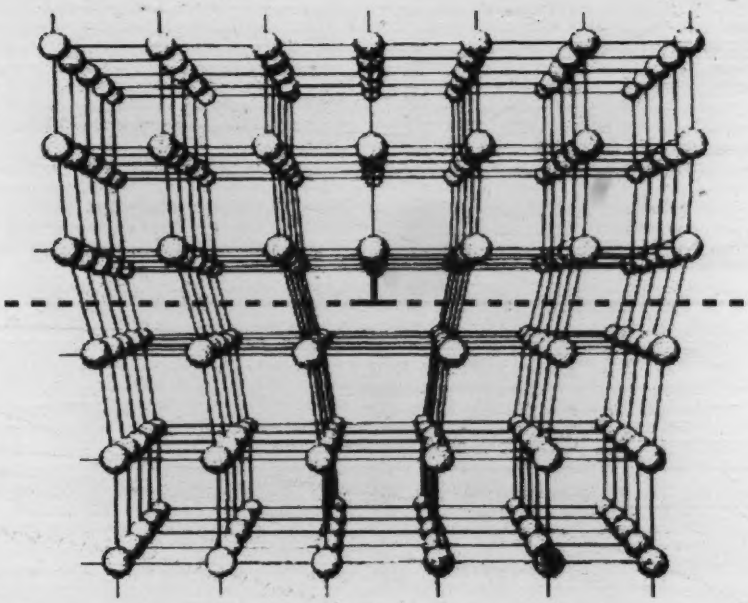

Figure 7.87: Schematic of an edge dislocation [171].

the dislocation line (ignoring the inverse-proportionally smaller elastic deformations that exist as we move away from the dislocation) and described at any point by its line vector $\vec{t}$(x,y,z).

The characteristic parameter of a dislocation is its Burgers vector, denoted $\vec{b}$(x,y,z), which specifies the magnitude and direction of the lattice distortion of dislocation in a crystal lattice. To determine $\vec{b}$ of a dislocation, a closed circuit surrounding the dislocation is traced in the real crystal. This circuit is then mapped onto an ideal crystal; the circuit does not close and the closure vector defines $\vec{b}$. The Burgers vector is perpendicular to the direction of an edge dislocation, and is parallel to the direction of a screw dislocation. The magnitude of $\vec{b}$ (= b) is a measure for the strength of the dislocation, or the amount of elastic deformation in the core of the dislocation. The glide plane is the plane defined by the Burgers vector $\vec{b}$ and the line vector $\vec{t}$. (A pure screw dislocation has no particular glide plane since $\vec{b}$ and $\vec{t}$ are parallel and thus do not define a plane. In principle, then, a screw dislocation could move on any plane; in practice, certain restrictions exist.)

The existence of a Burgers vector implies that the bonds between atoms in the dislocation core itself are not in an equilibrium configuration (i.e., at their minimum enthalpy), and so dislocations possess both energy (per unit of length, with a greater contribution coming from the elastic field than from the core) and entropy. Note in Figure 7.87 how the region above the dislocation (with the inserted half-plane) is in compression, while the region below the dislocation (without the half-plane) is in tension. As these atoms are displaced from their perfect lattice sites, the resulting distortion produces a displacement field in the crystal around the dislocation. The displacement field is given by $\vec{u}$(x,y,z), thus defining the displacement of atoms. The displacement field leads to the existence of a corresponding stress field and strain field. With the components u_x, u_y, u_z representing projections of $\vec{u}$ on the x, y, and z axes, the nine components of the strain tensor are directly given in terms of the first derivatives of these displacement components. The normal strains are given by the diagonal elements of the strain tensor:

$$\varepsilon_{xx} = \frac{du_x}{dx}; \quad \varepsilon_{yy} = \frac{du_y}{dy}; \quad \varepsilon_{zz} = \frac{du_z}{dz}. \tag{7.19}$$

The shear strains are given by the off-diagonal elements of the tensor:

$$\varepsilon_{yz} = \varepsilon_{zy} = \frac{1}{2}\left(\frac{du_y}{dz} + \frac{du_z}{dy}\right);$$

$$\varepsilon_{zx} = \varepsilon_{xz} = \frac{1}{2}\left(\frac{du_z}{dx} + \frac{du_x}{dz}\right); \tag{7.20}$$

$$\varepsilon_{xy} = \varepsilon_{yx} = \frac{1}{2}\left(\frac{du_x}{dy} + \frac{du_y}{dx}\right).$$

The dislocation, therefore, is a source of internal stress in the crystal. In all regions of the crystal except right at the center of the dislocation core, the stress is small enough to be treated by conventional linear elasticity theory. Moreover, it is generally sufficient to use isotropic theory, further simplifying things. If the elastic field is known, it is possible to calculate the force that a dislocation exerts on other dislocations, or, more generally, any interaction with elastic fields from other defects or from external forces can be calculated. It is also then possible to calculate the

energy contained in the elastic field produced by a dislocation. Calculations of this sort are beyond the scope of this thesis.

Also pertinent to the discussion of our results is that dislocations can be made to move, as shown in the cartoon of Figure 7.88. Panel A shows the application of an external force to the right on the top half of a crystal containing an edge dislocation and an external force to the left on the bottom half of the same crystal. When under the influence of external forces, internal stress are caused within the crystal. Panels B and C show how the bonds between atoms in the vicinity of the dislocation re-configure to minimize the internal stress. Panel D shows how the movement of a dislocation moves the whole crystal on one side of the glide plane relative to the other side. Plastic deformation therefore proceeds, atomic step by atomic step, by the (generation and) movement of dislocations.

If a dislocation is to move within a plane of atoms in the unit cell, a critical shear stress equal to the maximum of the Peierls potential is needed. The magnitude of this force varies periodically as the dislocation moves within the plane and through the crystal lattice. The Peierls stress also depends on the width of a dislocation core and the distance between planes. It decreases with increasing distance between atomic planes and, since the distance between planes increases with planar density, slip of the dislocation is preferred on closely packed planes.

7.7.2 Dislocation specifics

In a real crystal, dislocations will form a 3-dimensional network. The dislocations within the network are pinned at nodes where they intersect, and may be characterized by several parameters. Their Burgers vector $\vec{b}$ (on the order of an interatomic spacing) has already been discussed, but they may be further characterized by their density Λ (which is the total dislocation length per unit volume, and so carries units of m/m^3, or $\#/m^2$). The dislocation density Λ can vary in ^{4}He and is not easy to extract from measurements, which may not be sensitive to screw dislocations. The estimates of dislocation densities in solid helium come largely from analysis of acoustic/ultrasonic data. The ultrasonic estimates of [154, 155, 156] are the most likely to be quantitatively correct since they come from an analysis of the complete temperature and frequency dependence of sound velocities and attenuations. The low frequency acoustic measurements (e.g., [158]) and some of the ultrasonic measurements (e.g., [163]) are limited to a single low frequency or to temperatures

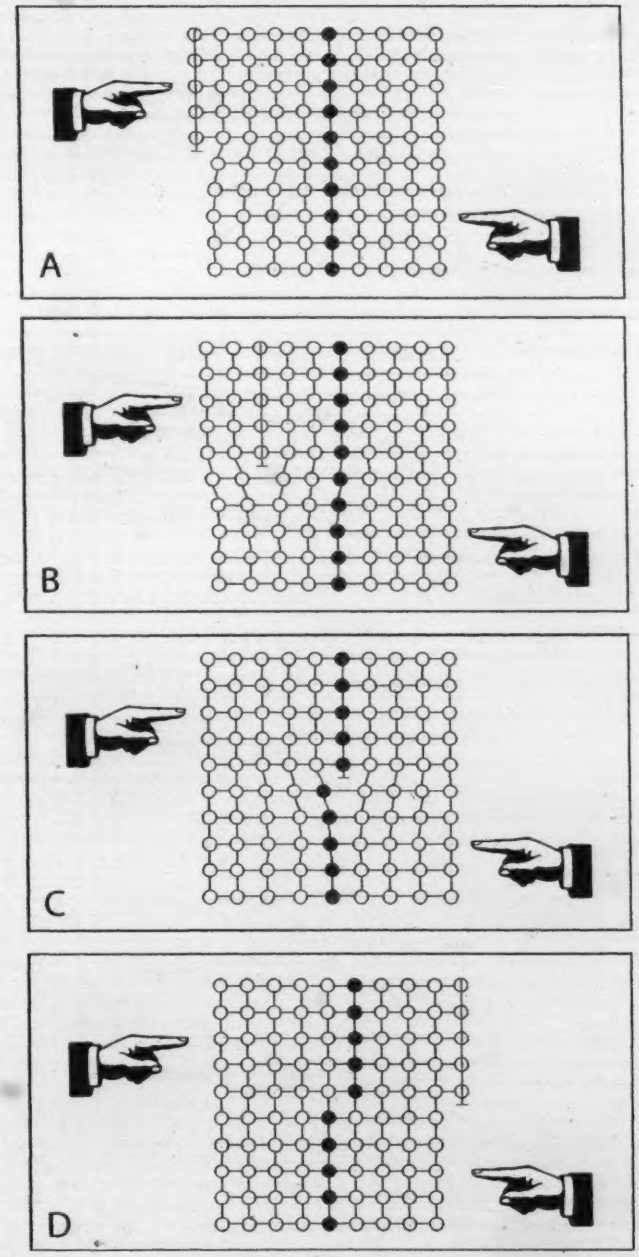

Figure 7.88: Schematic of dislocation movement.

relatively near melting. This is important, since the damping of dislocations is due to thermal excitations, largely phonons, and therefore is strongly temperature dependent ($\sim T^3$) and there is a frequency-dependent crossover from under-damped to over-damped motion of dislocations as T increases. As the ultrasonic measurements of [154, 155, 156] (3-50 MHz) required fairly high quality single crystals, they were all done with crystals grown at constant pressure. The work of [163] probably involved poorer quality crystals and might have inferred much higher dislocation densities. Typical values are $\Lambda = (10^6 - 10^5)$ cm^{-2}.

The network loop length between nodes L_N is another important characterizing parameter. Typical values are $L_N = (5 - 10) \times 10^{-6}$ m, but it should be noted that these come from ultrasonic measurements on relatively high quality single crystals [154, 155, 156]. Figure 7.89 shows a cartoon diagram of what is meant by the network loop length between nodes. More realistically, the dislocation loop length should likely be treated as an (exponential) distribution of lengths.

Dislocations can also be pinned, albeit less strongly, by crystallographic impurities - in the case of solid ^{4}He, by ^{3}He isotopic impurities. The impurity pinning length L_P (see Figure 7.90) is determined by the binding energy E_B between the impurity and a dislocation, the temperature T, and the impurity concentration x_3.

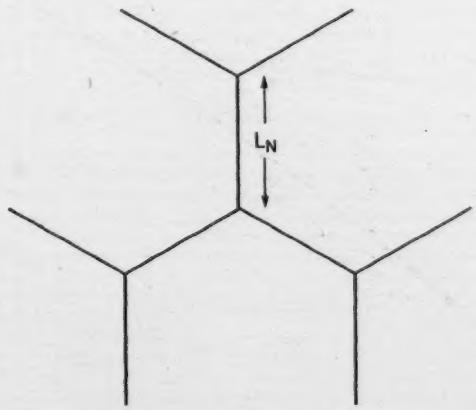

Figure 7.89: Schematic of a dislocation network, pinned at the intersection of dislocations.

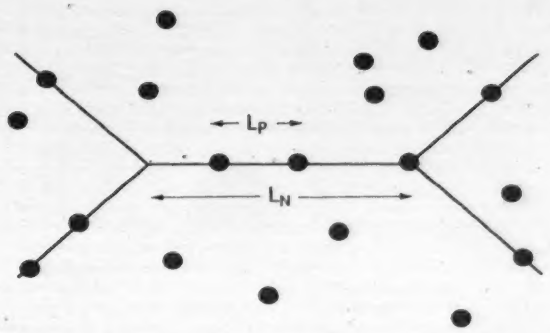

Figure 7.90: Schematic of a dislocation network, pinned at the intersection of dislocations and by ^{3}He impurity atoms (shown as small gray dots).

As outlined above, dislocations will move in response to a shear stress in their glide plane. For solid ^{4}He in the hcp phase, there is one dominant slip system (as in most hcp metals): edge dislocations gliding in the basal plane, perpendicular to the c-axis. (This motion is related to the total stress by an orientation factor R which accounts for the fact that only shear components of the stress normal to the Burgers vector act on the dislocation. R typically varies between 0 and 0.5 in hcp ^{4}He [172], and also depends on the type of dislocation.)

The motion of dislocations is well-described by the "vibrating string" model of Granato and Lücke [173]. In this model, a dislocation behaves like a damped vibrating string. The mathematical model for the equation of motion for the transverse displacement ξ(y,t) of the dislocation is

$$A\frac{\partial^2\xi}{\partial t^2} + B\frac{\partial\xi}{\partial t} - C\frac{\partial^2\xi}{\partial y^2} = b\sigma. \tag{7.21}$$

This is shown in Figure 7.91, where the plane of the paper is the slip plane. For Equation 7.21, A is the effective mass per unit length, B is the damping force per unit length, and C is the effective tension per unit length in a bowed out dislocation. The term on the right is the force per unit length exerted on the dislocation by the external shearing stress. The constants are given by $A = \pi\rho b^2$, where ρ is the density of the material and b is the Burgers vector, and $C = 2\mu b^2/\pi(1 - \nu)$, where μ is the shear modulus and ν is Poisson's ratio. Both the effective mass and the effective string tension result from the energy in the elastic strain field

around the dislocation. These expressions include only the elastic energy of the dislocation strain field and ignore the core structure of the dislocations, the effects of anisotropy, and the differences between edge and screw dislocations. The damping coefficient B is treated as a parameter to be determined from experiment, and is due to the interaction of thermal phonons with the dislocations (and, so, increase with temperature). The dominant contribution at low temperature is dislocation "flutter" [174] in the stress field of the thermal phonons, radiating energy and giving a low temperature damping $B \sim T^3$.

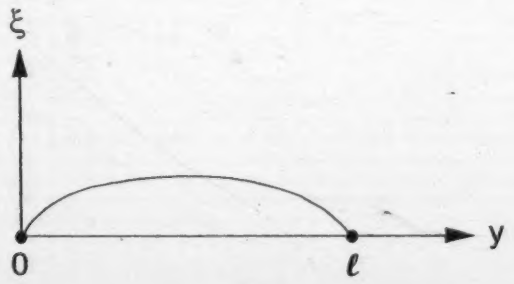

Figure 7.91: Bowed out dislocation. The dislocation has length ℓ. The displacement of the dislocation from its equilibrium position is given by ξ, while y denotes the coordinate of an element of the dislocation line.

Below the dislocation loops' resonance frequencies (typically in the MHz range), inertia and damping are not important and they simply bow out between pinning points like a rubber band, as was shown schematically in Figure 7.91. Such displacement creates a strain which adds to the elastic strain of the crystal and reduces the solid's shear modulus. For example, as this dislocation bows outward by some average displacement $\bar{\xi}$, an area $\bar{\xi}\ell$ is displaced by one Burgers vector b, giving a strain (due to dislocations):

$$\epsilon_d = R\Lambda b\bar{\xi}, \tag{7.22}$$

where the orientation factor R is included to find the strain in a particular direction (e.g., along an applied stress). In the static/DC limit, we ignore time-dependent

effects and Equation 7.21 simplifies to

$$-C\frac{\partial^2 \xi}{\partial y^2} = b\sigma, \tag{7.23}$$

for constant stress σ (i.e. independent of y). The solution to Equation 7.23 is

$$\xi(y) = -\frac{b\sigma}{2C}y^2 + dy + e. \tag{7.24}$$

Applying the boundary conditions $\xi(0) = 0$ and $\xi(\ell) = 0$ yields

$$\xi(y) = -\frac{b\sigma}{2C}y^2 + \frac{b\ell\sigma}{2C}y. \tag{7.25}$$

The average displacement of a dislocation, then, is

$$\overline{\xi} = \frac{1}{\ell}\int_0^\ell \xi(y)dy$$

$$= \frac{1}{12}\frac{b\ell^2\sigma}{C}$$

$$= \frac{\pi(1-\nu)}{24}\frac{\ell^2}{\mu b}\sigma. \tag{7.26}$$

Equation 7.22 can then be re-written as

$$\epsilon_d = \frac{\pi(1-\nu)}{24}R\Lambda\ell^2\frac{\sigma}{\mu}. \tag{7.27}$$

With $\sigma/\mu = \epsilon$, and ϵ_d equal to the dislocation-responsible change in this value (i.e., $\Delta\epsilon$), we find that

$$\frac{\Delta\epsilon}{\epsilon} = \frac{\Delta\mu}{\mu} = \frac{\pi(1-\nu)}{24}R\Lambda\ell^2. \tag{7.28}$$

In the absence of impurity pinning, ℓ is simply the network length L_N, which is largest for low density dislocation networks with few intersections. In annealed crystals with well-defined networks, $\Lambda L_N{}^2$ is a geometric constant (e.g., 3 for a

cubic network) and $\Delta\mu$ can be nearly independent of the dislocation density. (From ultrasound measurements of single crystals [175, 176, 154], it is usually found that $0.1 < \Lambda L_N{}^2 < 0.2$.) For the random orientations expected in polycrystalline samples, the average anisotropy factor R is about 0.2, so dislocations can reduce μ by as much as 30%.

When impurities are added, L_P can become smaller than L_N (recall Figures 7.89 and 7.90), reducing the dislocation strain. Impurity pinning is very effective since a single pinning site at the middle of a loop reduces its contribution to μ by a factor of four. At temperatures below E_B, impurities condense onto dislocations giving an enhanced concentration $x_D = x_3\, e^{\frac{E_B}{k_B T}}$, where x_3 is their bulk concentration. Pinning will be significant when x_D increases to the point where a typical dislocation loop has an impurity bound to it (i.e., when $x_D \approx a/L_N$, where a is the atomic spacing along the dislocation). This implies that the shear modulus will recover to its intrinsic value below a pinning temperature which decreases with impurity concentration:

$$T_P = -\frac{E_B}{k_B}\frac{1}{ln(\frac{L_N x_3}{a})} \tag{7.29}$$

Our results are consistent with this picture. Ultrasonic measurements [154, 155, 156] on helium single crystals give dislocation densities $\Lambda \sim 10^6$ cm^{-2} (polycrystals are expected to have higher densities). Typical loop lengths are ~ 5 μm, giving resonant frequencies ~ 15 MHz. Values of $R\Lambda L^2$ range from about 0.01 in ultrasonic experiments to 1.0 in a low frequency measurement [158]. The dominant slip system for hcp ^{4}He is edge dislocations gliding in the basal plane [177]. ^{3}He impurities bind to these with E_B/k_B in the range 0.3 K [154] to 0.7 K [158]. Using values $E_B/k_B = 0.6$ K, $a = 0.35$ nm, and $L_N = 5$ μm, we arrive at $T_P = 110$ mK for $x_3 = 0.3$ ppm, decreasing to 54 mK for $x_3 = 1$ ppb. This is very close to the temperatures where we observe μ to increase.

As a brief aside, Chan and collaborators also contemplate a crossover from network-pinning to impurity-pinning (when the average distance L_P between condensed ^{3}He atoms becomes less than L_N). Their x_3-dependent crossover temperature accounts for zigzagging of dislocations for energy minimization and is of the form

$$T_P = -2E_B\left(ln\left[\frac{{x_3}^2 {L_P}^3 E_B}{4\mu b^6}\right]^{-1}\right). \tag{7.30}$$

Here, b is the magnitude of the Burger's vector of a dislocation and μ is the shear modulus of ^{4}He. In order to reveal a possible connection between ^{3}He impurity-pinning and the observed x_3 dependence of NCRI, they identify crossover temperatures (i.e., the onset of NCRI) for varying levels of x_3 and fit Equation 7.30 to their data by adjusting the parameters L_P and E_B. Their best fit parameters ($L_P \sim 1.5$ μm and $E_B \sim 0.5$ K) are not inconsistent with those found in the literature.

A pinned dislocation is not forever immobile, however. Large stresses can tear dislocations away from ^{3}He pinning sites and reduce the shear modulus. The critical stress for this breakaway can be estimated [173] as about 4 Pa for $L_P = 5$ μm. This corresponds to a strain of $\epsilon \sim 3 \times 10^{-7}$, a level where we see strong amplitude dependence. Stress-induced breakaway can also produce hysteresis (e.g., if impurities are unable to bind to rapidly moving dislocations when a sample is cooled at large drive amplitudes [158]).

It is also useful to determine a relevant displacement (e.g., the amplitude of dislocation motion when behaviour of the shear modulus anomaly $\Delta\mu$ shows amplitude dependence). The maximum deviation of a dislocation is determined by setting $y = \ell/2$ in Equation 7.25 and is given by

$$\xi_m = \frac{\pi}{16}(1-\nu)\frac{\ell^2}{\mu b}\sigma. \tag{7.31}$$

Using typical values $\nu \approx 0.3$, $\ell \approx 5 \times 10^{-6}$ m, $b \approx 3.5 \times 10^{-10}$ m, and $\mu \approx 1.5 \times 10^7$ Pa, we get $\xi_m \approx (6.5 \times 10^{-10})\sigma$. In other words, the maximum displacement is roughly 2 lattice spacings per Pa. Our shear modulus measurements were made at stress levels $\sigma \approx 0.33$ Pa, corresponding to $\xi_m \approx 0.2$ nm. The amplitude dependence of $\Delta\mu$ was measured to set in at stress levels ~ 0.68 Pa, corresponding to $\xi_m \approx 0.4$ nm, or about one lattice spacing. As a comparison, the "critical displacement" inferred from torsional oscillator experiments is ~ 2 nm (the displacement of a dislocation can be much larger than the amplitude of torsional oscillator motion).

The increase in μ, its magnitude and frequency dependence, the temperature at which stiffening occurs and its dependence on ^{3}He concentration, the amplitude dependence and its associated hysteresis - these are all consistent with a picture of a network of dislocations pinned by ^{3}He impurities (using dislocation parameters determined in earlier experiments on hcp ^{4}He). The effects of annealing can be

understood in terms of changes in dislocation density Λ; note that $\Delta\mu$ depends only on the combination ΛL_N^2 and so can increase, decrease, or even remain unchanged when dislocations disappear.

To help illustrate this point, Figure 7.92 shows a cartoon example of a (cubic) network of dislocations. The dislocation density is given as the total dislocation length ($3L_N$) per unit volume (L_N^3), so that $\Lambda L_N^2 = 3$.

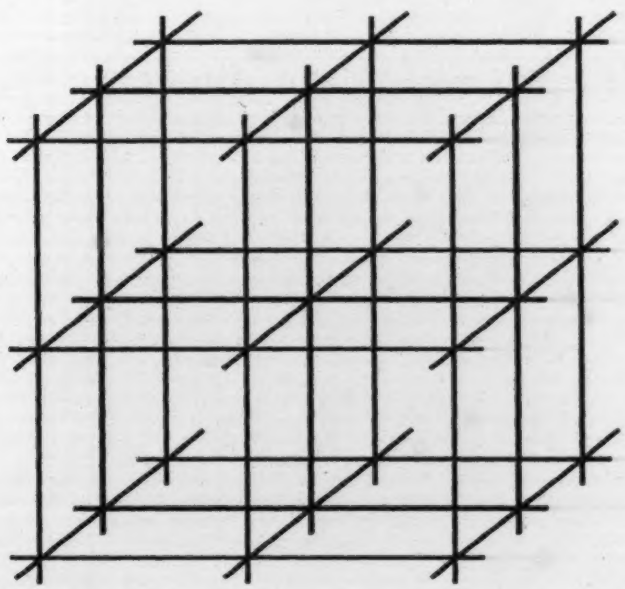

Figure 7.92: Schematic of a (cubic) dislocation network, pinned at the intersection of dislocations.

Annealing will result in some of these dislocations disappearing from the network. Figure 7.93 shows a cartoon of the (cubic) network of dislocations from Figure 7.92, with roughly half of the dislocations annealed away (i.e., removed). In this carefully chosen example, L_N has doubled, but Λ has been quartered, meaning that still $\Lambda L_N^2 = 3$. Removal of a different number of dislocations and/or of different specific dislocations can result in an increase or decrease in the product ΛL_N^2.

Large stresses were also observed to change $\Delta\mu$, probably by introducing more

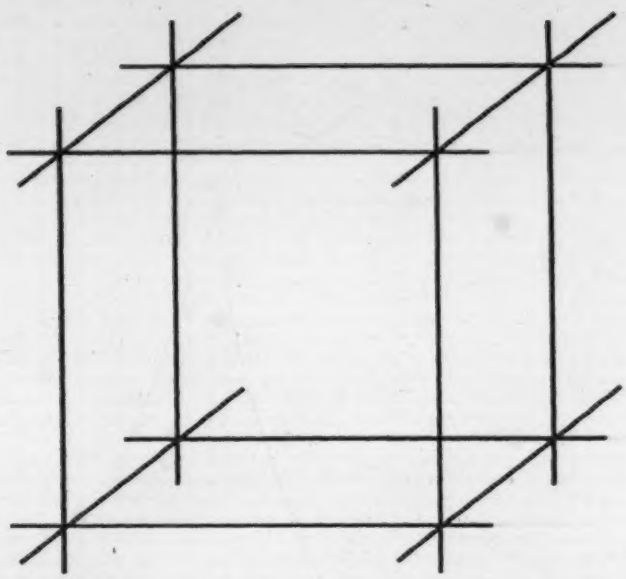

Figure 7.93: Schematic of an "annealed" (cubic) dislocation network, pinned at the intersection of dislocations.

dislocations or pinning existing ones, an effect also seen in ultrasonic measurements [156]. Overall, our experiments show that the low temperature modulus is largely unaffected by annealing or stressing, as expected since dislocations are then pinned by impurities. Instead, μ softens when the temperature is raised to the point where ^{3}He impurities are able to "boil off" from the dislocations, thereby allowing them to move in response to shear stress.

In contrast to our results, previous torsional measurements [158] on the shear modulus of solid hcp ^{4}He at comparable strains ($\epsilon = 10^{-7}$) showed no change between 0.5 K and 17 mK. The torsional oscillators in such experiments are run with solid ^{4}He only in the torsion rod (as opposed to also in the torsion bob); here, a torsional oscillator was used to make shear modulus measurements on solid ^{4}He at 331 Hz with torsional standing waves. With commercially pure ^{4}He (0.3 ppm ^{3}He) and at strains $\epsilon = 10^{-7}$, no change in μ was observed below 0.5 K. Interestingly, they do observe a softening of the solid sample, but at temperatures near 1 K. The temperature at which this transition occurs can be made to decrease with increasing strain, nearing 100 mK at relatively high strains $\epsilon = 10^{-5}$. With ultra-pure ^{4}He (nominally 2.4 ppb ^{3}He), no change in μ is observed at all, down to 17 mK. This is an apparent

discrepancy with our results. Unfortunately, it is not possible to be more specific since this difference is not understood, nor is it easy to speculate without more details on how they calibrated their strains and ^{3}He impurity concentrations.

7.7.3 In summary

The key features of the data presented in this chapter may all be well-understood in terms of the dislocation model of Granato and Lücke, outlined above, in which the dislocation lines between stable nodes can bend when stress is applied to the crystal. This elastic dislocation motion reduces the shear modulus.

^{3}He impurity atoms tend to bind to the dislocation lines at low temperatures and pin this dislocation motion. Such pinning decreases dislocation loop lengths and results in an intrinsic shear modulus μ at low temperature which is essentially unaffected by annealing or stressing the sample (processes which presumably change both dislocation number and density within the sample).

When the temperature is increased, the ^{3}He impurity atoms unbind from the dislocation lines and a break away occurs. Dislocation line lengths increase and the shear modulus μ of the solid softens; namely, we observe that $\Delta\mu/\mu \leq 30\%$, as expected from Equation 7.28. Furthermore, the temperature at which this crossover behaviour occurs as a function of bulk ^{3}He impurity concentration makes sense, as given by Equation 7.29.

As the applied strain is increased, the speed at which dislocations move increases and the more difficult it becomes for a ^{3}He impurity atom to condense on or "grab on" to dislocations. The result is that fewer ^{3}He impurity atoms serve as pinning sites and the dislocation loop lengths will, to a greater extent, remain unchanged as the temperature is reduced. With that, the magnitude of the shear modulus anomaly $\Delta\mu$ is decreased (and, under sufficiently high strain, made to disappear). If these quickly moving dislocations are then made to slow down (i.e., the applied strain is reduced) at low temperature, ^{3}He impurity atoms can then pin - and stay pinned - on the dislocations back up to large strains.

Chapter 8

Summary

This thesis began with an introduction to some of the basic concepts behind superfluidity and an extension of them to the solid phase of ^{4}He. Experimental data were then presented for: the freezing of ^{4}He under confinement; the pressure-induced flow of solid ^{4}He under confinement and in bulk; and, the elastic properties of solid ^{4}He at low temperatures, amplitudes, and frequencies. In this final chapter, I will try to bring together these concepts with the results of our experiments.

8.1 Summary of background material

Helium behaves quite differently from the heavier inert gas solids and solid helium is a uniquely 'quantum' solid. The van der Waals attraction is not capable of overcoming the quantum zero-point motion of the atoms and, unless external pressures are applied, helium will remain a liquid all the way down to absolute zero. Quantum effects play an important role in the fluid phase, as superfluidity exemplifies, and are likewise significant in the solid phase; consequently, it is important to study the fundamental properties of quantum solid helium.

One of the first works to consider the quantum nature of solid ^{4}He was by Andréev and Lifshitz [28], who proposed that its significant quantum fluctuations might, at low enough temperature, permit for a dilute gas of vacancies (i.e., non-thermal zero point vacancies) within the solid and that these could Bose-Einstein condense, resulting in a crystal that was neither a solid nor a liquid. This supersolid phase would possess the characteristic properties of a regular solid (e.g., a periodic lattice, a non-zero-shear modulus) but also share some properties with a superfluid namely (e.g., frictionless flow).

It wasn't until 2004, however, when Kim and Chan [9, 10] provided the first

supporting experimental evidence for supersolidity.

Using a solid ^{4}He-filled torsional oscillator, they have made observations consistent with a portion of the solid ^{4}He ceasing to oscillate with the rest of the system, flowing through the solid matrix without encountering any frictional resistance: namely, a supersolid phase transition. Importantly, the same result with solid ^{4}He has been reproduced in at least four other groups [53, 54, 55, 56].

8.2 Summary of experimental results

The four experiments described in this thesis, presented in the order in which they were performed, were all motivated by the remarkable supersolid interpretation of recent torsional oscillator results on solid ^{4}He. With them, we are able to provide evidence that supports the supersolid claim, as well as confounding it. The overall picture that emerges from these studies is that solid ^{4}He is proving to be at least as weird as anyone ever could have predicted. As strange as it is, however, we still find success in defining some of its fundamental mechanical properties.

8.2.1 Dielectric measurements of helium freezing in Vycor

In our first experiment, we studied how ^{4}He freezes when it is subjected to confinement on the nanometer scale, in porous Vycor glass (i.e., the system in which the supersolid state was first observed) [78]. This was directly motivated by the fact that obvious alternative explanations to the superfluid-like behaviour observed in the torsional oscillator experiments existed.

Some of these possible mechanisms were tied to the understanding that confinement can restrict freezing: perhaps the superfluid-like signal was actually coming from a liquid portion of the system. With that, we took some dielectric measurements of ^{4}He freezing in the pores of Vycor. We were able to confirm that the density change associated with freezing is substantially smaller than in bulk, which implies that not all of the ^{4}He in the pores is actually participating in solidification. (It could also mean, although this seems more unlikely, that all of the ^{4}He does indeed solidify, but that the volume change associated with freezing, for unknown reasons, is small in the pores of Vycor.) If some of the confined ^{4}He remained liquid, say as some thin film that coats the pore wall, then it is perfectly plausible that the superfluid-like behaviour observed in the torsional oscillator experiments is nothing more than superfluidity in that thin film. (Should this be the case, however, we

expect that the thickness of this film would be a function of pressure. Our measurements suggest otherwise, that the amount of ^{4}He that solidifies in the pores is independent of pressure.)

The presence of a persistent liquid layer, then, cannot be ruled out. In fact, there very likely exists an amorphous ^{4}He film strongly adsorbed to the pore wall, having a density already near that of the solid phase and thereby minimally contributing to the change in density upon freezing. Path Integral Monte Carlo (PIMC) simulations [142] and Variational Monte Carlo simulations [143] both support the persistent liquid layer model to explain the NCRI observations. Our density change measurements of solid ^{4}He in Vycor ($\sim$ 70% of the bulk value) suggest a thickness of this film corresponding to 3-4 layers of adsorbed ^{4}He and is consistent with these Monte Carlo results.

Some other potential mechanisms are cultivated from the understanding that a torsional oscillator is a highly sensitive probe of the moment of inertia of a system (i.e., its total mass along with how that mass is distributed). For example, the pores of Vycor are small enough that it isn't obvious which (if any) crystallographic phase the solid ^{4}He within takes. Should the solid undergo a crystallographic phase transition, it might re-distribute its mass and, therefore, change the system's moment of inertia. Just as a figure skater spins faster by pulling in her arms, so too might a torsional probe oscillate more quickly if its solid ^{4}He matrix shuffles into a tighter packing fraction.

Alternatively, one should keep in mind that solid ^{4}He is a notoriously poor wetter of surfaces. It is known that solid H_2 undergoes a de-wetting transition from Vycor at reduced temperatures [116], causing the solid H_2 to be expelled from its Vycor confines and reducing the period of the torsional probe taking measurements on that very same piece of Vycor. It was worth confirming that a similar phenomena does not occur with solid ^{4}He. Indeed, it does not. We found no evidence of any sudden density changes, such as a crystallographic phase transition, nor any signs of the solid ^{4}He leaving the Vycor, such as a de-wetting transition, at low temperatures. Any such behaviour would have altered the moment of inertia in a torsional oscillator and could have mimicked mass decoupling. Our results leave little doubt that the solid ^{4}He stays put at low temperatures.

8.2.2 Pressure-induced flow of solid helium

Our first set of measurements, described in the previous section, effectively ruled out some of the most obvious alternative explanations to the NCRI observed for solid ^{4}He in Vycor: they seemed to strengthen the supersolid claim. With that, it became extremely interesting to see whether solid ^{4}He would exhibit any of the other unusual flow properties of a superfluid. Of course, no one could say how a supersolid should behave - no one had ever studied one before. All one could go on was the (perhaps naïve) assumption that a supersolid would behave in roughly the same way as a superfluid. Besides, if we knew exactly what we were doing, it wouldn't be research.

Some of the unusual properties of superfluids that one could explore in solid ^{4}He include superleaks, persistent currents, second sound, and quantized vortices. We chose to study the response of solid ^{4}He to pressure differences, in order to look for unusual flow properties that might be associated with supersolidity. Superflow is a hallmark of superfluidity in liquid ^{4}He; it is natural to look for this in the region where solid ^{4}He decouples from torsional oscillators. An early experiment [41] solidified ^{4}He in two chambers with pressure differences (of order 1 bar) between them, but saw no flow through the solid ^{4}He in the connecting capillaries, implying either that superflow only occurred below the lowest temperature of the measurement (30 mK) or that it had a critical velocity much smaller than the 10 μm/s inferred from Kim and Chan's torsional oscillator results. A later experiment [43] extended to lower temperatures (4 mK) without seeing any flow through solid ^{4}He. The pressure difference was established by different liquid-solid interface heights in a U-tube, so this experiment was necessarily done at coexistence on the melting curve.

While two null results had already been obtained, neither studied solid ^{4}He in the pores of Vycor. We also felt that we could significantly improve on the sensitivity of these previous measurements. So, we studied the flow of solid ^{4}He in response to pressure differences: in our first such experiment, the ^{4}He was confined in the pores of Vycor [78]; in the second, we studied bulk solid [79] in an experiment conceptually similar to that of Greywall [41]. Both experiments used a beryllium copper cell with a flexible diaphragm and an in situ capacitive pressure gauge. The diaphragm was coupled to an external piezoelectric (PZT) actuator stack to compress the ^{4}He

inside the cell. In both sets of experiments, the ^{4}He was always solidified using the blocked capillary method and the cell was always initially filled with liquid at sufficiently high pressure to ensure that the ^{4}He in all internal volumes would freeze at low temperatures. Pressure gradients grown into the sample during solidification were eliminated by annealing our samples near their melting temperatures before beginning our flow measurements.

8.2.2.1 Vycor

For the Vycor experiment, our sample was a Vycor disc onto which copper electrodes were evaporated, to measure (via the sample's capacitance) the density of the helium within the pores. A typical flow measurement then involved suddenly compressing the ^{4}He by applying a voltage to the piezoelectric actuator, forcing the ^{4}He to flow into the pores of the Vycor, while monitoring it via the sample capacitance.

The sample responded to the applied pressure step in two stages. First, there was an initial jump in density capacitance simply due to the elastic compression of the Vycor capacitor. Second, as solid ^{4}He then flowed into the Vycor pores to equilibrate the pressures after compression, the density capacitance increased further, at a slower rate reflecting the flow velocity of the solid ^{4}He. The rate of flow was strongly dependent on temperature, occurring most rapidly at higher temperatures (e.g., equalizing pressures in less than a minute very near to melting). Below about half of the melting temperature (in the neighborhood of 1 K), the flow was too slow to measure. The temperature dependence that we observed was consistent with mass transport via a thermally activated process, with an activation energy of about 8 or 9 K. Lower temperature measurements (e.g., around 0.5 K) showed no flow (and only the initial elastic jump).

The most interesting question, of course, was whether or not we would observe any flow in the temperature range below 200 mK, where Kim and Chan saw decoupling of solid helium from Vycor [9]. The answer to that question was no. Our data allowed us to put an upper limit of 3 nm/s on any superflow at low temperatures. This limit is considerably smaller than the critical velocity of about 10 μm/s inferred from the torsional oscillator measurements.

8.2.2.2 Bulk

For the bulk experiments, the cell was divided into two chambers. The larger chamber (0.49 cm^3) included the diaphragm and the smaller one (0.01 cm^3) had a pressure gauge. The chambers were separated by a glass capillary array (GCA), a plate containing 36,000 parallel capillaries, each 3 mm long and 25 μm in diameter, through which the ^{4}He could flow. The ^{4}He was always solidified using the blocked capillary method and the cell was initially filled with liquid at sufficiently high pressure to ensure that all the ^{4}He in and around the GCA channels would freeze at low temperatures. Pressure gradients grown into the sample during solidification were eliminated by annealing our samples near their melting temperatures before beginning our flow measurements. Our bulk flow measurements were done in a similar way to those of Vycor: a typical flow measurement involved suddenly compressing the ^{4}He by applying a voltage to the piezoelectric actuator, forcing the ^{4}He to flow through the channels of the GCA, while monitoring the flow into the smaller chamber via the pressure gauge.

Not surprisingly, we found that liquid flows easily through the GCA channels, keeping the two chambers in pressure equilibrium after a compression and serving as a calibration of our diaphragm and piezoelectric stack. (A voltage step of 150 V applied to the stack produced a pressure change of 84 mbar, implying a volume change of 0.03% and a diaphragm deflection of about 1 μm.) Also not very surprisingly, we observed that the solid near melting (e.g., within about 10 mK) does flow in response to an applied pressure difference; the pressures in the two chambers equilibrated within about half an hour (compared to a second or less for liquid helium). As the temperature is lowered, even if just by another 10 mK, the pressures did not completely equilibrate. Below about half of the melting temperature of the crystal (around 1 K) we saw no evidence of flow. For example, the effect of a compression at 0.5 K was an immediate smaller (38 mbar) pressure response in the second chamber, but this was simply a reflection of the elastic bending of the GCA plate (analogous to the elastic compression of the Vycor sample) due to the pressure gradient across it. (A pressure difference of 100 mbar due to compressing the solid in the larger chamber bent the plate by about 30 nm, thus compressing the solid ^{4}He in the smaller chamber and producing this observed pressure step.) There was no subsequent pressure change that would indicate flow between the two chambers

and the pressure returned immediately to its original value when the diaphragm was released.

We looked for unusual pressure-induced flow below 200 mK, again and to no avail. The response of a squeeze at 35 mK was identical to the response at 0.5 K, with no evidence of flow through the channels. After having monitored the pressure following a squeeze for up to 20 hours with the same null result, we put an extremely stringent limit on the pressure-induced superflow in solid ^{4}He at low temperatures of 1.2 x 10^{-12} m/s. This is seven orders of magnitude smaller than the 10 μm/s critical velocity inferred from the torsional oscillator amplitude dependence.

In these experiments, we also compared the flow of isotopically pure ^{4}He (about 1 ppb ^{3}He) to that of commercial helium (about 0.3 ppm ^{3}He). The behavior was essentially identical, making it unlikely that ^{3}He impurity atoms are somehow responsible for the absence of flow at low temperatures.

In short, our experiments show that static pressure gradients do not produce superflow at low temperatures in solid ^{4}He. If the NCRI seen in torsional oscillator measurements is due to supersolidity, we conclude that its behavior must be quite different from that of a superfluid.

Of course, the amplitude dependence of the decoupling seen in the torsional oscillator measurements does not have to be due to a critical velocity v_c (about 10 μm/s). For example, it could be due to an effect that depends on the maximum displacement $x_c = v_c/\omega$ (about 2 nm) or one that depends on the maximum acceleration $a_c = v_c\omega$ (about 0.1 m/s^2) of the solid ^{4}He, and the distinction is important in comparing experiments at different frequencies. For example, a limit on displacement could prevent a DC measurement (like ours) from observing superflow. Alternatively, a limit on acceleration could prevent high frequency ultrasonic measurements (like those on solid ^{4}He in Vycor [104, 144]) from observing the decoupling of a supersolid component.

Keeping this in mind, we looked for AC flow in our measurements (albeit at rather low frequencies, 0.01 to 1 Hz) but saw no evidence of solid ^{4}He motion through the GCA channels at low temperatures. With these AC measurements, we put an upper limit on the average displacement of the ^{4}He in our work of about 0.03 nm. If only the 1% NCRI fraction moves, this corresponds to a 3 nm motion: slightly larger than the displacement at which NCRI starts to decrease in Kim and Chans experiments. So, we can not rule out the possibility of a critical displacement.

Dislocations provide one mechanism for limiting displacements in solid ^{4}He. This was the line of thinking that carried us into our final set of experiments.

8.2.3 Shear modulus study of solid helium

Mass can be transported by the motion of dislocations, and dislocations can be pinned by ^{3}He impurities, even at the ppm level [154, 175], or by interactions with other defects and surfaces. That the torsional oscillator results [52] are so extremely sensitive of ^{3}He (down to the ppb level!) might serve as a clue that dislocations are somehow or another involved in the observed NCRI. Decoupling is usually larger in narrow annuli than in open cylinders [57] but begins at similar temperatures; its magnitude (and its elimination) also depends on how the solid ^{4}He was grown and annealed, and strongly suggests that the NCRI behavior involves defects. Theoretical work [71, 61, 81, 75, 83, 153] also suggests that defects are involved. These should also affect the solid's mechanical behaviour and this was the driving force behind our final set of experiments.

In an investigation of elastic properties, we have made the first direct measurement of the shear modulus of solid ^{4}He at low temperatures. This study required the development of a new experimental technique, although conceptually quite simple. A sample of solid ^{4}He is grown between two parallel plates (piezoelectric shear transducers). One plate, the driving transducer, is moved in a direction parallel to the second plate. The solid ^{4}He transmits the resulting elastic shear stress between the plates, and this is measured by the second plate, the detecting transducer. This new method allowed us to measure the shear modulus μ of solid ^{4}He directly at strains (stresses) as low as $\varepsilon = 2.2 \times 10^{-9}$ ($\sigma = 0.03$ Pa). this is two to three orders of magnitude lower than in previous torsional [158], internal friction [157], and ultrasonic measurements [154, 155]. We also measured μ at frequencies as low as 20 Hz, far lower than in any previous experiments.

What we found was that the shear modulus μ of solid ^{4}He increases by about $\Delta\mu \sim 10\%$ as the temperature is reduced from 200 mK to 20 mK. More significant than the existence of $\Delta\mu$ alone was that the temperature dependence of $\Delta\mu$ closely tracks the decoupling in the torsional oscillator experiments. Furthermore, it has the same dependence on measurement amplitude, ^{3}He impurity concentration, and annealing as the decoupling seen in torsional oscillator experiments.

This unusual effect was confirmed through a simultaneous measurement of the

frequency and damping of a resonance in our sample (outside of the gap, surrounding the transducers). This resonance was also found to have the same dependence on temperature, measurement amplitude, ^{3}He isotopic impurity concentration, and annealing as the torsional oscillator results. This is the first clear observation of directly related phenomena in other properties of solid ^{4}He.

Upon observing this phenomena, thought was given to what might be the root cause of these effects. While a solid's strength and shear modulus are indeed a function of the intrinsic nature of the perfect crystalline solid, they also depend strongly on defects within the solid (such as dislocations and grain boundaries). Noteworthy is the knowledge that the same seems to be true for the torsional oscillator experiments, in which the results depend on the quality of the crystal, with the largest effects seen in the most defective samples. Indeed, dislocations can dramatically affect elastic properties (e.g., can produce a frequency-independent reduction of the shear modulus [173] as large as 30%) and lead to unusual behaviour in quantum crystals [162].

The results we obtained are well-explained as the behaviour of dislocations and their interaction with trace amounts of ^{3}He impurities in the solid ^{4}He. When dislocations are free to move in response to a shear stress, they can relax the stress in a crystal and so lower its shear modulus. Impurities of ^{3}He tend to bind to dislocations in solid ^{4}He at low temperatures [154] and so can restrict their motion. As the temperature is increased, the ^{3}He unbinds from the dislocations and a breakaway, allowing the dislocations to move more freely and reducing μ. The observed dependence of the shear modulus on the concentration of ^{3}He is consistent with this idea.

As it was torsional oscillator results which motivated this work and as the two sets of measurements share all essential features (even though they measure very different properties - shear modulus and sound speed versus moment of inertia and density), one can't help but ask: is the shear modulus anomaly directly related to the frequency shifts and dissipation in torsional oscillator experiments?

The anomalous behaviours have the same temperature dependence and both transitions are accompanied by similar dissipation peaks. They are both strongly amplitude dependent (starting at comparable stress levels) as well as having very similar amplitude-dependent hysteresis at low temperatures. In both types of measurements, the magnitude of the anomaly is frequency independent, but its onset

is broadened and shifts to higher temperature with increasing frequency. Tiny ^{3}He impurity concentrations have the same sort of dramatic effect on the onset temperature, and annealing changes the magnitude of both anomalies.

Considering these remarkable similarities, it seems safe to say that the two sets of effects are related. This, then, raises the more challenging issue of determining how the two sets of effects are related.

One possibility is that the modulus increase stiffens the torsional oscillator, increasing its frequency and mimicking mass decoupling. Interpreting a torsional oscillator frequency as a direct measure of mass assumes that the oscillator head is infinitely stiff and that the solid helium moves rigidly with its walls, neither of which is exactly true. We initially stated [178] that an increase in the shear modulus of ^{4}He would improve its coupling to the torsional oscillator and thus decrease its frequency (that is, the opposite of the observed behaviour). However, we have since been shown that this statement is incorrect [179]; namely, that the stiffening of the solid ^{4}He shear modulus would increase the frequency of a torsional oscillator. The question then is whether the increase in the ^{4}He shear modulus observed at low temperatures (which will increase the torsional oscillator frequency and so mimic decoupling) is of the right magnitude. The answer to this query is reserved for another student, and another thesis.

Alternatively, an increase in μ could raise the frequency of a torsional oscillator by increasing the stiffness of its head (which is assumed to be infinite for an ideal model of a torsional oscillator). Preliminary estimates for typical oscillators suggest that this effect is several orders of magnitude too small to account for the observed decoupling. However, simulations are underway in an effort to confirm the magnitude of these sorts of effects [160], as the effect is sensitive to the details of the torsional oscillator design. It should also be remembered that when the flow path in a torsional oscillator annulus is blocked the decoupling is nearly eliminated, even though this would barely change the contribution by the solid ^{4}He to its stiffness. Our observations do not provide an obvious mechanical, non-supersolid explanation of the frequency changes in torsional oscillators (recall that there is strong evidence for frequency independence of the NCRI).

It is perfectly plausible that the μ anomaly and the decoupling observed in torsional oscillator measurements are both fundamental properties of a supersolid phase [94]. If this were the case [83, 153], then it would be natural for them to have

a common dependence on temperature, ^{3}He, et cetera.

However, it is not unreasonable to argue that mobile dislocations could affect a supersolid response. Perhaps the torsional oscillators truly are observing a supersolid state, and our shear experiment has allowed for us to observe behaviour which kills the supersolid state. For example, vortices [96] could be pinned by stationary dislocations but could introduce dissipation and destroy the supersolidity when dislocations begin to move above 100 mK.

The decoupling seen in porous media [10] remains a puzzle, as it is hard to imagine dislocations existing, let alone moving, in the 7 nm pores of Vycor glass. The precise connection between our elastic measurements and decoupling of solid helium from torsional oscillators is not certain, but it is clear that the two are closely related and that models of supersolidity should consider the effects of moving dislocations.

Bibliography

[1] M. W. Meisel, Physica B **178**, 121 (1992).

[2] N. Prokof'ev, Adv. Phys. **56**, 381 (2007).

[3] nobelprize.org.

[4] J. F. Allen and A. D. Misener, Nature **141**, 75 (1938).

[5] P. Kapitza, Nature **141**, 74 (1938).

[6] F. London, Nature **141**, 643 (1938).

[7] L. Tisza, Nature **141**, 913 (1938).

[8] L. Landau, Phys. Rev. **60**, 356 (1941).

[9] E. Kim and M. H. W. Chan, Science **305**, 1921 (2004).

[10] E. Kim and M. H. W. Chan, Nature **427**, 225 (2004).

[11] J. Wilks, *The Properties of Liquid and Solid Helium*, Clarendon Press, Oxford, 1967.

[12] D. R. Tilley and J. Tilley, *Superfluidity and Superconductivity*, Adam Hilger, Ltd, Bristol, 1986.

[13] T. Guenault, *Basic Superfluids*, Taylor & Francis, New York, 2003.

[14] J. F. Allen and A. D. Misener, Proc. R. Soc. A **172**, 467 (1939).

[15] J. D. Reppy and D. Depatie, Phys. Rev. Lett. **12**, 187 (1964).

[16] A. D. Woods and A. C. Hollis Hallett, Can. Phys. J. **41**, 596 (1963).

[17] E. L. Andronikashvili, Zh. Eksp. Teor. Fiz. **16**, 780 (1946).

[18] A. J. Leggett, Science **305**, 1921 (2004).

[19] G. B. Hess and W. M. Fairbank, Phys. Rev. Lett. **19**, 216 (1967).

[20] W. Meissner and R. Ochsenfel, Naturwiss. **21**, 787 (1933).

[21] D. G. Henshaw and A. D. B. Woods, Phys. Rev. **121**, 1266 (1961).

[22] J. R. Beamish, *Handbook of Elastic Properties of Solids, Liquids, and Gases*, volume 2, Academic Press, San Diego, 2001.

[23] C. Domb and J. S. Dugdale, Prog. Low Temp. Phys. **2**, 338 (1957).

[24] J. de Boer, Physica **14**, 139 (1948).

[25] O. Penrose and L. Onsager, Phys. Rev. **104**, 576 (1956).

[26] L. D. Landau and E. M. Lifshitz, *Statistical Physics*, Pergamon Press, Oxford, 1958.

[27] M. Liu, Phys. Rev. B **18**, 1165 (1978).

[28] A. F. Andreev and I. M. Lifshitz, Sov. Phys. JETP **29**, 1107 (1969).

[29] G. V. Chester, Phys. Rev. A **2**, 256 (1970).

[30] A. J. Leggett, Phys. Rev. Lett. **25**, 1543 (1970).

[31] W. M. Saslow, Phys. Rev. Lett. **36**, 1151 (1975).

[32] R. A. Guyer, Phys. Rev. Lett. **26**, 174 (1971).

[33] R. P. Giffard and J. Hatton, Phys. Rev. Lett, **18**, 1106 (1967).

[34] D. S. Miyoshi, R. M. Cotts, A. S. Greenberg, and R. C. Richardson, Phys. Rev. A **2**, 870 (1970).

[35] B. A. Fraass, P. R. Granfors, and R. O. Simmons, Phys. Rev. B **39**, 124 (1989).

[36] R. O. Simmons, J. Phys. Chem. Solids **55**, 895 (1994).

[37] A. F. Andreev, K. Keshishev, L. Mezhov-Deglin, and A. Shal'Nikov, Sov. Phys. JETP Lett. **9**, 306 (1969).

[38] H. Suzuki, J. Phys. Soc. Japan **35**, 1472 (1973).

[39] V. L. Tsymbalenko, Sov. Phys. JETP Lett. **23**, 653 (1976).

[40] N. E. Dyumin, S. V. Svatko, and V. N. Grigor'ev, Sov. J. Low. Temp. Phys. **15**, 295 (1989).

[41] D. S. Greywall, Phys. Rev. B **16**, 1291 (1977).

[42] D. J. Bishop, M. A. Paalanen, and J. D. Reppy, Phys. Rev. B **24**, 2844 (1981).

[43] G. Bonfait, H. Godfrin, and B. Castaing, J. de Phys. **50**, 1997 (1989).

[44] W. H. Keesom and A. P. Keesom, Leiden. Comm. **224**, d (1933).

[45] D. D. Osheroff, R. C. Richardson, and D. M. Lee, Phys. Rev. Lett. **28**, 885 (1972).

[46] W. P. Halperin, C. N. Archie, F. B. Rasmussen, R. A. Buhrman, and R. C. Richardson, Phys. Rev. Lett. **32**, 927 (1974).

[47] E. D. Adams, M. W. Meisel, S. E., and J. S. Xia, Bull. Am. Phys. Soc. **35**, 1080 (1990).

[48] P. G. van de Haar, C. M. C. M. van Woerkens, M. W. Meisel, and G. Frossati, J. Low Temp. Phys. **86**, 349 (1991).

[49] G. A. Lengua and J. M. Goodkind, J. Low Temp. Phys. **79**, 251 (1990).

[50] E. Kim and M. H. W. Chan, J. Low. Temp. Phys. **138**, 859 (2005).

[51] E. Kim and M. H. W. Chan, Phys. Rev. Lett. **97**, 115302 (2006).

[52] E. Kim, J. S. Xia, J. T. West, and M. H. W. Chan, Bull. Am. Phys. Soc. **52**, 610 (2007).

[53] M. Kondo, S. Takada, Y. Shibayama, and K. Shirahama, J. Low Temp. Phys. **148**, 695 (2007).

[54] A. S. C. Rittner and J. D. Reppy, Phys. Rev. Lett. **97**, 165301 (2006).

[55] A. Penzev, Y. Yasuta, and M. Kubota, J. Low Temp. Phys. **148**, 677 (2007).

[56] Y. Aoki, J. C. Graves, and H. Kojima, Phys. Rev. Lett. **99**, 015301 (2007).

[57] A. S. C. Rittner and J. D. Reppy, Phys. Rev. Lett. **98**, 175302 (2007).

[58] A. C. Clark, J. T. West, and M. H. W. Chan, Phys. Rev. Lett. **99**, 135302 (2007).

[59] L. Reatto, Phys. Rev. **183**, 334 (1969).

[60] C. N. Yang, Rev. Mod. Phys. **34**, 694 (1962).

[61] N. Prokof'ev and B. Svistunov, Phys. Rev. Lett. **94**, 155302 (2005).

[62] B. K. Clark and D. M. Ceperley, Phys. Rev. Lett. **96**, 105302 (2006).

[63] L. H. Nosanow, Phys. Rev. Lett. **13**, 270 (1964).

[64] H. Zhai and Y.-S. Wu, J. Stat. Mech. **July**, P07003 (2005).

[65] B. Chadhuri, F. Pederiva, and G. V. Chester, Phys. Rev. B **60**, 3271 (1999).

[66] D. E. Galli, M. Rossi, and L. Reatto, Phys. Rev. B **71**, 140506(R) (2005).

[67] P. W. Anderson, W. F. Brinkman, and D. A. Huse, Science **310**, 1164 (2005).

[68] M. Boninsegni, N. Prokof'ev, and B. Svistunov, Phys. Rev. E **74**, 036701 (2006).

[69] M. Boninsegni et al., Phys. Rev. Lett. **97**, 080401 (2006).

[70] F. Pederiva, G. V. Chester, S. Fantoni, and L. Reatto, Phys. Rev. B **56**, 5909 (1997).

[71] D. M. Ceperley and B. Bernu, Phys. Rev. Lett. **93**, 155303 (2004).

[72] D. E. Galli and L. Reatto, Phys. Rev. Lett. **96**, 165301 (2006).

[73] D. M. Ceperley, Rev. Mod. Phys. **67**, 279 (1995).

[74] R. R. Aziz, A. R. Janzen, and M. R. Moldover, Phys. Rev. Lett. **74**, 1586 (1995).

[75] M. Boninsegni, N. Prokof'ev, and B. Svistunov, Phys. Rev. Lett. **96**, 105301 (2006).

[76] D. E. Galli and L. Reatto, J. Low Temp. Phys. **124**, 197 (2001).

[77] G. D. Mahan and H. Shin, Phys. Rev. B **74**, 214502 (2006).

[78] J. Day, T. Herman, and J. Beamish, Phys. Rev. Lett. **95**, 035301 (2005).

[79] J. Day and J. Beamish, Phys. Rev. Lett. **96**, 105304 (2006).

[80] E. Burovski, E. Kozik, A. Kuklov, N. Prokof'ev, and B. Svistunov, Phys. Rev. Lett. **94**, 165301 (2005).

[81] L. Pollet et al., Phys. Rev. Lett. **98**, 135301 (2007).

[82] S. Sasaki, R. Ishiguro, F. Caupin, H. J. Maris, and S. Balibar, Science **313**, 1098 (2006).

[83] M. Boninsegni et al., Phys. Rev. Lett. **99**, 035301 (2007).

[84] J. G. Dash and J. S. Wettlaufer, Phys. Rev. Lett. **94**, 235301 (2005).

[85] G. D. Mahan and H. Shin, Euro. Phys. Lett. **78**, 36002 (2007).

[86] A. C. Clark and M. H. W. Chan, J. Low Temp. Phys. **138**, 853 (2005).

[87] A. V. Balatsky, M. J. Graf, Z. Nussinov, and S. A. Trugman, Phys. Rev. B **75**, 094201 (2007).

[88] Z. Nussinov, A. V. Balatsky, M. J. Graf, and S. A. Trugman, Phys. Rev. B **76**, 014530 (2007).

[89] I. Iwasa, unpublished.

[90] G. Baskaran, *arXiv:cond-mat/0505160.*

[91] N. Kumar, Pramana J. Phys. **67**, 101 (2006).

[92] W. M. Saslow, Int. J. of Mod. Phys. B **20**, 5093 (2006).

[93] J. Ye, Phys. Rev. Lett. **97**, 125302 (2006).

[94] A. T. Dorsey, P. M. Goldbart, and J. Toner, Phys. Rev. Lett. **96**, 055301 (2006).

[95] D. T. Son, Phys. Rev. Lett. **94**, 175301 (2005).

[96] P. W. Anderson, Nature **3**, 160 (2007).

[97] X. Lin, A. C. Clark, and M. H. W. Chan, Nature **449**, 1025 (2007).

[98] V. N. Grigorev et al., *arXiv:cond-mat/0702133.*

[99] I. A. Todoshchenko et al., Phys. Rev. Lett. **97**, 165302 (2006).

[100] I. A. Todoshchenko, H. Alles, H. J. Junes, A. Y. Parshin, and V. Tsepelin, JETP Lett. **85**, 454 (2007).

[101] S. O. Diallo et al., Phys. Rev. Lett. **98**, 205301 (2007).

[102] M. A. Adams, J. Mayers, O. Kirichek, and R. B. E. Down, Phys. Rev. Lett. **98**, 085301 (2007).

[103] E. Blackburn et al., Phys. Rev. B **76**, 024523 (2007).

[104] T. Kobayashi, S. Fukazawa, J. Taniguchi, M. Suzuki, and K. Shirahama, AIP Conf. Proc. **850**, 333 (2006).

[105] Y. Mukharsky, O. Avenal, and E. Varoquaux, J. Low Temp. Phys. **148**, 689 (2007).

[106] Y. Aoki, X. Lin, and H. Kojima, J. Low Temp. Phys. **148**, 659 (2007).

[107] W. M. Saslow, Phys. Rev. B **15**, 173 (1977).

[108] private communication with R. B. Hallock.

[109] private communication with J. C. S. Davis.

[110] G. C. Straty and E. D. Adams, Rev. Sci. Inst. **40**, 1393 (1969).

[111] www.tra-con.com.

[112] H. Preston-Thomas, Metrologia **27**, 3 (1990).

[113] R. L. Rusby et al., AIP Conf. Proc. **684**, 77 (2003).

[114] D. S. Greywall and P. A. Busch, J. Low Temp. Phys. **46**, 451 (1982).

[115] P. M. Berglund, H. K. Collan, G. J. Ehnholm, R. G. Gylling, and O. V. Lounasmaa, J. Low. Temp. Phys. **6**, 357 (1972).

[116] M. Schindler, A. Dertinger, Y. Kondo, and F. Pobell, Phys. Rev. B **53**, 11451 (1996).

[117] D. Wallacher and K. Knorr, Phys. Rev. B **63**, 104202 (2001).

[118] E. Molz, A. P. Y. Wong, M. H. W. Chan, and J. R. Beamish, Phys. Rev. B **48**, 5741 (1993).

[119] D. W. Brown, P. E. Sokol, and S. N. Erlich, Phys. Rev. Lett. **81**, 1019 (1998).

[120] D. E. Silva, P. E. Sokol, and S. N. Erlich, Phys. Rev. Lett. **88**, 155701 (2002).

[121] E. D. Adams, K. Uhlig, Y.-H. Tang, and G. E. Haas, Phys. Rev. Lett. **52**, 2249 (1984).

[122] E. D. Adams, Y.-H. Tang, K. Uhlig, and G. E. Hass, J. Low Temp. Phys. **66**, 85 (1987).

[123] J. R. Beamish, A. Hikata, L. Tell, and C. Elbaum, Phys. Rev. Lett. **50**, 425 (1983).

[124] www.besoptics.com.

[125] P. Levitz, G. Ehret, S. K. Sinha, and J. M. Drake, J. Chem. Phys. **95**, 6151 (2004).

[126] A. Khurana, Physics Today **42**, 21 (1989).

[127] M. Chan, M. Ryschkewitsch, and H. Meyer, J. Low. Temp. Phys. **26**, 211 (1976).

[128] T. K. Herman, *Liquid-vapor critical behavior in silica aerogel*, PhD thesis, University of Alberta, 2005.

[129] C. J. Grebenkemper and J. P. Hagen, Phys. Rev. **80**, 89 (1950).

[130] D. F. Brewer and D. C. Champeney, Proc. Phys. Soc. London **79**, 855 (1962).

[131] R. Pelster, Phys. Rev. B **59**, 9214 (1999).

[132] D. Wallacher, V. P. Soprunyk, A. V. Kityk, and K. Knorr, Phys. Rev. B **66**, 014203 (2002).

[133] D. N. Bittner and E. D. Adams, J. Low Temp. Phys. **97**, 519 (1994).

[134] H. K. Christenson, J. Phys.: Condens. Matter **13**, R95 (2000).

[135] S. Balibar, D. O. Edwards, and C. Larouche, Phys. Rev. Lett. **42**, 782 (1979).

[136] E. R. Grilly, J. Low Temp. Phys. **11**, 33 (1973).

[137] E. R. Grilly and R. L. Mills, Ann. Phys. **18**, 250 (1962).

[138] E. R. Grilly and R. L. Mills, Ann. Phys. **8**, 1 (1959).

[139] S. Hunklinger and M. von Schickfus, *Amorphous Solids; Low Temperature Properties*, Springer, Berlin, 1981.

[140] S. Hunklinger and W. Arnold, *Physical Acoustics*, Academic, New York, 1976.

[141] N. Mulders, *Helium in Vycor: An Ultrasonic Study*, PhD thesis, University of Delaware, 1990.

[142] H. Nishiyama, H. Akimoto, Y. Okuda, and H. Ishimoto, J. Low Temp. Phys. **89**, 727 (1992).

[143] S. A. Khairallah and D. M. Ceperley, Phys. Rev. Lett. **95**, 185301 (2005).

[144] M. Rossi, D. E. Galli, and L. Reatto, Phys. Rev. B **72**, 064516 (2005).

[145] J. R. Beamish, N. Mulders, A. Hikata, and C. Elbaum, Phys. Rev. B **44**, 9314 (1991).

[146] J. F. Jarvis, K. Ramm, and H. Meyer, Phys. Rev. **170**, 320 (1968).

[147] N. V. Zuev, V. V. Boiko, N. E. Dyumin, and V. N. Grigorev, J. Low Temp. Phys. **11**, 597 (1998).

[148] C. Herring, J. App. Phys. **21S**, 437 (1950).

[149] Obtained from U.S. Bureau of Mines, Amarillo, Texas.

[150] www.collimatedholes.com.

[151] www.americanpiezo.com.

[152] www.comsol.com.

[153] J. Toner, *arXiv:0707.3842.*

[154] I. Iwasa, K. Araki, and H. Suzuki, J. Phys. Soc. Japan **46**, 1119 (1979).

[155] J. R. Beamish and J. P. Franck, Phys. Rev. B **26**, 6104 (1982).

[156] J. R. Beamish and J. P. Franck, Phys. Rev. B **28**, 1419 (1983).

[157] V. L. Tsymbalenko, Sov. Phys. JETP **47**, 787 (1978).

[158] M. A. Paalanen, D. J. Bishop, and H. W. Dail, Phys. Rev. Lett. **46**, 664 (1981).

[159] www.bostonpiezooptics.com.

[160] private communication with M. H. W. Chan.

[161] D. A. Huse and Z. U. Khandker, *cond-mat/0702243.*

[162] P.-G. DeGennes, C. R. Physique **7**, 561 (2006).

[163] Y. Hiki and F. Tsuruoka, Phys. Rev. B **27**, 696 (1983).

[164] J. R. Beamish and J. P. Franck, Phys. Rev. Lett. **47**, 1736 (1981).

[165] V. L. Tsymbalenko, Sov. Phys. JETP **49**, 859 (1979).

[166] L. P. Mezhov-Deglin, Sov. Phys. JETP **19**, 1297 (1964).

[167] L. P. Mezhov-Deglin, Sov. Phys. JETP **47**, 1297 (1966).

[168] L. P. Mezhov-Deglin, Sov. Phys. JETP **25**, 568 (1967).

[169] S. C. Lau and A. J. Dahm, Bull. Am. Phys. Soc. **23**, 317 (1978).

[170] I. Iwasa, Phys. Rev. B **66**, 144111 (2002).

[171] www.techfak.uni-kiel.de/matwis/amat/def_en/index.html.

[172] J. R. Beamish, *Dislocations and sound propogation in solid 3He and 4He*, PhD thesis, University of Alberta, 1982.

[173] A. Granato and K. Lucke, J. Appl. Phys. **27**, 583 (1956).

[174] T. Ninomiya, Phys. Soc. Jap. **36**, 399 (1974).

[175] I. Iwasa and H. Suzuki, J. Phys. Soc. Japan **49**, 1722 (1980).

[176] R. Wanner, I. Iwasa, and S. Wales, Solid State Commun. **18**, 853 (1976).

[177] F. Tsuruoka and Y. Hiki, Phys. Rev. B **20**, 2702 (1979).

[178] J. Day and J. Beamish, Nature **450**, 853 (2007).

[179] private communication with N. Prokof'ev.